The University Of Sheffield.

SHEFFIELD CENTRE FOR ADVANCED MAGNETIC MATERIALS AND DEVICES

The Role of Microstructure on the Performance of Sintered Nd-Fe-B Magnets

By

Ghaiath Abbas Fadhil

A thesis submitted in partial fulfillment of the requirement for the degree of Doctor of Philosophy

The Department of Materials Science and Engineering

The University of Sheffield

September, 2017

Abstract

A combination of electron microscopy analysis and micromagnetic modelling was used to study the microstructure role on the performance of commercial sintered Nd-Fe-B magnets that are used in wind power units. These magnets were observed to be composed of $Nd_2Fe_{14}B$ phase grains with different Dy content, size distribution and anisotropy orientation. The grains were surrounded by intergranular phases with different Fe/rare-earth ratios. The magnetic characterisation of these samples revealed that it is possible for Dy-free samples to have higher coercivities than Dy-containing samples with the control of the microstructure. Micromagnetic modelling revealed that decreasing the angular dispersion of $Nd_2Fe_{14}B$ grain anisotropy provides the most significant increase to coercivity. For example, decreasing this angular dispersion from 30° to 1° increased the coercivity by 25% of its initial values. In addition, the presence of intergranular phases with high Fe/rare-earth ratios (Fe-like) led to the generation of reversed domain walls at low applied field. The formation of non-ferromagnetic intergranular phases (low Fe/rare-earth) led to 8% increase in coercivity; however, it led to step-wise hysteresis loops. On the other hand, the effect of grain size distribution on coercivity was found to be less significant compared to previous features. Micromagnetic modelling of grain boundary diffused samples revealed that the coercivity may increase with increasing the thickness and Dy concentration of Dy-rich shells. In addition, the higher rare-earth content at the intergranular regions of these samples was revealed to be beneficial to coercivity. Finally, the possibility of twinning in main phase grains showed a detrimental effect on the coercivity. The formation of non-ferromagnetic intergranular phases may reduce the effect of twinned grains and increase coercivity but no significant increase in remanence and maximum energy density was observed. These insights could be useful to produce sintered Nd-Fe-B magnets with higher coercivity and lower heavy rare-earth content.

Acknowledgments

First and foremost, I would like to express my sincere gratitude to my supervisor Professor Dan A. Allwood for recommending me for this project and for the continuous support during my Ph.D. study. Our diverse conversations helped me on academic and personal levels, especially at hard times when my country seemed going towards non-existence. I was very lucky to have him as a mentor at this stage of my life.

Besides, I would like to thank my secondary supervisor Dr Julian Dean for his encouragement, advice and insightful comments. His enduring induction for modelling and programing was essential for my research. In addition, I am thankful for his support to my teaching career through the Sheffield teaching assistant scheme.

My sincere thanks also go to my fellow group members at the Sheffield centre for advanced and magnetic materials and devices (SCAMMD). Our fruitful conversations were vital for my research and academic career.

I would like to thank my lovely wife, Aliaa, for being next to me in this journey. She went through every high and low bit of it and expressed nothing but support and understanding. I am thankful for my daughter, Noor, for bringing happiness and joy to my life and I hope my present day efforts will be valuable for her in future. This Ph.D. study would not have been possible without the financial and emotional support and encouragement of my dearest father, Abbas. Not forget to mention the support of my mother, Iman, who always believed in me and pushed me not to limit my ambitions. Thanks to my mother-in-law, Anwar, for being understanding and supportive to me and my family the whole time we were away from her. I am also grateful for my brother, Ammar, for his restless trips to finish the paperwork on my behalf in dusty and crowded streets of Iraq. Finally, I am also thankful to my other brothers, sisters, my dear friends in Iraq and in the UK.

To all whom mentioned above, I hope that your belief in me was accurate and I hope I will be able to return some of your favours either in the near or distant future.

Ghaiath

September, 2017

Academic conferences

I have contributed my research in the following academic conferences:

- The University of Sheffield Engineering Symposium (USES), May 2015. ‘Improved Rare-Earth Permanent Magnets for Clean Energy Production’ (poster).
- The 13th Joint MMM-Intermag Conference, January 11-15, 2016, San Diego, California, USA. ‘Micromagnetic simulations of the dependence of sintered Nd-Fe-B permanent magnets performance on processing conditions’ (oral talk).
- The IOP Magnetism 2016 in Sheffield, UK. ‘Micromagnetic simulations of the dependence of sintered Nd-Fe-B permanent magnets performance on processing conditions’ (poster).
- Sustainable Functional Materials (SFM) 2016 in Scarborough, UK. ‘Micromagnetic Simulations of Rare-Earth Permanent Magnets Performance Dependence on The Processing Conditions’ (poster).
- The IOP Magnetism 2017 in the University of York, UK. ‘Micromagnetic Simulations of the Role of Intergranular Phases in Sintered Nd-Fe-B Magnets’ (oral talk).

List of abbreviations

Here, the abbreviations are listed in term of their appearance in the thesis.

H	The applied magnetic field
B	Magnetic induction
μ_0	Permeability of free space
M	Magnetisation
χ	Susceptibility
E_e	Exchange energy
J_{ex}	Exchange integral
S_i, S_j	Spin quantum numbers of two electrons
θ_s	Angle between two spins
A_{ex}	Exchange stiffness constant
T_c	Curie temperature
E_a	Magnetocrystalline anisotropy energy
K_0, K_1 & K_2	Anisotropy constants
θ_m	Angle between magnetisation vector and the easy axis
H_d	Demagnetisation field
E_m	Magnetostatic energy
N_d	Demagnetising field
E_z	Zeeman energy
θ	The angle between magnetisation vector and the applied field
E_t	Gibbs free energy
H_s	Saturation field
M_s	Saturation magnetisation
M_r	Remnant magnetisation
H_c	Coercive field
BH_{max}	Maximum energy field
H_A	Anisotropy field
RE	Rare-earth
F.T.M.	Ferromagnetic transition metals
B_r	Remnant magnetic induction
a & c	Lattice parameters
fcc	Face-centered-cubic structure

hcp	Hexagonal close packed
dhcp	Double-hexagonal close packed
S_{RE}	Substituents of RE atoms.
S_{Fe}	Substituents of Fe atoms.
D_1	Dopants reacting with RE atoms
D_2	Dopants reacting with B atoms.
d_s	Magnetic domain size
δ_w	Domain wall width
B_T	Temperature coefficient of remnant induction
H_T	Temperature coefficient of coercive field
α_i	Microstructural inhomogeneities and misalignment of grains parameter
N_{eff}	Effective demagnetization factor
H_N	Nucleation field
D_{th}	Grain diameter at thermal stability limit
D_R	Grain diameter close domain wall width
D_s	Grain diameter equal to single-domain particle size
D	Grain diameter
EB	Electric bikes
HEV	Hybrid electric vehicles
FBEV	Full-battery electric vehicles
3D	Three dimensional
PSA	Post-sintering annealing
GBD	Grain boundary diffusion process
Dy-free	A sample with no Dy content
Red-Dy	A sample with reduced Dy content
Dy-rich	A sample with the highest Dy content
XRD	X-ray diffraction
a.u	Arbitrary units
n	An integer
λ	X-ray wavelength
d, d_1 & d_2	Interplanar spacing
θ_i	X-ray incident angle
h, k & l	Miller indices
ICDD	The international centre for diffraction data
PDF	Powder diffraction file

SEM	Scanning electron microscopy
Elec.	Electrons
BSE	Backscattered electron imaging
SE	Secondary electron imaging
EDX	Energy dispersive X-ray spectroscopy
wt.%	Weight percentage
at.%	Atomic percentage
EBSD	Electron backscattered diffraction
MAD	Mean angular deviation
Ref.	Reference
IPF	Inverse pole figure
D_x	Mean grain diameter along *x*-axis
R_x	Number of rows in *x* direction
P_x	Number of pixels in *x* direction
S	Step size
N_x	Number of grains counted in *x* direction
D_y	Mean grain diameter along *y*-axis
N	Number of grains counted in the sample
δ	Standard error
σ	standard deviation of the diameter
2D	Two dimensional
m	Magnetic moment
H_{ext}	External field
H_{eff}	Effective field
LLG	Landau-Lifshitz-Gilbert equation
α	Gyromagnetic dimensionless factor of damping
t	Time
J	Magnetisation vector
γ	Gyromagnetic precession factor of damping
FDM	Finite difference method
FEM	Finite element method
l_{ex}	Exchange length
K_u	Uniaxial anisotropy energy
VSM	Vibrating sample magnetometer
Z	The atomic number

BC	Band contrast
β	The angle between the z pole of the object to the Z-axis.
α	The angle between the x pole of the object to the X-axis.
γ	The angle between the x pole of the object and the XY plane
SE	Standard error
GB	Grain boundary
3DAP	3-dimensional atom probe
GSD	Grain size distribution
+ve	Positive
-ve	Negative
C	Concentration
Remnant E_t	The value of Gibbs total free energy at the remanence field
Max E_t	The maximum value of Gibbs total free energy
x	Reduction factor
d_A	The diameter of grain A
d_B	The diameter of grain B
θ_A	The angle between the anisotropy of grain A and the applied field
θ_B	The angle between the anisotropy of grain B and the applied field
ϕ	angular dispersion of grains alignment
$C_{surface}$	Concentration at surface
C_{core}	Concentration at core
D_c	Diffusion coefficient
t	Dy-rich shell thickness
C	Dy concentration at point x in the sample
θ_1 & θ_2	The angle between the anisotropy of twinned regions and applied field
θ_t	The total twinning angle
H_f	The forming field
ϕ	The angle between the twinning boundary and the applied field

Table of contents

1.Introduction

1.1 The market demand

The production of sintered Nd-Fe-B magnets increased from 6,000 tons in the mid-1990s to more than 65,000 tons in 2009 due to the suitability of their magnetic characteristics to a wide variety of applications [1]. Nd-Fe-B magnets are pre-eminent in terms of their high energy density and coercivity and they are widely used despite their poor high temperature performance, machinability and corrosion resistance. [1]. The applications of Nd-Fe-B magnets nowadays are very diverse in type and size but the biggest share of their use is in generators, motors and hard disk drives (fig. 1.1) [1-4]. Reducing the cost of high performance permanent magnets is essential for technologies such as energy generation and electric vehicles.

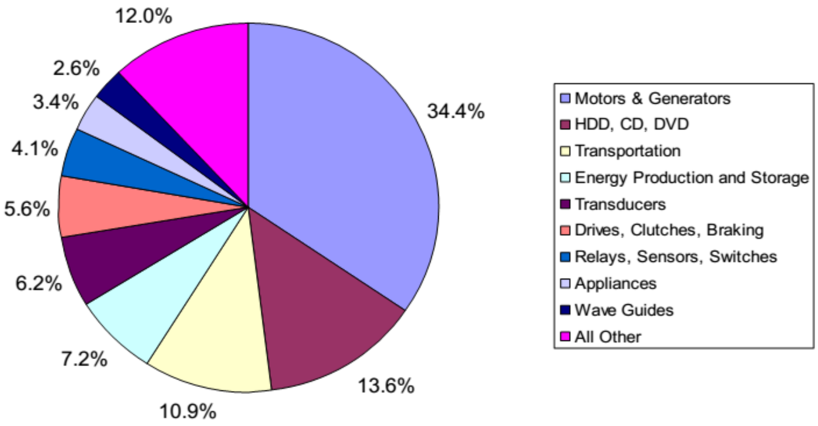

Figure 1.1 The most common applications of rare-earth magnets for year 2012 [4]. Copyright of Journal of Sustainable Metallurgy.

Electric generators based on using Nd-Fe-B magnets have more room for improving their reliability and output due to the stronger remanence of these magnets [1, 2]. The hard disk drive (HDD) industry uses Nd-Fe-B magnets in the motors that spin the disks and move the read/write heads [2, 4]. Although the size of these devices has been reduced rapidly over the years, they represent a big share of the Nd-Fe-B market due to the sheer number of devices produced [4]. Nd-Fe-B magnets are used in other applications such as iPods, children toys, magnetic separation units, sensors, braking systems and battery-operated applications [1, 2, 4] The latter category includes mobile phones, electric assisted vehicles and magnetic-resonance imaging (MRI) units [2]. This wide range of application caused a significant growth in the Nd-Fe-B magnets market, which was estimated to be ~12% per year [1]. The clean energy industry is gaining more attention currently due to the issues of pollution and scarcity of energy supply [2]. This has also been driven by the fear of failure in nuclear energy industry and the issues of nuclear waste [2]. Wind power units and hybrid electric vehicles (HEV) are essential parts of clean energy industry and they both rely on permanent magnets in their use and, most prominently, on sintered Nd-Fe-B magnets [2, 3, 5].

In clean energy production, HEVs are emerging as an important part of the automotive industry since the use of Nd-Fe-B magnets in their electric motor reduced the size of motors, increased the magnet’s torque and lowered its weight [1]. In addition, the improvements in the design and output of wind power units has opened a new market for installation [2]. For example, China’s wind power installation was almost non-existent before 2005 but it is leading in the number of units installed nowadays with about half of the world’s total [2]. The Nd-Fe-B based wind power units caused a constant growth in the installed wind power capacity as revealed by World Wind Energy Association (WWEA) data for years 2000-2015 (fig. 1.2) [6]. In addition to China, there are other countries turned their attention to wind power energy, such as Uruguay and the USA [6]. The installed capacity of wind power units reached 500,000 MW by the end 2016, which is double the capacity at 2012 [6]. The demand for Nd-Fe-B magnets is expected to be higher in the next few years. While Fe and B resources are more abundant, rare-earth elements supply is the major issue [7, 8].

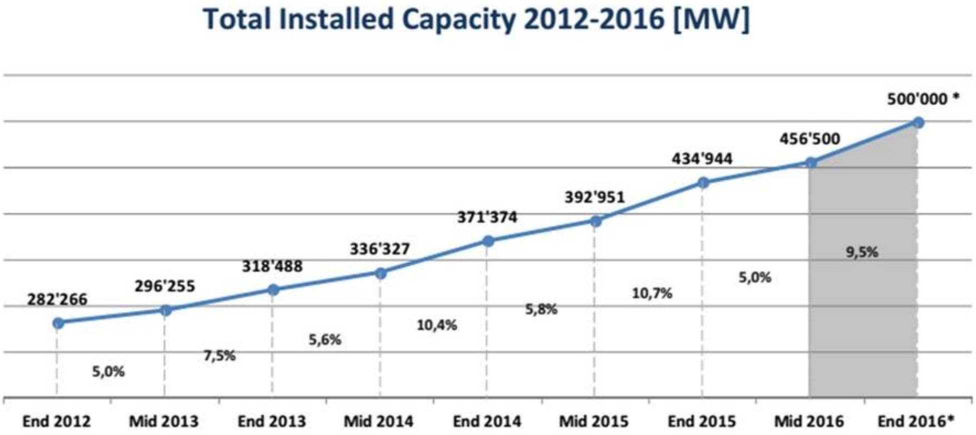

Figure 1.2 Total installed capacity (MW) of wind power units in the period 2012-2016. Data from World wind energy association [6]. Reprinted with permission of WWEA, Germany.

1.2 Current issue

The resources of rare-earth elements are spread over some regions around the world; however, about 90% of these resources are in China [2] and the clean energy industry relies on China’s export of these elements [2]. Nd is relatively more abundant and has a cheaper price but Dy has caused the most of the industry’s concern [2, 9]. This is due to the instability of rare-earth elements prices, which underwent severe fluctuations in 2011 when the prices of Nd and Dy hit a record value of more than 300 times their price before that year [1]. This disturbance was caused by many factors: firstly, the laws issued by the Chinese government to increase the tax on rare-earth exports to about more than 25% in order to limit the foreign exports of rare-earth elements [2]; secondly, the huge demand inside China for these elements due to the high number of wind unit installations [1, 2] and finally, the high demand of rare-earth elements in the global market [1]. The prices of rare-earth elements dropped after 2011, but they remained at more than 10 times higher than their prices before 2011 (fig. 1.3). However, any imbalance between the supply and demand of these elements is expected to bring further unrest to their prices, which is a major concern for the clean energy industry. For these reasons, the US Department of Energy has identified the supply of Nd and Dy as being at a high risk for the period 2015-2025 [2].

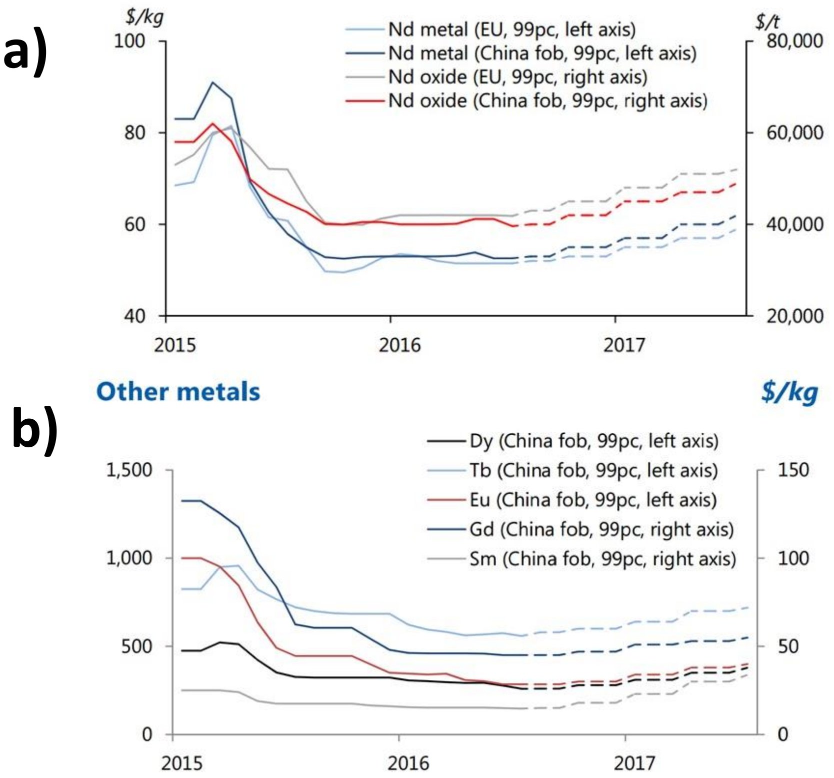

Figure 1.3 The average price of (a) Nd- metal and oxides and (b) other heavy rare-earth elements over the period 2015-2017 [10]. Reprinted with permission of Argus Media group, http://www.argusmedia.com/.

Nd is a main constituent element of the $Nd_2Fe_{14}B$ alloy, while Dy is only used to partially replace Nd concentration in order to improve the coercivity of the magnet and its thermal stability [9]. Since the coercivity of permanent magnets is related to the magnet's microstructural features [11-13]; eliminating the use of Dy could be possible through the successful control of these magnets' microstructure. The current focus of research is to develop a Nd-Fe-B magnet with lower Dy additions [5, 13, 14]. This is encouraged by the fact that $Nd_2Fe_{14}B$-based magnets are currently at 20-30% of the theoretical coercivity of the

$Nd_2Fe_{14}B$ phase [5], which highlights the need to improve the understanding of the microstructure role on the magnetic properties in these magnets. Such understanding is essential for the success of hardening mechanisms working to achieve sintered Nd-Fe-B magnets with reduced Dy additions.

1.3 Thesis outline

The main aims of this thesis are to:

1. Provide a comprehensive analysis of the microstructural features of commercial sintered Nd-Fe-B magnets that are used in wind power units and the possible effect of these features on the overall magnetic properties of each magnet.
2. Develop a micromagnetic modelling approach to simulate the hysteresis loops and demagnetisation processes in hard magnets.
3. Combine the microstructure analysis and micromagnetic modelling to provide an assessment of possible coercivity hardening mechanisms through the control of intergranular phases, angular dispersion of grain anisotropy, grain size distribution and grain boundary diffusion processes. This is also accompanied by studying the effect of twinned main phase grains on the magnet's coercivity.

This thesis includes nine chapters (this being Chapter 1) where Chapter 2 presents the fundamentals of ferromagnetic materials and their main magnetic characteristics. Chapter 3 reviews the development, the microstructural and magnetic characteristics of sintered Nd-Fe-B magnets. This is accompanied by a discussion on the research efforts to understand the magnetic behaviour of these magnets and efforts to improve their maximum energy density. Chapter 4 introduces the main experimental and modelling methods used in this work. This includes x-ray diffraction, scanning electron microscopy, backscattered electron diffraction and micromagnetic modelling.

Chapter 5 presents magnetic, X-ray diffraction and electron microscopy analysis of sintered Nd-Fe-B samples. This includes the use of scanning and backscattered electron imaging and also the use of energy dispersive X-ray analysis. In chapter 6, the angular dispersion of grain alignment is examined using backscattered electron diffraction. This is accompanied by a comparison between the grain size distributions of the studied samples. Chapter 7 demonstrates the use of finite element method for micromagnetic modelling of the effect of microstructural features revealed by experimental analysis on the coercivity of sintered Nd-Fe-B magnets. This includes studying the effect of intergranular phases, anisotropy alignment of main phase grains and grain size distribution. Chapter 8 describes the use of micromagnetic modelling to study the effect on the internal structure of $Nd_2Fe_{14}B$ grains in the case of grain boundary diffusion processes and twinned grains on the coercivity of sintered Nd-Fe-B magnets. Chapter 9 summarizes the main outcomes of the thesis and considers future implications.

2.Introduction to Magnetism and Magnetic Materials

Magnetic materials are central to a large number of applications in modern life, for instance: in power generation, computing, transportation, domestic appliances and medical devices [15, 16]. The widespread use of magnetic materials has been enabled by the efforts of researchers to understand magnetic properties and their origin [15, 16]. Some of the basic principles of magnetism are explained in this chapter. The focus is on introducing the phenomena relevant to later chapters of this work.

2.1 Magnetisation and magnetic materials

Most materials produce a magnetic field in response to an applied external field. However, materials are referred to be magnetic only if they are able to exhibit a magnetic field even with the absence of external fields [17, 18]. The response to magnetic field is known as magnetism, which is related to and determined by the magnetic moments of electrons and the electronic configuration of atoms [17, 18]. Each electron in an atom contributes a magnetic moment due to (a) its orbital motion around the nucleus and (b) its quantum mechanical spin property [18]. The total magnetic moment of an atom is a combination of spin and orbital magnetic moments [18, 19].

When a magnetic field is applied (H) to a material, the generated magnetic induction (B) in the material is a result of the external field strength and the net magnetic moment of that material [17, 18]. This magnetic induction is expressed by:

$$B = \mu_0 (H + M) \tag{2.1}$$

where μ_0 is the permeability of free space and M is the magnetisation of the material [16, 18]. Each material will have a different M because of the differences in the number of electrons in atoms and molecules [18]. The relationship between the applied field and the magnetisation of the sample is known as the magnetic susceptibility (χ), which is expressed by:

$$\chi = \frac{M}{H} \tag{2.2}$$

The magnetic susceptibility values are characteristic to each particular material [16, 18], as it will be detailed in the next section.

2.2 Types of Magnetic Materials

Materials may be categorised according to their susceptibility to the magnetic field applied [15, 20]. These categories are:

- Diamagnetic materials, which have small and negative values of $\chi<1$ (fig. 2.1a) [16]. The application of magnetic field to these materials causes a change in the orbital motion of electrons, which creates a magnetic moment that is both very small and have an opposite direction to the applied field [18]. All materials have diamagnetism but it is usually not observed in the presence of other types of magnetism [16]. However, there are some materials that have only this type such as Cu, Au and Si [16, 18].
- Paramagnetic materials where χ is typically small and positive ($<10^{-3}$) (fig. 2.1a) [16]. This type of magnetism exists in materials that have atomic magnetic moments with random alignment in the absence of applied field [18]. The application of magnetic

field will induce an alignment of moments; however, the thermal energy will continue to disorder this alignment [16, 20, 21]. Examples of paramagnetic materials are Al and Na [16]. Both diamagnetic and paramagnetic materials are considered to be non-magnetic materials.

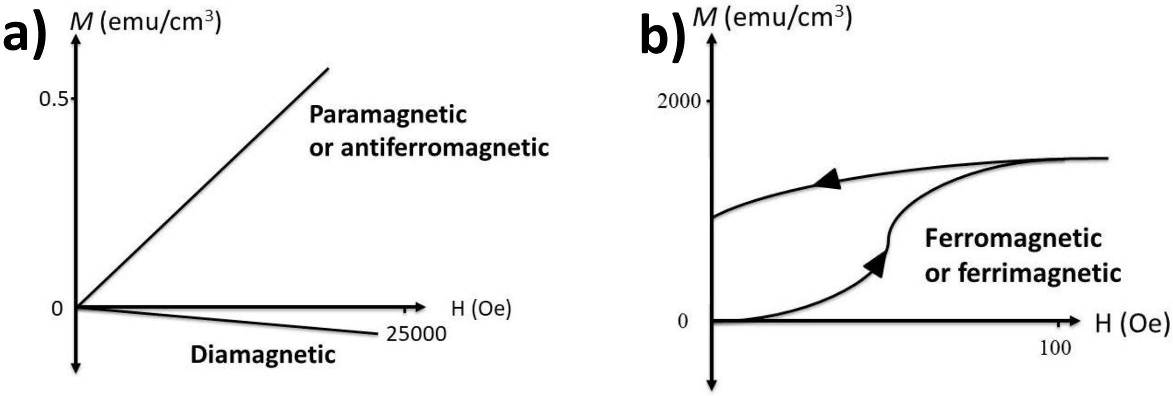

Figure 2.1 Magnetisation curves of (a) diamagnetic, paramagnetic and antiferromagnetic and (b) ferromagnetic and ferrimagnetic materials [21]. Reprinted with permission of Cambridge University Press.

- Ferromagnetic materials have a positive and larger χ compared to previous categories (>10^3) (fig. 2.1b) [21]. Ferromagnetic materials have a magnetic moment in the absence of applied magnetic field [16, 18] and their magnetisation is very high compared to other types of magnetism even with small applied field. Examples of ferromagnetic elements are Ni, Co, Fe and Gd [18]. Ferromagnetic materials are very useful and the ferromagnetic behaviour is the base for a wide range of everyday applications. Further details about the ferromagnetic behaviour will follow in §2.3.
- Anti-ferromagnetic behaviour exists in materials that has a magnetic moments coupling, but other than the ferromagnetic materials [16, 21]. The difference in these materials from ferromagnetic materials is that magnetic moments are aligned opposite to each other, which leads to a zero net magnetisation [18]. Also, χ values are positive

and low compared to ferromagnetic materials (fig. 2.1a). Examples of anti-ferromagnetic materials are Mn, Cr and their compounds [18].

- Ferrimagnetic type of magnetism occurs in ceramics and Fe_3O_4, for instance [18]. These materials exhibit a magnetisation with a strength dependent on their elemental composition [16, 21]. The reason behind this lower magnetisation is that atomic magnetic moments are not equal in strength and aligned opposite to each other [18]. As a result, the moments will cancel each other and the net magnetic moment will depend on number of atoms in the material. Ferrimagnetic materials have comparable χ values to ferromagnetic ones (fig. 2.1b).

2.3 Ferromagnetism

2.3.1 Magnetic energies

In order to understand the magnetic behaviour of ferromagnetic materials, it is important to understand the atomic magnetic moment interactions with crystal lattice of these materials and with the applied field. These interactions are explained as the result of minimisation of four energy terms [17]. The first term is the **exchange energy**, which results from the long-range ordering force that creates a tendency in magnetic moments to align parallel to each other even in the absence of applied magnetic field [18, 19]. The origin of exchange energy in ferromagnets is related to the electron spin moments explained by Pauli Exclusion Principle and Hund's first rule [16, 19]. The energy of exchange (E_e) depends on the relative spin alignments of electrons:

$$E_e = -2J_{ex}S_iS_j = -2J_{ex}S^2 \cos\theta_s \tag{2.3}$$

where J_{ex} is the exchange integral, S_i and S_j are the spin quantum numbers of two electrons and θ_s is the angle between two spins [17, 18]. The definition of E_e indicates that it is energetically favourable for spins to align parallel if $J_{ex}>0$, which is the case in ferromagnetic materials. On the contrary, it is energetically favourable for spins to align antiparallel if $J_{ex}<0$, which is true in antiferromagnetic materials [3]. The strength of the exchange energy in any magnetic material is expressed by a quantity known as the exchange stiffness constant (A_{ex}), which is dependent on the electronic structure of the atoms [17-19]. It should be noted that temperature can influence A_{ex} [19]; for example, increasing the material's temperature can reduce A_{ex}. This is manifested by an increased misalignment between magnetic moments, which will lead to reduced magnetisation [17, 21]. The reason behind this effect is that the increased thermal energy at higher temperatures reduces the ordering molecular field, which disrupts the alignment between exchanged magnetic moments [17, 18]. The material's magnetisation may be zero at a certain temperature where the magnetic moments alignment will become random. This temperature is known as the Curie temperature (T_c) [16, 18, 21].

The second energy term is the **magnetocrystalline anisotropy** energy, which is represented by the preference of ferromagnetic materials to be magnetised along a known crystallographic direction called 'the easy axis' [16-18]. Magnetising a material along its easy axes requires lower magnetic field than other axes. While the atomic magnetic moments arise from the spin and orbital motion of its electrons (see §2.1), it should be noted that spin magnetic moments of electrons interact with the magnetic field of their orbital motion leading to what is known as 'spin-orbit coupling' [16, 18]. Thus, an extra energy is needed to rotate the spins of atoms when a magnetic field is applied due to this spin-orbit coupling. However, the orbital itself is also coupled to the crystal field of the material's lattice [18]. For this reason, magnetocrystalline anisotropy energy is attributed to the spin-orbit coupling [18, 19].

Spin-orbit coupling is weak in most materials such as single element Fe or Co, hence their magnetocrystalline energy is low [16, 18]. However, the effect of spin-orbit coupling increases with higher atomic number of materials [18]. Hence, rare-earth compounds have a stronger spin-orbit coupling [17, 18], which results in a higher magnetocrystalline energy, as we will see in Chapter 3. Examples of easy axes are <100> for *bcc*-Fe, <111> for *fcc*-Ni and <1000> for *hcp*-Co (fig. 2.2) [17]. The uniaxial magnetocrystalline anisotropy energy (E_a) can be calculated from:

$$E_a = K_0 + K_1 \sin^2 \theta_m + K_2 \sin^4 \theta_m + \cdots \qquad (2.4)$$

where K_0, K_1 *and* K_2 are the anisotropy constants and θ_m is the angle between the magnetisation vector and the easy axis [17, 18].

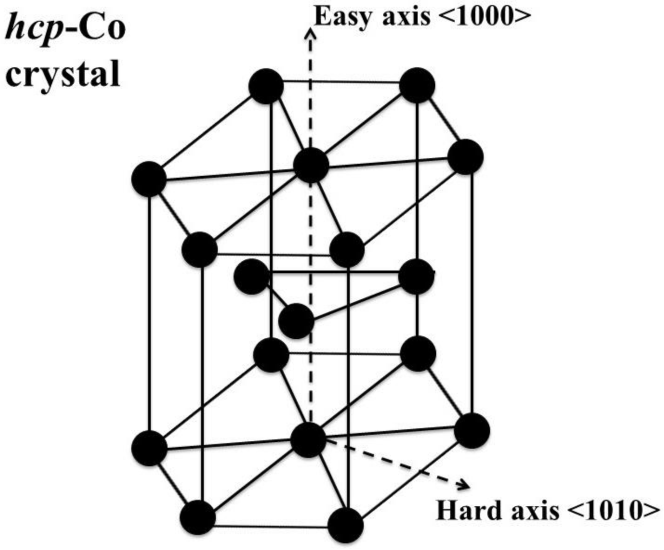

Figure 2.2 A schematic representation of the easy and hard axes in *hcp*-Co crystal. The lattice parameters are exaggerated in order to show the easy and hard axes clearly.

The third energy term is the **magnetostatic energy**. When a ferromagnetic sample is magnetised, it will create a magnetic field in the opposite direction of the sample magnetisation [16, 18]. This field represents the tendency of the magnetic field of a material to de-magnetise itself, hence it is called the demagnetisation field (H_d) [16, 18]. The demagnetising field contributes to the magnetostatic energy (E_m) [18], which can be calculated from:

$$E_m = \frac{1}{2}\mu_0 H_d M \tag{2.5}$$

H_d can be calculated from:

$$H_d = -N_d M \tag{2.6}$$

where N_d is the demagnetising factor, which can have values between 0-1 [18, 19]. Another effect contributes to magnetostatic energy is known as shape anisotropy. This effect is related to sample dimensions and shape.

The last energy term is the **Zeeman** energy, which arises from the interaction between the applied field and the magnetic moment of the material. This energy represents the external magnetic field contribution to the total magnetic energy of the system. Zeeman energy (E_z) can be calculated from:

$$E_z = -\mu_0 M H \cos\theta \tag{2.7}$$

where θ is the angle between the applied field and the sample's magnetisation. There are other energy contributions that play a part in determining the total energy of the system such as: magnetostrictive energy. The total energy of the system is known as Gibbs free energy (E_t), which can be calculated from:

$$E_t = E_e + E_a + E_m + E_z \tag{2.8}$$

2.3.2 Magnetic domains and their walls

At temperatures lower than T_c and in the absence of external magnetic field, the magnetic structure of ferromagnetic materials consists of regions of uniform magnetisation known as 'the magnetic domains' [17, 19]. The magnetisation alignment is the same inside each domain, but has different alignment to other domains. The mechanism of the formation of these domains and what affect their size and orientation is much understood and explained by the energies competing inside the ferromagnetic material [16, 19]. The effect of exchange energy in aligning the magnetic moments parallel to each other was explained earlier (see §2.3.1). This means exchange energy favours a single domain magnetic structure with minimum misalignment of magnetic moments. However, single domain materials have a strong demagnetising energy (fig. 2.3a) [22]. In order to minimise this energy, the material tends to divide itself into domains that leave no free magnetic poles at sample's surface (fig. 2.3b & -c).

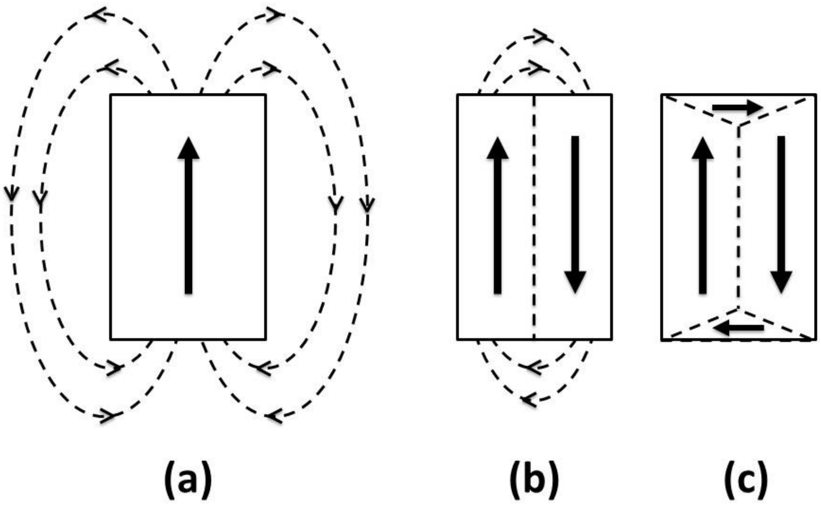

Figure 2.3 A representation of minimizing magnetostatic energy in ferromagnets by dividing the material itself from (a) one domain into (b) higher number of domains until (c) it leaves no surface poles. Adapted from reference [16], and reprinted with permission of Cambridge University Press.

The interface between different domains will have regions where magnetisation direction is changed. This change in magnetic moments' orientation is gradual to the extent that these boundaries thickness varies between 5 nm to 10 µm [21]. These boundaries are known as domain walls [16, 19]. The width of domain walls is determined by the characteristic magnetic properties of the material [19]. Magnetocrystalline energy favours thin domain walls, while exchange energy favours wider walls. However, the most favourable domain walls are the ones that produce no poles inside the material and the ones that achieve the lowest energy possible [17]. There are several types of domains such as: Néel walls and Bloch walls (fig. 2.4) [16].

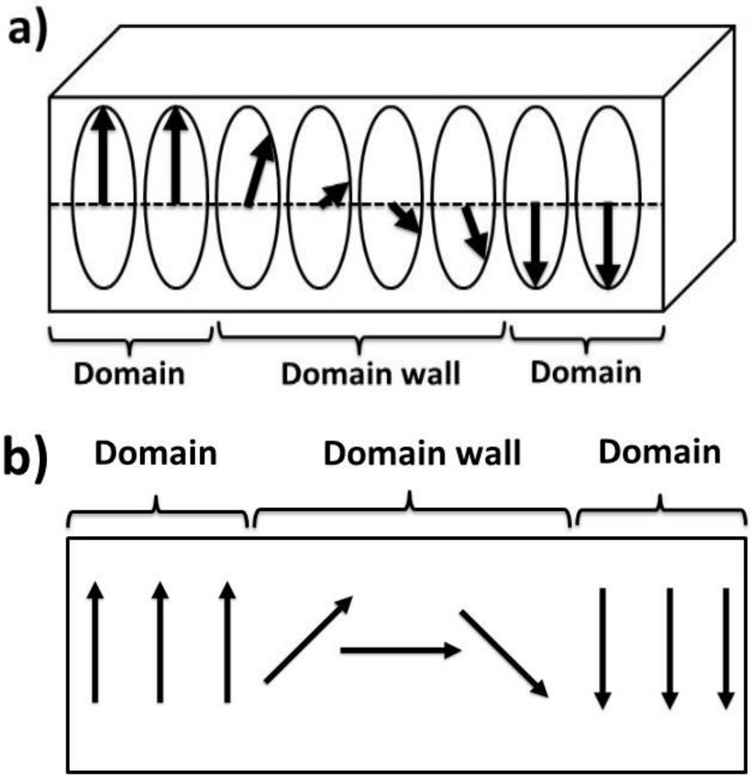

Figure 2.4 An illustration of (a) Bloch and (b) Néel walls adapted from reference [23].

The final domain structure will result from compromising the magnetic energies to produce the most favourable structure possible [19]. Exchange energy prefers aligned moments, magnetostatic energy prefers no surface poles, applied magnetic field prefers magnetic moments aligned in the field direction and magnetocrystalline energy prefers moments aligned parallel to the easy direction. The energy cost of creating domain walls is also important in determining the domain structure. This energy increases with increasing the domain area [23].

2.3.3 Hysteresis loops

Ferromagnetic materials at a relaxed state are likely to consist of magnetic domains that are separated by domain walls (I in fig. 2.5) [16, 18]. The shape and size of these domains change when a magnetic field is applied causing the movement of domain walls inside the sample. The domains that have the closest alignment to the applied magnetic field will grow in size at the expense of domains that are misaligned to the field direction (II and III) [16]. The continuous increase of the applied field will lead to the formation of a single domain structure (IV). The full alignment of this domain in the field direction will mark the saturation point and the field value at this appoint is called 'the saturation field' (H_s) [16]. The amount of magnetisation achieved at this point is called the saturation magnetisation (M_s). Any further increase in the field beyond this point will cause no change in the magnetic structure [16, 21].

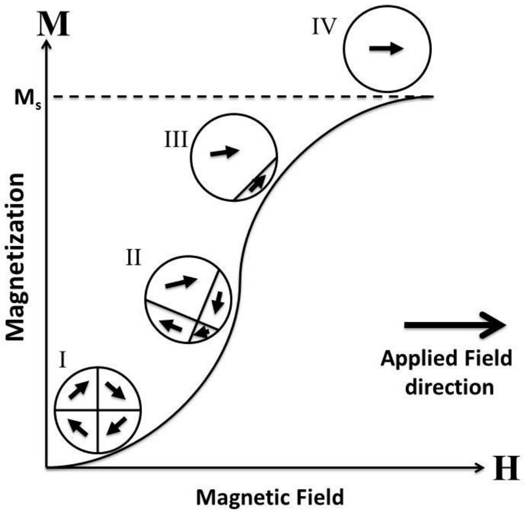

Figure 2.5 A schematic illustration of the magnetisation process of a sample from no field applied until saturation adapted from reference [16] and reprinted with permission of Cambridge University Press.

When the applied field is gradually removed, the domain magnetic moment will start rotating back to its easy axis [16, 19]. The domain walls will start moving back to adjust to the changed system's total energy. However, domain structure does not retrace back to its zero field structure and also the domain walls will not return back to their original positions. This is mainly attributed to the inability of the demagnetising field to overcome the energy barriers of pinning sites [21]. Examples of these pinning sites are structural defects, impurities and grain boundaries [16]. For this reason, some domains will preserve their orientation and energy. This hysteresis behaviour of magnetisation is characteristic of magnetic materials. The amount of magnetisation that resides in the material is called 'the remanence' (M_r) and magnetic materials that retain some magnetisation in their structure are called 'permanent magnets' [15, 17]. In order to remove the residual magnetisation from the material, a magnetic field should be applied in the opposite direction to the original field direction. The strength of the opposite magnetic field required to return the magnetisation to zero values is called the 'coercive field' (H_c) [21]. The full cycle of magnetising and demagnetising magnetic materials is called 'the hysteresis loop', which is illustrated in fig. 2.6 with the main magnetic parameters M_s, M_r and H_c noted.

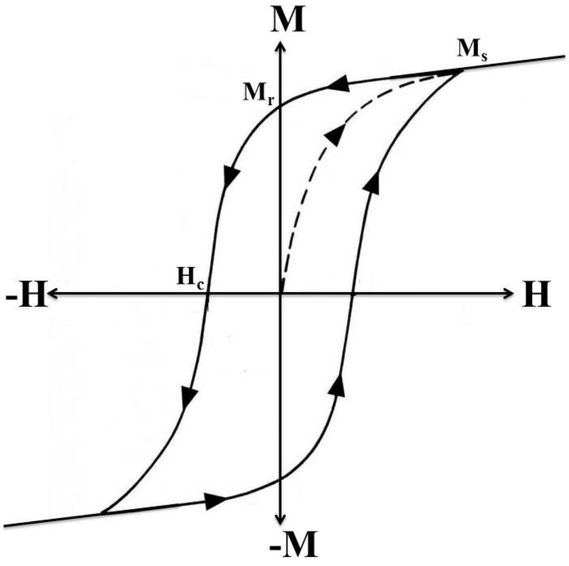

Figure 2.6 An illustration of a typical full hysteresis cycle of magnetisation/demagnetisation process in ferromagnetic materials.

2.4 Hard magnetic materials

2.4.1 Overview

The hysteresis loops of ferromagnetic and ferrimagnetic materials are of a major importance in practical applications [17, 18]. The characteristics of the hysteresis loop are used to classify ferromagnetic and ferrimagnetic materials [18]. Materials with low coercivity and high initial permeability are known as 'soft magnets' [16]. Examples of soft magnets are NiFe and pure Fe. On the other hand, magnets that have lower initial permeability are called 'hard (or permanent) magnets' [16]. Hard magnets have relatively higher coercivity, which means a broader hysteresis loop [17]. Fig. 2.7 illustrates a comparison between hysteresis loops of hard and soft magnets.

Hard magnets require high magnetic field strength to be magnetised, also the energy losses are much higher than soft materials [21]. However, they have high internal demagnetising fields [16]. The field generated by the magnetisation outside the magnet is known as 'the stray field' [16]. This field is responsible for all the forces and torques of the magnet and for this reason hard magnets applications make use of this stray field in their performance [7]. Hard magnets are used in a variety of applications; most notably in automotive industry and power generation [7, 8].

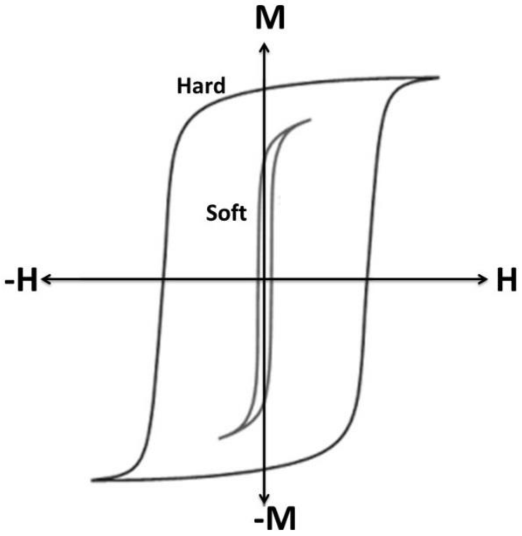

Figure 2.7 A relative illustration of M-H loops of hard and soft magnets**.**

2.4.2 Energy density

One of the engineering quantities that are used in characterising hard magnets is the maximum energy density or the energy product (BH_{max}) of the magnet [8]. This quantity represents the maximum energy that a magnet can store before full reversal. Theoretically, BH_{max} is deduced from the ideal square loop at the second quadrant of B-H loop (fig. 2.8). BH_{max} represents the area of the maximum product of the B-H values [8, 21]. For a compact magnet with an optimized design, BH_{max} can be calculated through [8]:

$$BH_{max} = \mu_0 \, M_s^2/4 \ldots \qquad (2.9)$$

Permanent magnets can be classified according to the ranges of BH_{max} they can preserve [21]. Magnets with BH_{max} values between 2-80 $kJ.m^{-3}$ are known as ‘conventional’ hard magnets [21]. Examples of these materials are ferrites, steel and alnico (Al-Ni-Co). On the other hand, magnets that exceed 80 $kJ.m^{-3}$ are known as ‘high energy density’ magnets [21]. Examples are Sm-Co and Nd-Fe-B magnets [13].

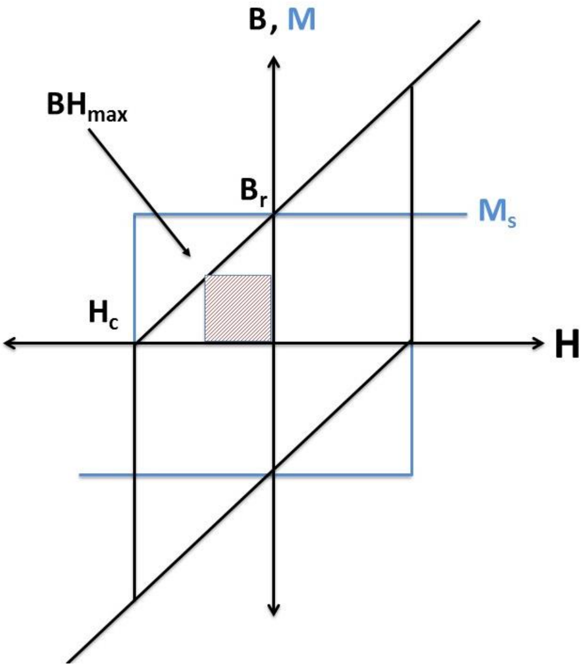

Figure 2.8 An illustration of the energy density of hard magnets (shaded area).

2.4.3 Brown's Paradox

Stoner-Wolfharth introduced the model of coherent rotation of magnetisation in ferromagnetic materials [19]. This model is known as 'Stoner-Wolfharth model', which describes mechanism of the magnetisation rotation of a single domain particle to the opposite direction [19]. In this model, the field required to rotate the magnetisation of a single domain particle a coherently to the demagnetised state is known as the anisotropy field (H_A) and it can be calculated from [8]:

$$H_A = {}^{2K_1}/_{M_s} \tag{2.10}$$

where K_1 is the magnetocrystalline anisotropy constant. According to this model, the coercivity of ferromagnetic materials should be the equal to the anisotropy field (H_c=H_A). In experimental samples, coercivity of Nd-Fe-B magnets are about (20-30%) of their anisotropy field values [7, 8]. This difference between theoretical and experimental values of coercivity is known as ‘Brown’s paradox’ and it attributes this difference to the effect of microstructural features in the magnet’s microstructure [8, 13]. Brown’s paradox represents the need to improve the understanding of the relationship between the magnetic behaviour and these microstructural features. This improved understanding is likely to narrow the discrepancy between theoretical and real values of magnetic properties in hard magnets.

3.Literature Review

In this chapter, the history and magnetic properties of rare-earth magnets will be reviewed. This includes a more in details focus on sintered Nd-Fe-B magnets, the materials of interest in this study.

3.1 Developments of rare-earth magnetic compounds

Permanent magnets made of ferrites and Nd-Fe-B alloys dominate the current global permanent magnets market, although Sm-Co and Alnico magnets still have some contribution to it (fig. 3.1) [2]. The market of Nd-Fe-B magnets noticed a rapid growth since the material was discovered in the early 1980s and they occupy about 60% of the current market [2, 7]. This is mainly represented by the use of these magnets in power generation applications, computer hard disk drives and recording media [2, 7].

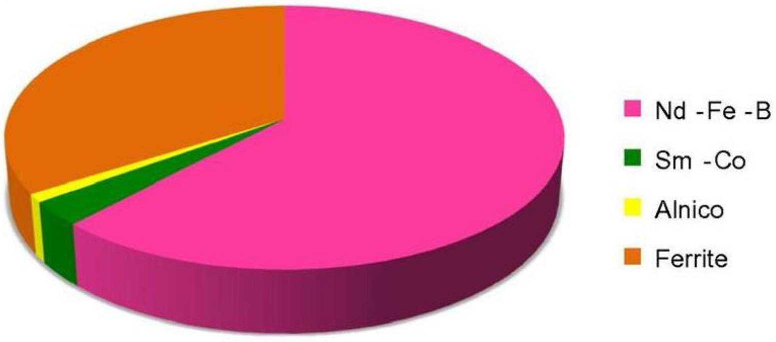

Figure 3.1 The permanent magnets shares in overall $9 billion global sales in 2010 [13]. Reprinted with permission of John Wiley and Sons, Inc.

The intermetallic combination between the 3d transition metals and 4f rare-earth elements is an important feature of rare-earth (RE) permanent magnets [7, 8]. Ferromagnetic transition metals (F.T.M.) such as Fe, Co and Ni exhibit a ferromagnetic behaviour at room temperature with high magnetic moment and Curie temperature. For this reason, most of the magnetic applications have at least one of these metals. The carrier for the magnetism in these metals is the 3d shell electrons [18]. On the other hand, the carriers for magnetism in RE elements are the 4f electrons [18]. These elements are divided into light elements (La, Ce, Pr, Nd, Sm and Eu) and heavy elements (Gd, Tb, Dy, Ho, Er and Tm) depending on the number of 4f electrons. Light RE elements mostly have low Curie temperatures and weak exchange interaction, which causes them to exhibit an antiferromagnetic behaviour at low temperatures [18]. Heavy RE elements have higher Curie temperatures and ferromagnetism at low temperatures [18]. The magnetic exchange between the spins of 3d and 4f atoms in the RE-F.T.M compounds is responsible for their M_s and K_1. The spin-orbit coupling in RE elements provides these compounds with high uniaxial K_1, while the transition metal provides it with its magnetisation and Curie temperature [18].

$SmCo_5$ was the first RE permanent magnet discovered in 1966 [7, 8]. The $SmCo_5$ phase has a hexagonal structure that produces a high uniaxial K_1~17.2 $MJ.m^{-3}$, M_s=860 $kA.m^{-1}$ and BH_{max}=190 $kJ.m^{-3}$ [7, 8]. Further development on the processing of $SmCo_5$ magnet led to the production of the Sm_2Co_{17} compound, which has a much higher magnetisation [7, 8]. This compound has K_1=4.2 $MJ.m^{-3}$ and M_s=0.97 $MA.m^{-1}$ in its hexagonal or rhombohedral crystal compared to the $SmCo_5$ [7, 8]. By the 1970s, BH_{max} of 260 $kJ.m^{-3}$ was possible to produce using Sm_2Co_{17} magnets [7, 8]. Since then, RE-based magnets have become the base of industrial high-performance permanent magnets.

The use of Sm-Co magnets has stumbled upon the abundancy of their raw materials. For instance, the global availability of Co is about 2000 times less than Fe [7, 8]. In addition, Fe is more abundant than all the materials in the RE and F.T.M. categories. However, Sm and Fe couple antiferromagnetically, which reduces the magnetisation of any Sm-Fe compounds significantly [7, 8]. In contrast, Nd is more abundant than Sm and its electronic spins couple ferromagnetically to Fe spins [18]. However, there are no stable compounds of Nd-Fe at room temperature and a third element is needed to stabilize the Nd-Fe alloy [7, 8] that should cause the least reduction in M_s and K_1. In 1982, two groups produced tetragonal $Nd_2Fe_{14}B$ by sintering [24] and melt-spinning [25] and measured its M_s to be 1.28 $MA.m^{-1}$ and BH_{max}=474 $kJ.m^{-3}$. Since then, the use of Nd-Fe-B magnets in many everyday-life applications has expanded significantly due to the capacity they exhibited [5].

Nowadays, Nd-Fe-B magnets have a very high demand in various applications, especially in clean energy technologies such as wind turbines and electric vehicles [2]. The improved understanding of their microstructural features will lead, most likely, to achieve improved coercivity and thermal stability with reduced consumption of raw materials. A lower-priced Nd-Fe-B magnet with improved high temperature performance will see a proliferation of their use. In the following sections, the focus will be on sintered Nd-Fe-B magnets as they are the materials of interest.

3.2 Processing of sintered Nd-Fe-B magnets

Nd-Fe-B magnets are produced through many processing techniques but each creates differences in intergranular phases, anisotropy strength, grain size, BH_{max} and H_c [5, 14, 26, 27]. Sintered Nd-Fe-B magnets make up to 90% of the Nd-Fe-B magnets in the market [1, 3, 8] due to the high BH_{max} they exhibited, while melt-spun Nd-Fe-B magnets make up the rest 10% [8]. The main advantages of the sintering process are that 1) it produces Nd-Fe-B magnets with strong permanent properties and 2) being better suited to industrial-scale fabrication than other methods [26]. The main steps of sintering process of Nd-Fe-B magnets can be summarized into [26]:

a) Powder production.
b) Compaction and powder alignment in molds.
c) Sintering at ~1100 °C.
d) Machining to the required shape.
e) Coating.
f) Magnetisation.

The sintering process of Nd-Fe-B magnets has been improved significantly over past decades [26]. These improvements focused on enhancing the control of the oxygen content in the sintering process atmosphere and decreasing inhomogeneities in the produced microstructure [13].

The stoichiometric composition of $Nd_2Fe_{14}B$ phase is $Nd_{11.8}Fe_{82.3}B_{5.9}$ [28, 29]. This composition has 100 vol.% of $Nd_2Fe_{14}B$ material [26]. However, using an alloy powder with this composition for sintering was reported to lead to the formation of α-Fe precipitates in the final product due to oxidation of some of the Nd & B content [26, 30]. These precipitates were suggested to have a detrimental effect on the magnetic and mechanical properties of the final magnet [26]. To avoid the formation of α-Fe phase, the concentration of Nd & B was increased to higher than their stoichiometric concentrations [26]. A common composition of Nd-Fe-B alloys with excessive Nd and B content is $Nd_{14}Fe_{78}B_8$, which has about 89 vol% of $Nd_2Fe_{14}B$ [26, 28]. This ratio was reported to produce a magnet with higher BH_{max} than the 100 vol.% ratio [26]. The higher BH_{max} was attributed to the formation of Nd-rich phases in the magnet's microstructure, which were thought to have a beneficial effect on the coercivity of the final sample [5, 30]. Limiting the α-Fe precipitates improved the crushability of the melt, which led to a refined grain size and grain size distribution [26].

The powder particles are compacted in moulds under the presence of a strong magnetic field (up to 1 MA.m^{-1}), which is necessary to align the easy axes of particles in the same direction [26]. The efficiency of the alignment could significantly affect the remanence (B_r) and BH_{max} of the produced magnet [26]. This alignment step could be achieved with a magnetic field parallel or perpendicular to the pressing axis (fig. 3.2) [26]. The most common pressing methods are transverse die pressing, rubber and cold isostatic pressing [26]. Isostatic methods have been reported to achieve up to 98% alignments in the compacts and hence higher B_r and BH_{max} than die pressing [26].

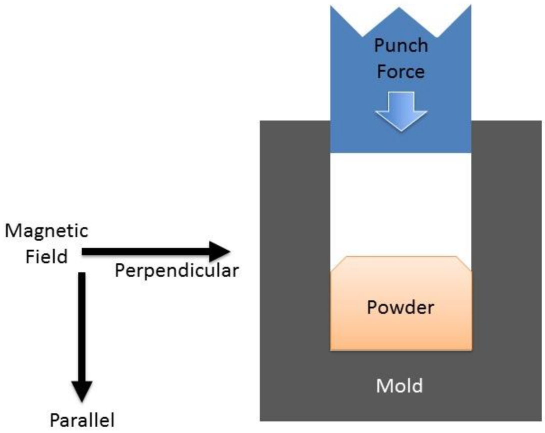

Figure 3.2 An illustration of powder pressing method inside the mold prior to sintering step.

Several other factors are important in the sintering process before densification. For instance: minimising the oxygen content in the atmosphere and achieving a small powder size [13, 26]. High levels of O_2 will lead to the oxidation of particles, while very low O_2 levels are likely to cause an abnormal grain growth [13]. Higher Nd than stoichiometric concentrations increase the densification process, which leads to a microstructure with less abnormal grain growth [13]. In addition, high level of particle packing must be ensured in order to avoid particles relocation, which causes grain anisotropy misalignment [26]. The sintering step is usually performed at ~1100 °C in an Ar gas atmosphere [13, 26]. The produced magnet is then machined for shape optimization. Nd-rich phases in Nd-Fe-B magnets have a high tendency to form Nd-hydroxides, which will embrittle the magnet and leads to surface corrosion [26]. For this reason, Nd-Fe-B magnets are usually coated with Co, Cu, Ga or Al.

3.3 Sintered Nd-Fe-B magnets

In this section, the microstructural features of sintered Nd-Fe-B magnets will be discussed, together with the resulting magnetic properties.

3.3.1 Microstructural features

Figure 3.5 shows the ternary phase diagram of Nd-Fe-B systems. The alloy composition used in sintering to produce the maximum volume of $Nd_2Fe_{14}B$ phase in the resulted magnet has a higher Nd and B at.% than the stoichiometric composition [26]. The typical resulting alloy composition is $Nd_{14}Fe_{78}B_8$, which has been identified to produce three principal compounds [14]. These compounds are the main phase $Nd_2Fe_{14}B$, the B-rich $Nd_1Fe_4B_4$ phase and the Nd-rich phase, which are noted on fig. 3.3 as T_1, T_2 and T_3, respectively. The volume fraction of each phase is determined by initial alloy composition. However, there are other phases that occur as a result of the sintering process conditions, such as Nd-oxides (fig. 3.4) [5, 31].

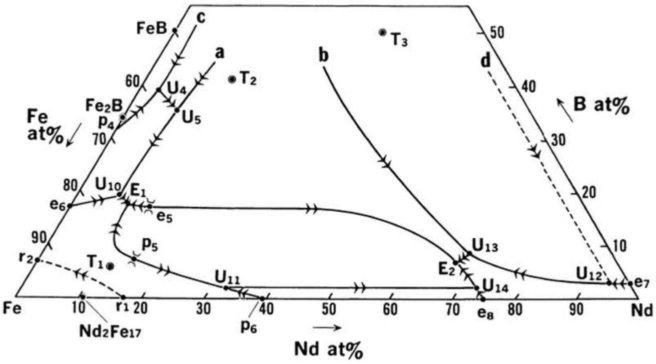

Figure 3.3 The ternary phase diagram of Nd-Fe-B alloy [27]. Reprinted with permission of Japanese Journal of Applied Physics.

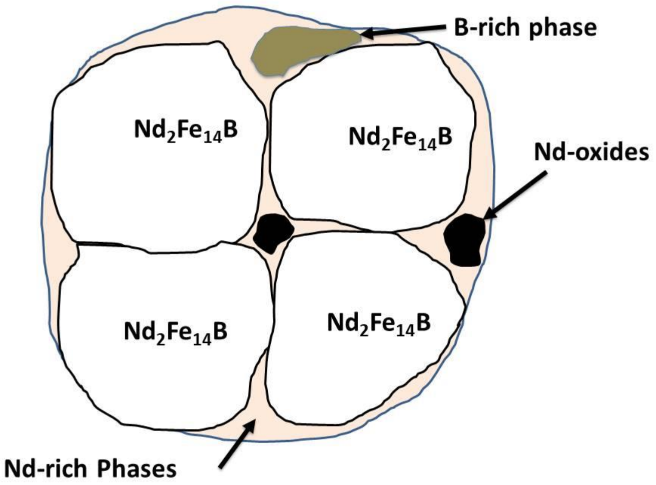

Figure 3.4 A schematic illustration of the main features of sintered Nd-Fe-B magnets microstructure.

The crystal structure of the $Nd_2Fe_{14}B$ phase at room temperature has a tetragonal shape that consists of four $Nd_2Fe_{14}B$ unit cells with a total of 56 atoms of Fe, 8 atoms of Nd and 4 atoms of B (fig. 3.5) [25, 27]. The unit cell dimensions are a= 0.88 nm and c=1.221 nm [32, 33] (the magnetic properties will be discussed in details in §3.3.2). The space group of $Nd_2Fe_{14}B$ is $P4_2$/mnm (structure no. 136 in the international table of crystallography) [34]. $Nd_2Fe_{14}B$ phases exist in sintered Nd-Fe-B magnets in form of irregular shaped grains (fig 3.4) with a size between 3-200 μm [27, 30]. The shape of these grains is related to the powder particles' shape and can be controlled during powder production, while the average grain size and its distribution are strongly affected by the sintering process conditions [26]. Oxygen content and densification rate of intergranular phases during sintering also affects the range of grain sizes in the produced magnet [5, 13, 26].

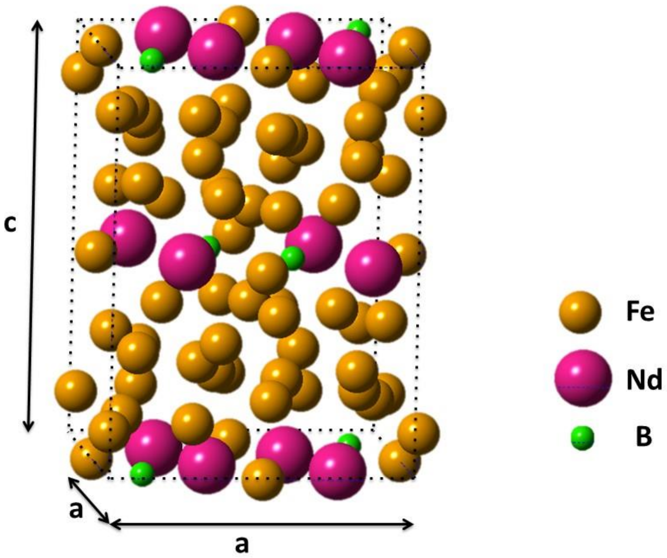

Figure 3.5 An illustration of the tetragonal unit cell of $Nd_2Fe_{14}B$ phase adapted from reference [34].

$Nd_1Fe_4B_4$ phase has a composition of $Nd_{1+e}Fe_4B_4$, where e is usually close to 0.1 [27]. This phase has a body-centred tetragonal crystal structure with lattice parameters of a=0.71 nm and c= 0.32 nm. The space group of its structure is I4/mmm (no. 139) [27, 35, 36]. This phase exists in the form of small particles at the boundaries of the main phase grains. Yin et al reported a high density of faults in this phase, however it has an insignificant volume fraction in sintered Nd-Fe-B magnets [37]. For this reason, it was considered to have a very low effect on the overall properties of the magnet.

Nd-rich phases, on the other hand, form mostly as thin layers at the intergranular regions between grains [31, 35]. The composition of these phases is non-uniform and their crystal structure is ambiguous due to their narrow thicknesses and reactive chemical nature [14, 31]. For these reasons, the preparation of samples for phase characterisation is challenging. The composition of Nd-rich phases varies depending on densification rate, elemental composition and the heat treatment performed after sintering process [14, 26]. The most common Nd-rich phase is thought to be an *fcc*-Nd phase, which has a low melting temperature [38]. This phase has a cubic crystal lattice with *a*=0.52 nm according to transmission electron microscopy diffraction analysis [37].

The presence of oxygen during sintering process leads the formation of Nd-oxides in the final microstructure [13, 26]. These phases are mostly located at the triple junctions between grains in direct contact with $Nd_2Fe_{14}B$ grains or encapsulated by Nd-rich phases [14, 29, 39]. The most reported oxide phase is the cubic Nd_2O_3 phase, which has a lattice parameter of *a*=1.108 nm and a structure of Ia3 (no. 206) [36, 40]. Other types of oxides are present such as Nd_2O and NdO, but their presence has been confirmed in only a few cases [31, 40, 41]. Other microstructural features might occur due to the inhomogeneities in the molten alloy include impurities, carbide (Nd-C) phases and porosity [26, 27].

Kronmüller et al highlighted the effect of microstructural inhomogeneities in the nucleation of reversed domains in sintered Nd-Fe-B magnets [42]. There are four common types of inhomogeneities that might cause the nucleation of reversed domains [42]:

a) Nonmagnetic grains (fig. 3.6a).
b) Non-existent or very thin magnetic regions at grain boundaries leading to exchanged grains (fig. 3.6b).
c) Misaligned grains in comparison to the overall grain alignment direction (fig. 3.6c).
d) Regions with reduced magnetocrystalline anisotropy (fig. 3.6d).

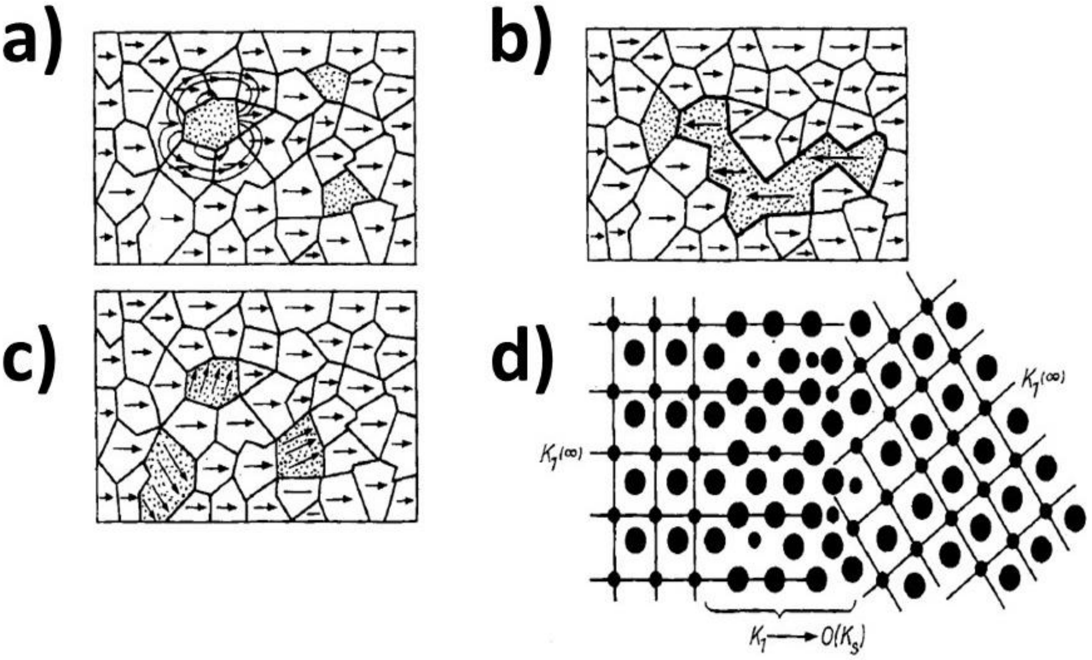

Figure 3.6 A schematic sketch of (a) non-magnetic particles, (b) exchanged grains, (c) misaligned grains and (d) regions with lower K_1 than the main phase [42]. Reprinted with permission of John Wiley and Sons, Inc.

Alloying elements are used in order to improve the magnetic and mechanical properties of Nd-Fe-B magnets and to produce a more homogeneous microstructure [26, 30, 43, 44]. These elements can be categorised into [30]:

1) Substituents of RE atoms (S_{RE}) such as Pr, Dy and Tb.
2) Substituents of Fe atoms (S_{Fe}) such as Co, Ni and Cr.
3) Dopants that react with RE atoms (D_1) such as: Al, Cu, Zn, Ga, Ge, and Sn.
4) Dopants that react with B atoms (D_2) such as: Ti, Zr, V, Mo, Nb and W.

The effect of these substituents and dopants depends on their solubility range. If they are soluble at temperatures higher than the sintering temperature 1100 °C, they dissolve in the main phase grains [26, 30, 43, 44]. This is mostly the case for S_{RE} and S_{Fe}, hence their categorization. If these elements have lower solubility at the sintering temperature, they will form new intergranular phases [32]. This is the case for D_1 and D_2 dopants. The importance of these elements lies in their effect on the magnetic properties of the magnet. A detailed description of their magnetic effect will follow in the next section.

3.3.2 Magnetic properties

Sintered Nd-Fe-B magnets have the highest BH_{max} values among all other permanent magnets [5]. It is possible now to produce magnets that have BH_{max} values of 400 kJ.m^{-3} at room temperature. B_r of these magnets can have values up to 1.23 T, while their coercivity (μ_0H_c) is around 1.2 T [8, 11]. The strong spin-orbit coupling of RE elements produces a strong uniaxial magnetocrystalline anisotropy at room temperature with values up to 4.9 MJ.m^{-3} [8, 45], while its theoretical anisotropy field (H_A) is 7.7 T. The high transition metal content ensures a large μ_0M_s=1.61T at 300K. The magnet's H_c and B_r of the magnet depend strongly on the microstructure of the magnet and a change in the microstructural features is likely to induce a change in these properties [13].

The formation of domains and their walls in ferromagnetic materials was discussed in §2.3.2 and attributed to tendency of the system to minimise its total energy. The maximum single domain size (d_s) for a spherical particle with N_d=1/3 can be calculated through [46]:

$$d_s = \frac{72}{\mu_0 M_s^2}\sqrt{A_{ex}K_1} \qquad (3.1)$$

Thus, d_s of spherical grains of $Nd_2Fe_{14}B$ phase was estimated to be ~260 nm [17, 46]. This size is smaller than most of other permanent magnets (d_s in Sm_2Co_{17} is ~500 nm) [46]. On the other hand, typical domain wall width (δ_w) in these magnets is around 4.2 nm [47, 48]. These characteristic length scales have a strong impact on the mechanism of demagnetisation, as will be detailed in the next section.

The magnetic properties of ferromagnetic materials deteriorate with increasing temperature and especially at temperatures close to T_c [11]. The temperature coefficients of B_r and H_c are B_T and H_T, respectively, and are calculated through:

$$B_T = B_r^T / B_r^0 \tag{3.2}$$

$$H_T = H_c^T / H_c^0 \tag{3.3}$$

where B_r^T and H_c^T are the B_r and H_c values at any specific temperature, respectively, while B_r^0 and H_c^0 are the values at 0 K [13]. T_c of $Nd_2Fe_{14}B$ phase is 588K and typical values of B_T and H_T for sintered Nd-Fe-B magnets are -1260 ppm/K and -6000 ppm/K, respectively [2]. These values are high compared to other permanent magnets, which mean Nd-Fe-B magnets show lower thermal stability of magnetic properties compared to Sm-Co, for instance (fig 3.7).

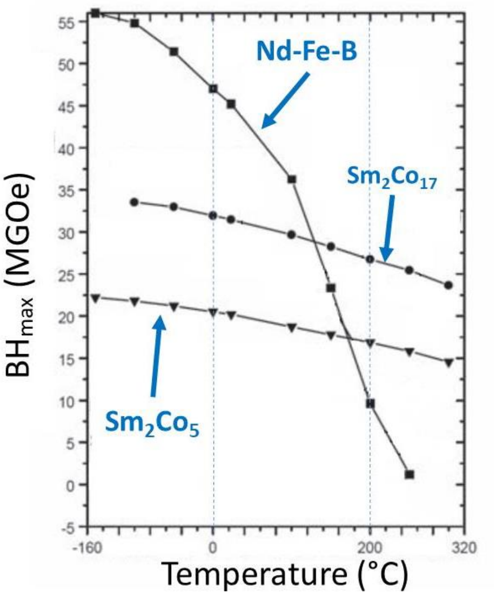

Figure 3.7 BH_{max} at different temperatures for Nd-Fe-B and Sm-Co magnets adapted from reference [2]. Reprinted with permission of John Wiley and Sons, Inc.

The addition of substituents and dopant elements changes some of the magnetic characteristics of the main phase or the nature of exchange between main phase grains [30, 43]. For example, S_{RE} elements will replace the Nd atoms in the main phase. In the case of Pr, the main phase will have a higher densification rate, which improves the smoothness of interfacial grains and enhances the grain size refinement [30]. Heavy RE elements such as Dy and Tb replace Nd and lead to an increase in K_1 of the main phase which leads to an increase in H_c and its thermal stability [30]. For example, H_c increases from 12 kOe in Dy-free Nd-Fe-B magnets to 30 kOe when 40% of the Nd is replaced with Dy [9]. However, this replacement will cause a drop in B_r of the main phase due to the antiferromagnetic exchange of heavy RE elements atoms with Fe atoms [30, 43]. S_{Fe} elements replace the Fe atoms and influence T_c, K_1 and M_s independently. For example, $Nd_2(Fe_{0.9}Co_{0.1})_{14}B$ has a lower $\mu_0 M_s$~1.53T and an improved T_c~610 K [30].

Dopants change the magnetic properties of the main phase if they are soluble at the sintering temperature (1100°C), especially Al and Ga [30]. In this case, they replace Fe atoms in the main phase leading to changes in M_s, T_c and K_1 [30]. However, these elements are mostly used to improve the distribution of intergranular phases in the magnet and the material's corrosion resistance [27, 30]. D_1 elements (reacting with Nd) improve the wetting behaviour of the liquid phase during sintering, which leads to the formation of D_1-Nd and D_1-Fe-Nd phases [30]. These phases decrease the magnetic exchange between grains leading to H_c increase [30]. In addition, the formation of D_1-Nd phases instead of pure-Nd phases improves the corrosion resistance of the magnet [30]. D_2 dopants (reacting with B) form D_2-B and D_2-Fe-B phases that precipitate either within the main phase or at its grain boundaries [30]. D_2-Fe-B has been reported to increase H_c of Nd-Fe-B and this is thought to be due to the decreased magnetic exchange between $Nd_2Fe_{14}B$ grains [19]. V and Nb additions behave as D_2 dopants to suppress abnormal grain growth, which also improves H_c [30, 43]. Finally,

B_r of Nd-Fe-B magnets depend strongly on grain alignment. A reduction in grain alignment results in reduced B_r and therefore a lower BH_{max} (fig.3.8) [13].

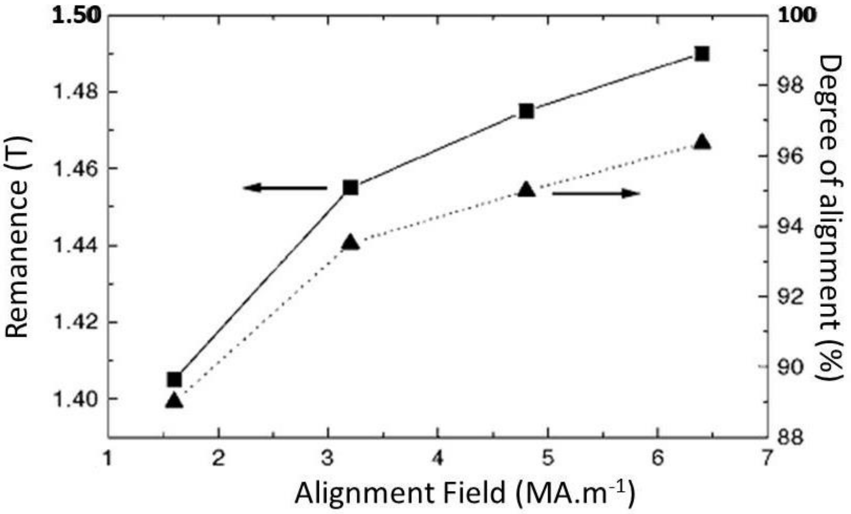

Figure 3.8 The dependence of B_r on the degree of grain alignment as a function of the alignment field [13]. Copyright and reprinted with permission of Journal of Physics D.

3.4 Demagnetisation mechanism

It is important to understand carefully the magnetic interactions inside Nd-Fe-B magnets to able to resolve the discrepancy between theoretical and experimental values of magnetic properties (Brown's paradox) [7, 8]. The theoretical models that explain the demagnetisation process in Nd-Fe-B magnets are discussed briefly in this section.

3.4.1 Nucleation of reversed domains

Kronmüller *et al* suggested that H_c of hard magnets is dependent on the nucleation field of reversed domain walls, which is affected by the microstructure of the magnet [42]. As soon as this nucleation occurs, the entire grain will be demagnetised inevitably since no pinning sites are expected inside $Nd_2Fe_{14}B$ grains [42]. The coercivity at a fixed temperature can be described by [42]:

$$H_c = \alpha H_A - N_{eff} M_s \quad (3.4)$$

where H_A is the anisotropy field, α is a parameter describes the microstructural inhomogeneities and misalignment between grains and N_{eff} is the effective demagnetisation factor that represents the values of grain's self-demagnetising field and demagnetisation from the interaction with neighbouring grains. Typical values of α and N_{eff} are shown in table 3.1. Kronmüller's model gives consideration to the effect of microstructural inhomogeneities in the nucleation of reversed domains. It suggests that magnetically exchange-decoupled aligned main phase grains will take the least role in the nucleation of reversed domains. The reversed domains will thermally nucleate in a small volume at grain boundaries and expand inside towards the grain centre [42].

Table 3.1 Typical values of α and Neff in different types of Nd-Fe-B magnets [5].

Sample type	**α**	**N_{eff}**
Sintered magnets	0.6-0.7	1.4-1.8
Hot deformed	0.6-0.9	0.75-1.0
Thin films	0.26-0.41	0.05-0.42

Gao *et al* suggested a nucleation field theory, in which the reversed volume has a width comparable to domain wall thickness and its subsequent growth is driven by the irreversible domain wall movement [33]. In order to hinder this movement, an extra Zeeman energy is required. Kronmüller and Gao's approaches include the consideration of the direct magnetic exchange between grains but neglects long-range magnetostatic interactions between grains. In experimental samples, these magnetostatic interactions often far stronger than direct-contact magnetic exchange [33].

Pinning reversed domain walls in Nd-Fe-B magnets has been suggested to be possible by the formation of non-magnetic intergranular phases between $Nd_2Fe_{14}B$ grains [13]. This approach forms the base of wide research efforts to improve the coercivity of sintered Nd-Fe-B magnets. These non-magnetic phases are likely to reduce direct-exchange interactions between grains [42]. An effect that is thought to enable each grain to act as an individual magnet [13]. However, long-range magnetostatic interactions are far stronger and expected to persist even with non-magnetic intergranular phases [5, 14].

3.4.2 Angular dependence of coercivity

The coercivity of sintered magnets shows a strong dependence on the alignment of easy axes of grains [49-51]. The angular dependence of coercivity was studied in detail by Stoner-Wohlfarth for single domain particles [19]. Angular dependence of coercivity of Stoner-Wohlfarth model is shown in fig. 3.9.

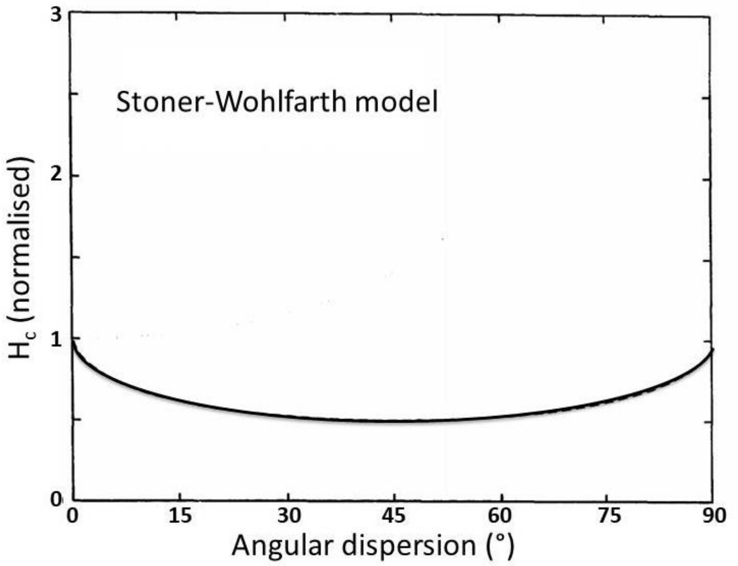

Figure 3.9 The coercivity change in a Stoner-Wohlfarth model [52]. Copyright and reprinted with permission of Journal of Magnetism and Magnetic Materials.

Experimental results of sintered Nd-Fe-B magnets showed a deviation from Stoner-Wohlfarth behaviour, which indicates that grains in sintered Nd-Fe-B magnets are not perfectly aligned and that switching is not happening through coherent rotation of grains magnetisation [51, 53]. Non-magnetic phases have been reported to increase H_c [54]; however, the values of H_c are still far from their theoretical limits set by this model.

3.4.3 Grain size dependence of coercivity

H_c in hard magnets has a strong dependence on the diameter of the main phase grains [46, 55]. Fig. 3.10 shows a model of the dependence of H_N on the grain size of sintered hard magnets with four critical diameter values [46]:

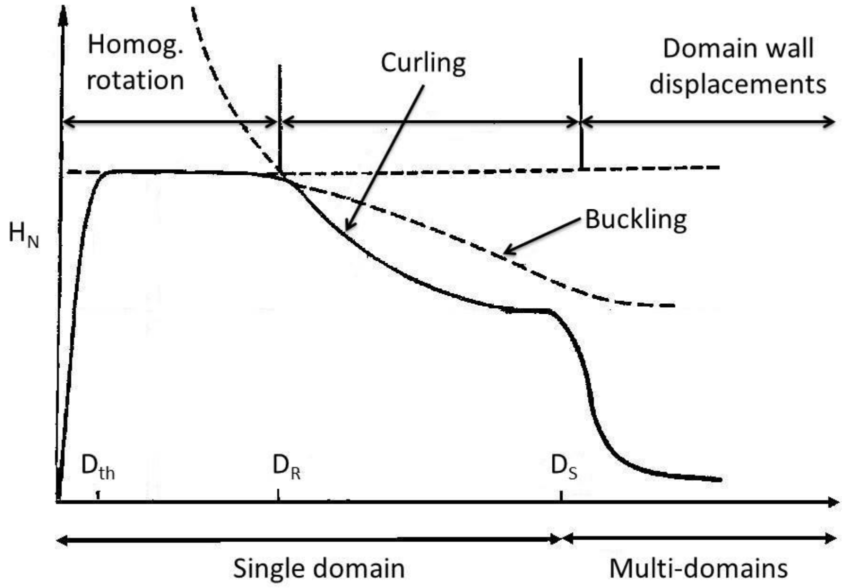

Figure 3.10 The dependence of nucleation field on the grain size of sintered magnets [46]. Reprinted with permission of Cambridge University Press.

- Diameters at the thermal stability limit (D_{th}), where thermal fluctuations are strong enough to rotate the magnetisation. The values of D_{th} are suggested to be around 2-3 nm.

- Diameters (D_R) at values close to δ_w (domain wall width), where demagnetisation occurs through coherent rotation of magnetisation, as was described in Stoner-Wohlfarth model (see §3.4.2).
- Diameters below the single-domain particle size ($<D_s$), where demagnetisation takes place by homogeneous rotation. At these diameters, the rotation of magnetisation takes place through the curling and buckling modes [46].
- Diameters above D_s, where demagnetisation takes place by domain wall displacement.

The diameter of main phase grains in sintered Nd-Fe-B magnets has been reported to be higher than D_s (>300nm), which means that demagnetisation is likely to occur via domain wall displacement [12]. Fig. 3.10 suggests that further improvements in H_c could be achieved with grain size refinement, which represents a very effective approach to improve H_c in hard magnets. However, H_c of sintered Nd-Fe-B magnets was reported to increase with decreasing the grain size for values D>3µm [56]. The drop in H_c at samples with grain size smaller than 3µm was mainly attributed to the oxidation of Nd-rich phases at the grain boundaries [56]. As this is a consequence of the processing technique, overcoming this limitation offers a useful approach to improve H_c in sintered Nd-Fe-B magnets.

3.5 Heavy rare-earth elements

Currently, there are many types of electric vehicles that use sintered Nd-Fe-B magnets [2], For example: electric bikes (EB), hybrid electric vehicles (HEV) and full battery electric vehicles (FBEV). The use of Nd-Fe-B magnets in the electric motor of these vehicles reduced the size of motors, increased the magnet's torque and lowered its weight [1, 2]. HEV operate at higher temperatures than other types of electric transportation and their industry demands a magnet with μ_0H_c=2 T at 200°C [39], which can be a limitation for using sintered Nd-Fe-B magnets. For this reason, thermal stability improvements are required for Nd-Fe-B magnets in order to be used in HEV.

The current solution is to replace 10-30% of Nd in Nd-Fe-B magnets with a heavy RE element [5, 14], often Dy as it is cheaper than Tb. The magnetic properties of $(Dy_{47}Nd_{53})_2Fe_{14}B$ magnets are K_1~5.17 $MJ.m^{-3}$ and M_s~1.15 T at room temperature [57]. The higher anisotropy is a result of replacing Nd atoms by Dy in the $Nd_2Fe_{14}B$ unit cell, while the lower value of magnetisation is a consequence of the antiferromagnetic coupling between Fe and Dy atoms. (Dy, Nd)-Fe-B magnets show H_c of ~26 kOe and ~6 kOe at temperatures of 25°C and 200°C, respectively [9]. This is compared to ~12 kOe at 25°C and ~1 kOe at 200°C for Dy-free Nd-Fe-B magnets (fig. 3.8) [9].

The drawbacks of using Dy are the drop in M_s and increased production cost [9]. Recent 3D atom probe analysis revealed that Dy distribution inside the (Dy, Nd)-Fe-B samples is non-uniform across the microstructure [9]. Higher Dy at.% was found at the grain boundaries of main phase grains. In addition, Dy was found to replace Nd in the oxides at the triple junctions between grains. This non-uniform distribution was attributed to the high oxygen affinity of Dy [9] and it indicates that further reduction to Dy content is possible. Improvements of sintered Nd-Fe-B magnets are required by HEV market to improve the thermal stability of magnetic properties up to 200 °C with using the least additions of heavy RE elements. This will decrease the HEV cost and increase its viability in existing markets.

3.6 Recent approaches to improve Nd-Fe-B magnets

In this section, a summary of the main efforts to improve sintered Nd-Fe-B magnets is presented.

3.6.1 Post-sintering annealing

Kronmüller’s model suggested that further H_c improvements are possible by the magnetic isolation of grains from their surrounding [42], *e.g.* by the formation of a non-magnetic intergranular phases between $Nd_2Fe_{14}B$ grains. Post-sintering annealing (PSA) was used in order to improve the distribution of grain boundary phases in Nd-Fe-B magnets by reheating the alloy to 600°C with trace additions of Cu (usually 0.1 at%) or Ga to the alloy to decrease the melting temperature of Nd-rich phase [58, 59]. Sepehri-Amin suggested that the Nd-rich phase diffused with temperature increase and penetrated between the main phase grains by the effect of capillary forces [29]. PSA process has been reported to increase H_c by about ~30% of the initial magnet (fig. 3.11a). The thin Nd-rich phase in PSA samples was reported to have a thickness between 1-5 nm that surrounds the majority of main phase grains (fig. 311b) [29].

The improved H_c in PSA samples was attributed to several reasons [31]. Firstly, the improvements in the distribution of Nd-rich phase as a consequence of alloying elements additions [30]. These alloying elements decreases the melting temperature of the Nd-rich phase leading to an improved distribution between main phase grains [30, 31]. Cu additions increase the solubility of the phase and Ga increased its wettability [30]. Secondly, PSA was suggested to relieve strain at the grain boundaries of the main phase [31]. Other studies suggested an anisotropic relationship between the Nd-rich phase and $Nd_2Fe_{14}B$ grains, which reduces some of the interfacial energy between these two phases [31]. Finally, PSA process was suggested to dissolve metastable ferromagnetic compounds at intergranular areas [31]. The precise reason behind the improved H_c of PSA samples is still subject to investigation.

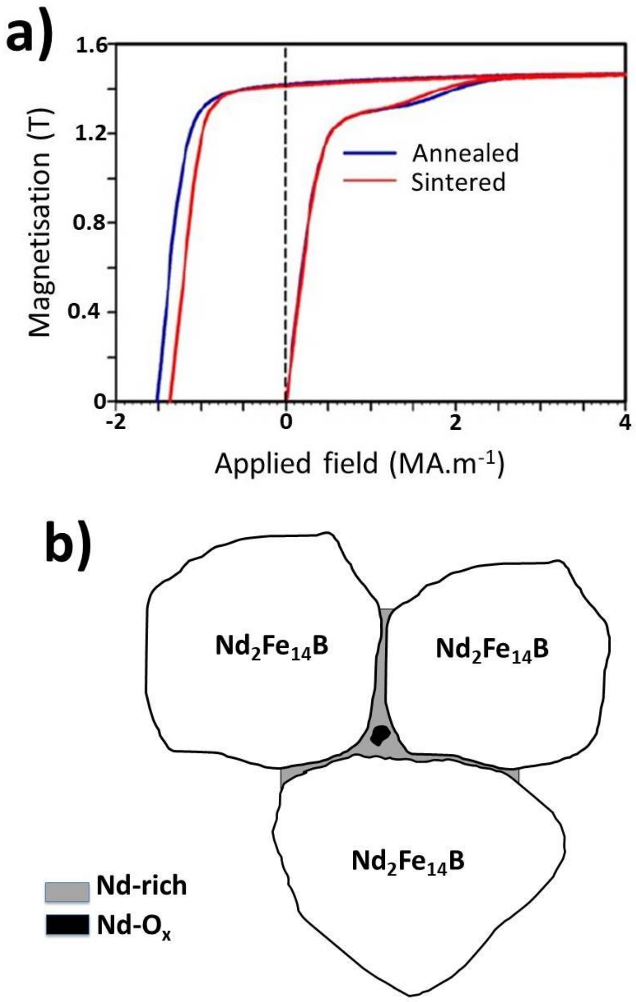

Figure 3.11 (a) A comparison between H-M loops and (b) the main microstructural features of the PSA Nd-Fe-B magnet adapted from [29]. Reprinted with permission of Scripta Materialia.

Recent electron microscopy has suggested that the thin Nd-rich phase is an amorphous Nd-Fe-Cu phase [29, 40]. While Nd was indeed found to be up to ~35 at.% in this phase, high Fe concentrations were reported (up to 65 at.%) [29]. The sources of these high concentrations of Fe are unknown, but their presence suggests that the Nd-rich phase is likely to be ferromagnetic. The magnetic measurements of this phase are challenging; however, due to its very thin and reactive nature [60]. A precise quantification of the elemental and magnetic features of Nd-rich phase is vital for the efforts working on improving sintered Nd-Fe-B magnets. The microstructure characterisation in Chapters 5 and 6 and the micromagnetic modelling in Chapter 7 will shed the light on the role of grain boundary phases on the performance of Nd-Fe-B magnets

3.6.2 Grain size refinement

The dependence of H_c of hard magnets on their grain size was discussed in §3.4.3. This dependence provides a useful tool to improve the properties of sintered Nd-Fe-B magnets. However, the fabrication of Nd-Fe-B magnets with a grain size smaller than their single domain particle size (300 nm) is rather challenging [56]. This is due to the vast oxidation of Nd-rich phases with powder particles smaller than 3 µm in conventionally sintering processes [56].

Recently, the use of press-less sintering process has succeeded in the production of magnets with D~1µm and a minimum Nd-rich phase oxidation [61]. This method resulted in H_c=1.51 MA.m^{-1} compared to 0.95 MA.m^{-1} of conventional sintered Nd-Fe-B magnets. Sepehri-Amin et al suggested that the improvement in H_c with decreasing grain to <1 µm is attributed mainly to the reduced stray field of $Nd_2Fe_{14}B$ grains [48]. Improvements in the sintering process to produce smaller grain sizes may lead to enhancements in H_c of Nd-Fe-B magnets. An investigation to the average size and distribution of main phase grains in experimental samples will be presented Chapter 6, while Chapter 7 will demonstrate the micromagnetic modelling of the effect grain size variation on H_c of Nd-Fe-B magnets.

3.6.3 Grain boundary diffusion

Grain boundary diffusion (GBD) process was inspired by PSA processes but it is performed at higher range of temperatures 685-1000 °C [38]. The process was achieved by coating sintered Nd-Fe-B magnets with Dy compounds. Examples of these Dy compounds are DyF_3 [62], DyH_3 [63] and DyO_3 [38]. The heating of the sample allows the diffusion of the Dy-coating between main phase grains and replace Nd in the outer regions of these grains leading to the formation of $(Dy, Nd)_2Fe_{14}B$ shells [38]. The replaced Nd is discharged to intergranular regions leading to a higher Nd at these areas (fig. 3.12) [64].

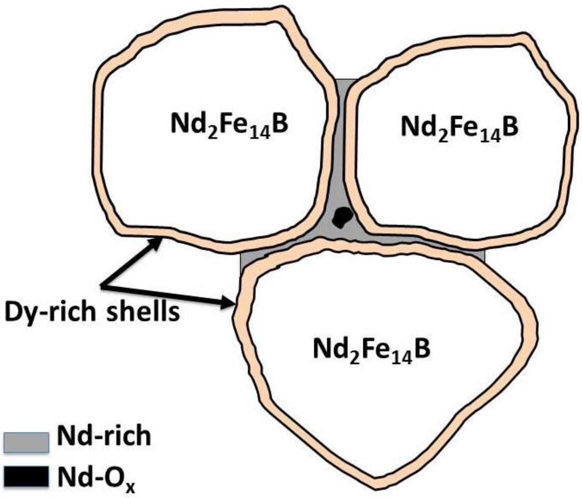

Figure 3.12 An illustration of the main microstructural features of grain boundary diffused samples.

H_c of GBD samples was reported to increase from 1.04 to 1.62 $MA.m^{-1}$ with a negligible drop in M_r [38]. However, the thickness of the Dy-rich shells in diffused samples was found to be non-uniform across the sample, which was very noticeable in samples with thickness higher than 5 mm [63]. The main phase grains that are located closer to surface of the sample were reported to have higher thickness of shells and higher Dy concentration [63]. In addition, Dy at.% was found to be about 3.3% at shells close to the edge of the sample compared to 1.1% at shells close to the centre of the sample [38]. Other samples revealed an anisotropic nature of Dy diffusion with rapid diffusion parallel to the *c*-axis of main phase grains [63].

Previous magnetic measurements revealed a significant difference in H_c of magnets diffused at temperatures of 700, 800, 900, 1000 °C [65]. While the diffusion at 900 & 1000

°C is suggested to occur by the melting the outer edges of main phase grains and re-solidifying as Dy-rich shells with cooling the sample, the diffusion at lower than 900 °C is most likely to be a solid state process [65]. The difference in the magnetic properties of these samples raises many ambiguities about the role of Dy-rich shells and Nd-rich phases in diffused samples. Clarifying the major source of coercivity increase in diffused samples is vital for success diffusion processes as it will determine the amount of Dy used and the optimum diffusion temperature. This will be assessed using micromagnetic modelling in Chapter 8.

3.6.4 Micromagnetic modelling

Micromagnetic modelling of the microstructure and magnetic behaviour of hard magnets emerged as an effective method to suggest improvement approaches for Nd-Fe-B magnets [49, 66]. Modelling these magnets benefited from the higher-resolution characterisation techniques that became available recently and from the increased capacity of computing capabilities [66]. The information obtained from the characterisation was used to enrich the models that represent the microstructure of magnets in order to simulate the size, shape and chemistry close to the microstructure of real magnets. The micromagnetic modelling of hard magnets is achieved through dividing the models to smaller parts, solving Landau-Lifshitz-Gilbert equation of motion and performing energy minimisation at each part to predict the magnetic structure of the whole model [66].

The main aims of micromagnetic modelling are 1) interpreting the demagnetisation mechanism of current Nd-Fe-B magnets, 2) investigate the effect of various microstructural features on H_c and M_r of the magnets and 3) to predict and compare the limits of the proposed hardening mechanisms [49, 66]. Previous modelling attempts attributed the deviation of H_c

values from theoretical values to the misorientation of grain alignment from the field direction [67]. Schrefl *et al* suggested that the magnetostatic interactions between adjacent main phase grains also contribute to this deviation of H_c values [68]. These studies suggested that non-magnetic GB phases can eliminate, to a high extent, the effect of misaligned angles and granular magnetostatic interactions [67, 68].

Previous modelling studied the effect of different Nd-rich phases on H_c of Nd-Fe-B magnets. Suess *et al* suggested that the grain boundaries of main phase grains have defect layers where K_1 values are close to 0 $J.m^{-3}$ leading to nucleation of reversed domains at lower magnetic field [69]. Hrkac *et al* revealed that thickness of these distorted layers, which result from the interface of main phase grains and intergranular phases, will have a critical effect on H_c of single and magnetically-exchanged grains [35, 36]. On the other hand, Nd-rich phases were proposed as a capable solution to reduce the effect of inhomogeneities and adverse magnetostatic interactions [48, 70]. This effect is thought to increase nucleation field of reversed domain walls and hence increase H_c of Nd-Fe-B magnets. Modelling Nd-Fe-B magnets also looked into the effect of grain size and suggested that H_c increases with grain size reduction due to weaker magnetostatic interactions of smaller size grains [48]. On the other hand, Bance *et al* attributed the improvements in H_c and its thermal stability in smaller grains to the reduction in the effective demagnetisation factor (N_{eff}) of magnetically-exchanged grains [71].

Micromagnetic simulations of grain boundary diffused samples predicted that a 4 nm Dy-rich shells may cancel the adverse effect of defect layers at grain boundaries, which explains the improvement in H_c of these samples [57]. The simulations performed by Oikawa *et al* reported a linear increase of H_c with increasing Dy content in the Dy-rich shells [72]. In addition, they revealed that improving H_c of GBD samples does not require a Dy-containing composition prior to diffusion, which provides further reductions to the magnet cost. Understanding the role of microstructural features on the behaviour Nd-Fe-B magnets has been improved significantly through micromagnetic modelling. However, revealing what hardening mechanism is the most effective is still a subject of continuing research. The answer to this question is vital for the fabrication of Nd-Fe-B magnets that have lower heavy RE content, a sufficient H_c and thermal stability for clean energy applications.

3.7 Twinning in $Nd_2Fe_{14}B$ grains

Twinning, as a deformation mechanism, is originated from the plastic deformation of phases [73, 74]. The resulted shear strain from this deformation can be accommodated by dislocations or deformation twinning [73-75]. This exploitation occurs at low temperatures, as opposed to grain rotation or sliding of grain boundaries at higher temperatures [73]. In both cases of dislocations and twinning, an interruption to the stacking sequence of the atomic structure of phases occurs inside a particular phase [73, 74]. Dislocations are represented by gliding a whole plane to new positions, while twins is represented by an interruption to the stacking sequence of atomic planes around a specific plane [76]. High stacking faults energy favours dislocations, while lower energies favours twinning [73, 74].

A twinned area is represented by shearing the phase into a new shape (fig 3.13). The old lattice positions are called the parent, the new positions are called the twin [73, 75]. The twin and a parent are related by either a reflection or a rotation in a plane by an angle up to 180° around the twinning boundary, which may be considered a low-energy grain boundary [75]. The structural attribution of twinning is the insufficient slip systems available to accommodate the deformation [75]. A sufficient number is suggested to be at least five independent active slip systems for polycrystalline materials [73, 75].

The possibility of deformation by dislocations in $Nd_2Fe_{14}B$ phase is lower than twinning because of the low stacking fault energy of its crystal structure [14]. This correlates with previous reports that suggested no dislocations were present inside main phase grains [14]. This means if shear stress occurs; the formation of deformation twinning is more likely than dislocations. The crystal structure plays a major part in determining the stacking fault energy, *e.g. fcc* crystal has been widely reported to accommodate twins [73, 75]. The tetragonal structure of $Nd_2Fe_{14}B$ phase favours twinning to occur on the {110} and {101} planes [73, 77]. Chu *et al* reported twinning in the majority of $Nd_2Fe_{14}B$ grains in rapidly-solidified die-upset samples [77]. Hubert *et al* reported the presence of twinned $Nd_2Fe_{14}B$ phase with a 13° and 52° misorientation angles [22]. Twinning is likely to lead to a multiple anisotropy-direction grain.

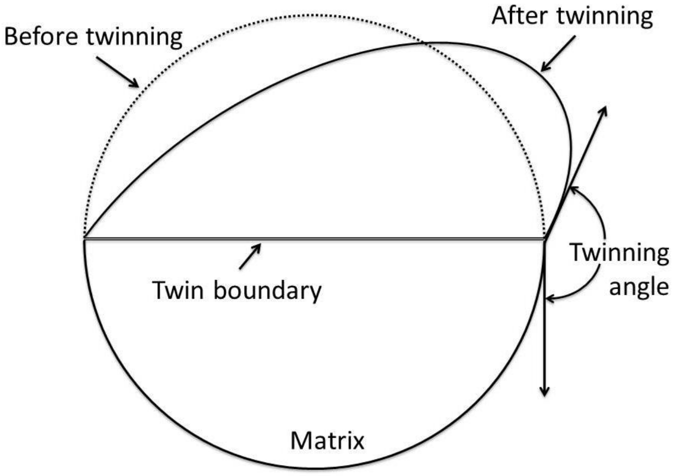

Figure 3.13 An illustration of deformation twinning around a twinning boundary adapted from reference [73]. Reprinted with permission of Progress in Materials Science.

Twinning has been reported to be influenced by the microstructural features of the alloy, *e.g.* coarse-grained phases have a higher probability to accommodate twins compared to nanoscale grains [73, 75]. On the other hand, a high texture of grains was reported to create large differences between the types of stress inside grains [76]. This means tension, compression and shear stresses were expected to have different loads in a textured sample compared to isotropic sample. Alloying elements can affect the twining occurrence in metals and alloys, however their effect is rather characteristic to each element and structure [76].

Twinning was reported to have a positive impact on the strength and ductility of nanocrystalline alloys [75]. However, twinning occurs when stacking sequence of atomic position is disrupted and a new sequence is created after the twin boundary [73, 75]. This means twinning occurs on a dimension of a crystal distance. According to this hypothesis, the exchange energy between the twin and parent is not likely to be affected. However, this abrupt change might cause a change in J_s and K_1. This change will be limited at the transition area, which is in the $Nd_2Fe_{14}B$ phase is around 0.8-1.2 nm (the lattice parameters of $Nd_2Fe_{14}B$ phase) [34]. The twinning structure in Sm-Co magnets was suggested to act as pinning sites for reversed domains [78]. However, the effect of twinning in $Nd_2Fe_{14}B$ grains on H_c has not been studied previously. Micromagnetic modelling in Chapter 8 will look into the effect of twinning on H_c of Nd-Fe-B magnets.

3.8 Summary

$Nd_2Fe_{14}B$ phase, as an intermetallic magnetic compound, benefits from the high uniaxial anisotropy produced by the Nd in addition to the magnetisation and Curie temperatures of Fe. $Nd_2Fe_{14}B$-based magnets are the main component of clean energy and data storage applications due to their high maximum energy density. They control about 60% of the global permanent magnets market, with 90% of this share belonging to sintered Nd-Fe-B magnets. Current sintered Nd-Fe-B magnets consist of alloys with excessive Nd and B concentrations than the stoichiometric composition of $Nd_2Fe_{14}B$ phase. This led to a microstructure that consists of $Nd_2Fe_{14}B$ grains, which are surrounded by a variety of intergranular Nd-rich and

B-rich phases. In addition, oxidation of some of the excessive Nd leads to the formation of Nd-oxides. The microstructure of Nd-Fe-B magnets is the subject of vast research efforts to understand its role on their magnetic properties. The addition of alloying elements (Ga, Cu and Co) to Nd-Fe-B alloy leads to different effects depending on their solubility at processing temperature. Elements that replace Nd and Fe atoms in $Nd_2Fe_{14}B$ phase may affect its saturation magnetisation and magnetocrystalline anisotropy, while dopants in the intergranular phases can lead to higher solubility; hence an improved distribution between $Nd_2Fe_{14}B$ grains and increased corrosion resistance.

The use of Nd-Fe-B magnets in hybrid electric vehicles stumbled upon their low coercivity at temperatures close to 200°C. This limitation was resolved by replacing 10-30% of the Nd concentration in Nd-Fe-B alloy with heavy rare-earth elements. These elements improved the coercivity and its thermal stability, but they led to reductions in their remanence and they lead to a significant increase in the magnet's cost. Improving the coercivity of Nd-Fe-B magnets and its thermal stability is the focus of wide research efforts. Several approaches have been suggested to explain the demagnetisation of Nd-Fe-B magnets. These approaches highlight the effect microstructural inhomogeneities on the nucleation of reversed domains in $Nd_2Fe_{14}B$ grains. For example, the elimination of non-magnetic particles and misaligned grains has been suggested to improve the coercivity of Nd-Fe-B magnets. These approaches are the base of wide research efforts working on improving Nd-Fe-B performance. These efforts can be summarized into post-sintering annealing of sintered magnets, grain size refinement and grain boundary diffusion processes. On the other hand, twinning may occur in $Nd_2Fe_{14}B$ grains; however, its effect on the remanence and coercivity of these magnets has not been studied yet. The ultimate objective of research efforts working on Nd-Fe-B magnets is to produce a magnet with lower content of heavy rare-earth elements and improved magnetic coercivity and maximum energy density, especially at temperatures ~200°C.

4.Methodology

4.1 Introduction

This study included experimental characterisation of the microstructure of commercial Nd-Fe-B magnets and development of finite element modelling of the magnetic behaviour of these magnets. This chapter details the sample preparation procedure, the characterisation techniques and the micromagnetic modelling tools used in this work.

4.2 Samples and Sample preparation

Three commercial Nd-Fe-B sintered magnets from different suppliers were provided by Siemens Wind power in 2014. These samples are different in the amount of Dy with either no Dy content (Dy-free), a reduced amount of Dy (Red-Dy) and a higher amount of Dy (Dy-rich). Each magnet was field aligned and sintered by the producers and presented a representative range of sample microstructures found in Nd-Fe-B magnets for wind turbine applications. The hysteresis loops of the three samples were measured by the samples manufacturer at room temperature using a vibrating sample magnetometer and the resulting loops will be presented in Chapter 5.

The samples were cut to dimensions of 10x9x10 mm^3 using a Buehler cutting machine (Isomet 5000) with abrasive cut-off (R/Al_2O_3) wheels. The samples were subsequently mounted in moulds in epoxy resin and allowed to dry for 12 hours. Samples grinding was performed by using CarbiMet SiC grinding papers with smoothness degree of 320º, 600º, 1000º and 2500º on the Automet (Ecomet 250pro) machines. Grinding time was about 3 – 7 minutes for each of the grinding degrees mentioned above. Polishing was performed with the same machine using polishing cloths of 6, 3, 1 and 0.25 μm particle size and alcohol based diamond suspension with same particle sizes as the cloths on Automet machine. An oil lubricant (alcohol based with polyethylene glycol) was used in addition to the diamond suspension in order to increase the wetting of the cloths. The final polishing step used colloidal silica with a particle size of 0.04 μm to obtain a damage-free surface with no residual scratches or contamination, which was inspected using an optical microscope. The samples were immersed in isopropanol to reduce the oxidation of the highly reactive microstructure. It was found that a few minutes of exposure to atmosphere reduced the smoothness of sample's surface leading to lower imaging quality.

4.3 X-ray diffraction

X-ray diffraction (XRD) is a non-destructive technique that can reveal information about the crystallographic structure of a material, including the crystal structure of phases in the sample and their lattice parameters (fig. 4.1) [79]. This is achieved using Bragg's law to calculate the *d*-spacing between crystal planes [79]:

$$n\lambda = 2d\ sin\theta_i \qquad 4.1$$

where n is an integer, λ is the X-ray wavelength, d is the interplanar spacing and θ_i is the incident angle [79]. It is possible using Bragg's equation to reveal the Miller indices (*hkl*) from the values of d. For example, the lattice parameters of tetragonal crystals are calculated from [80]:

$$\frac{h^2+k^2}{a^2} + \frac{l^2}{c^2} = \frac{1}{d^2} \qquad 4.2$$

where h, k and l are Miller indices of the plane, while a and c are the lattice parameters.

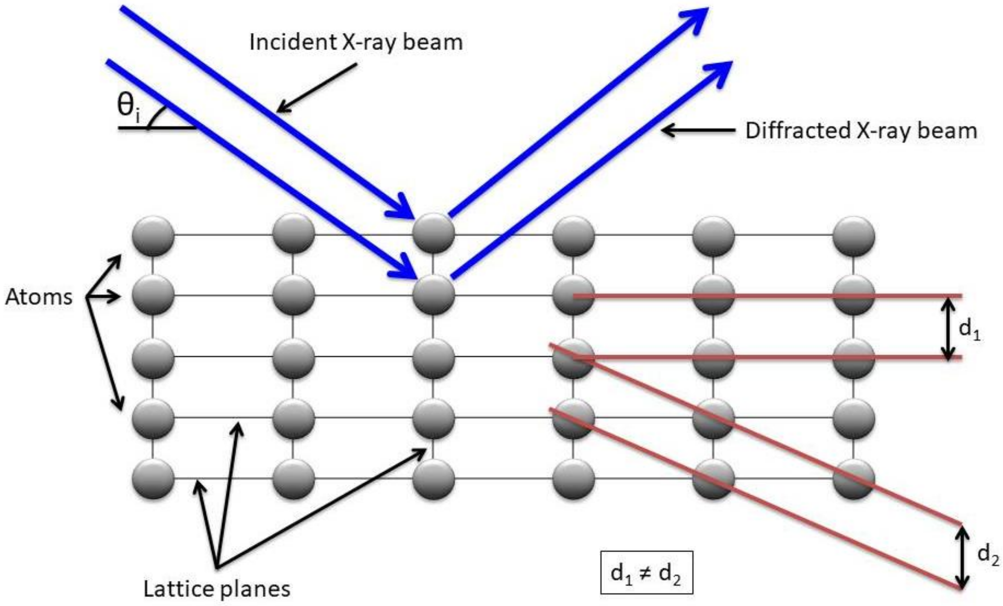

Figure 4.1 A schematic illustration of the interaction between X-ray and matter. Here, d_1 and d_2 are interplanar spacing distances adapted from reference [80].

The applied x-ray transmits the studied sample and collides with its atoms [81]. The negatively-charged electrons of these atoms interact with the electromagnetic field of the incident X-ray leading to its elastic scattering away from the sample [81]. In addition, the electrons oscillate due to the field of the incident X-rays, which leads to the emission of electromagnetic waves that are identical in phase and wavelength to incident X-rays (fig. 4.2) [81]. In crystalline solids, the atoms are periodically ordered and the diffracted X-rays from equally-spaced atoms will interfere with the incident X-ray to form diffraction patterns that are characteristic to *d*-spacing of crystal lattice [81]. The diffraction of X-rays from non-ordered materials interfere destructively that it is not possible to identify patterns [81]. The elastic scattering of X-rays dominates in elements with high atomic number leading to higher intensity patterns, while inelastic scattering in low-atomic-number elements is more prominent. A detector then collects the diffracted X-rays and records their intensity. The application angle of X-ray to the sample surface is then varied and the data from different application angles is recorded [80].

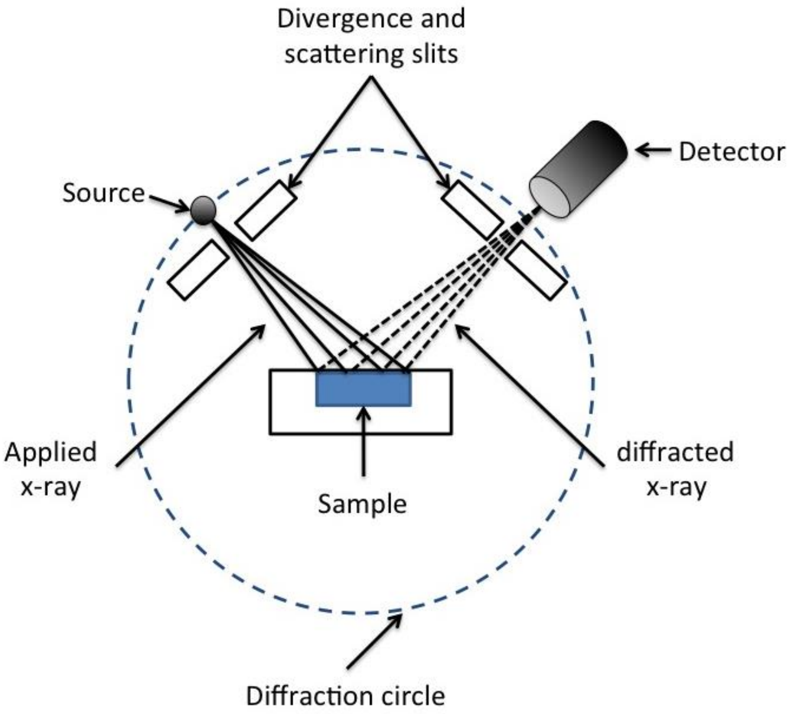

Figure 4.2 A schematic sketch of the basic parts of XRD diffractometer adapted from reference [80].

The reason for using XRD in this work was to identify the phases in different samples and provide the required database for other techniques. The XRD was performed using a Siemens D5000 (Cu, GA-XRD) diffractometer with Cu Kα radiation (wavelength λ = 1.54178 Å) and 2 mm wide slits for incident and diffracted beams. This equipment was also provided with a secondary beam monochromator to reduce fluorescence and background noise, but with no element restrictions. The samples were mounted flat to the holder surface and to 0° tilt, and held with non-elastic Apiezon Q Sealing Compound putty. Although measures were taken to ensure no tilting in the sample mounting, small shifts of 0.01° are possible to occur. Such tilts can be adjusted during the computer analysis of the data. The data can be presented as a spectrum of intensities of diffracted x-ray at different incident angles (fig 4.3).

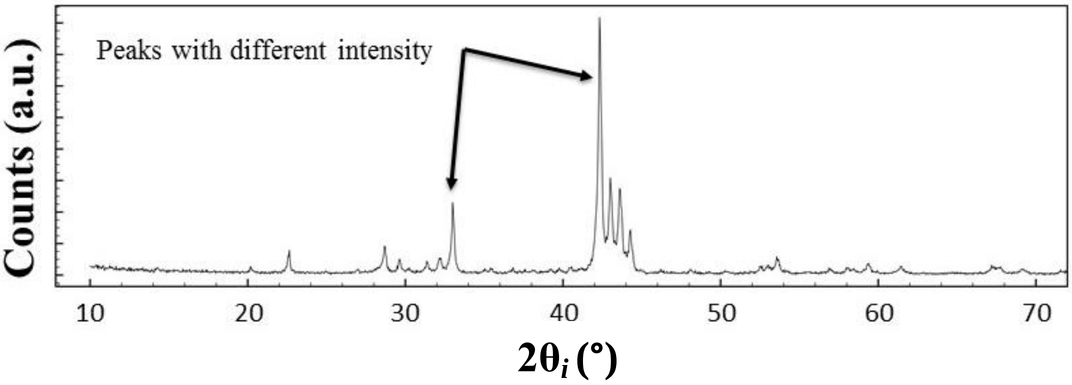

Figure 4.3 An example of a collected X-ray diffraction (XRD) spectrum.

Sleve+ software is provided by the International Centre for Diffraction Data (ICDD) with a built-in access to their database [80]. ICDD data are stored as ‘powder diffraction file’ (PDF), often called PDF cards, which contain the lattice parameters, *d*-spacing and crystal geometry for a large number of phases (more than 354200 phases) [80]. The software runs a matching process that lists the phases according to the highest number of matching *d*-spacing to the measured ones.

4.4 Scanning electron microscopy

Scanning electron microscopy (SEM) offers a variety of measurements that each depend on the interaction of an applied beam of electrons with materials in different ways [81]. Each type of interaction causes a characteristic emission or diffraction of electrons or X-rays that enable sample features, chemistry and morphology to be imaged with high spatial resolution (fig. 4.4) [81].

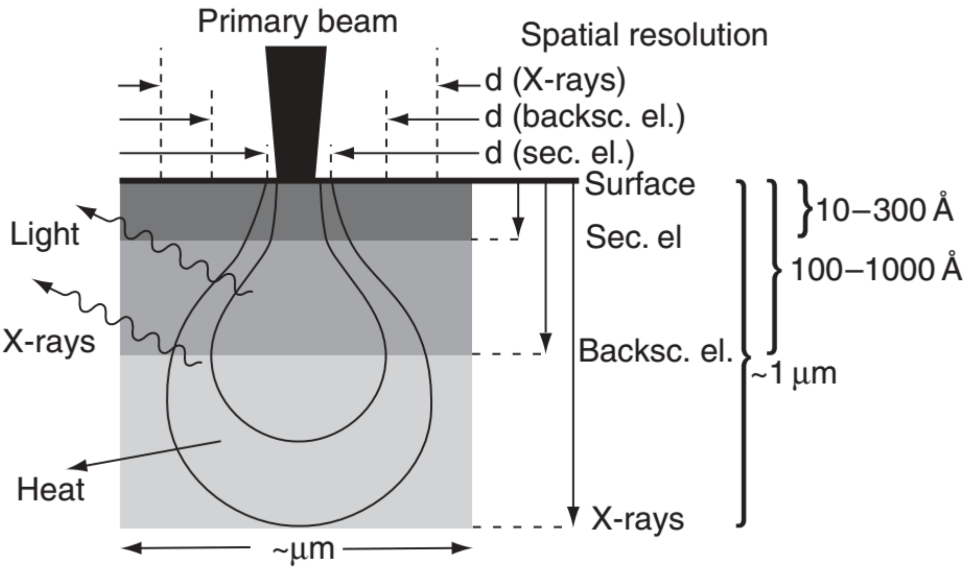

Figure 4.4 A schematic sketch of the various emissions resulting in the interaction of an electron beam with matter and their relative distances from surface [81]. Reprinted with permission of John Wiley and Sons, Inc.

In SEM systems, electrons from a thermionic or field emission source are accelerated and focused onto a sample surface. The beam is scanned across a sample using electron deflection plates and spot sizes of 5 nm can be achieved, although this reduces/increases with increasing/decreasing beam acceleration voltage. The acceleration voltage also controls the energy of incident electrons, which changes the volume of interaction beneath the sample surface. The two most common methods of SEM imaging are Secondary electrons (SE) and backscattered electrons (BSE). SE are electrons with kinetic energies less than 50 eV that succeed in escaping the sample [81]. The region they are associated with is close to sample surface and hence they can be used reveal information about the morphology of thin surface areas of the sample (generally >100 nm in metals) [81]. This will be manifested as a magnified image with contrast difference that represents the difference in scattering of secondary electrons at different locations on the sample surface. The contrast variation across SE images can be used to reveal information about the different phases, grains and their boundaries [81]. On the other hand, BSE are generated from the elastic scattering of incident electrons at deeper areas in the sample compared to SE (up to ~1 µm). Hence, BSE imaging is used to reveal information about areas that are more buried in the sample [81]. The data presented by BSE image shows the difference in the atomic number of elements, which can be used to identify phases with different composition [81].

The SEM systems used in this work were JOEL JSM 6400 and FEI inspect-F NanoSEM 450. The author performed all the measurements that were made using the JOEL JSM 6400. Dr. Amit Rana of the Mercury Centre for Materials characterization participated in the imaging using the latter two SEM systems. SEM and BSE images were obtained with acceleration voltages of 20 and 30 kV, respectively. The probe size was 5 nm for all the measurements.

4.5 Energy dispersive X-ray spectroscopy

Energy dispersive X-ray (EDX) spectroscopy is a useful tool for quantitative and qualitative phase analysis by allowing the relative amounts of different elements in a particular sample area to be determined [81]. The origin of X-rays used in this technique is the excitation of an electron in an inner shell of an atom when it is struck by a beam of charged electrons. This excitation leads to the ejection of this electron from its shell leaving an electron hole that is filled by another electron from an outer shell. The difference in the electron energy at the outer and inner shells is emitted as X-rays [81]. Each element yields X-rays with a characteristic wavelength, which can be used to determine sample composition. INCA software, provided with SEM system, performs this composition identification process automatically and provides the weight (wt. %) and atomic (at.%) ratio of each element in the sample.

EDX spectra and element identification were performed using EDX facilities provided on SEM devices mentioned earlier. The time of acquisition using spot indexing was varied between 90, 120 and 150 seconds for each spectrum. The EDX-maps were obtained using same software used in EDX but with longer time of acquisition, generally 750-900 seconds.

4.6 Electron backscattered diffraction

4.6.1 Underlying Principles

Electron backscattered diffraction (EBSD) is a sub-micrometre scale technique that uses the diffraction of backscattered electron to reveal microstructural information about the sample [81, 82]. An incident beam of electrons interacts with a crystalline sample leading to some electrons backscattering by atoms away from the sample while others diffracting near Bragg angles. The periodicity of atoms in crystalline samples leads to a constructive interference of electrons diffraction to create a form of patterns. This diffraction follows Bragg law and the patterns consist of two parallel lines that each has a Bragg angle to the atomic plane [82]. These two lines are known as Kikuchi bands and the distance separates them from each other is the band-width [82]. The intersection of bands of different planes is known as the zone axis. At each point of electron beam incidence on a crystalline element, the sample will project a pattern of many Kikuchi bands and zone axes; these are known as the Kikuchi patterns (fig. 4.5) [82]. These patterns can be collected and used to reveal information about crystallographic structure of phases and its orientation [82].

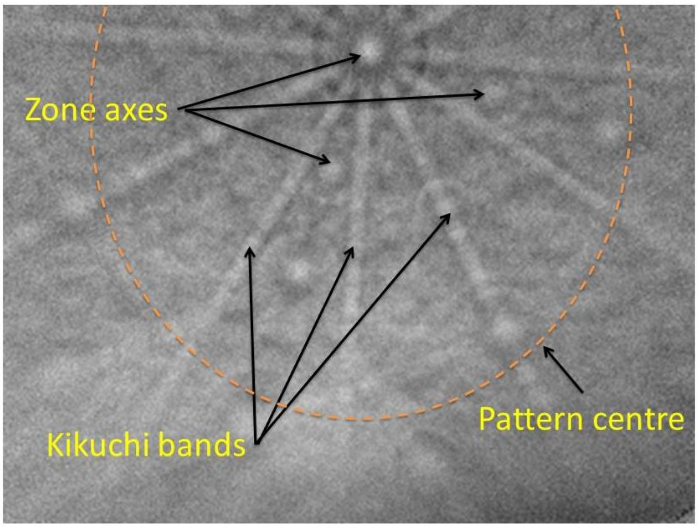

Figure 4.5 An example of a Kikuchi pattern from the Dy-free sample. The image shows typical layouts of zone axes, Kikuchi bands and the pattern centre.

4.6.2 Instrumentation

The essential components of equipment for observing EBSD are an electron beam source, a phosphor screen, a backscattered electron detector and the sample (fig. 4.6). The phosphor screen in EBSD systems allows these patterns to be observed and recorded [83]. Currently, software analysis of Kikuchi bands allows comparison with database information to reveal the crystal structure and orientation [82, 84]. The goodness of match of this indexing process is characterized by the mean angular deviation (MAD) [83]

The equipment used for EBSD was FEI Sirion field emission gun SEM. The sample holder requires samples with dimensions of 10 mm x 9 mm and a maximum thickness of 1 cm. SEM acceleration voltage used was 20 kV for all measurements. Higher voltages will increase the interaction volume and reduce spatial resolution [81, 83] while lower voltages (e.g. 10 kV) decrease the signal/noise ratio, which reduces band contrast and leads to difficulties in band detection [83]. This EBSD system is equipped with a phosphor camera (manufactured by Nordlys Co.) to collect Kikuchi patterns. EBSD measurement is controlled through Flamenco software provided on the system.

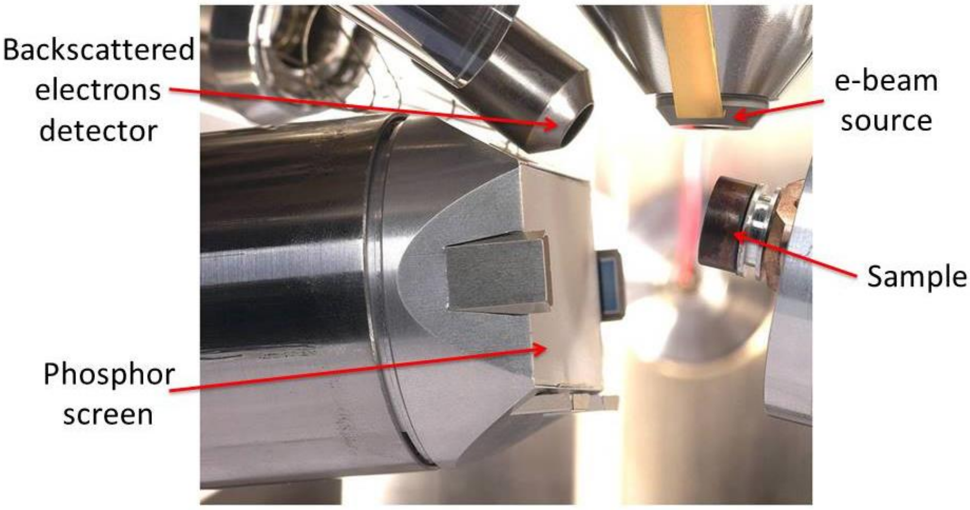

Figure 4.6 A screenshot of the main components of EBSD system.

4.6.3 Standard protocols

EBSD uses diffracted electrons from a depth of tens of nanometres in the sample [85]. Hence, EBSD is highly surface sensitive and the quality of that surface plays a major part in the accuracy of collected data. Any remnant scratches at an area on the sample will distort the collected bands, which often results in non-usable data [86]. For this purpose, the polishing steps at sample preparation must ensure a high quality of surface preparation. However, over-polishing the sample can produce a non-flat surface, which makes it difficult to achieve acceptable distance calibration between the camera and sample surface. The variation in height, even as small as few nanometres, will affect the measured bandwidths on the phosphor screen. This in turn will cause non-accurate indexing for patterns, which is known as mis-indexing [83].

EBSD technique is one of the most advanced techniques in materials science [85]. The measurement consists of many steps that have significant effect on the collected data [83]. Each step has a set of parameters that must be defined by the user. Fig. 4.7 shows the main steps of the EBSD measurement.

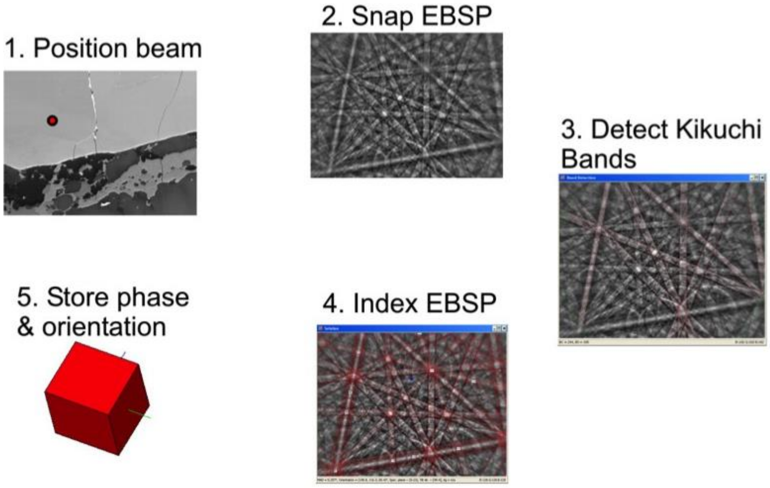

Figure 4.7 The main steps of electron backscattered patterns (EBSP) acquisition process.

Positioning the electron beam encompasses the process of calibrating the distance of sample surface to the beam source before moving to EBSD acquisition. A standard SEM imaging procedure was followed for this purpose. This was followed by tilting the sample to a 70° angle and inserting the phosphor camera to its designated position. A high number of Kikuchi bands are usually present but only certain bands are useful for indexing. To eliminate the non-useful bands, a background removal step was executed that includes the parameters:

- The number of frames, which has a standard value of 64.
- The binning parameters help reducing the measurement time by clustering together a group of pixels. All measurements used a binning of 2x2 pixels.
- The gain of the camera is important to increase its sensitivity to bands but with making sure that noise levels are acceptable. Here, the values used are between 5 to 9.
- Time per frame value assigns the acquisition time of each pattern. The values used were between 20-24 ms.

The background contrast is acquired and subtracted from the collected patterns. It is possible to assess the success of this process using the colour tool provided by acquisition software.

Detecting the bands is the most important step because it defines the features of the patterns at each pixel (or a group of pixels). The features are the bands, the angles between them, the zone axes, their intensity and bandwidths. The settings used are:

- The detection parameter controls whether to use the band edges or the band centre for detection. In this work, band edges were only used for band detection.
- Number of bands is the most important parameter in the band detection setting. Choosing high numbers of bands requires longer acquisition times but results in more accurate indexing [83] and often produces more non-indexed patterns, (known as **zero solutions).** Lower minimum numbers of bands reduces the number of zero solutions but leads to less accurate indexing. The minimum number of bands used here was eight, while the maximum number was 12.
- Hough space is parameter that controls the procedure of transforming the data of bands intensity, angles between bands and the zone axes' positions [83]. Here, the used Hough space values are 50-60.

The final step is to index the Kikuchi patterns from each sample position to simulated patterns obtained from the predefined crystallographic data either from the database of ICDD or using a user-created phase. Table 4.1 shows the crystallographic data of the phases relevant to Nd-Fe-B material and their lattice parameters, while table 4.2 shows the atomic coordinates of the $Nd_2Fe_{14}B$ unit cell.

Table 4.1 prototype, space groups and lattice parameters of common phases in Nd-Fe-B samples.

Phase	**Prototype**	**Space group**	**Lattice parameters (nm)**		**Ref.**
			a	**c**	
$Nd_{1.11}Fe_4B_4$	$NdCo_4B_4$	*Pccn*	0.7117	3.507	[31]
NdO	NaCl	*Fm-3m*	0.507-0.524		[31]
Nd_2O_3	La_2O_3	*P-3m1 - hcp*	0.39	0.61	[31]
Nd_2O_3- cubic	Mn_2O_3	*Ia-3*	1.1		[31]
NdO_2	CaF2	*Fm-3m*			[31]
$Nd_2Fe_{14}B$		$P4_2/mnm$	0.880	1.221	[38]

Table 4.2 atomic occupancies and coordinates of $Nd_2Fe_{14}B$ crystal [34].

Compound	**Space group**	**Atom**	**Site**	**Occupancy**	**x**	**y**	**z**
$Nd_2Fe_{14}B$	$P4_2/mnm$	Nd	*F*	4	0.266	0.266	0.0
		Nd	*G*	4	0.139	-0.14	0.0
		Fe	*K1*	16	0.224	0.568	0.128
		Fe	*K2*	16	0.039	0.359	0.176
		Fe	*J1*	8	0.097	0.097	0.205
		Fe	*J2*	8	0.318	0.318	0.247
		Fe	*E*	4	0.5	0.5	0.113
		Fe	*C*	4	0.0	0.5	0.0
		B	*g*	4	0.368	-0.37	0.0

Flamenco software of EBSD system stores the data collected from each point on the sample as grid points, where each point on the grid has a set of data numbers. These numbers include band contrast, Euler’s angles, the pattern’s MAD, number of bands used for indexing and the name of the phase chosen as a most accurate match. The latter depends on the discriminators specified by the user and the lowest value of MAD among the matched solutions. The data of indexed points can be viewed through software called HKL Channel 5, which is provided by Oxford instruments.

There are two main length scales in EBSD system that can influence the data collected. The first one is between the patterns emission point on the sample and the phosphor camera; the other is the distance between the pole piece of the electron beam source and the sample [82, 83]. These distances should be identified and fixed at all measurements. To ensure a correct definition of these distances, a calibration that eliminates any differences is always needed [83]. After performing the calibration step, it is possible to start indexing jobs. Large areas of mapping could be conducted using an automated process.

The success of EBSD sessions is measured by a value known as ‘the hit rate’, which is represented by:

$$Hit\ rate = \frac{no.of\ successfully\ matches\ points}{no.of\ total\ measured\ points} \qquad (4.3)$$

The successful indexing means that a match is found between the collected pattern and pre-acquisition defined patterns. The parameters listed above have been set and optimised to achieve high hit rates (>80% success) for indexing steel and Ti-alloys. Little or no changes were made previously to these parameters.

4.6.4 Grain size determination

The size of main phase grains plays an important role in determining the magnetic properties of sintered Nd-Fe-B magnets [48, 71, 87]. The refinement of grains size has been reported to be an effective tool in improving these properties and their thermal stability (see §3.6.2) [48, 56]. For this reason, the comparison between the three samples studied in this work should include the grain size statistics. The linear intercept method is an established method for calculating the mean grain size [88] and it was used to measure the average grain size along the *x*-axis of the band contrast maps obtained by EBSD. It should be noted that the grain size here refers to the grain's diameter. An intercept line taken though an image allows the mean grain diameter (D_x) to be calculated according to [83]:

$$D_x = \frac{R_x\, P_x\, S}{N_x} \tag{4.4}$$

where R_x is the number of rows, P_x is the number of pixels in the x-axis and S is the step size of the EBSD acquisition. The mean diameter along the y-axis (D_y) is measured in a similar manner. The overall mean grain diameter (D) is the average of D_x and D_y. The standard error of this mean diameter (δ) can be calculated from [88]:

$$\delta = \frac{\sigma}{\sqrt{N}} \tag{4.5}$$

where σ is the standard deviation of the diameter of grains from the mean and N is the number of the grains used.

The calculations of the average grain diameter provide an insight in the microstructure of Nd-Fe-B magnets and their powder size before sintering [13, 26]. However, these calculations assign a single average grain size value for the whole sample. The size distribution of grains is also of major importance in defining the magnetic properties of sintered Nd-Fe-B magnets [48, 72, 87]. Here, the grain size (diameter) distribution of each sample was calculated by using the average of D_x and D_y of each grain (equation 4.4).

4.7 Micromagnetics

Domain theory has provided some explanations to the magnetism of ferromagnetic materials and the interactions between magnetic energies [17, 46, 89]. However, some of the magnetic characteristics need more in-depth analysis in order to fully understand the behaviour of magnetic materials [17, 46]. An example of which is the deviation of the coercive field of high energy density permanent magnets from the theoretical values [53]. Micromagnetics is an approach to study magnetisation dynamics at a length scale larger than crystal lattice dimensions but smaller than magnetic domains size, which is a concept was first introduced by Brown *et al* [49, 66]. Micromagnetics gained more consideration in research with the increased availability of high-power computing and it is widely used now to study a variety of systems, for example: hard magnets [12], information technology [66] and recording media [66]. An overview of micromagnetics is presented in this section with a focus on the micromagnetic tools used in this work.

4.7.1 Gibbs free energy

Micromagnetic theory provides a numerical framework that approximate the magnetic structure and demagnetisation mechanisms in magnetic materials [46]. It derives the important contributions of magnetic energies and uses them to predict the magnetic dynamics [66]. These energies are the exchange energy (E_e), magnetocrystalline anisotropy energy (E_a), magnetostatic energies (E_m), and the Zeeman energy (E_z). The latter describes the energy arising from an applied field and has its minimum when the magnetisation of the material is parallel to the applied field direction [17, 20]. The total Gibbs free energy can be expressed by [46]:

$$E_t = E_e + E_a + E_m + E_z \tag{4.6}$$

where E_t is the total Gibbs free energy.

The minimisation of the total Gibbs energy gives an approximation to the static magnetic structure of the system and the upper bound values of its remanence and coercivity [66]. This minimisation with respect to system volume can be written in the equation [46, 66]:

$$E_t = \int [\, A_{ex} \sum (\nabla m_i)^2 - K(\boldsymbol{m} \cdot \boldsymbol{u})^2 - \mu_0 M_S (\boldsymbol{m} \cdot \boldsymbol{H_{ext}}) - \frac{\mu_0 M_S}{2} (\boldsymbol{m} \cdot \boldsymbol{H_d}) \,] dV \tag{4.7}$$

where A_{ex} is the exchange stiffness constant, m is the magnetic moment vector, m_i is the magnetic moment components in the x, y and z directions, K is the magnetocrystalline anisotropy constant, H_{ext} the external field and H_d is the demagnetisation field. Here, the total Gibbs energy (equation 4.7) gives a static approximation to the magnetic structure. This principle was further developed to calculate the time evolution of the magnetic structure of the system [46, 66]. The equation that describes the processional path of magnetisation were introduced by Landau and Lifshitz [66]. Landau-Lifshitz equation was later modified by Gilbert to take into account the gyromagnetic damping (α) (fig. 4.8) [66]. The modified version is known as Landau-Lifshitz-Gilbert (LLG) equation [10]:

$$\frac{\partial \mathbf{M}}{\partial \mathrm{t}} = -\frac{|\gamma|}{1+\alpha^2}\mathbf{M} \times \mathbf{H}_{\mathrm{eff}} - \frac{\alpha}{M_s}\frac{|\gamma|}{1+\alpha^2}\mathbf{M} \times (\mathbf{M} \times \mathbf{H}_{\mathrm{eff}}) \quad (4.8)$$

where γ is the gyromagnetic ratio of the free electron spin and α is the dimensionless term of damping. Often, α is specified to have a value between 0.1-1.0 [66]. The exact values of α can be obtained from magnetic resonance measurements of magnetic materials [66]. $\mathbf{M}$ here represents the magnetisation response to the magnetic torque and is represented by:

$$\mathbf{M} = M_s\, \boldsymbol{m} = M_s\left(m_x, m_y, m_z\right) \quad (4.9)$$

LLG equation (equation 4.8) presents the concept of the effective field (H_{eff}), which describes the torque that rotates the magnetic polarization towards a particular direction [66]. H_{eff} is represented by:

$$\mathbf{H}_{\mathrm{eff}} = -\frac{\mathbf{1}}{\boldsymbol{\mu}_\mathbf{0}}\frac{\delta \mathrm{E_t}}{\delta \mathbf{M}} \quad (4.10)$$

LLG equation describes the path that magnetisation follows to equilibrium. The integration of LLG equation gives the demagnetisation curve in dynamic calculations [66]. This is achieved by assuming that the magnetic system is saturated and the applied field is decreasing gradually. The repeated solving of LLG equation overtime with changes in the applied external field can provide a full hysteresis loop for the magnetisation of the system [66].

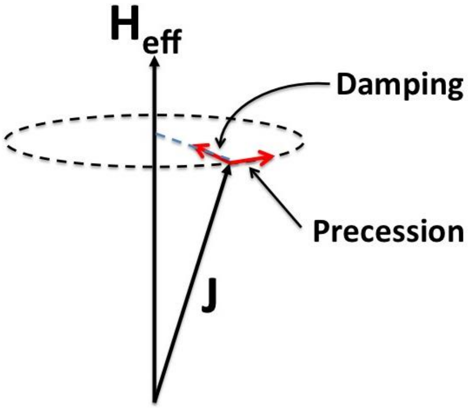

Figure 4.8 An illustration of the gyromagnetic damping and precession motion of magnetic polarization [66]. Reprinted with permission of Journal of Physics D.

Due to the complexity of the numerical calculations of micromagnetics; it may take a long time to solve with requiring a large computing memory [46, 66]. Recent developments in computing capacities provided improved processing methods, which have led to a reduction in time of computation of these micromagnetic simulations [66, 90, 91]. Several tools are available now for this purpose such as: finite difference method (FDM) and finite element method [46]. In FDM, the discretisation is achieved by dividing the system into rectangular meshing elements. The magnetisation is assumed to be homogeneous in each element and the magnetic energies interactions between elements are calculated in each model [46]. FDM is limited for simple geometries, while finite element methods, on the other hand, are more flexible and can handle complex shapes.

4.7.2 Finite Element Method

Finite element method (FEM) has increased in use during the past few years [92, 93]. It has been used in various engineering studies such as structural analysis [92], electromagnetism

[92] and thermodynamic analysis [92, 93]. The concept of the finite element method depends on the discretization of the system into a finite number of smaller parts [92]. These elements, which are known as 'the mesh', may have various shapes such as 2D elements (triangles, squares or rectangles) and 3D with tetrahedrons, cubes or hexahedrons shapes [92]. The physical phenomena represented by its governing equation is then applied and solved for each element [91, 92].

The finite element method package used in this study is FEM-Micromagnetics (FEMME), which is developed by Schrefl and Suess [90]. This method relies on the discretization of the Gibbs free energy equation as its governing equation. The discretization of this equation uses the Galerkin method, which is achieved by dividing the system into small subdivisions [90]. In FEMME, the system geometry is created and the magnetic characteristics (such as: exchange energy, anisotropy, etc.) of the system are defined. Then, a finite number of nodes are defined inside the system. The energy minimisation is performed by evaluating the magnetic polarisation at each nodal point using polar (θ and ϕ) coordinates (fig. 4.9) [66]. Then, the polarization values in the x, y & z directions will be calculated at each node and interpolated linearly to represent the magnetic values of the elements. The final step is to sum the values of integral energy for the whole shape/system.

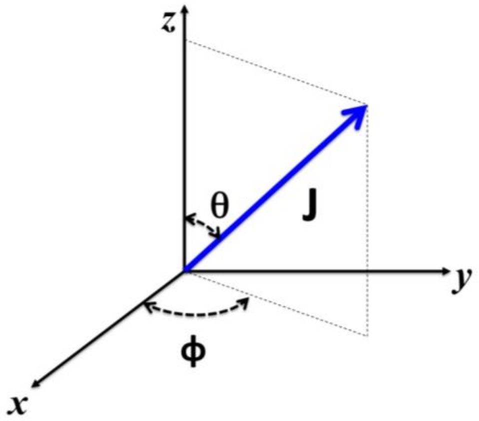

Figure 4.9 The polar coordinates that define the direction of a single magnetic polarization at each nodal point.

FEMME uses hybrid method to deal with the open boundaries for its systems [66]. This has brought significant improvements to the accuracy and effectiveness of demagnetisation fields as it eliminates the need to extend the mesh outside the system. In addition, the calculation of the magnetostatic field is now pre-computed leading to savings in processing time [66].

4.7.3 Shapes and meshing

The model creation package uses the open-source Gmsh software. Gmsh (version 2.9.0) is a 3D finite element grid generator software that have a CAD interface [94]. The final version of the model creation package has a fast, light interface that is able to produce 3D models with different shapes and sizes. In addition, the meshing capability has been developed to be able to mesh the created shapes by different types of mesh and different mesh size. These shapes were created by seeding points at random coordinates in the space. Then, the shapes were grown by connecting these points at a defined velocity in each direction to create the volumes of shapes, which is known as Voronoi tessellation. These volumes (grains) could be defined to have individual magnetic properties and alignment. It is also possible to create thin regions separating these grains, which were used to represent grain boundary phases. These grains could be created with variety of shapes such as cubic, rectangular and polyhedral shapes. Further improvements have enabled adding randomness to the location of these seed points in order to create models that represent close-to-real features of samples microstructure.

The next step is to create the mesh, which is done by Gmsh software. The element size defined in a particular structure is very critical to the accuracy of the simulation[66] . In hard magnets, this criticality is manifested in three characteristic length scales. The first parameter is known as the exchange length (l_{ex}), which is calculated from [11, 46]:

$$l_{ex} = \sqrt{\frac{A_{ex}}{K_u}} \qquad (4.11)$$

where K_u is the uniaxial magnetocrystalline anisotropy. The value of l_{ex} defines the strength of the exchange between magnetic moments in the material [76]. For example, l_{ex} of $Nd_2Fe_{14}B$ phase is ~1.7 nm. The second parameter is known as the magnetostatic exchange length (l_{mex}) and can be calculated from [46, 95]:

$$l_{mex} = \sqrt{\frac{2A_{ex}}{\mu_0 M_s^2}} \qquad (4.12)$$

This parameter represents the effect of the dominating magnetostatic energy and it has a value of ~3.4 nm for $Nd_2Fe_{14}B$ phase. The third parameter is the domain wall width (see §2.3.2). The simulation of hard magnets with mesh scale comparable to these values can provide a higher resolution to the simulations of magnetisation/demagnetisation processes [66]. On the other hand, the number of elements determines the time length of the simulation and reducing this number can significantly reduce the time required for simulation. However, this will be at the expense of accuracy of calculations. One method is to reduce the number of elements with maintaining the best possible resolution to create a dense mesh at areas where reversal is expected to occur [66].

5.Experimental Characterisation

5.1 Introduction

The three sintered Nd-Fe-B magnets used in this study were produced for wind turbines applications in 2014. These magnets are different in the amount of Dy with no Dy content, a reduced amount of Dy (<0.3%) and a higher amount of Dy (~0.36%) and they will be denoted hereafter according to this Dy amount as Dy-free, Red-Dy and Dy-rich, respectively. In this chapter, the results of experimental characterisation of each magnet are presented. The samples were characterised using vibrating sample magnetometer (VSM), X-ray Diffraction (XRD) and scanning electron microscopy (SEM). The information obtained throughout this work was used to inform the development of micromagnetic models shown in later chapters.

5.2 Vibrating sample magnetometer

The hysteresis loops were measured at room temperature and revealed coercivities (H_c) of 1.51, 1.34 and 1.27 MA.m^{-1} for Dy-free, Red-Dy and Dy-rich magnets, respectively (fig. 5.1). On the other hand, the maximum energy density (BH_{max}) value for Dy-free sample was the highest with 372 kJ.m^{-3} compared to 358 kJ.m^{-3} for Red-Dy and 359 kJ.m^{-3} for Dy-rich samples. Typical BH_{max} values in sintered Nd-Fe-B magnets are between 326-470 kJ.m^{-3} [7, 8, 26, 30].

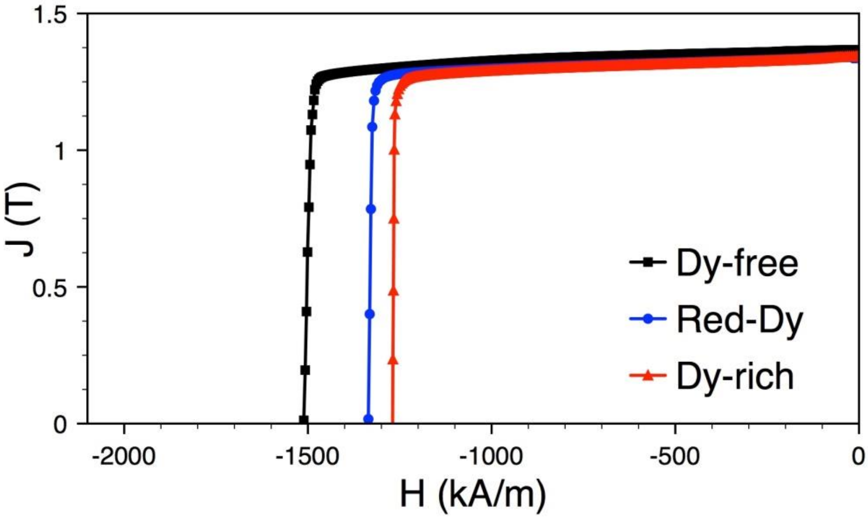

Figure 5.1 The 2nd quadrant of the hysteresis loops of Dy-free, Red-Dy and Dy-rich samples obtained through VSM measurements.

The partial replacement of Nd with Dy in sintered Nd-Fe-B magnets was reported to increase their H_c and to decrease BH_{max} slightly [5, 9, 14]. For example, substituting 40% of Nd concentration with Dy in sintered Nd-Fe-B magnets increased H_c from 954 kA.m^{-1} to 2390 kA.m^{-1} [9]. Here, it is interesting that the Dy-free sample produced higher H_c with no Dy additions compared to Red-Dy and Dy-rich samples, which have Dy additions. In addition, Red-Dy sample produced a higher H_c compared to Dy-rich sample, although the latter has the highest Dy content compared to the other two samples. H_c of Nd-Fe-B magnets depend strongly on their microstructure [39, 61, 96], which determines the field required for reversed domain walls generation and propagation across the magnet. Hence, the difference in H_c of the three samples presented above was related to the difference in their microstructure. This difference in H_c also indicates that 1) increasing H_c of Nd-Fe-B magnets is possible with no Dy additions and that 2) higher Dy additions does not necessarily produce higher H_c. The microstructural analysis of the three samples can help to shed the light on the main differences in their microstructural features that might lead to such differences in their

H_c. These features include alloy composition, the size and orientation of main phase grains and the composition of intergranular phases.

5.3 X-ray diffraction

XRD was used in order to identify the lattice parameters of the main phases in Dy-free, Red-Dy and Dy-rich magnets. XRD spectra of the three samples (fig. 5.2) confirmed the presence of the main tetragonal $Nd_2Fe_{14}B$ phase with a=0.879 nm and c=1.217 nm [97] and also revealed the presence of a range of secondary phases. The strongest peaks in the three spectra matched the peak positions of the $Nd_2Fe_{14}B$ phase. These peaks were indexed as (105) and (314) planes in both Dy-free and Red-Dy samples and they matched the (410), (411) and (314) planes in the Dy-rich magnet. The matched crystallographic planes of the $Nd_2Fe_{14}B$ phase in the three samples are similar to previous reports in [28] and [70]. The difference in the main phase peaks between the Dy-free, Red-Dy and Dy-rich samples can be attributed to the difference in sample orientation during sample preparation for XRD analysis.

The peaks at 2θ=38°, 45° and 53.5° in all samples matched the (002), (110) and (103) crystallographic planes of the hexagonal Nd_2O_3 phase with a=0.303 nm and c=0.599 nm [41]. The peak at 2θ= 62° was observed strongly in Dy-free and Red-Dy samples and with lower intensity in Dy-rich magnet and it matched the (311) plane in the double-hexagonal NdO with a=0.35 nm and c=1.18 nm [98]. The minor peak at 2θ~24° in Dy-free and Red-Dy samples matched the (200) plane of the B-rich rhombohedral $Nd_{1.1}Fe_4B_4$ with a= 0.71 nm and c= 3.5 nm [49]. Other peaks, such as 2θ~32°, did not match any of the likely phases in Nd-Fe-B magnets.

XRD analysis of the three samples confirmed the presence of the main $Nd_2Fe_{14}B$ phase Nd-oxides and B-rich phases that were reported previously in sintered Nd-Fe-B magnets (see

§3.3.1) [28, 41]. Although XRD identification of the structure of these phases correlates with reported structures in previous studies [31, 41], further analysis of the microstructure is needed to identify the present Nd-rich phases. These phases are smaller in size compared to other phases and their chemical composition and crystal structure are still under investigation [29, 40]. The successful characterisation of Nd-rich phases can improve the understanding of their role in the demagnetisation process in sintered Nd-Fe-B magnets, which is essential to explain the significant difference in the H_c of the Dy-free, Red-Dy and Dy-rich samples.

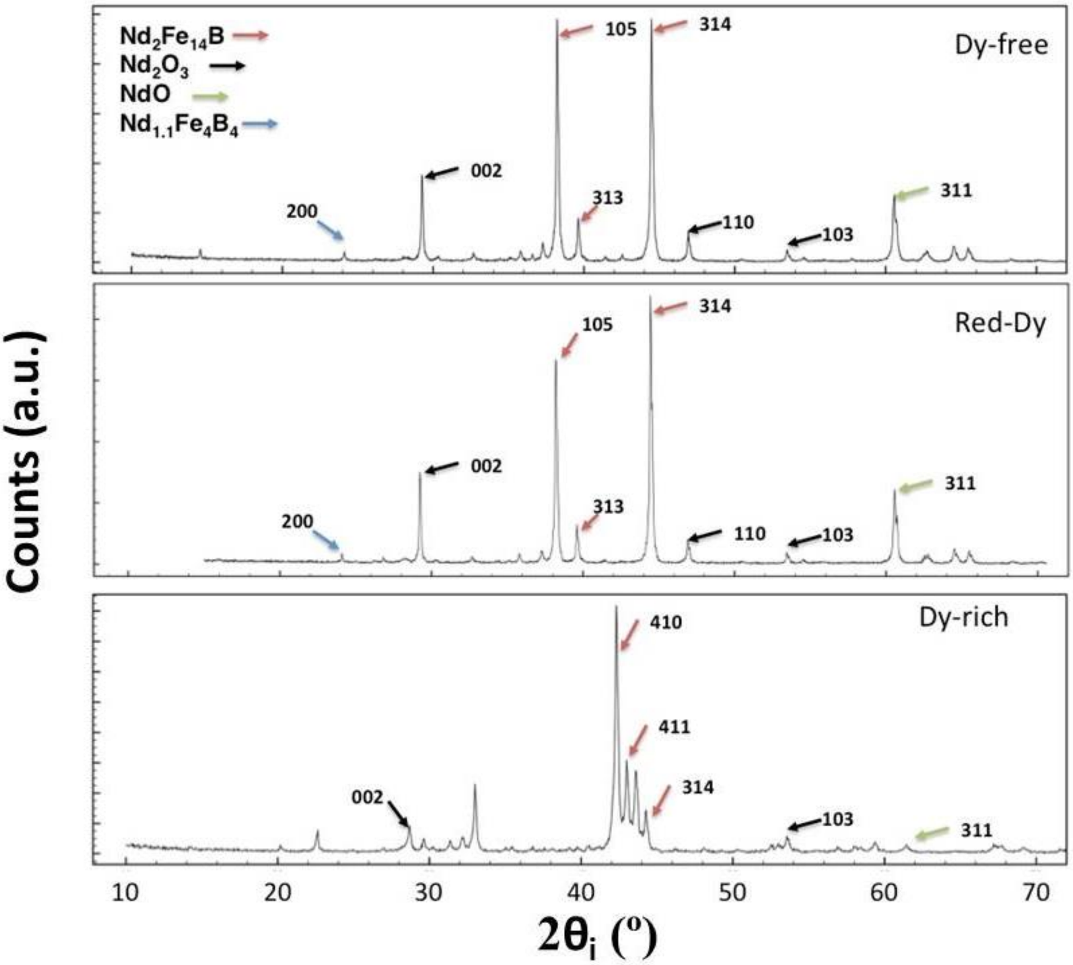

Figure 5.2 XRD spectra of Dy-free, Red-Dy and Dy-rich free magnets. The coloured arrows represent the crystallographic planes of the indexed phases

5.4 Electron microscopy imaging

Secondary electron (SE) and backscattered electron (BSE) imaging was performed at many points across the samples using different sample sizes. This was supported by energy dispersive X-ray (EDX) analysis to obtain elemental composition at these points. It is common for sintered Nd-Fe-B magnets to contain more than one type of rare-earth (RE) elements, such as Pr and Dy in addition to Nd [9, 30]. This means the RE concentration in $Nd_2Fe_{14}B$ grains and intergranular phases is likely to be comprised of more than one RE element. Hereafter, these phases will be denoted $Nd_2Fe_{14}B$, RE-rich phases and RE-oxides for simplicity.

5.4.1 Dy-free magnet

Previous SE imaging of sintered Nd-Fe-B magnets reported the presence of dominant dark-grey contrast regions, which are likely to be the main $Nd_2Fe_{14}B$ phase [40, 99]. These regions are accompanied by a spread of lighter grey contrast regions, which are likely to be RE-rich phases, and a darker contrast regions, which are likely to be RE-oxides [99] or porosity. This distribution of phases was confirmed in EDX elemental maps of the Dy-free sample where Fe has a higher intensity at the dominant grey contrast regions, but appears to be lower at triple junction regions outside the main phase (fig 5.3a). The intensity of RE elements Nd (fig 5.3c) and Pr (fig. 5.3d) appears to be higher at some of the dark regions (A in fig. 5.3) and at the triple junction regions (B), but has a lower intensity at the main phase regions (C). The O content (fig. 5.3e) was observed to have a low intensity at the main phase regions and higher intensity at the dark regions. On the other hand, Al appears to be uniform across the sample except for the darkest contrast regions where it appears lower compared to other regions (fig. 5.3f). Al was reported to diffuse in the main phase grains [30] and also to exist in the intergranular phases [30] in sintered Nd-Fe-B magnets.

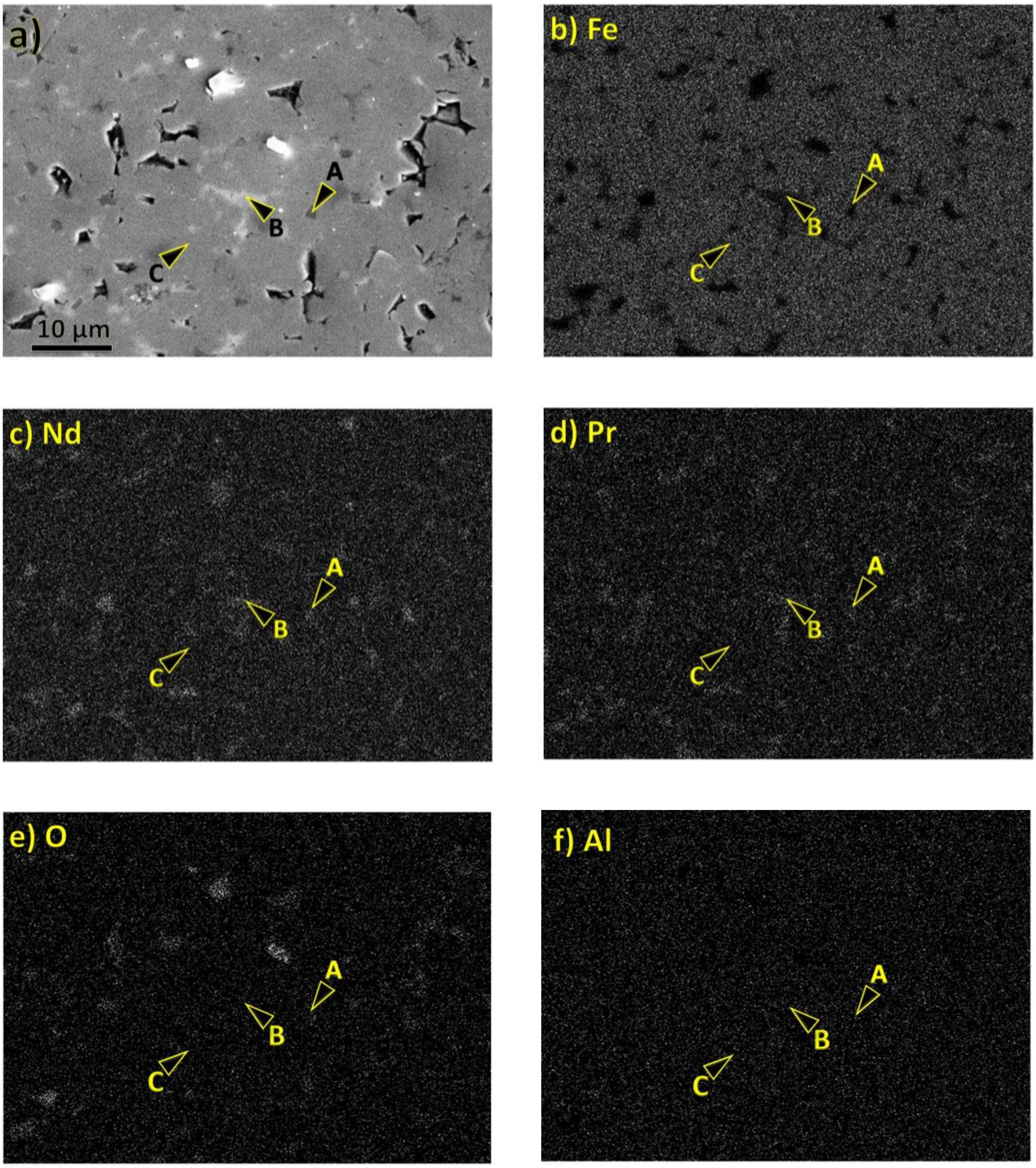

Figure 5.3 energy dispersive X-ray (EDX) elemental maps of the Dy-free sample showing (a) a secondary electron (SE) image and elemental maps of (b) Fe, (c) Nd, (d) Pr, (e) O and (f) Al. Points A and B represent two points that are darker and brighter than main phase point (C), respectively

EDX spectrum of the area in fig. 5.3 resulted in an average concentration of Fe~75.3 at.% and 14 at.% RE elements, which indicates that Dy-free magnet has an excess Nd compared to the stoichiometric composition of the main phase (fig. 5.4). Here, Fe/RE ratio of this area is 5.3, which is lower than the stoichiometric ratio (Fe/RE~7). On the other hand, O represents ~9.2 at.% of the sample and there is a minor Al content of 1.5 at.%. Obtaining B element distribution through EDX is not possible due to its low atomic number (*Z*) compared to other constituent elements in the alloy of Nd-Fe-B magnets [97], which means a lower intensity of X-ray radiation from B atoms.

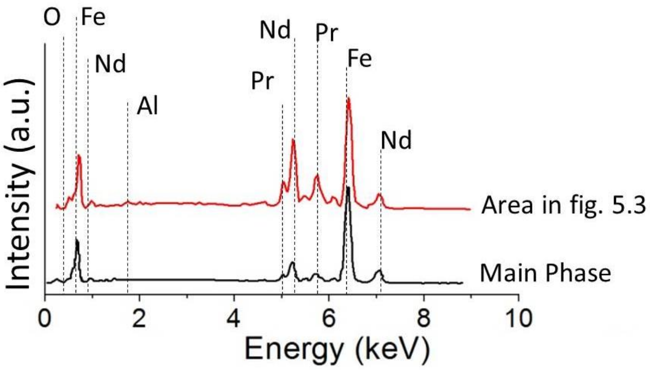

Figure 5.4 EDX spectra of a typical main phase and the area in fig. 5.3 with main peak noted. Both spectra obtained from Dy-free sample.

Dy-free magnet was revealed by VSM measurements (§5.2) to have the highest H_c and BH_{max} compared to the other two samples used in this work and these high properties are likely to be related to its microstructure. BSE image of the microstructure of Dy-free sample (fig. 5.5a) also shows the dominant dark grey contrast of the main phase that was seen in SE image in fig. 5.3a. This image also shows that the main phase is surrounded by intergranular phases that are located at the triple junctions between main phase grains with either a light (1 & 2) or a dark contrast (3 & 4) regions compared to the matrix phase. Points 1 & 2 have a similar contrast in SE image (fig. 5.5b), suggesting that both are the same phase, but different contrast in BSE image, which suggests that other elements might be enriched at one point than the other [97]. Points 3 & 4 have a darker contrast in both SE and BSE images (fig. 5.5). The dark contrast in SE image means that these phases have lower conductivity than the matrix phase [97]. In BSE images, the dark contrast means a region with a lower average atomic number (*Z*) from the main phase [68]. This indicates that both points are oxides, porosity or voids of particles removed during the polishing process. These dark regions were observed to have an average width up to 3.5 µm compared to an average width of up to 700 nm for light contrast regions. The average grain size of the main phase will be discussed in §6.7.

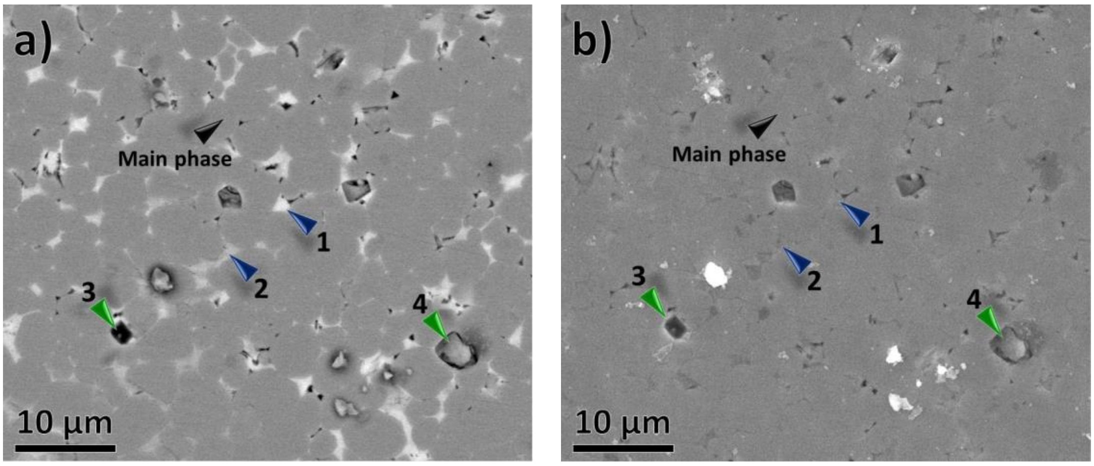

Fig 5.5 (a) backscattered electron (BSE) and (b) SE images of Dy-free magnet showing the main phase, RE-rich phases (1&2) and pores (3&4) that are likely to be resulted from the polishing process.

In addition to the triple junctions, the light contrast phases were also observed to be located between two neighbouring grains in Dy-free magnet (*i* and *ii* in fig. 5.6a). These grain boundary (GB) phases are likely to be RE-rich phases according to their higher contrast in the BSE image (fig. 5.6a), which were reported previously to have a thickness of 1-4 nm [39]. In addition, the similar contrast in SE image indicates that both *i* and *ii* are the same phase (fig. 5.6b). However, the EDX elemental analysis of point *i* showed a close composition to the neighbouring main phase with both having an Fe/RE ratio higher than 5.7 (table 5.1).

Although point *ii* showed a higher RE content compared to point *i*, the Fe content at this points is still very high. The narrow thickness of these GB phases increases the possibility of EDX volume overlap with other phases, which may explain the high Fe/RE ratio. Hereafter in the Dy-free sample, EDX elemental analysis will focus on identifying RE-rich phases at the triple junction areas because of their relatively larger size, hence reduced volume overlap. The phases at triple junctions have been suggested to have the same composition and structure as their connected thin GB phases [100]. In addition, RE-rich phases at triple junctions represent the source of thin GB phases formed in post-sintering annealing processes [38, 100].

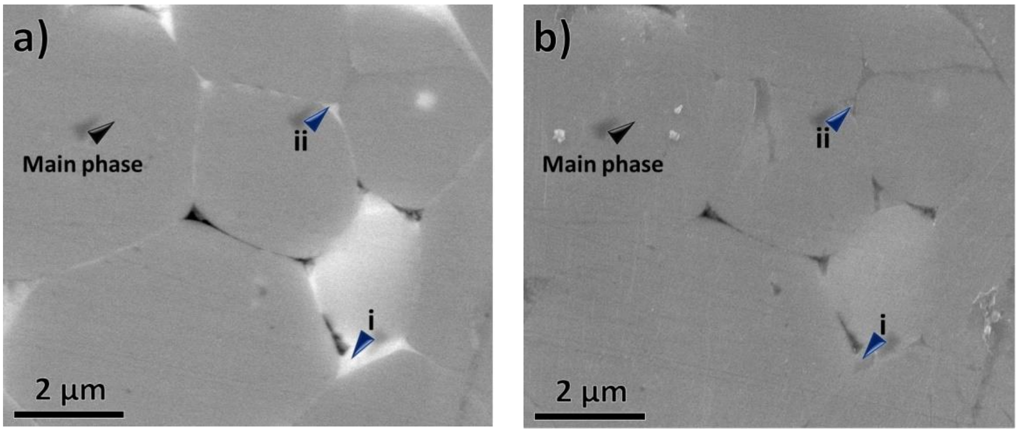

Fig 5.6 (a) Backscattered electron (BSE) and SE images of Dy-free magnet showing the main phase, RE-rich phases (*i* and *ii*)

Element	Main phase	*i*	*ii*
Fe (at.%)	85.2	85.0	75.1
RE (at.%)	14.8	14.9	18.8
Fe/RE	5.8	5.7	4.0
O (at.%)	-	-	6.1

Table 5.1 The EDX elemental analysis of the main phase, *i* and *ii* points in fig. 5.6.

Further EDX elemental analysis of points A-E in Dy-free sample (fig. 5.7) revealed two compositions at regions where Fe/Re ratio is lower than the main phase (table 5.2). The first composition is enriched with alloying elements such as Cu, Ga and sometimes Co region, which indicates that these phases are metallic RE-rich phases (points A & B fig. 5.7a) [29]. The O concentration at points A and B has been suggested to stabilize the amorphous nature of metallic RE-rich phases into *fcc*-NdO structure [41]. However, the enrichment of Cu, Ga and Co at these RE-rich phases has been suggested to represent a segregation of thin Nd-Cu phase between RE-oxides and main phase grains [29]. The exact elemental composition and magnetic properties of this Cu-enriched RE-rich phase are not clear yet and it is the subject of micromagnetic modelling in Chapter 7. The second composition has no alloying elements and it was observed at points B, C (fig. 5.7a) and E (fig. 5.7b). The SE contrast of these points indicates that they are likely to be RE-oxides with *fcc*-NdO structure. The points D and E appear to be two RE-rich phases around the same grain, yet EDX elemental analysis suggests significant differences in their concentrations.

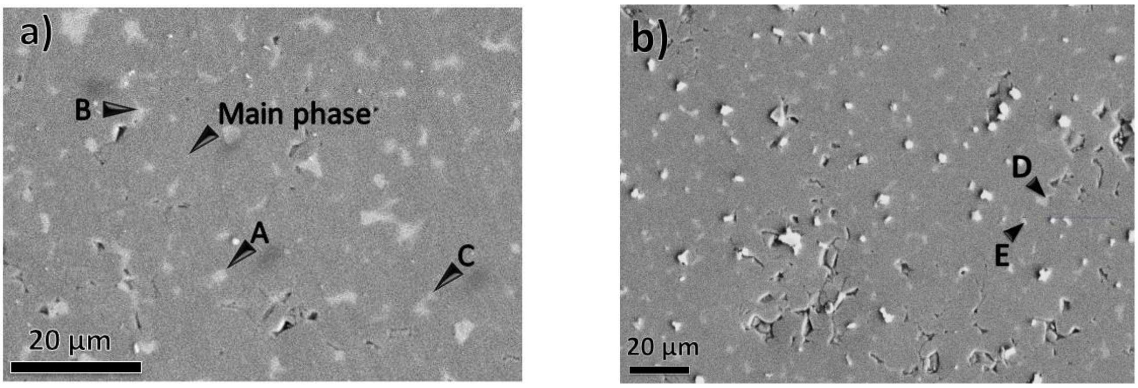

Figure 5.7 SE images of two different regions in Dy-free magnet showing (a) points A, B & C, (b) points D & E.

Element	Main phase	A	B	C	D	E
Fe (at.%)	84.1	59.1	66.4	61.7	34.8*	55.1
RE (at.%)	14	26.4	22.8	16.4	43.0	26.4
Fe/RE	6	2.2	2.9	3.8	0.8	2.1
O (at.%)	-	11.2	9.8	21.9	17.0	17.1
Al (at.%)	1.85	1.6	1.1	-	1.1	1.3
Cu (at.%)	-	1.0	-	-	1.4	-
Ga (at.%)	-	0.9	-	-	2.9	-

Table 5.2 The EDX elemental analysis of main phase and A-E points in fig. 5.7. (*) Fe at.% here includes traces of Co.

Point A in fig. 5.8a represents a triple junction area with a darker contrast and higher O enrichment compared to previous RE-rich points, which suggests that this phase is likely to have an Nd_2O_3. This phase appears to be in direct contact with the main phase. Nd_2O_3 with an *hcp* structure has been suggested to cause the largest distortion at the interface with main $Nd_2Fe_{14}B$ phase compared to other Nd-oxides [35]. Points B and C in fig. 5.8b also appear to be in direct contact with the main phase but with a lighter SE contrast compared other RE-phases, which has been suggested to be a RE-rich phase with pure Nd with *dhcp* structure [29]. However, EDX elemental analysis revealed an O enrichment (table 5.3), which does not correlate with previous reports [41].

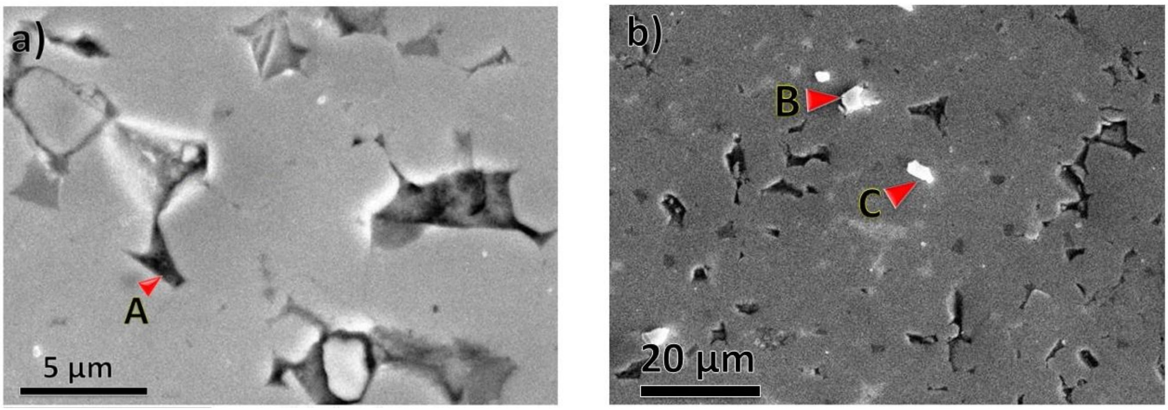

Figure 5.8 SE images of Dy-free sample with (a) point A and (c) points B & C.

Element	Main phase	A	B	C
Fe (at.%)	84.1	58.1	9.2	4.5
RE (at.%)	14	14.5	13.9	21.7
Fe/RE	6	4.0	0.7	0.2
O (at.%)	-	26.1	76.9	73.8
Al (at.%)	1.85	0.8	-	-

Table 5.3 the EDX elemental analysis of points A-C in fig. 5.8 compared to main phase point in fig. 5.7.

The electron microscopy analysis showed that Dy-free sample has a high density of intergranular phases adjacent to main phase grains. The intergranular phases were distributed at the boundaries of two adjacent grains or at the triple junctions between main phase grains. The EDX elemental analysis of these phases revealed the presence of Cu-enriched RE-rich phases that have concentrations of Cu, Ga and sometimes Co. The Fe content in these Cu-enriched phases is non-uniform and the Fe/RE ratio varies between 0.8-2.2 at different regions across the microstructure. In addition, the main phase grains in the Dy-free sample were observed to be mostly in direct contact with each other, *i.e.* grains are likely to be magnetically exchanged. These observations will be compared to other Red-Dy and Dy-rich samples and will be used to inform microstructural models in Chapter 7.

5.4.2 Red-Dy magnet

The microstructure of Dy-Red sample also has dominant grey SE contrast regions (A), which are likely to be the main phase, and smaller size regions that have either lighter (B) or darker (C) contrast, which are likely to be the intergranular phases (fig. 5.9a). The EDX elemental maps of this sample revealed the higher Fe intensity at the dominant contrast regions compared to other regions, which confirms that these regions are the main phase grains (fig 5.9b). The intensity of Nd (fig 5.9c) and Pr (fig. 5.9d) in this sample is higher at the triple junction regions, but appears to be lower at the main phase regions. Interestingly, the Dy intensity distribution appears to be similar to Fe and opposite to other RE elements in this sample (fig. 5.9e). Previous electron microscopy analysis of (Dy, Nd)-Fe-B magnets reported that Dy is likely to be present at intergranular phases and also to form its own oxides [9]. Here, Dy concentration appears to be present in main phase grains only. An overlap between the intensity of Fe and Dy is possible because of their close shell energy values, where K_α energy of Fe=6.405 keV and L_α shell energy of Dy=6.498 keV (fig. 5.10). Such overlap might lead to mis-indexing Fe K_α peaks as Dy L_α.

On the other hand, O appears to have a low intensity at the main phase grains but appears to have concentrations at some of intergranular (light contrast) regions (fig. 5.9f). The Al map (not shown here) revealed a uniform Al content across the sample. Although region (D) has a SE contrast similar to main phase grains, it has a higher RE and lower Fe intensities, which suggests that this region is the $Nd_{1.1}Fe_4B_4$ phase.

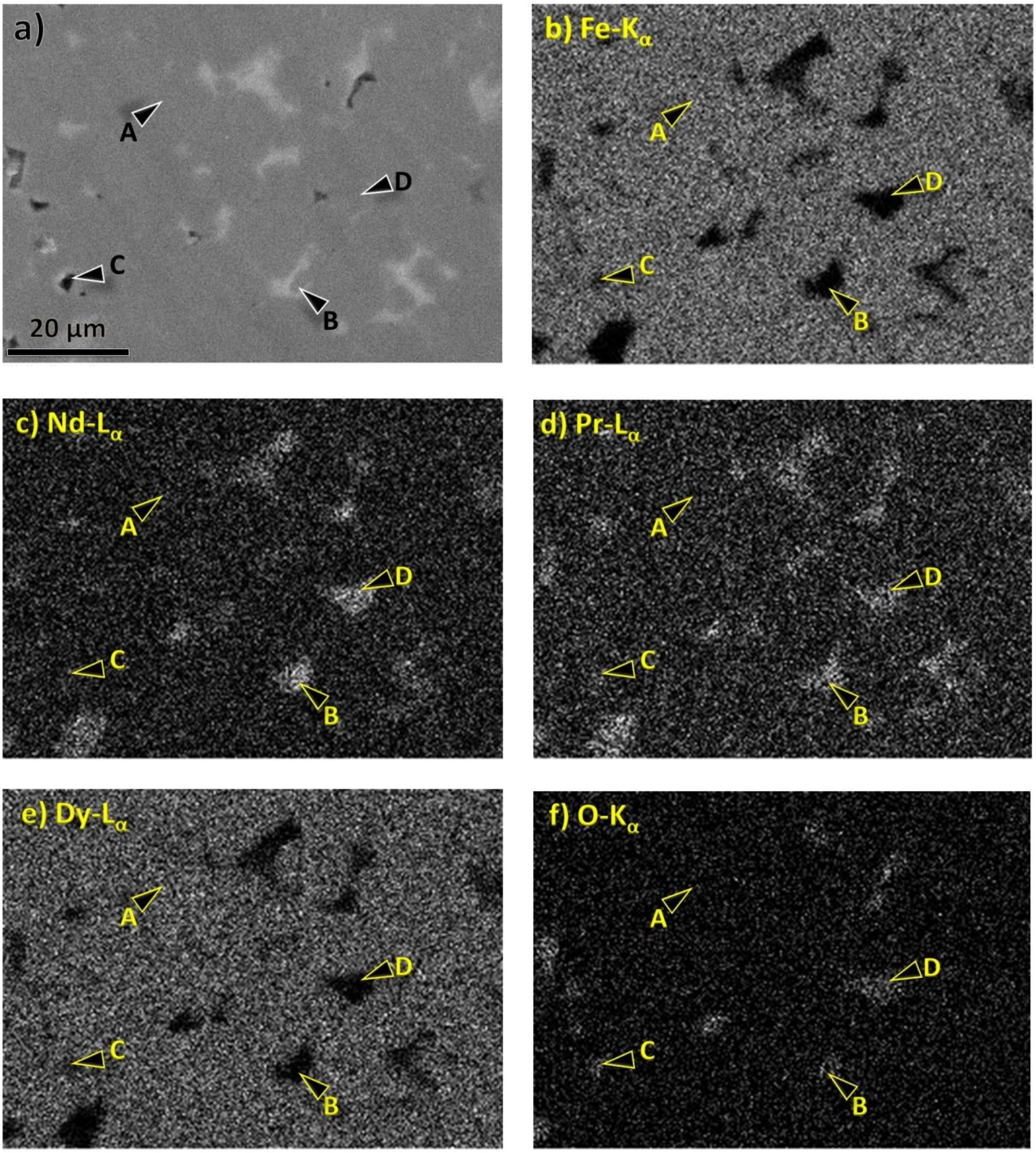

Figure 5.9 (a) SE image of a Red-Dy sample and EDX elemental maps of (b) Fe, (c) Nd, (d) Pr, (e) Dy and (f) O with points A, B, C and D.

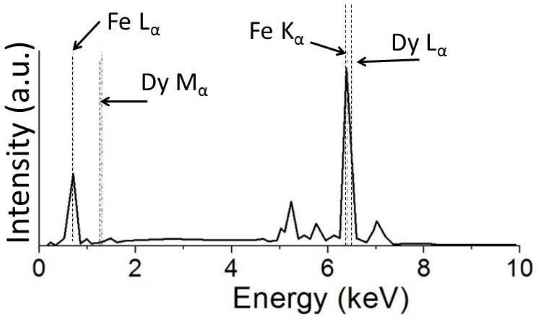

Figure 5.10 EDX spectrum of the area in fig. 5.9 showing an overlap between Fe K_α and Dy L_α. For other peaks identity, refer to fig. 5.4.

BSE image of Red-Dy microstructure shows that main phase grains are neighboured by intergranular phases at triple junction areas across sample (fig. 5.11a). However, no intergranular phases were observed between adjacent grains, which means that grains are likely to be in direct contact with each other and hence they are likely to be magnetically exchanged. The intergranular phases at triple junctions consist of the RE-rich phases (point 1 fig. 5.11a) with lighter contrast than the main phase in both BSE and SE images and RE-oxides (2) at triple junction regions with a slightly darker contrast than RE-rich phases in both types of images. Area 3 with the darkest contrast in SE and BSE images is likely to be porosity.

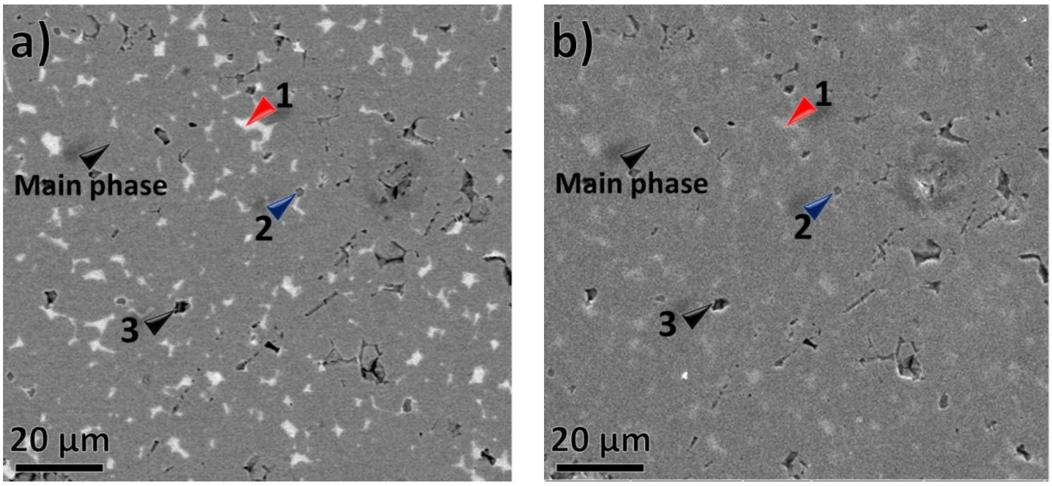

Figure 5.11 (a) BSE and (b) SE images of Red-Dy sample showing the main phase, RE-rich (1), RE-oxide (2) and porosity (3).

The EDX elemental analysis of typical regions on Red-Dy sample shows that light contrast phases at points *i*, *ii* and *iv* in fig. 5.12 are the Cu-enriched RE-rich phases, which is confirmed by the higher RE compared to the main phase and the Cu concentration (table 5.4). These phases appear to exist at triple junctions only and disappear from other regions, which indicate that main phase grains are likely to be in direct contact to each other. In addition, the unexpectedly high Fe concentration of RE-rich phases in Dy-free sample is also observed here. On other hand, Cu-enriched phases are sometimes accompanied by an RE-oxide at centre of the triple junction area (point *iii* in fig. 5.12a). The EDX elemental analysis of this 4 ±0.5µm wide RE-oxide suggests that it has an *hcp*-Nd_2O_3 structure (table 5.4).

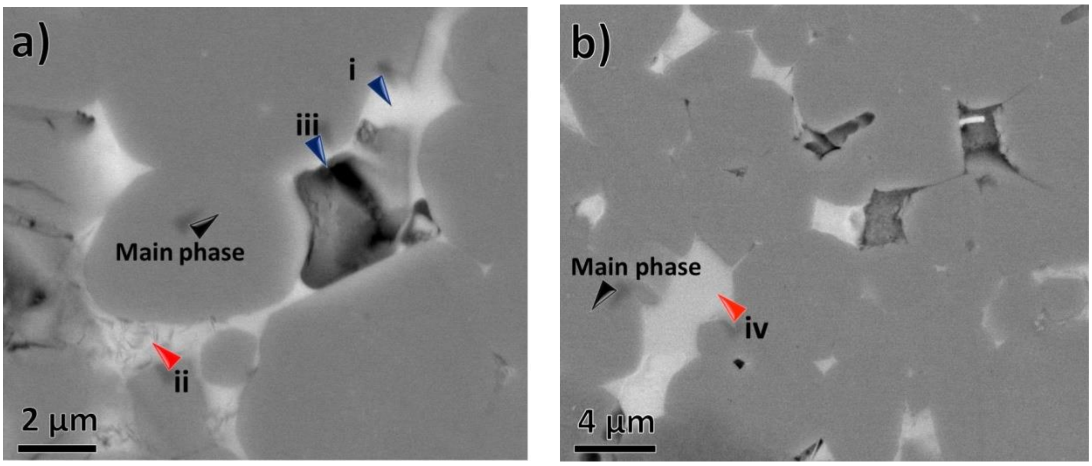

Figure 5.12 (a & b) BSE images of typical regions in Red-Dy sample showing points *i-iv*.

Element	Main phase (a)	*i*	*ii*	*iii*	*iv*
Fe (at.%)	83.2	52.4*	50.0	19.1	49.8
RE (at.%)	14.8	37.7	31.6	25.9	34.3
Fe/RE	5.6	1.4	1.6	0.7	1.5
O (at.%)	-	6.5	5.9	54.8	8.7
Al (at.%)	2.0	-	3.4	-	5.6
Cu (at.%)	-	3.4	3.7	-	1.6

Table 5.4 The EDX elemental analysis of main phase and *i-iv* points in fig. 5.12. (*) Fe at.% here includes traces of Co.

The Cu-enriched RE-rich phases are also present at other triple junction regions (A and B in fig. 5.13a), which also have some Co concentration (table 5.5). In addition, darker contrast phases were observed to accompany the Cu-enriched phase at C and F points in fig. 5.13a and b, respectively. Here, the EDX elemental analysis of point C revealed an Fe-rich composition that is close to Fe/RE ratio of the main phase, while point F is likely to represent an *fcc*-NdO phase. The dark contrast region (E) appears to cover the whole triple junction area and its composition also shows an Fe-rich composition. The high Fe at.% (table 5.5) at these phases suggests that they have ferromagnetic nature, which means that they are likely to behave as soft magnetic regions between hard-magnetic main phase grains. Points D and G appear to be RE-oxides with an *hcp*-Nd_2O_3 structure according to their SE contrast and RE:O ratios.

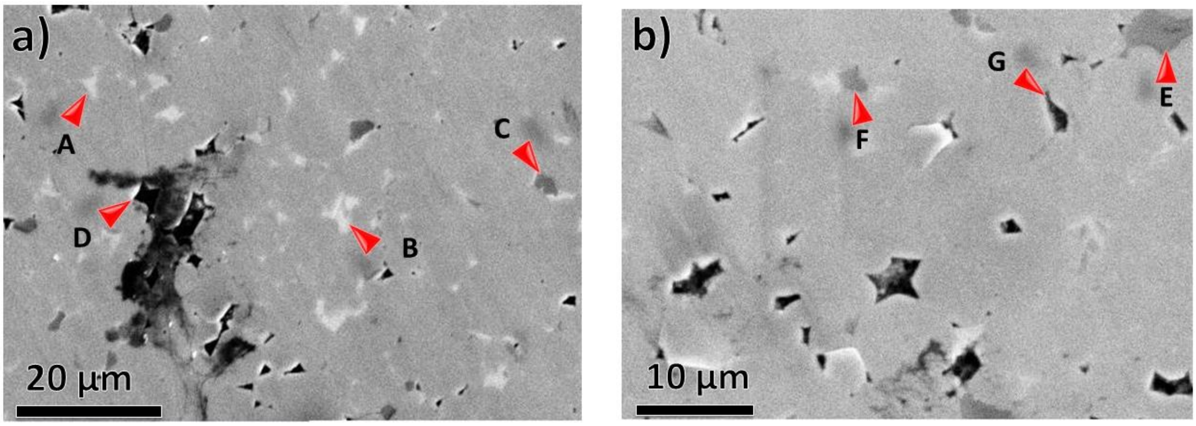

Figure 5.13 (a & b) SEM images of two different regions in Red-Dy magnet with A-G points noted.

Element	Main phase	A	B	C	D	E	F	G
Fe (at.%)	83.2	72.7*	35*	82.8	30.1	74.5	41.8	61.2
RE (at.%)	14.8	24.0	44.3	15.2	25.4	14.5	26.6	14.3
Fe/RE	5.6	3.0	0.8	5.5	1.2	5.1	1.6	4.3
O (at.%)	-	-	13.7	-	40.7	9.0	30.7	23.2
Al (at.%)	2.0	1.9	1.8	2.1	0.6	2.0	0.9	1.4
Cu (at.%)	-	1.4	5.2	-	-	-	-	-

Table 5.5 The EDX analysis of points A-G on fig. 5.13 compared to the main phase point in fig. 5.12. (*) Fe at.% here includes traces of Co.

Cu-enriched RE-rich phases were observed at points *i* and *ii* (fig. 5.14a) in Red-Dy sample to have a close composition to previous points, where they have a higher RE content than the main phase and concentrations of Cu, Al and Co in some occurrences (table 5.6). In addition, Ga concentrations were observed at Cu-enriched phase at points *iii* and i*v* (fig. 5.14a & b), which was also observed in Dy-free sample and in previous reports [29, 100]. Point *v* shows an RE-oxide phase sharing the triple junction area with a light contrast RE-rich phase, which is likely to be Cu-enriched.

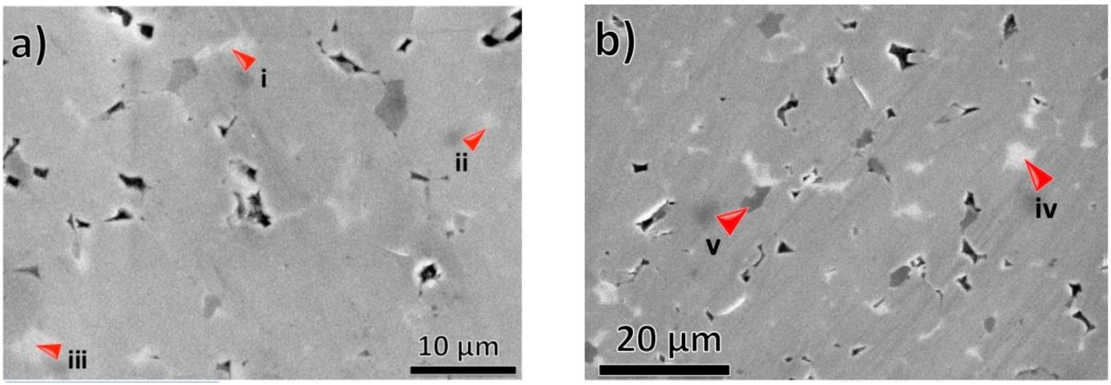

Figure 5.14 (a & b) SE images of typical regions in Red-Dy samples showing *i-iv* points.

Element	Main phase	*i*	*ii*	*iii*	*iv*	*v*
Fe (at.%)	83.2	63.2*	68.2	45.5	54.1*	14.0
RE (at.%)	14.8	23.9	19.6	35.0	29.3	42.0
Fe/RE	5.6	2.6	3.5	1.3	1.8	0.3
O (at.%)	-	7.4	6.9	9.4	8.2	43.4
Al (at.%)	2.0	3.6	3.9	5.1	4.5	-
Cu (at.%)	-	2.0	1.4	3.9	3.1	0.6
Ga (at.%)	-	-	-	1.0	0.9	-

Table 5.6 The EDX elemental analysis of points *i-iv* in fig. 5.14 compared to main phase point in fig. 5.12. (*) Fe at.% here includes traces of Co.

Red-Dy sample has 1) a higher Dy content but lower H_c and BH_{max} compared to Dy-free sample and 2) the Dy content was observed to exist at main phase regions only. The intergranular phases at triple junctions between grains were observed to have larger areas compared to Dy-free sample but also consist of 1) the Cu-enriched RE-phase with some concentration of Ga and Co and 2) RE-oxides. The Fe/RE ratio varied between 0.3-3.5 at different triple junction regions across the microstructure. In addition, the EDX elemental analysis of Red-Dy sample revealed the presence of Fe-rich regions at triple junctions with

Fe at.% close to main phase regions. The presence of these regions at the interface with the main phase represents an interface between soft and hard magnetic regions. Further investigation of the effect of the magnetic properties of the Cu-enriched and Fe-rich phases on the performance of sintered Nd-Fe-B magnets will follow in Chapter 7.

5.4.3 Dy-rich magnet

Dy-rich sample has the highest Dy content but the lowest H_c and BH_{max} compared to the other samples. EDX elemental maps of the microstructure in this sample revealed that the dominant grey contrast regions (A in fig. 5.15a) have a higher intensity of Fe (fig. 5.15b) and lower Nd intensity (fig. 5.15c) than the lighter contrast regions. This indicates that this dominant grey contrast is the main $Nd_2Fe_{14}B$ phase. The intensity of Nd (fig. 5.15c) and Pr (not shown here) at point B, C and D is higher than the main phase, which indicates that these regions are the RE-rich intergranular phases. However, Dy was observed at the main phase only (fig. 5.15d), which is similar to Dy distribution in Red-Dy sample (see fig. 5.9e). O intensity (fig. 5.15e) appears to be higher at the dark regions (C and D) compared to the light contrast regions (B). The elemental composition of this region revealed a slightly higher RE content (~14 at.%) than the stoichiometric composition of the main phase, which indicates that Dy-rich sample is likely to be a RE-rich sample.

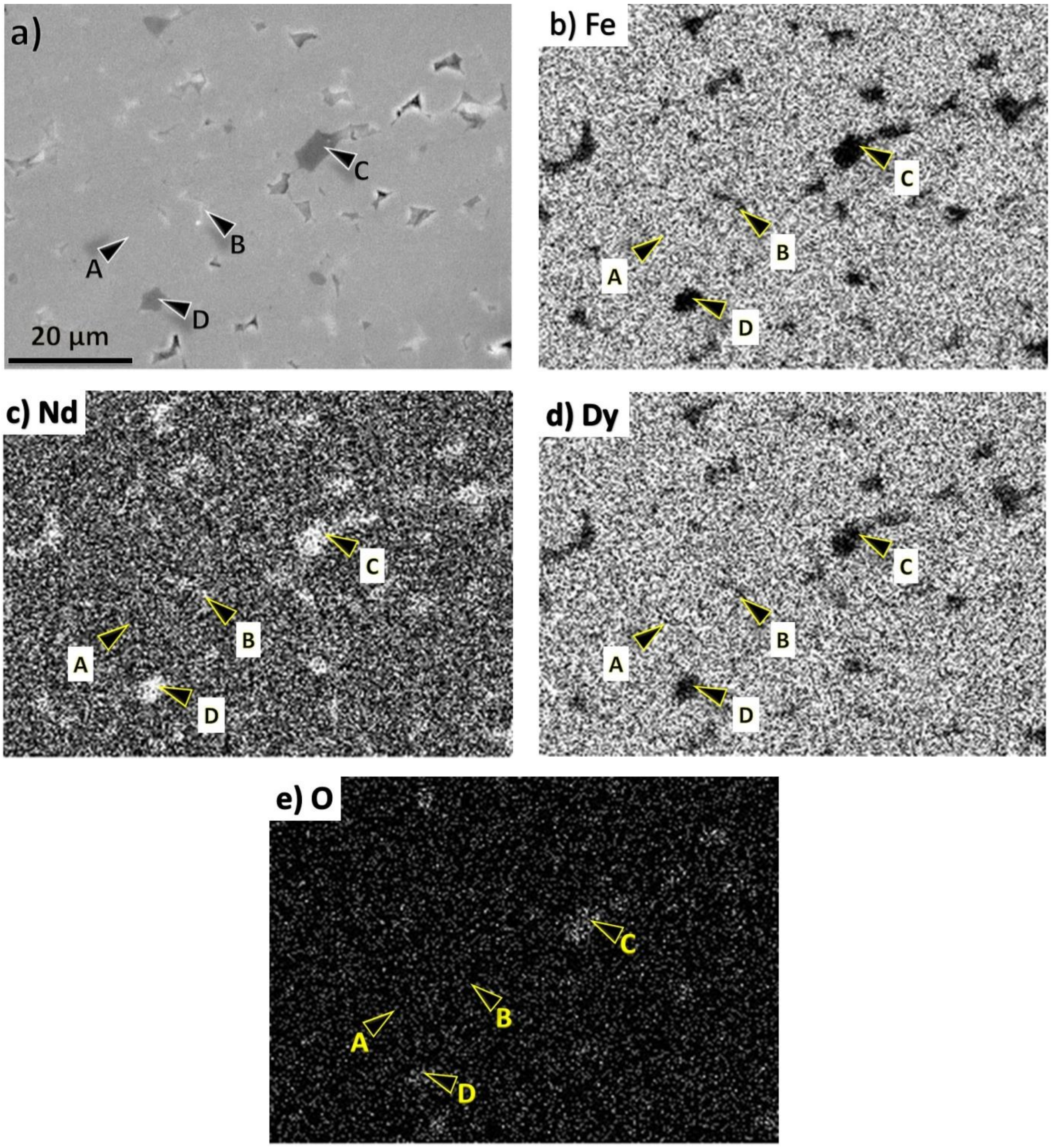

Figure 5.15 (a) SE image of the Dy-rich magnet with EDX elemental maps of (b) Fe, (c) Nd, (d) Dy and (e) O.

The identification of intergranular phases through comparing the contrast of BSE and SE images (fig. 5.16) showed that points A and B have a lighter contrast in the BSE image but a similar contrast to the main phase in the SE image, which does not correlate to any of the previously identified phases in Dy-free and Red-Dy samples. In addition, the microstructure of Dy-rich sample appeared to be more inhomogeneous compared to the other types of samples. For example, large non-uniform areas, such as C in fig. 5.16, were observed across the microstructure in the BSE and SE images. The origin of this inhomogeneous microstructure is likely to be related to the composition and the processing conditions of this sample.

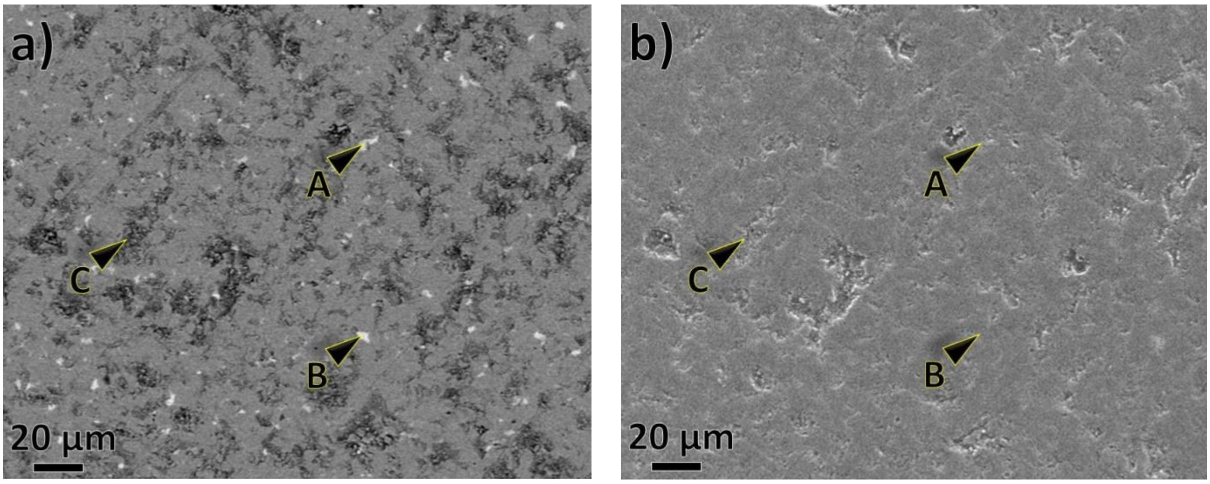

Figure 5.16 (a) BSE and (b) SE images of Dy-rich sample showing points A-C.

EDX elemental analysis showed that the light contrast regions in *i* (fig. 5.17a) and *iii* (fig. 5.17b) have a lower Fe/RE ratio than the main phase (table 5.7), which indicates that they are RE-rich phases. The BSE contrast of these points and their elemental composition suggests they have an *fcc*-Nd structure. The points *ii* (fig. 5.17a) and *iv* (fig. 5.17b) show close Fe/RE ratios to the main phase, which indicates that they non-homogeneous main phase regions. The interesting EDX observation is that Al content in the main phase exists at some points (fig 5.17a) and disappears at others (fig. 5.17b), which may indicate a non-uniform elemental distribution across the Dy-rich sample.

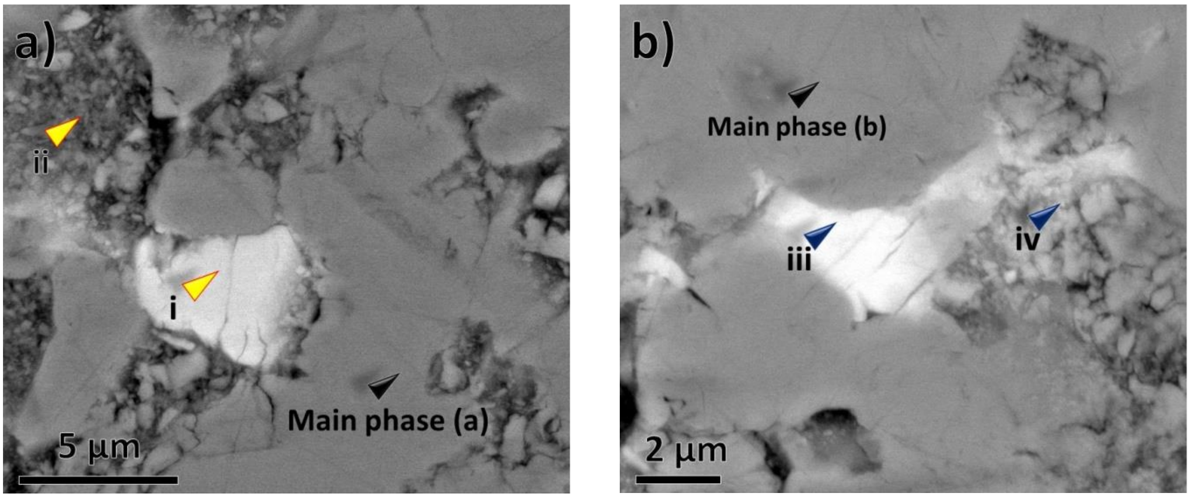

Figure 5.17 BSE images of Dy-rich sample showing (a) the main phase, *i* and *ii* points and (b) iii and iv points.

Element	Main phase in (a)	*i*	*ii*	Main phase in (b)	*iii*	*iv*
Fe (at.%)	82.6	4.3	57.8	81.4	6.8	66.1
RE (at.%)	12.4	61.5	10.5	13.2	58.1	12.6
Fe/RE	6.6	0.1	5.5	6.1	0.1	5.3
O (at.%)	5	34.3	31.7	3.4	35.1	20.0
Al (at.%)	-	-	-	2	-	1.3

Table 5.7 The EDX elemental analysis of main phase and *i*-*iv* points in fig. 5.17.

The EDX elemental analysis of Dy-rich sample also revealed the presence of Cu-enriched RE-rich phase (fig. 5.18). For example, points 1-4 have a light contrast, Cu content and smaller Fe/RE ratios than the main phase (table 5.8), which indicates that these points represent the Cu-enriched RE-rich phase. The slight difference in the Fe/RE ratios of these points could be attributed to the difference in their size. In addition, points 1 and 2 share the triple junction regions with points 5 and 6, respectively. The RE:O ratio and the presence of Cu at points 5 and 6 (table 5.8) do not correlate to known RE-oxide phases but their dark SE contrast suggest that they are O-enriched (*i.e.* RE-oxides). The likely structure of RE-oxides with the darkest SE contrast at points 5 and 6 is *hcp*-Nd_2O_3 and the presence of Cu concentration could be RE-Cu phase segregated at this region.

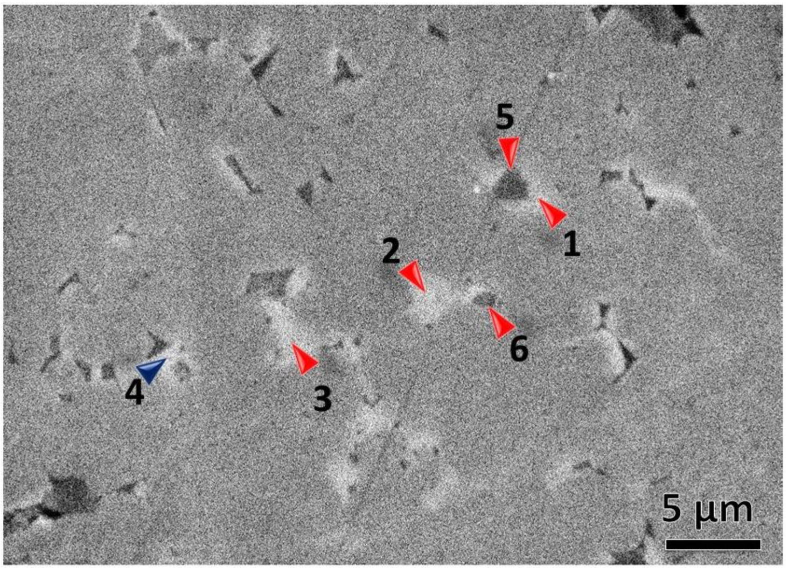

Figure 5.18 (a) SE image of a region in Dy-rich magnet showing points 1-6.

Element	Main phase	1	2	3	4	5	6
Fe (at.%)	82.6	62.3	62.6	52.7	51.1	27.8	49.8
RE (at.%)	12.5	22.2	29.2	30.3	26.1	37.4	30.7
Fe/RE	6.6	2.8	2.1	1.7	2.0	0.7	1.6
O (at.%)	5.0	8.0	-	8.3	18.2	29.8	16.6
Al (at.%)	-	4.3	4.9	5.2	1.9	2.6	-
Cu (at.%)	-	2.2	3.4	3.5	2.7	2.5	3.0

Table 5.8 The EDX elemental analysis of points 1-6 in fig. 5.18 compared to main phase point in fig. 5.18a.

Other intergranular phases were identified in EDX analysis from other points in fig 5.18. For example, point A has a dark contrast (fig. 5.19a) but a high Fe at.% (table 5.9). On the other hand, points B (fig. 5.19a) and D (fig. 5.19b) has a similar contrast to A but with an elemental composition that indicates an *hcp*-Nd_2O_3 structure, which suggests that point A also has the same structure. Point C has a light SE contrast but no Cu content, which suggests an *fcc*-NdO structure. Point D has an Fe-rich composition with only RE and Fe. However, there are no stable RE-Fe compounds at room temperature as was explained in §3.1 and a volume overlap with the main phase at this area is possible. Either way, it indicates that Fe-rich phases might be present in Dy-rich sample.

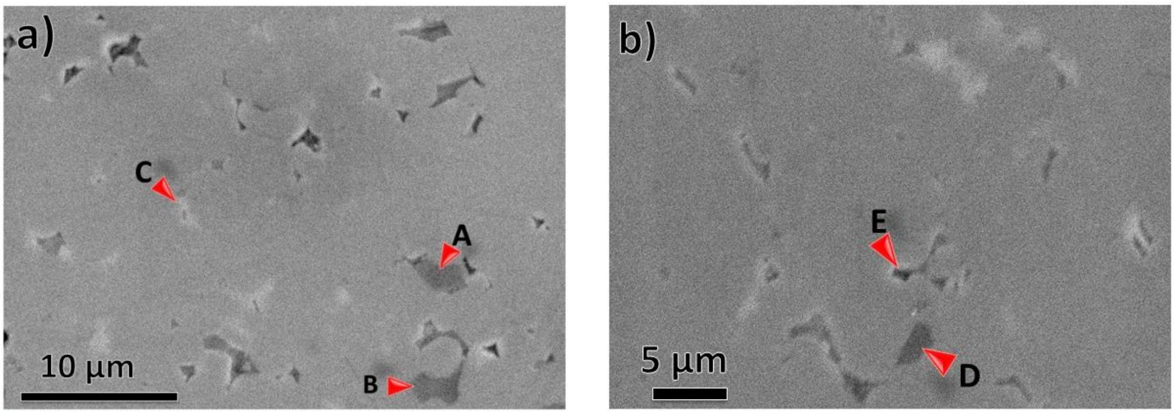

Figure 5.19 SE images of different areas in the Dy-rich magnet showing points (a) A, B, C, (b) D and E.

Element	Main phase	A	B	C	D	E
Fe (at.%)	82.6	75.3	12.3	56.6	19.8	90.7
RE (at.%)	12.5	17.0	37.6	29.1	36.6	9.3
Fe/RE	6.6	4.4	0.3	1.9	0.7	9.7
O (at.%)	5.0	7.7	50.1	9.6	43.6	-
Al (at.%)	-	-	-	4.8	-	-

Table 5.9 The EDX elemental analysis of points A-E in fig. 5.19 compared to main phase point in fig. 5.18a.

The microstructure of Dy-rich sample appears to have large inhomogeneous regions with a composition close to the main phase, which might be grains that were fractured during the sample preparation. The Dy-rich sample also has some Cu-enriched RE-rich phases with Fe/RE ratios of 2.2-4.8, which is larger than the Fe/RE range in other two samples. In addition, RE oxides were observed at the triple junction regions where their Fe/RE ratios and SE contrast suggested that they have *fcc*-NdO and *hcp*-Nd_2O_3. The Fe-rich phase was observed in one case only with a Fe/RE ratio that is higher than the main phase. This information can be used to understand the relatively lower H_c and BH_{max} compared to other two samples.

5.5 Conclusions

The magnetic characterisation of the samples revealed that the Dy-free sample had the highest coercivity and maximum energy density compared to Red-Dy and Dy-rich samples, although the composition of the latter two samples benefits from the partial replacement of Nd with Dy in the main $Nd_2Fe_{14}B$ phase. XRD analysis revealed that the microstructure of the three samples consists of the main phase, RE-oxides and B-rich phases, which were commonly reported in previous studies [29-31]. This significant difference in the coercivity of the three samples while having similar constituent phases suggests that their microstructural features is the main source of different magnetic properties. These features include the chemistry and size of intergranular phases, the grain size and its distribution and the grains texture.

The electron microscopy analysis of the three samples using SE and BSE revealed their microstructure consists of a dominant main $Nd_2Fe_{14}B$ phase neighboured by a network of intergranular phases that are accommodated at the triple junctions of grains and sometimes at the thin region between two adjacent grains. While Dy-free appeared to have a uniform size and distribution of triple junction areas, Red-Dy appeared to have larger and Dy-rich appeared to have fewer triple junction areas. The presence of thin grain boundary phase between two adjacent grains appeared at some regions in the Dy-free sample only. This indicates that some main phase grains in Dy-free sample are separated by this thin phase. However, main phase grains are in direct contact with each other at other areas where this thin grain boundary phase disappears, hence they are likely to be magnetically exchanged.

The EDX elemental analysis confirmed the presence of RE-oxides at the triple junctions. These oxides are mostly located at the centre of the triple junction area and have high melting temperatures. For example, the RE-oxide with *hcp*-Nd_2O_3 structure remains stable as a solid at temperatures below 2185K [29], which means it will not dissolve during post-sintering annealing processes at 873K and will remain floating at triple junction regions. EDX analysis also revealed the presence of an Fe-rich phase at the triple junction regions of Red-Dy and Dy-rich samples. The high Fe at.% of this phase suggests it has a soft magnetic properties and its interface with the main $Nd_2Fe_{14}B$ phase represents an interface between hard-soft regions, which is similar to the interfaces in exchange-spring magnets [101].

EDX elemental analysis also revealed the presence of the Cu-enriched RE-rich phase at the triple junction regions of the three samples. This Cu-enriched has concentrations of Cu, Al, Ga and in few cases Co but with lower Fe/RE ratios than the main phase. This phase is of a major importance since the presence of Cu suggests that it has a higher solubility than other RE-rich phases [29]. In addition, the presence of alloying elements suggest better wettability at the interfaces with $Nd_2Fe_{14}B$ grains [29, 31]. The higher solubility and wettability enable this phase to penetrate through intergranular regions leading to enhancement in its distribution across the sample, which is useful for post-sintering annealing and grain boundary diffusion processes. However, the remaining question regarding this Cu-enriched phase is whether it has ferromagnetic nature or not. Previous reports revealed that the $Nd_{33}Fe_{64}B_2Cu$ phase is ferromagnetic and hence main phase grains are magnetically exchanged [29]. However, our EDX elemental analysis revealed that the Cu-enriched phase has varied Fe/RE ratios at the different regions in the three samples, which indicates that the magnetic properties of this phase are likely to vary across the sample. The information obtained by the electron microscopy analysis in this chapter will be used to inform the micromagnetic models of sintered Nd-Fe-B magnets in the Chapter 7.

6.Electron Backscattered Diffraction Mapping

6.1 Introduction

Electron backscattered diffraction (EBSD) was used to map the crystallographic orientation, calculate the average size and distribution of the main phase grains. The maps presented in this chapter are examples from a wider set of maps and their data and analysis are typical of each sample. Here, the main features of the EBSD mapping process and the maps obtained from Dy-Free, Red-Dy and Dy-rich magnets are presented.

6.2 Improving the hit rate

The standard protocols of EBSD technique recommend a hit rate of 80% to obtain a measurement of a reasonable degree of confidence. However, our initial mapping of Nd-Fe-B samples using the standard settings achieved hit rates less than 10%. Several steps were performed in order to improve this value to acceptable ranges. These included:

- Decreasing the required number of bands to a minimum of four (compared to a standard value of 12) and a maximum of 5-6 bands (table 6.1). However, this is acknowledged as being likely to lead to some mis-indexing of phases.
- Increasing the number of reflectors from 70 to 100. This value specifies the multiplicities of planes and zone axes of each phase used to match Kikuchi patterns.

- Increasing MAD from default value of 1.3° to 5° to offer greater tolerance of deviation of measured lattice parameters and Wyckoff positions to these of the pre-defined phases.
- Indexing the main $Nd_2Fe_{14}B$ phase only to avoid mis-indexing the intergranular phases as the main phase solutions, which is likely to occur with higher limits Nd-rich phases have mostly cubic structures (*fcc*, *hcp* and *dhcp*) with lattice parameters close to at least one of the lattice parameters of the $Nd_2Fe_{14}B$ phase. The fact that the tetragonal phase has a cubic projection in (*h00*) planes will increase the possibility of this mis-indexing. This effect is known as Pseudosymmetry [86].
- Increasing Hough resolution from the default values of 50 to values of 60.
- Reducing step size of 0.08-0.2 µm and sampled areas to 30 µm x40 µm improved the hit rate and the calculations of average grain sizes and their distribution compared with using larger default values (fig 6.1).

These steps improved the indexing hit rate from very low values (~0-11%) to acceptable values (>80%) (Table 6.1). However, the mapping process produced same-grain points having a large misorientation angle (>70°) from each other, which is known as ‘mis-indexing’ and it could be a consequence of the low number of bands specified. The role of mechanical polishing used in sample preparation in this work on this mis-indexing issue was investigated using an argon ion beam system designed to polish and coat samples for SEM imaging and analytical techniques, which can eliminate any issues arising from mechanical polishing. The mapping of ion-beam-polished samples showed the same issue of mis-indexing, which confirms that phase mis-indexing is not a consequence of mechanical polishing.

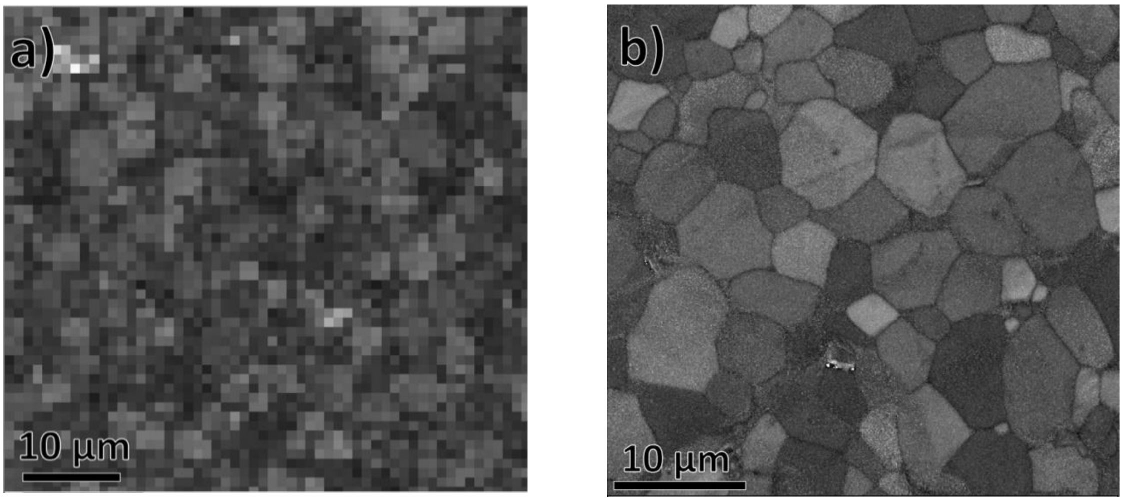

Figure 6.1 A comparison between band contrast (BC) maps of Dy-free sample with (a) 300x300 µm^2 and (b) 30x40 µm^2 scan sizes.

Number of bands	**MAD**	**Hough resolution**	**Step size (µm)**	**Hit rate (%)**
--	--	--	1	11
Yes	--	--	0.6	41
Yes	--	--	0.1	66
Yes	Yes	Yes	0.1	62
Yes	Yes	Yes	0.08	89

Table 6.1 the main changes in EBSD settings with the resulted hit rate after each change.

6.3 Post-processing

It is common for the EBSD mapping process to produce maps that have points with no matching between the collected patterns and the pre-defined phases, which are known as ‘zero points’ [86]. The post-processing software rectifies this issue of zero points by extrapolating the data of neighbouring points for these zero points. However, this extrapolating of the data of neighbouring points could create inaccurate maps since some of the matched points are mis-indexed (see §6.2). Here, zero points removal tool was used with

Dy-free and Dy-rich magnets only, since they have a high number of zero-points. This tool searches for zero points and then specifies an average value of band contrast, MAD and Euler's angles from the surrounding points to it. This tool removed zero points successfully from grains that have relatively lower number of zero points (A) but extrapolated multiple orientations at grains with higher number of zero points (B) (fig. 6.2), which is a direct consequence of extrapolating mis-indexed points.

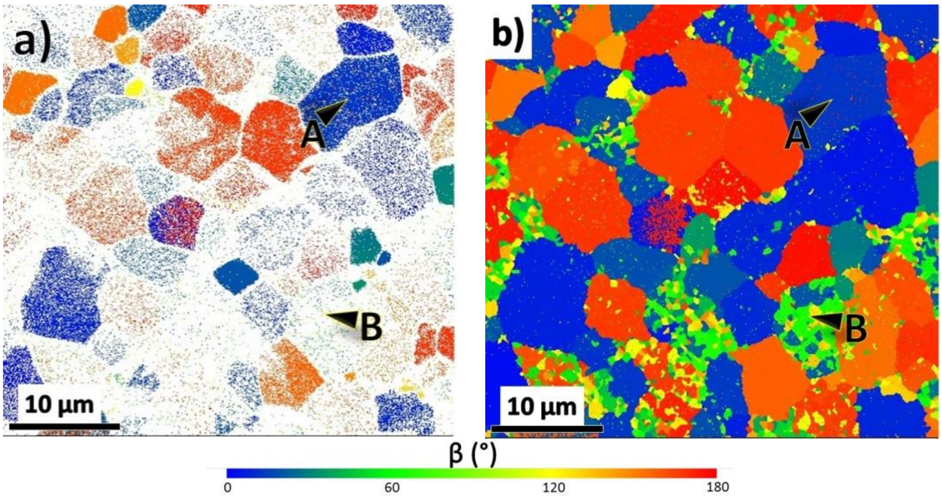

Figure 6.2 Maps of Dy-free sample (a) before and (b) after the zero points removal.

6.4 Dy-free sample

The Dy-free sample has the highest coercivity and maximum energy density compared to the other two sample (see §5.2). Here, the band contrast (BC) map of the Dy-free sample (fig. 6.3a) shows the main phase grains and their boundaries more clearly compared to SE and BSE images (fig. 5.5). Lower contrast areas in the BC map represent patterns from grain boundaries, which is a direct result of overlap of Kikuchi patterns at these regions [83]. BC map also shows more clearly that main phase grains have non-uniform shape with multiple truncated edges. The interesting feature in this map is the variation in the contrast between neighbouring grains (A & B), which indicates a variation in the crystallographic orientation of the main phase at different grains [83, 102].

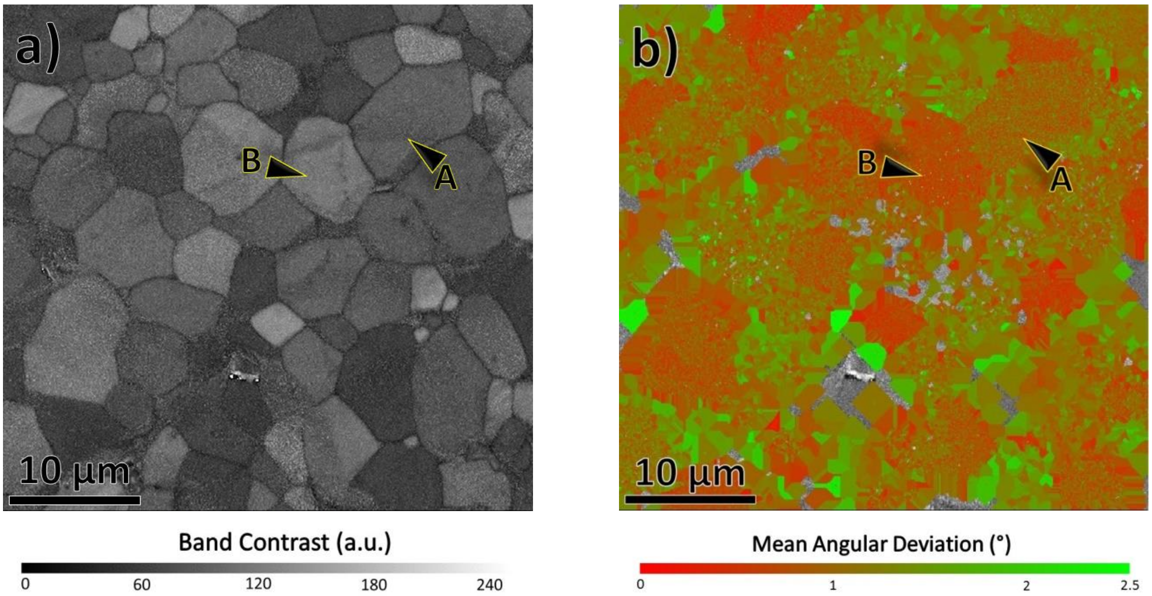

Figure 6.3 (a) Band contrast (BC) and (b) mean angular deviation (MAD) maps of a Dy-free sample showing A & B regions and the colour legends.

The mean angular deviation (MAD) map showed no gradient change of MAD values between the grain centres and their boundaries (fig. 6.3b). In addition, this map showed that lower MAD is mostly associated with brighter BC grains in fig. 6.3a, which suggests that the quality of matching the collected patterns to the predefined phases was affected by Kikuchi patterns contrast. The contrast variation could explain the low number of bands detected at each pattern in the Nd-Fe-B samples (see §6.2).

Euler's angles are used to represent the orientation of an object in XYZ space. In this system, β and α are the angles between the z and x poles of the object to the Z and X axes, respectively (fig. 6.4a). In addition, γ is the angle between the x pole of the object and the XY plane. Here, Euler's angles are used to define the orientation of the tetragonal $Nd_2Fe_{14}B$ cell. The β maps show that $Nd_2Fe_{14}B$ cells have a strong texture in the Z-direction where the majority of these grains have on orientation close to 0° (A) or close to 180° (B) (fig 6.4a). It is likely that both A and B grains have a small misorientation angle since their β angles have the same distance from 0° & π° angles. This mis-indexing is a direct result of low number of bands used in the indexing process. On the other hand, α (fig. 6.4c) and γ (fig. 6.4d) maps show that $Nd_2Fe_{14}B$ cells have a weak texture in X and Y directions, respectively, compared to the Z direction.

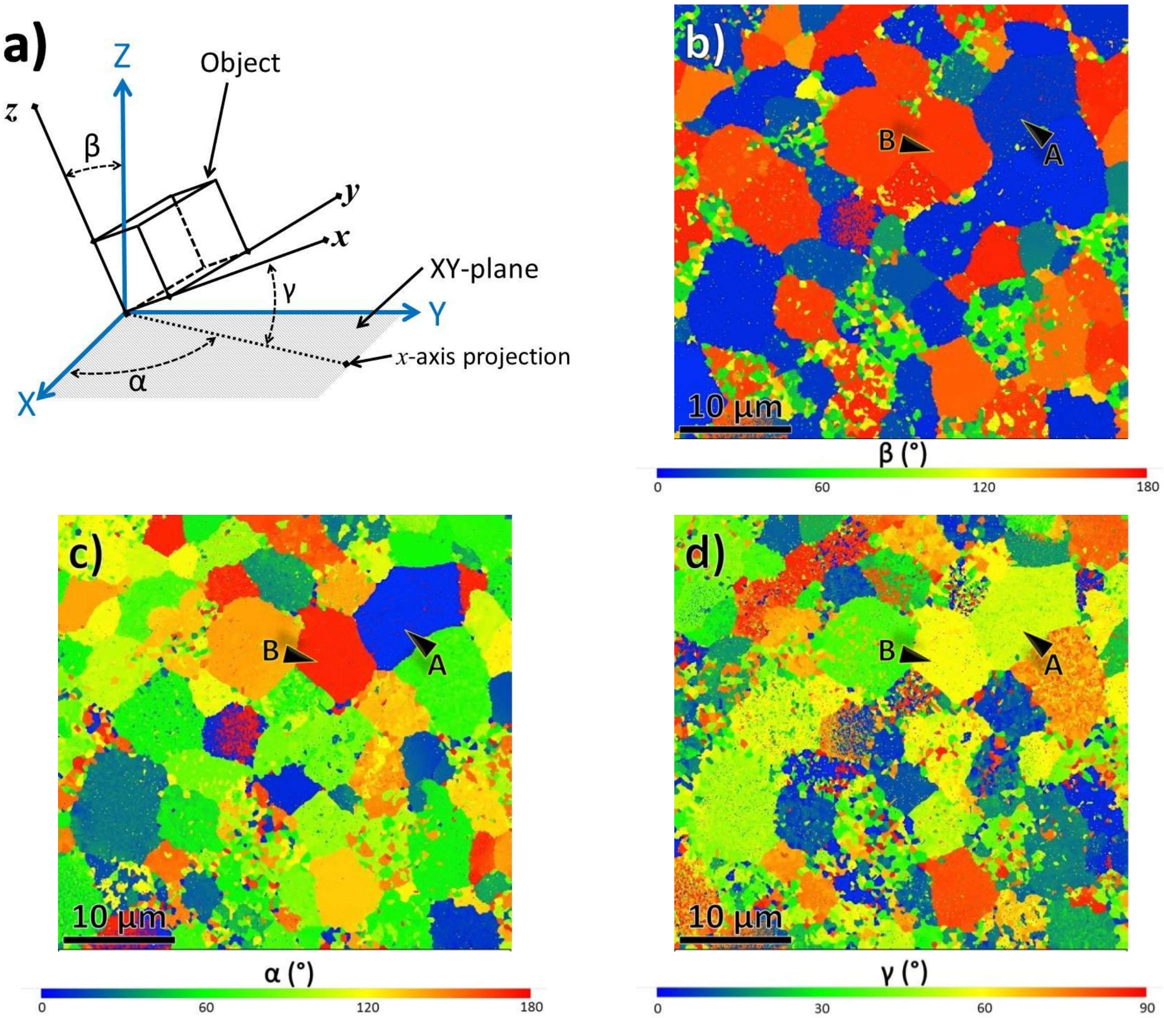

Figure 6.4 A schematic sketch of Euler's angles for an object in 3D space. Maps of (b) β, (c) α and (d) γ orientation angles of a Dy-free sample showing A & B regions and the colour legend of each angle.

The inverse pole figures (IPF) of main phase cells are used to create maps of the texture of grains in a particular axis. These maps use the stereographic projection to create a colour code for each pole alignment in either of X, Y or Z directions of the sample. Here, the IPF maps show the pole orientation of the {001} planes in a particular direction. The IPF maps show that main phase cells in the Dy-free sample have a strong texture in the <001> directions, *i.e.* Z direction (fig. 6.5a). Points A and B that were observed in β map (fig. 6.4a) to have a ~180° misalignment from each other are observed here to have almost the same pole orientation in the Z-direction. This confirms that the orientation of these points was mis-indexed and they are likely to be aligned in the same direction. In addition, the IPF maps in fig. 6.5b and 6.5c show that main phase cells have a weaker texture in X and Y directions, respectively.

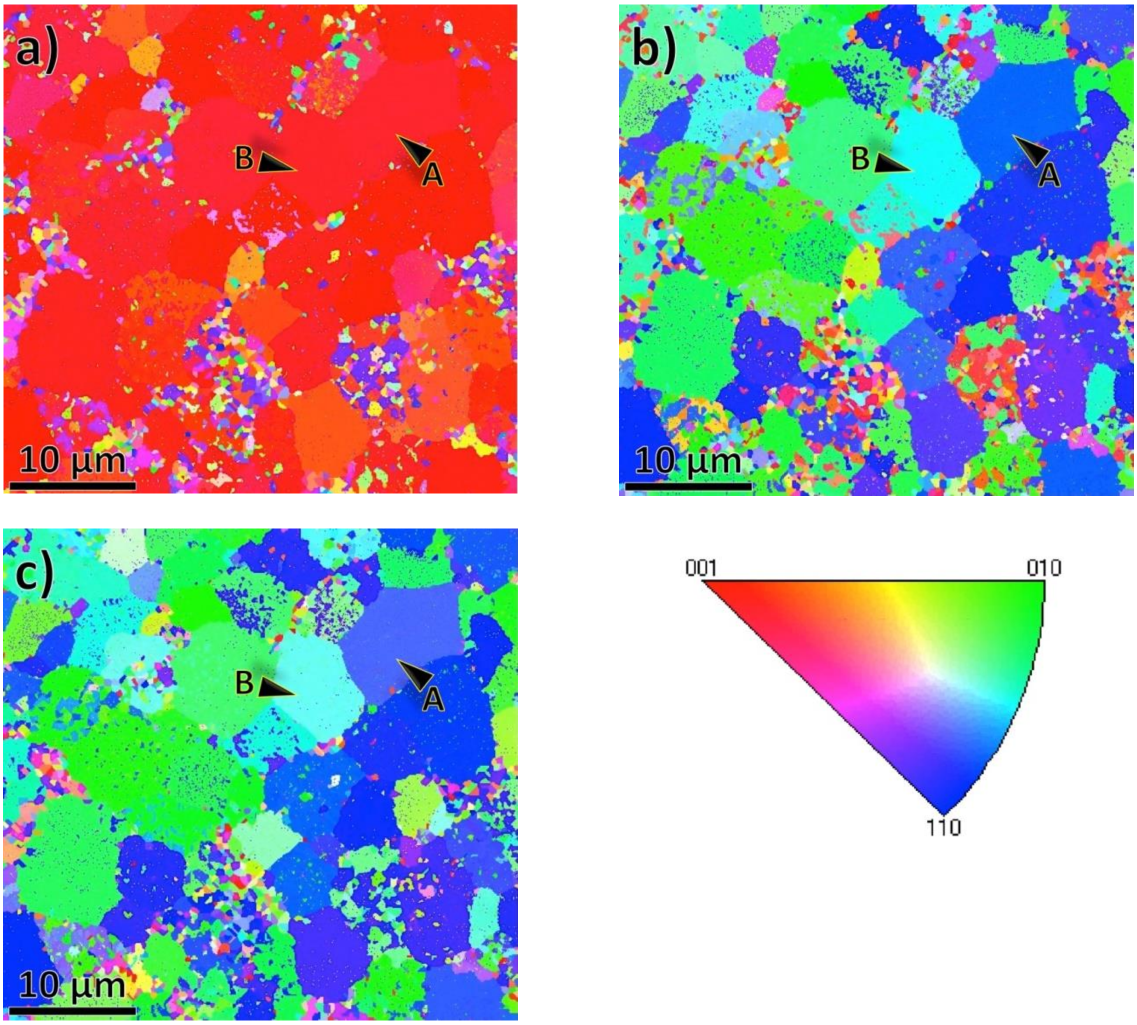

Figure 6.5 Inverse pole figure maps of a Dy-free sample in (a) Z, (b) X and (c) Y directions showing A & B regions. The legend shows the colour profile of poles orientation

Pole figures use the stereographic projection to show the angular distribution of main phase poles in relationship to a defined viewing axis, which is useful for the quantification of main phase cells texture in the sample [86]. For example, fig. 6.6a shows the {001}, {100} and {111} pole figures of the Dy-free sample viewed from sample normal (Z-direction). In addition, it is possible to view the strength of this texture more clearly using contour averaging, where same-orientation poles are replaced by a single orientation with increased weight (fig. 6.6b). Contouring defines uniform density of poles iterations and assigns a colour to each range of 'multiple uniform density' (m.u.d). The pole figures in fig. 6.6 shows that {001} poles of the main phase cells have a strong texture in the Z direction (out of the viewing plane). The strongest density of {001} poles is within a dispersion angle (ϕ) of 15°, which is similar to previous reports [31]. On the other hand, the pole distribution of {100} planes, which have four multiplicities, shows a non-uniform distribution in the Z-direction. The same non-uniform distribution was also found for the {111} poles, which have eight multiplicities.

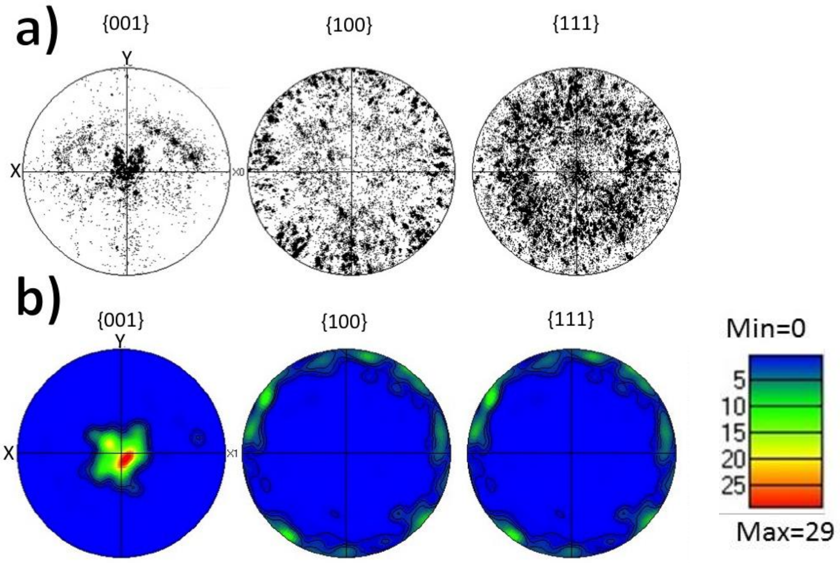

Figure 6.6 {001}, {100} and {111} pole figures of Dy-free sample with (a) no averaging and with (b) contour averaging using a clustering size of 5°.

The distribution of {001} poles in a particular direction can also be viewed by plotting the m.u.d as a function of pole angles for the pole figures in fig. 6.6b. For example, fig. 6.7a shows the majority of {001} poles in the Z direction having low angles smaller than 15°, which confirms that main phase grains in Dy-free sample have a strong texture in Z direction. While the average pole angle is 16.4°, larger pole angles were observed in this sample (~90°). Experimental errors could explain some of the largely misoriented cells; however, a considerable proportion of cells were observed in previous maps to have large misorientation angles from other cells (see fig. 6.4b and 6.5a). The majority of {001} poles of the main phase cells (~70%) are dispersed within an angle of 15° (fig. 6.7b), which will be denoted hereafter as the dispersion angle (ϕ) of the Dy-free sample. The value of ϕ at the same amount of main phase cells in the other two samples will be compared to this sample and will also be used in modelling the microstructure of sintered Nd-Fe-B magnets in Chapter 7.

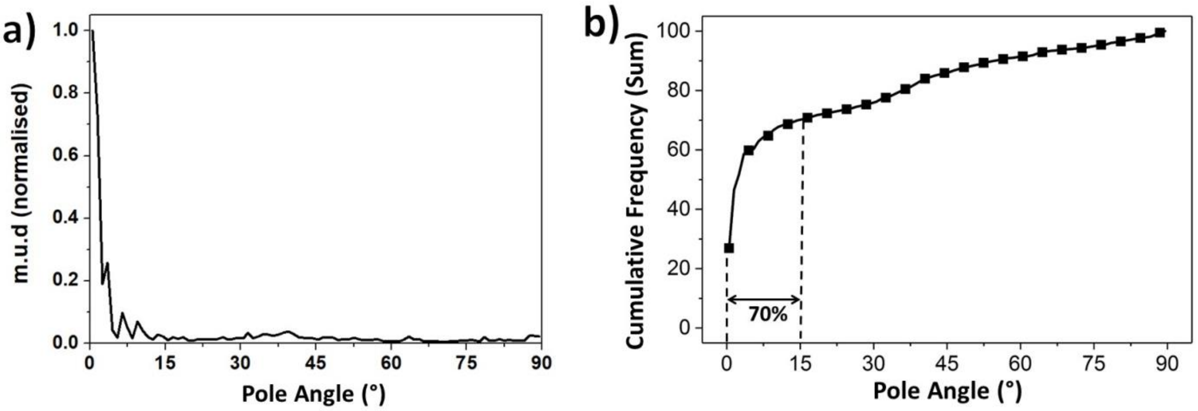

Figure 6.7 (a) the angular distribution of {001} poles in the Dy-free sample and its cumulative frequency.

The Euler β angle and the Z-direction IPF maps revealed that the main phase grains in the Dy-free sample are aligned in the Z-direction. The pole figure of the {001} planes revealed that about 70% of the $Nd_2Fe_{14}B$ cells have an alignment dispersion within an angle of 15° from the Z-direction. Although the majority of main phase grains show a strong texture, there are regions in Dy-free sample that are aligned within an angle 15°-90°.

6.5 Red-Dy sample

BC map of the Red-Dy sample also shows the non-uniform shape of main phase grains with a contrast variation between different grains (fig. 6.8a). The IPF map in fig. 6.8b shows that a high density of poles oriented in Z-direction (red points). However, a considerable number of points appear to deviate from the Z-direction (green points). The comparison between BC and Z-direction IPF maps shows that the regions with the brighter band contrast mostly have a significant misalignment from the Z-direction. It should be noted that no noise-removal efforts were performed on this IPF-Z map. BC and IPF-Z maps suggest that the Red-Dy sample had a higher misorientation between adjacent grains compared to the Dy-free sample.

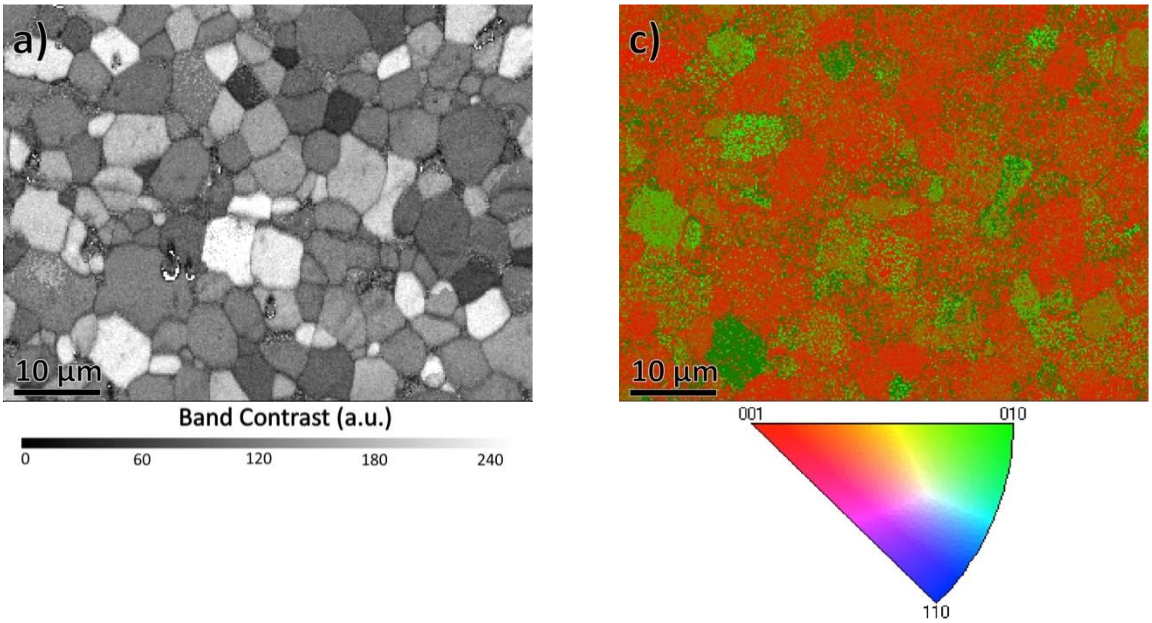

Figure 6.8 (a) BC and (b) Z-direction inverse pole figure map of Red-Dy sample with their colour legends.

The {001} pole figure revealed that the main phase grains in the Red-Dy sample are also appear to be aligned in the Z direction (fig. 6.9a) but over a wider distribution of angles compared to the Dy-free sample. This was confirmed by fig. 6.9b, which plots m.u.d of {001} poles at different angles. This plot shows that the strongest texture was found at angle smaller than 10° and the average pole angle is 24.5°. However, the analysis of the pole plot of the Red-Dy sample revealed that only 67% of the main phase cells are represented by this angular range (fig. 6.9c). Compared to the Dy-free sample, 70% of the main phase cells in the Red-Dy sample were aligned within ~30°, which will be considered as ϕ of this sample.

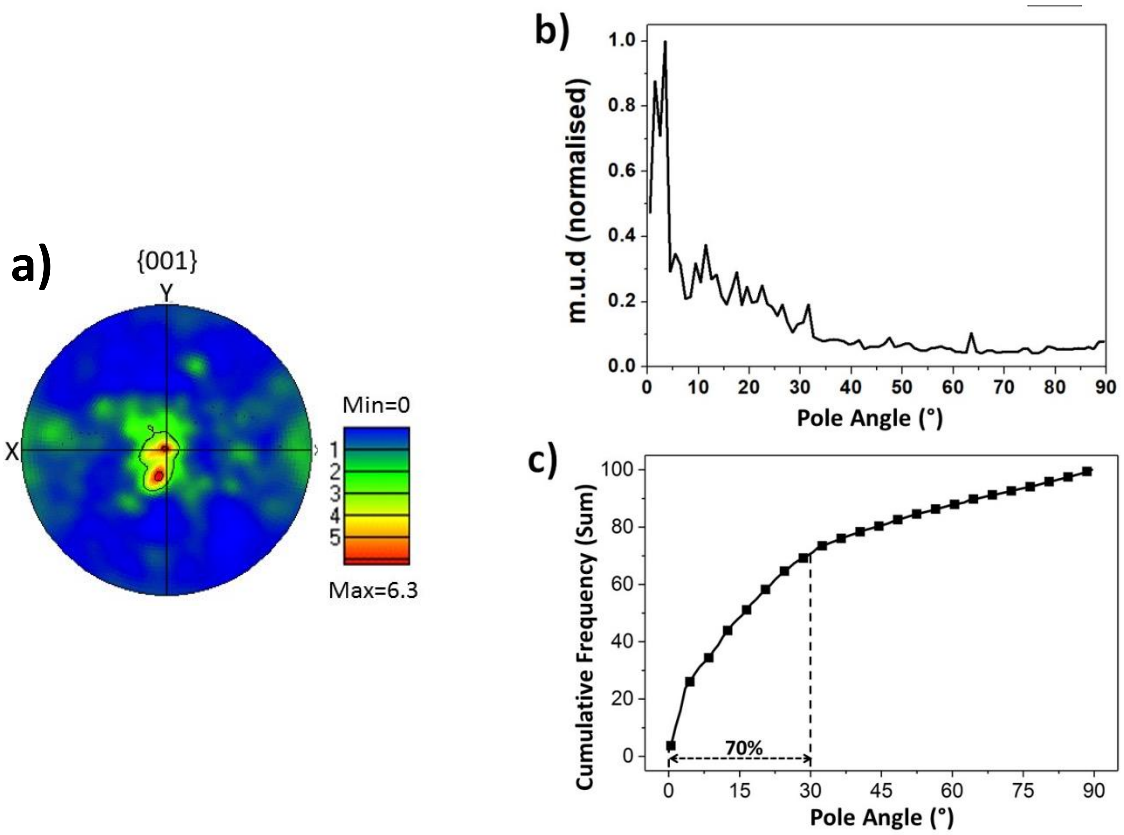

Figure 6.9 (a) The {001} pole figure of a Red-Dy sample, (b) {001} pole plot and (c) its cumulative frequency. The clustering size used in the pole figure contouring is 5°.

The EBSD analysis of Red-Dy sample revealed this sample also shows a strong alignment of main phase grains in the Z-direction. However, this alignment was distributed over a wider range compared to the Dy-free sample. The pole plot of {001} planes (fig. 6.9b) revealed that 70% of main phase cells are aligned within a dispersion angle (ϕ) of 30°.

6.6 Dy-rich sample

The Dy-rich sample was revealed by VSM analysis to have the lowest H_c and BH_{max} compared to other two samples (see §5.4). The BC map of this sample shows the main phase grains and their boundaries (fig. 6.10a). The Z-direction IPF map indicate a wider dispersion of grains orientation (fig. 6.10b). This is represented by having adjacent grains with distributed over a range of angles close to the {001}, {010} and {111} directions, which are 90° diverged from each other.

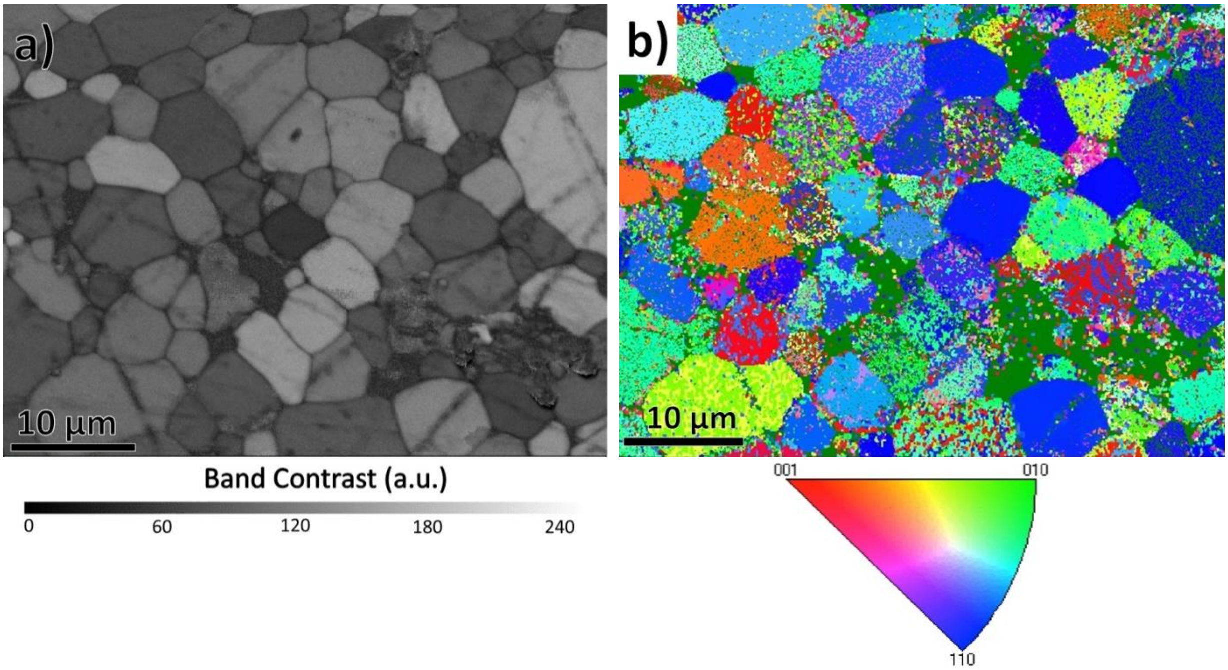

Figure 6.10 (a) Band contrast and (b) Z-direction inverse pole figure maps of a Dy-rich sample and their colour legends.

The weak alignment of main phase cells in the Z-direction of the Dy-rich sample was also observed in the X- and Y-direction maps shown fig. 6.11a and 6.11b, respectively. These maps confirm that Dy-rich sample has a weak alignment of main phase grains, which is likely to have a significant effect on the coercivity and remanence of this sample.

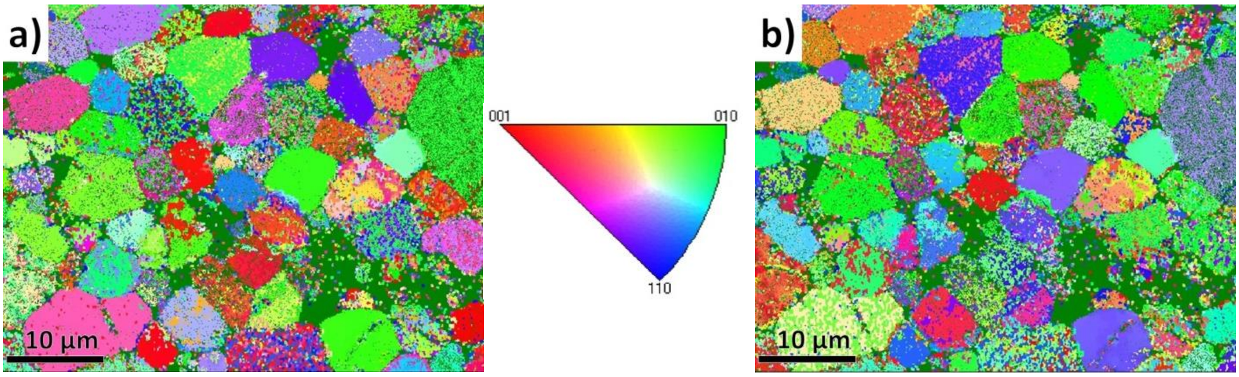

Figure 6.11 (a) X-direction and (b) Y-direction inverse pole figure maps of Dy-rich sample.

Figure 6.11a shows that the {001} poles have higher density at angles that are spread between 0°-90°, which confirms the large misorientation of main phase cells in this sample. In addition, the pole figures of {100} (fig. 6.12b) and {111} (fig. 6.12c) planes revealed no strong distribution in other directions.

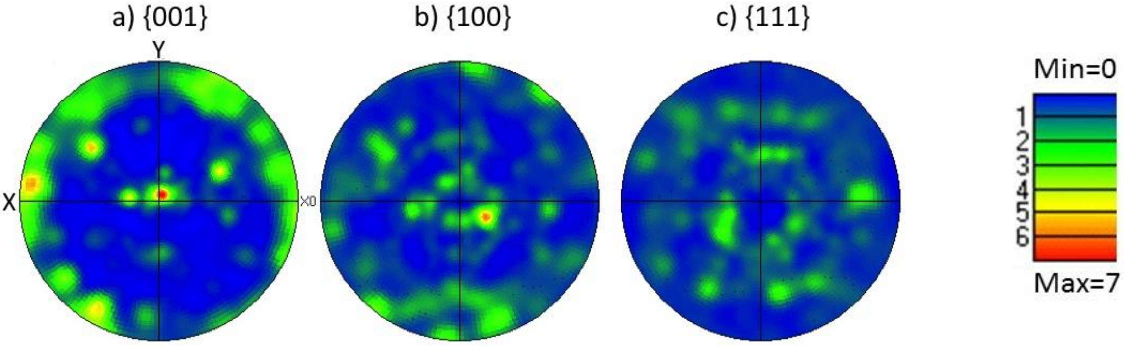

Figure 6.12 (a) {001}, (b) {100} and (c) {111} contour pole figures of Dy-rich sample. The clustering size used in contouring is 5°.

The {001} pole plot shows that higher pole distributions are observed at ~14° and ~90° but a considerable number of poles are distributed over the whole 0°-90° range (fig. 6.13a). Although the average pole angle of this sample is calculated to be 46.5°, about 70% of the poles are aligned at 0°-75° (fig.6.13b). The orientation analysis of main phase cells in Dy-rich sample shows that it has the weakest texture compared to the previous two samples. The dispersion angle (ϕ) of this sample is 75°.

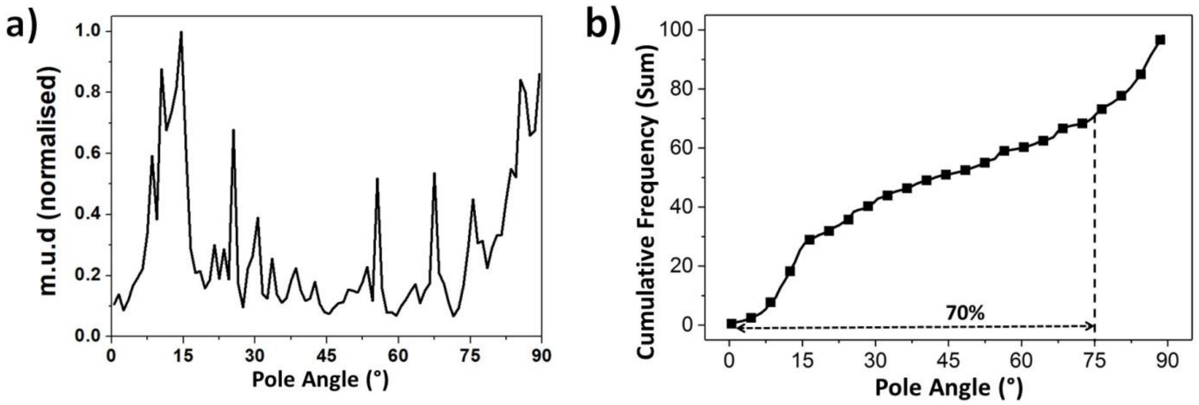

Figure 6.13 (a) The {001} pole plot of Dy-rich sample pole figure (fig. 6.12a) and (b) its cumulative frequency.

6.7 Grains size and distribution

The grain size (diameter) and it distribution was performed using linear intercept method explained in §4.6.4. A band contrast map from each sample was used for this calculation as they provide a better representation to the grains and their boundaries than SE and BSE images (fig. 6.14). Previous metallographic analysis suggested that the calculations of the grain size from 2D electron microscopy images using the number of grains in the three maps (in fig. 6.14) can provide a 95% confidence with an error of ±20% [88].

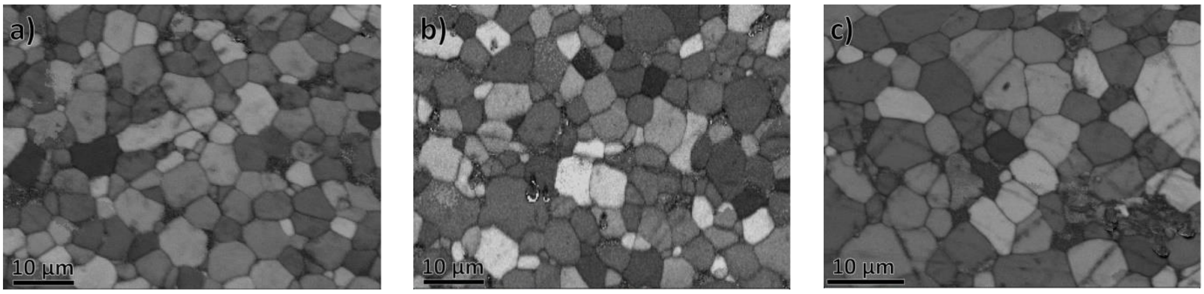

Figure 6.14 Band contrast maps of (a) Dy-free, (b) Red-Dy and (c) Dy-rich samples.

Using the linear intercept method (equations 4.1 & 4.2), the mean grain size (w) was found to be w_1= 4.27 ±0.67 µm with a standard error (SE) of 0.07 for the Dy-free sample, w_2= 4.39 ±0.52 µm and SE=0.07 for the Red-Dy sample and w_3= 6.4 ±1 µm with SE=0.28 for Dy-rich sample. This data revealed that $w_1 < w_2 < w_3$ and that Dy-rich sample has the largest mean grain diameter compared to the other two samples. These values of average grain size are related to the particle size of the initial powders used for these sample and to the conditions of the sintering process [103, 104]. The larger average grain size of Dy-rich sample suggests that it had a relatively larger powder particle size compared to the other two samples. In addition, the larger standard deviation and error of Dy-rich samples suggests it had lower control of particle size-distribution and processing conditions compared to Dy-free and Red-Dy samples.

The comparison between the grain size (diameter) distributions of Dy-free, Red-Dy and Dy-rich samples show a lognormal size distribution of Dy-free, Red-Dy and Dy-rich magnets (fig. 6.15a). The largest grain size in the Dy-free was ~8 μm compared to the Red-Dy and Dy-rich samples in which larger grains were observed to have 11 and 13 μm, respectively.

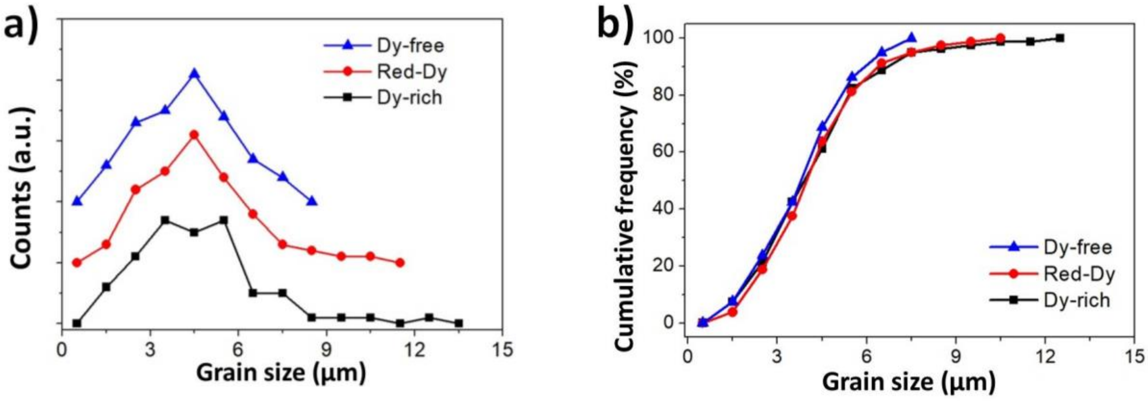

Figure 6.15 Main phase grain (a) size distribution and (b) its cumulative frequency of Dy-free, Red-Dy and Dy-rich samples. The class width of grain size is 1 μm.

These histograms reveal that the microstructure of Nd-Fe-B samples could have grains that are significantly larger in size compared to their adjacent grains, which is most noticeable in Dy-rich magnet. In addition, these calculations revealed the grain size distributions in all samples are broadly similar (fig. 6.15b) but Dy-free sample has a tighter spread and no evidence obtained of it having larger grains (>8 μm), unlike the other two samples. These observations indicate an improved grain size control in Dy-free sample, which may be combined to other microstructural observations in this sample (low Fe/RE ratios in the Cu-enriched RE-phase and stronger grains alignment) to explain the higher H_c of Dy-free sample compared to other two samples.

6.8 Conclusions

The angular dispersion of main phase cells was revealed by pole figures and their plots to be around 15° and 30° for Dy-free and Red-Dy samples, respectively. On the other hand, the weakest alignment of main phase cells was observed in Dy-rich sample. This angular dispersion was confirmed by the Z-direction inverse pole figures of the three samples. In addition, considerable main phase cells were observed to have larger orientation angles than 30° and up to 90°, which indicates that adjacent main phase grains can be considerably misaligned from each other. This misalignment can play a major role in determining the coercivity and remanence of sintered Nd-Fe-B magnets. The mean angular deviation of the collected Kikuchi patterns from the predefined patterns (simulated $Nd_2Fe_{14}B$ phase) was observed to vary at different points in the Dy-free sample. However, the observed deviation showed no obvious difference between grains centre and edges.

The average grain size determination revealed that Dy-free sample has the smallest grain average compared to the Red-Dy and Dy-rich sample. On the other hand, the grain size distribution of the three samples revealed a similar lognormal size distribution but was tighter in Dy-free sample. These distributions also revealed that it is possible to have grains that are significantly larger compared to adjacent grains. This difference in the size of main phase grains is likely to have a significant effect on the magnetic properties of sintered Nd-Fe-B magnets.

7.Modelling the Role of Grain Boundary Phases

7.1 Introduction

The experimental characterisation of sintered Nd-Fe-B samples in chapter 5 and in previous reports [29, 100, 105] revealed the presence of intergranular phases with 1) a non-uniform distribution across the samples and 2) different Fe/RE ratios in their composition at different regions, which indicates different magnetic properties. These intergranular phases are considered a source of reversed domain wall nucleation in sintered Nd-Fe-B magnets (see §3.3.1) [42]. Thin grain boundary (GB) phases have been suggested by Kronmüller *et al* to lead to magnetically exchanged $Nd_2Fe_{14}B$ grains [42]. On the other hand, Schrefl *et al* predicted that non-magnetic GB phases can exchange decouple $Nd_2Fe_{14}B$ grains and give significant improvements to the coercivity (H_c) of Nd-Fe-B magnets [68]. However, the exact magnetic characteristics of GB phases are not confirmed yet. Clarifying their effect on H_c and M_r is essential to improved understanding of the performance of Nd-Fe-B magnets.

This chapter describes the use of finite element modelling (FEM) to investigate the role of GB phases on current Nd-Fe-B magnet performance. The data obtained from electron microscopy analysis in Chapters 5 and 6 was used to inform the models that represent $Nd_2Fe_{14}B$ grains and their surrounding GB phases. This chapter includes studying the effect of mesh size on computing errors in FEM calculations, the role of GB phases on nucleation and propagation of reversed domains in $Nd_2Fe_{14}B$ grains and the significance of intergrain exchange in typical grain size distributions of sintered Nd-Fe-B magnets.

7.2 The influence of mesh size

FEM relies on discretising Landau-Lifshitz-Gilbert (LLG) equation at each element in the model (see §4.7.1). FEM modelling of hard magnets has size limitations prescribed by the exchange length of the material, which is l_{ex} = 1.7 nm for $Nd_2Fe_{14}B$ phase (see §4.7.3). Computation errors of mesh sizes larger than l_{ex} lead to unrealistic representation to the magnetic configuration of FEM models [66, 69, 72]. The sources of these systematic errors are mainly related to a mesh convergence error and mesh layout error. Both sources affect the numerical calculations of total Gibbs energy and hence the value of H_c.

The numerical error of different mesh sizes has been studied in order to validate the results of the modelling efforts of this work. It should be noted that the term mesh size in this study refers to the average edge length of each mesh element. Here, H_c and E_t values of single $Nd_2Fe_{14}B$ models are compared using single-phase $Nd_2Fe_{14}B$ grains with 100 nm diameter using two types of structures (full and core-shell). In the core-shell structure, the core radius was 45 nm and shell thickness 5 nm. The magnetic properties of $Nd_2Fe_{14}B$ phase at room temperature were defined to have a magnetocrystalline anisotropy K_1=4.5 $MJ.m^{-3}$, a saturation magnetisation μ_0M_s=1.61 T, exchange stiffness constant A_{ex}=12.1 $pJ.m^{-1}$ and a damping constant α=0.02 [101]. Magnetic hysteresis behaviour was simulated by applying an external field of 10 T was parallel to the easy axes of grains for 1000 ns with a rate of 50 $mT.ns^{-1}$ from +10T to -10T. FEM models of single-phase truncated octahedron shape and a grain diameter of 100 nm (fig 7.1a) that were meshed in different ways. The first type of meshing divided the shape into meshing elements of a uniform size across the sample, which means surface and core mesh elements have the same size. Hereafter, this model will be denoted as the ‘regular’ meshing method.

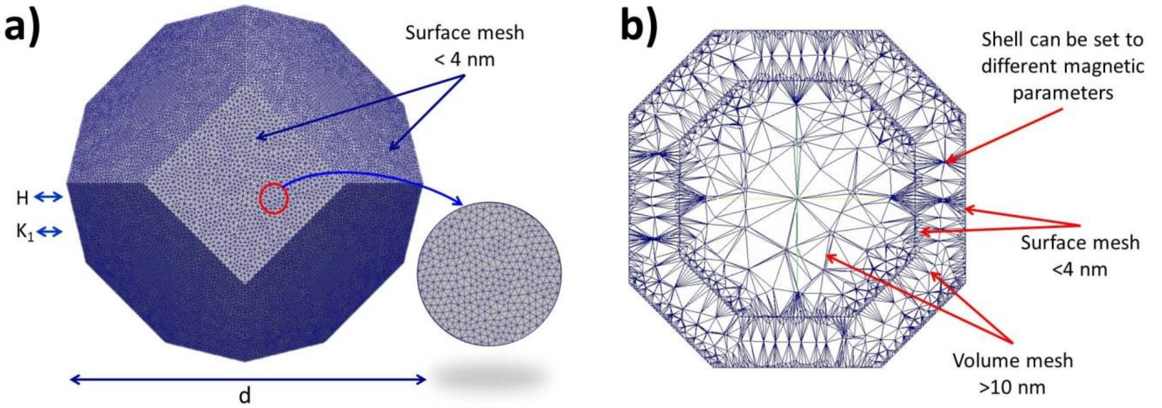

Figure 7.1 (a) single truncated octahedron shape that represents a grain with a diameter of 100 nm. (b) A volume cross section of the truncated octahedron shape showing the core-shell structure and the coarser mesh size compared to surface.

The second meshing method divided models into meshing elements with fine mesh sizes close to surface and coarser mesh sizes in the interior. Previous reports stress the importance of having a dense mesh at regions where generation of reversed domain walls occurs [52, 66, 106]. These regions include corners, edges and interfaces between $Nd_2Fe_{14}B$ grains and other phases [52, 66, 106]. These reports suggested that once reversed domain walls are nucleated at the boundaries of $Nd_2Fe_{14}B$ grains; they move freely inside the grain's volume, which reduces the need for a dense mesh in the grain model interior [52, 106]. However, the systematic error arising from the coarser interior mesh, in this case, should have the least effect on the calculation of H_c [49]. The coarse interior mesh can provide significant savings the number of elements and hence to processing capability, time and storage. For example, increasing the volume mesh size from 1.7 nm to 6 nm at a distance of 10 nm from the surface of a 100 nm grain decreased the number of elements from 728,464 to 36,604. This meshing method will be denoted hereafter to as the 'extended' meshing method.

Models with core-shell structures were used extensively in this work, where the outer surface of the truncated octahedrons was shrunk towards the centre with a defined thickness (fig. 7.1b). The shrunk area (shell) can then be used to represent a different phase from the core. For example, this shell may represent GB phases with different magnetic properties compared to the core $Nd_2Fe_{14}B$ grain. The systematic error of FEM calculations in the core-shell structures was studied using the regular and extended meshing methods described earlier in this section. This means core-shell models with regular mesh will have the same mesh size across the sample. Core-shell models with extended mesh will have a fine mesh at each of the surfaces of the core and the shell accompanied by coarser (>10 nm) in the interior of the core grain.

Figure 7.2 shows the dependence of H_c of $Nd_2Fe_{14}B$ grains on the mesh size. An identical model was meshed eight times for each mesh size with different detailed mesh configuration. H_c values at each mesh size represent the mean H_c of the eight models and *y*-error bars represent double the standard deviation (2σ). H_c values of regular meshing models (fig. 7.2a) were similar with different mesh sizes (fig. 7.2b). However, the imprecision of H_c values (2σ) at each regular mesh size increases with increasing the mesh size. The convergence of extended mesh models (fig. 7.2c) with 1.7 nm surface and a volume mesh sizes of 1.7, 2.8, 4, 7 and 10 nm shows a decrease in H_c with increasing the volume mesh sizes (fig. 7.2d). The H_c values of the extended mesh volumes show higher precision with increasing the mesh size.

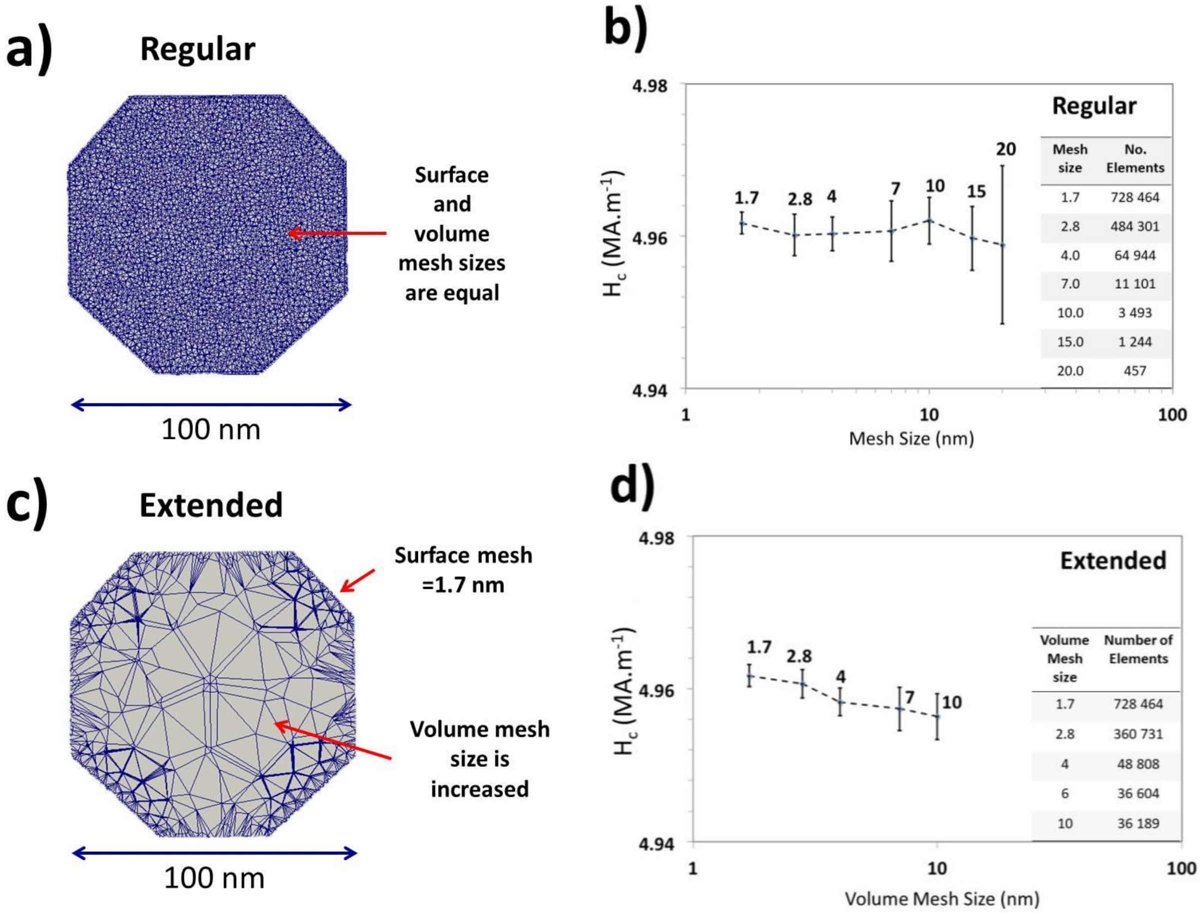

Mesh size	No. Elements
1.7	728 464
2.8	484 301
4.0	64 944
7.0	11 101
10.0	3 493
15.0	1 244
20.0	457

Volume Mesh size	Number of Elements
1.7	728 464
2.8	360 731
4	48 808
6	36 604
10	36 189

Figure 7.2 Examples of cross-section sketches of the (a) regular (c) extended mesh single grain (d=100nm) models with (b) & (d) their coercivity (H_c) values at different mesh sizes, respectively. The tables on the right of each plot show the average number of elements of each model.

In core-shell structures, both core and shell were defined to have the magnetic properties of $Nd_2Fe_{14}B$ phase. Each core-shell model was also meshed eight different times at each mesh size with a different mesh configuration (fig. 7.3a & c). As before, H_c values of core-shell models with regular meshing (fig. 7.3b) were very similar for all mesh sizes. The range of these H_c values of regular mesh models fluctuated but became larger at larger mesh sizes (*y*-error bars in fig 7.3b). H_c values slightly decreased for core-shell models with a 1.7 nm surface mesh and with increasing the core mesh size from 1.7 to 2.8, 4, 6 and 10 nm (fig 7.3d). These extended core-shell models showed a higher precision with increasing the volume mesh.

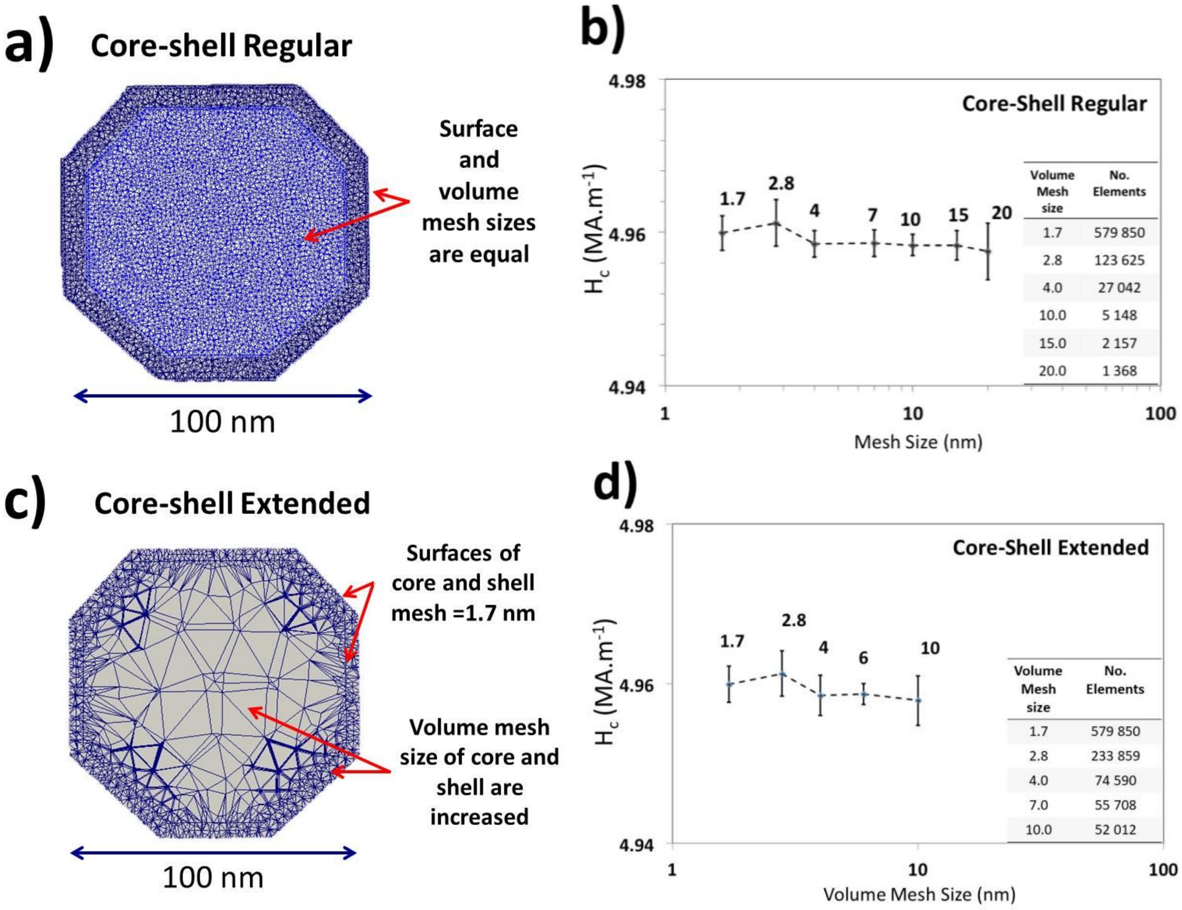

Volume Mesh size	No. Elements
1.7	579 850
2.8	123 625
4.0	27 042
10.0	5 148
15.0	2 157
20.0	1 368

Volume Mesh size	No. Elements
1.7	579 850
2.8	233 859
4.0	74 590
7.0	55 708
10.0	52 012

Figure 7.3 Examples of cross-section sketches of the core-shell models with (a) regular (c) extended mesh, (b) & (d) their coercivity (H_c) values at different mesh sizes, respectively. The tables on the right of each plot show the average number of elements of each model.

FEM simulates the behaviour of hard magnetic materials by calculating Gibbs total energy (E_t) total energy at each value of the external field (H_{ext}) (equation 4.6) and then by using these values of E_t to find the effective field value (equation 4.9) (see §4.7.1). When H_{ext} is increased to higher than 0 A.m^{-1} (fig. 7.4a), E_t decreases (fig. 7.4b ①) until it reaches its lowest values at the highest (+ve) H_{ext}. This decrease in E_t with increasing H_{ext} is induced by the increase in the Zeeman energy of $H_{ext.}$ Decreasing H_{ext} from its highest value towards 0 A.m^{-1} will retrace E_t back to its initial values (②). At H_{ext}= 0 A.m^{-1}, the system is at relaxation point with a remnant magnetisation (M_r) and the value of E_t at this point will be denoted hereafter as the 'remnant E_t'. Applying (–ve) H_{ext} will decrease the magnetisation of the sample and increase E_t until it reaches its highest value at a certain H_{ext} (③). At this point, the effect of Zeeman energy forces the magnetisation of the system to change its direction, which is initiated by the nucleation of reversed domain walls. The value of E_t at the start of magnetisation switching will be denoted hereafter as ‘max. E_t’. Then, further increase in (-ve) H_{ext} will increase the magnetisation in (-ve) direction and decrease E_t (④) until it reaches its lowest values at the highest (-ve) H_{ext} (⑤). Retracing H_{ext} back to 0 $A.m^{-1}$ will decrease E_t to its initial value (⑥). The remnant and max values of E_t represents the system has a major importance in the calculations of M_r and H_c of the sample in FEM.

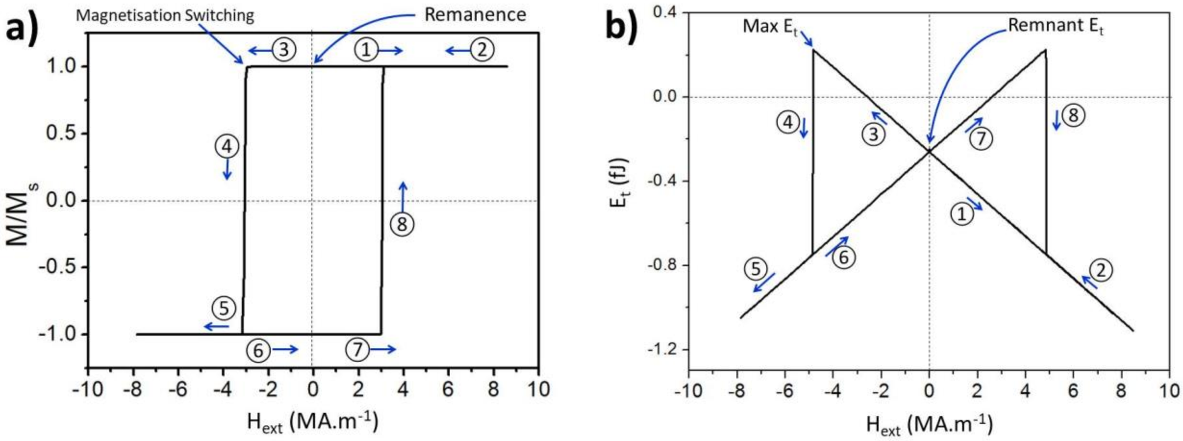

Figure 7.4 (a) The magnetisation and (b) total Gibbs free energy (E_t) change with changing the external field (H_{ext}) between -10T and +10T applied to a single 100 nm grain model with 1.7 nm regular mesh.

The comparison between remnant E_t for the single 100 nm grain models with regular and extended mesh showed almost identical values with increasing mesh size (fig. 7.5a & b). The max E_t of these two types of meshing also showed a strong agreement with increasing mesh size. However, max E_t calculations showed a relatively larger precision compared to the remnant E_t calculations (*y*-error bars in fig. 7.5a & b). The values of remnant and max E_t for core-shell models with regular and extended meshing show a strong convergence at different mesh sizes (fig. 7.5c & d). The lower precision of max E_t calculations compared to remnant E_t is also observed in core-shell models in both types of models. The effect of mesh size and type on E_t indicates that the systematic errors in the numerical calculations of H_c arise mainly from the low precision of max E_t calculation (fig. 7.2 & 7.3).

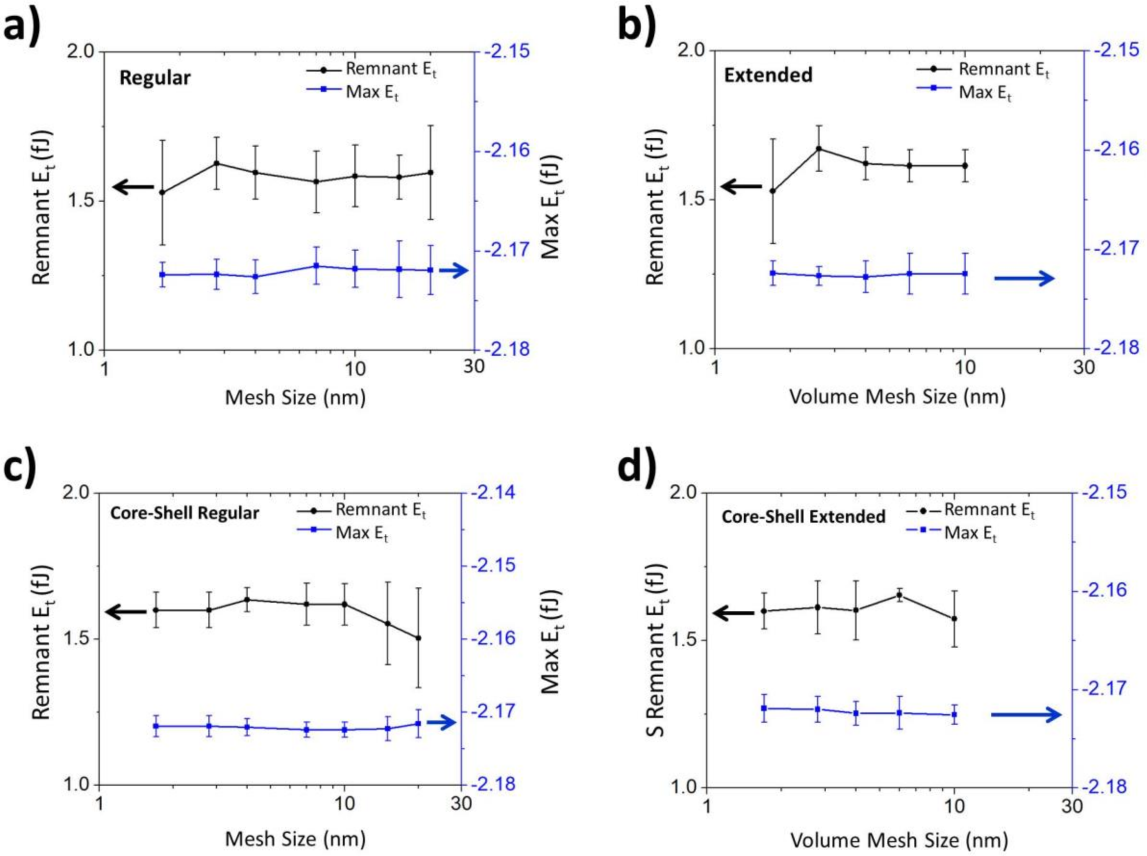

Figure 7.5 The remnant and max calculations E_t of single grains with (a) regular and (b) extended meshing and core-shelled grains with (c) regular and (d) extended meshing.

The convergence of H_c calculations using regular and extended meshing methods was investigated for single and core-shell models with a diameter 350 nm, which is larger than the diameter of single-domain particles D_S~260 nm (see §3.4.3). The single grain models with regular mesh were meshed with an identical mesh size (4-30 nm) at surface and across the volume, while the extended mesh models were defined to have a 4nm surface mesh size and a coarser volume mesh size between 4-30 nm. For the 350 nm core-shell models, the shell thickness was defined to be 10 nm. The mesh size of core-shell models was varied between 4-30nm for the regular meshing compared to a 4 nm surfaces mesh and 4-30 nm volume mesh for the extended meshing method. The comparison between H_c values at different mesh sizes revealed a strong convergence even at larger mesh sizes (fig. 7.6). However, these H_c values have lower precision with increasing the mesh size that is relatively larger than the 100 nm models.

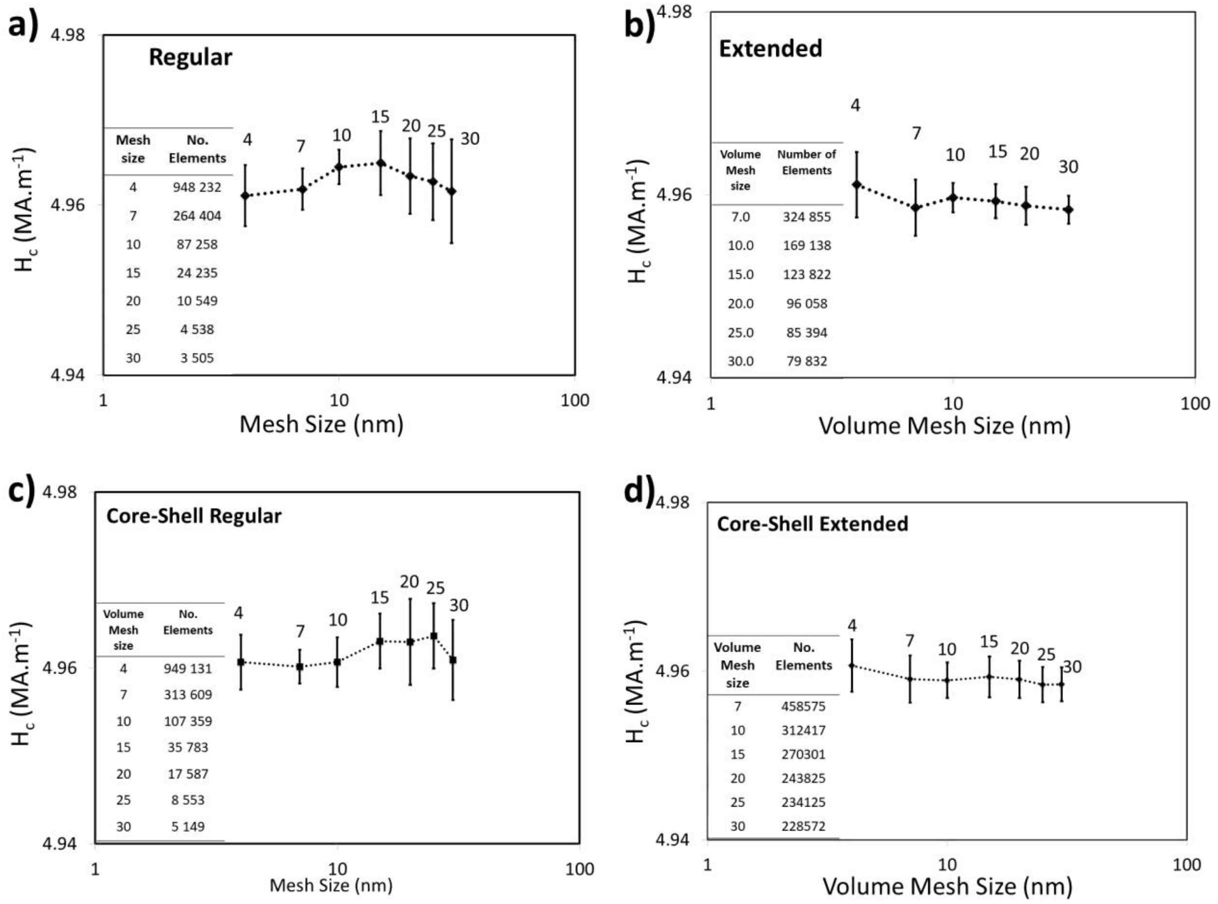

Mesh size	No. Elements
4	948 232
7	264 404
10	87 258
15	24 235
20	10 549
25	4 538
30	3 505

Volume Mesh size	Number of Elements
7.0	324 855
10.0	169 138
15.0	123 822
20.0	96 058
25.0	85 394
30.0	79 832

Volume Mesh size	No. Elements
4	949 131
7	313 609
10	107 359
15	35 783
20	17 587
25	8 553
30	5 149

Volume Mesh size	No. Elements
7	458575
10	312417
15	270301
20	243825
25	234125
30	228572

Figure 7.6 The mean H_c for single 350 nm grains where (a) regular (b) extended meshing, core-shelled grains with (c) regular and (d) extended meshing. The tables on the left of each plot show the average number of elements of each model

7.2.1 Computing time

Figure 7.7 plots of the time required for simulating the 100 nm models presented earlier. The data points represent the average time of processing models of single and core-shelled models using regular and extended mesh. The strong dependence of computing time on mesh size in micromagnetic models is well established [66]. Here, significant processing time savings can be achieved with increasing the volume mesh size from 1.7 nm to 4 nm while keeping the surface volume at 1.7 nm mesh size. This has reduced the required processing time to less than 0.05% of the time needed fine mesh models. Using the extended meshing method introduced in this work achieved significant savings to the number of elements of each model, and hence the computation time. Hereafter, single grain models with a diameter of 100 nm are generated with a 4 nm surface mesh and <10 nm volume mesh, which enabled producing models with a maximum number of 400,000 elements. This is compared to 5 million [47] and 20 million [72] tetrahedral elements of same model size in previous work. The computing time of the models used in this work was generally between 300-1000 minutes.

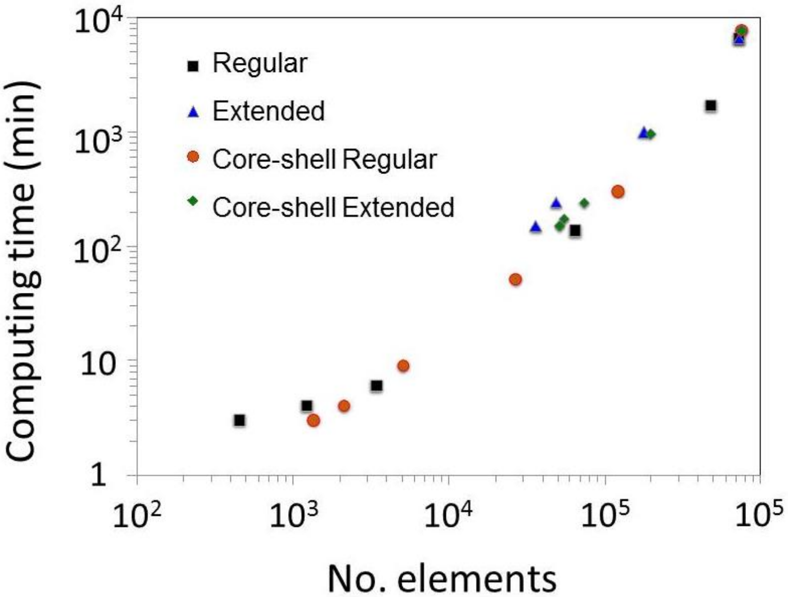

Figure 7.7 The dependence of processing time on the number of elements of 100 nm models.

7.3 The effect of grain boundary phases chemistry on single grains

EDX analysis in Chapter 5 revealed a non-uniform Fe/RE ratios of intergranular phases, which indicates that GB phases will have different chemistry and, therefore, different magnetic properties across the microstructure. In addition, the high amount of Fe in Cu-enriched intergranular phases indicates that they are likely to be ferromagnetic. Ferromagnetic GB phases are suggested to cause the nucleation of reversed domain walls at lower demagnetisation fields than the anisotropy field (H_A) of $Nd_2Fe_{14}B$ phase [29]. However, it is difficult to determine the precise magnetic properties of these GB phases experimentally with current capabilities. The difficulty lies in their relatively small size and reactive nature. Micromagnetic modelling is an effective tool that can provide a better understanding of the effect of possible GB phase magnetic properties.

In this work, truncated octahedron grains with 100 nm diameters were used to model main $Nd_2Fe_{14}B$ phase grains. This shape has been used previously to represent $Nd_2Fe_{14}B$ grains in the actual microstructure of Nd-Fe-B magnets [57]. Here, models with core-shell structures (see §7.2) were used. The model core was to represent the main $Nd_2Fe_{14}B$ phase with μ_0M_s=1.61 T, K_1=4.5 MJ.m^{-3}, A_{ex} = 12.1 pJ.m^{-1} and α=0.02 at room temperature [101]. The shells were used to represent GB phases and set to have a thickness of 2 and 4 nm. The magnetic properties of the GB phases were obtained by applying a reduction factor x=0, 0.25, 0.5, 0.75 to the values of the magnetic properties of α-Fe phase, which are μ_0M_s=2.15T and A_{ex} = 25 pJ.m^{-1} at room temperature [107]. The fraction of x may represent GB phases (*e.g.* Cu-enriched RE-rich phase) with different Fe/RE ratios. K_1 of GB phases is likely to decrease with increasing Fe content in GB phases. Hence, for crystalline GB phases, the values of K_1 were set to the value of $Nd_2Fe_{14}B$ phase at x=0 and decreased linearly with the factor $1-x$. Amorphous GB phases were set as K_1=0 except for x=0, which represents a grain with no surrounding GB phase, which means the magnetic properties of shells at x=0 point in amorphous and crystalline GB phases are equal to the magnetic properties of $Nd_2Fe_{14}B$ phase. The values of μ_0M_s, A_{ex} and K_1 parameters used to represent the GB phase in this study are in accordance with Fe/RE ratios observed in the EDX analysis. Using different values for the soft GB phase is expected to lead to the same findings obtained in this work even though the exact values of H_c and M_r might differ. The simulations started with saturating the granular model by applying H_{ext} of 10 T parallel to the easy axes of both of $Nd_2Fe_{14}B$ grains and GB phases. The hysteresis loops were obtained by changing H_{ext} at a rate of ±50 $mT.ns^{-1}$ from +10T to -10T.

Figure 7.8 compares the modelled demagnetisation curves of 100 nm $Nd_2Fe_{14}B$ grains surrounded by 2 nm amorphous GB phases. H_c of these models is dependent on the magnetic properties of GB phases. The highest H_c value was observed at x=0, *i.e.* when no GB is surrounding the main phase grains. H_c decreases gradually with increasing the value of x. For example, H_c drops from 4.71 $MA.m^{-1}$ at x=0 to 3.05 $MA.m^{-1}$ at x=1. This significant reduction in H_c is a direct consequence of the increasingly Fe-like magnetic properties of GB phases, which leads to magnetically soft regions surrounding the main phase grains. This gradual decrease in H_c is similar to the linear reduction of H_c of exchange-spring magnets with increasing the amount of the soft phase in their microstructure [107].

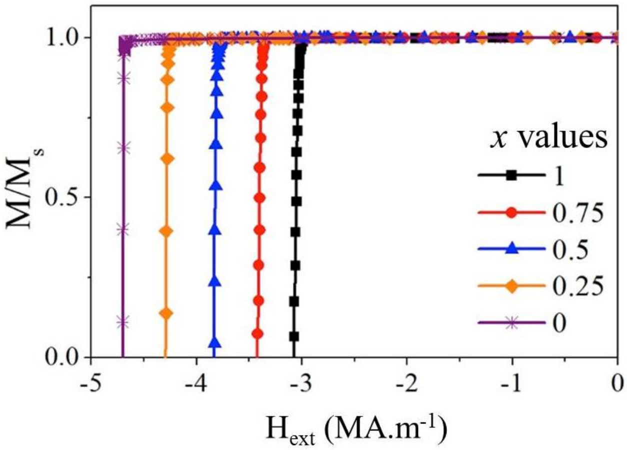

Figure 7.8 The modelled second quadrant of hysteresis loops of 100 nm $Nd_2Fe_{14}B$ grains surrounded by 2 nm grain boundary (GB) phases with different x.

The magnetisation configurations of a typical response of the sample when x=1 show that the demagnetisation process of magnetically saturated $Nd_2Fe_{14}B$ grains starts by the generation of reversed domains walls at H_{ext}=3.02 $MA.m^{-1}$ (fig. 7.9a). The reversed domain wall grows in size and propagates towards the centre of the sample, leading to its full demagnetisation at reversed H_{ext} of 3.18 $MA.m^{-1}$. The introduction of GB phases with weaker magnetic properties delays the nucleation of reversed domain walls, which increases H_c (fig. 7.9b). For example, introducing GB phases with x=0.25 leads to the generation of reversed domains walls at relatively higher reversed field (H_{ext} =4.22 $MA.m^{-1}$) compared to models with soft GB phases. The full demagnetisation of the sample was achieved at -4.37 $MA.m^{-1}$.

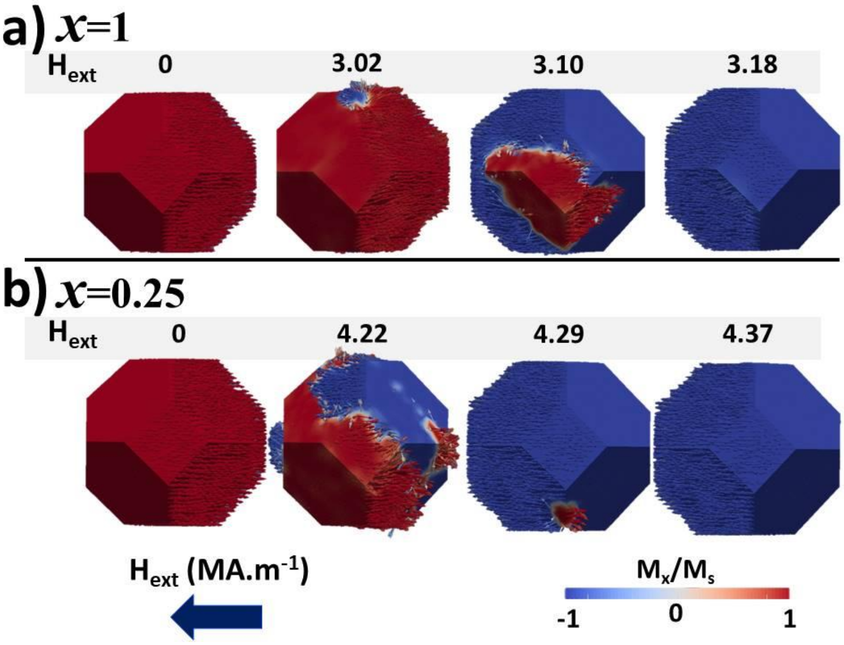

Figure 7.9 Screenshots of the magnetisation configurations of $Nd_2Fe_{14}B$ grain with 2 nm GB phase of x=1. The number above each screenshot represents the value of H_{ext} in $MA.m^{-1}$.

Figure 7.10a compares H_c values of a single 100 nm diameter $Nd_2Fe_{14}B$ grain surrounded by 2 nm or 4 nm amorphous GB phases. The highest value of H_c was observed in models with no GB phases (x=0). Increasing the value of x to 1 (*i.e.* soft GB phase) reduced H_c to 35% and 48% of the initial values for models with GB phases of 2 nm and 4 nm, respectively. Generally, thicker GB phases led to lower H_c values due to the increased volume of soft GB phases, which was represented by the comparison between 4 nm to 2 nm models. For example, H_c of models with 4 nm GB phases was ~21% less than models with 2 nm GB phases at x=1.

Introducing K_1 in GB phases resulted in identical values of H_c at $x \leq 0.25$ with 2 and 4 nm thickness (fig. 7.11b). This can be attributed to the high strength of K_1 at these values of x, which means that higher H_{ext} was required for the nucleation of reversed domain walls at the interface with GB phases. Higher values of x will lead to H_c reduction of 49% for x=1 models with 2 nm crystalline GB phases. In addition, increasing the thickness of crystalline GB phases from 2 nm to 4 nm led to a 17% drop in H_c at x=1. The values of H_c of $Nd_2Fe_{14}B$ grains in this study confirm that significant enhancement in H_c can be produced with weaker magnetic properties at GB phases. In addition, reducing the thickness of GB phases with soft magnetic characteristics leads to higher H_c, while thickness change shows less significant effect at GB phases with weaker magnetic properties (smaller x).

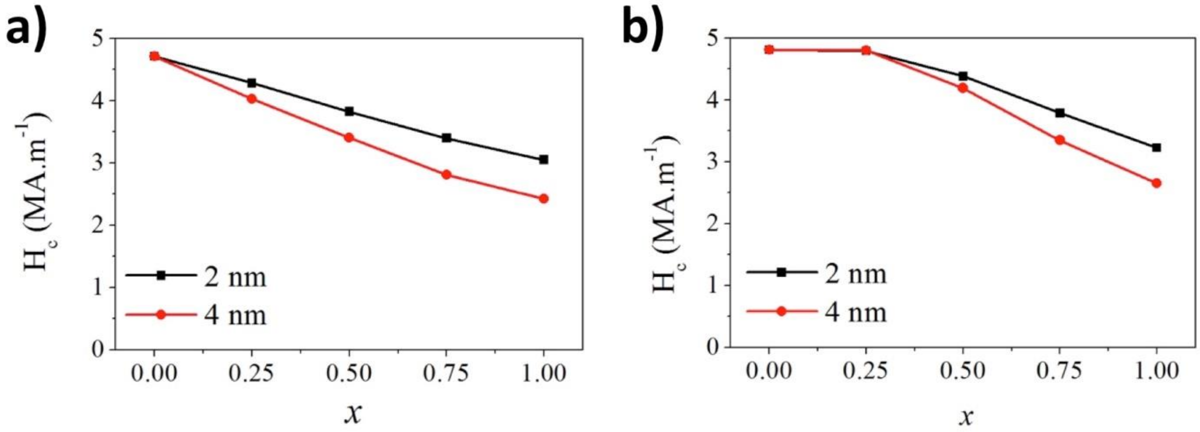

Figure 7.10 H_c values of 100 nm $Nd_2Fe_{14}B$ grains surrounded by (a) amorphous or (b) crystalline GB phases with 2 and 4 nm thicknesses.

The above models assessed the effect of GB phases with fractions of the Fe amount. It is interesting to investigate the effect of GB phases that have a broader range than the above study. For this reason, the same model was used to simulate $Nd_2Fe_{14}B$ grains with x fractions of α-Fe properties, where x in this case =1, 10^{-1}, 10^{-2}, 10^{-3} and 10^{-4}.

H_c values of single 100 nm $Nd_2Fe_{14}B$ grains with 2 and 4 nm thicknesses of GB phases were identical with increasing x from 10^{-4} to 10^{-2} (fig. 7.11). H_c values at this range were identical for models of 2 and 4 nm GB phases. At $x>10^{-2}$, H_c decreased with increasing x. For example, H_c drop to ~ 3% and ~35% at $x=10^{-1}$ and 1, respectively. The values of H_c of this study confirmed the insignificant effect of the thickness of GB phases when they possess weaker (less Fe-like) magnetic properties.

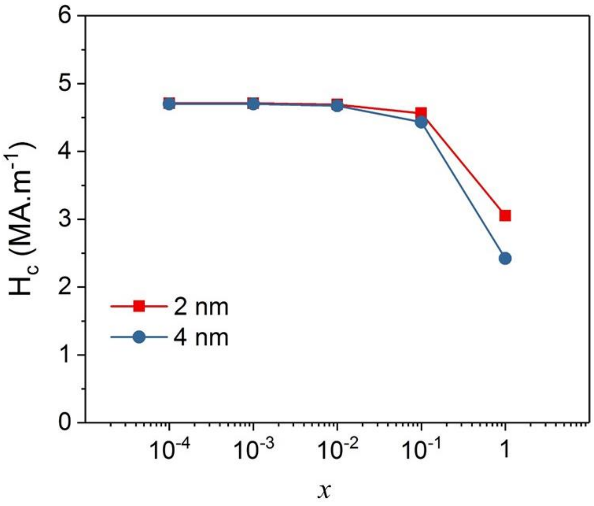

Figure 7.11 A comparison between H_c of 100 nm $Nd_2Fe_{14}B$ grains surrounded by 2 and 4 nm GB phases with x fractions of α-Fe magnetic properties.

7.4 The anisotropic relationship of grain boundary phases and $Nd_2Fe_{14}B$ grains

EDX analysis revealed a difference in composition for GB phases that surrounds the same grain (see fig. 5.7). Recent 3DAP analysis suggested that GB phases are mostly amorphous when they are parallel to *c*-axes of main phase grains and crystalline when they are in perpendicular to the *c*-axes of these grains [100], which suggests that the formation of GB phases depends on alignment direction of main phase grains. It is interesting to understand the difference between the role of GB phases on H_c when they are parallel or perpendicular to the easy axes of the main phase grains. In this study, the effect of anisotropic nature of GB phases was investigated using two $Nd_2Fe_{14}B$ grains with 100 nm diameter (A & B) (fig. 7.12a). The magnetic properties of $Nd_2Fe_{14}B$ phase are identical to the values used earlier in §7.2. Both grains are surrounded by 2 nm shells that represent GB phases (fig. 7.12b).

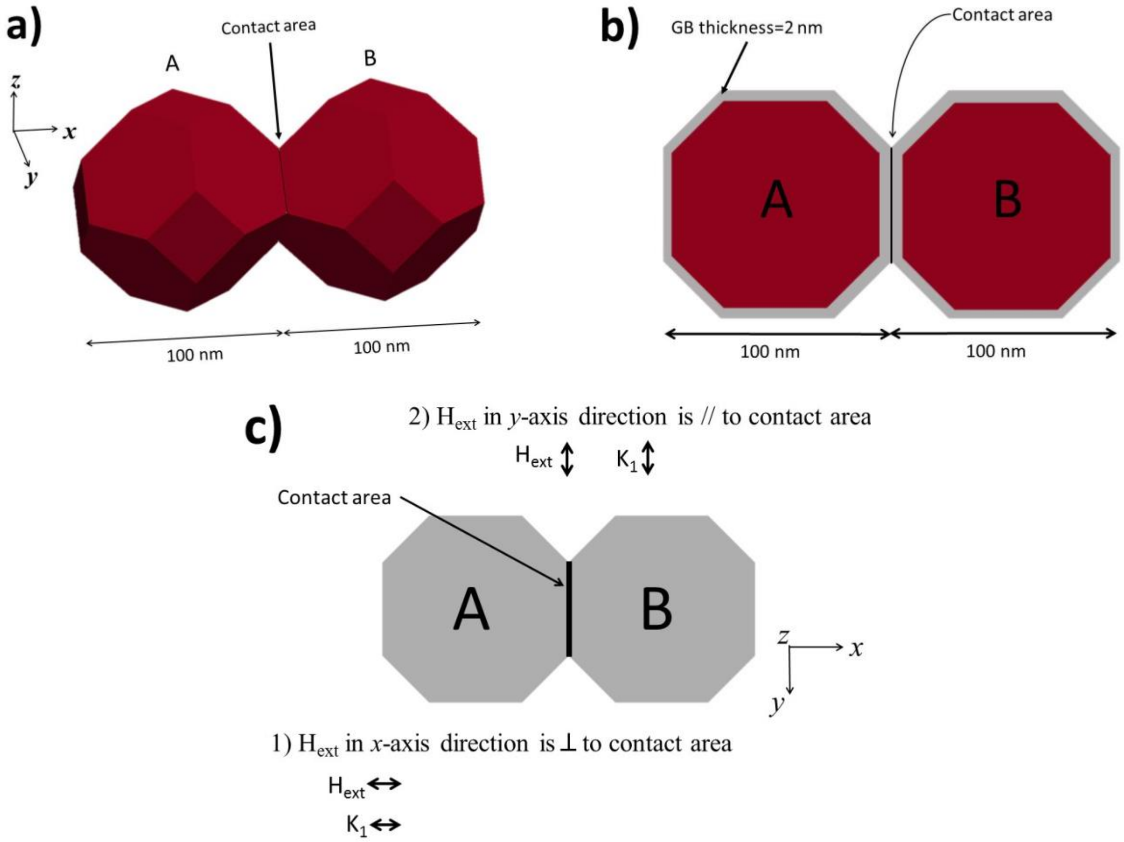

Figure 7.12 (a) A schematic sketch of the two 100 nm grains model and (b) the 2 nm GB phase. (c) A sketch shows the external field (H_{ext}) applying directions.

The magnetic properties of crystalline and amorphous GB phases were defined by using x fractions of M_s and A_{ex} of α-Fe phase, where x=0, 0.25, 0.5, 0.75 and 1. For crystalline GB phases, the values of K_1 were set to the value of $Nd_2Fe_{14}B$ phase at x=0 and decreased linearly with the factor $1-x$, while K_1 was defined to be 0 $J.m^{-3}$ for amorphous GB phases. The hysteresis behaviour of magnetisation in these models was simulated by varying H_{ext} between 10T and -10T with a rate of (±50 $mT.ns^{-1}$). The direction of H_{ext} was either 1) parallel to the x-axis and perpendicular to the contact area or 2) parallel to y-axis and parallel to the contact area (fig 7.12c). The direction of K_1 in $Nd_2Fe_{14}B$ grains was defined to be always parallel to H_{ext} direction.

H_c of models with amorphous GB phases decreased with increasing *x* from 0 to 1 when H_{ext} applied in the same direction (either *x* or *y*) (fig. 7.13a). These models produced higher H_c when H_{ext} was applied in *x*-axis direction compared to *y*-axis direction. For example, H_c was 22% higher when H_{ext} is in the *x*-direction compared to when it is in *y*-direction. For models with crystalline GB phases, H_c showed identical values at *x*=0 and 0.25 for *x*-axis models, which was also observed for *y*-axis models (fig. 7.13b). H_c decreased with increasing *x* to values higher than 0.25. For both amorphous and crystalline GB phases, H_c showed higher values when H_{ext} was parallel to *x*-axis (fig. 7.14b). These values are 21% higher than H_c of the same models when H_{ext} was applied parallel to *y*-axis.

The difference in H_c when GB phases are parallel or perpendicular to H_{ext} direction is a result of the different magnetostatic interactions between the two adjacent $Nd_2Fe_{14}B$ grains. The interaction between the stray fields of the two grains was disadvantageous when H_{ext} was applied parallel to the contact area between the two grains and GB phases, which was confirmed by H_c of models with no separating GB phases (*x*=0). Although weaker magnetic properties at GB phases increased H_c of these models, the effect of the stray field interactions appears to persist even with less Fe-like GB phases. These observations indicate that an anisotropic distribution of GB phase composition can be utilised to improve H_c. For example, this can be achieved by confining the inevitable Fe-rich GB phases to areas perpendicular to H_{ext} and easy axes of $Nd_2Fe_{14}B$ grains. This approach, if possible, could be successful only with the condition that discharging Fe-rich phases to these areas lead to higher RE-rich phases at areas parallel to H_{ext}.

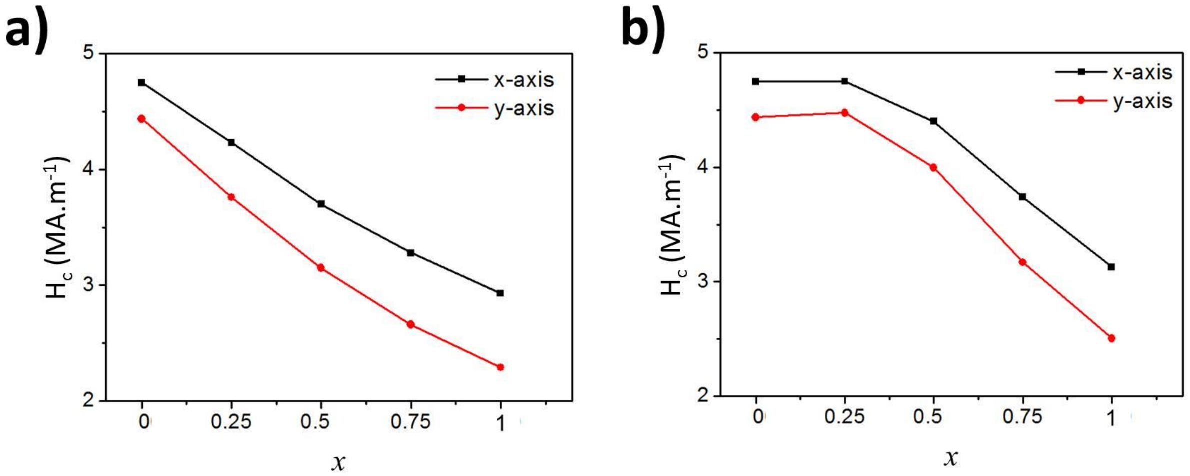

Figure 7.13 H_c of single grain models with (a) amorphous and (b) crystalline GB phases when H_{ext} is applied in *x* or *y* direction as described in fig. 7.12.

7.5 The role of grain boundary phases on the propagation of reversed domain walls

It has been suggested that non-magnetic GB phases isolate $Nd_2Fe_{14}B$ grains leading to an individual magnetisation reversal at each grain [66, 69, 105]. This effect was thought to improve H_c to higher values due to pinning of domain walls movement at grain boundaries. However, our EDX analysis revealed higher Fe concentrations at GB phases (see §6.4), which means $Nd_2Fe_{14}B$ grains are likely to be ferromagnetically exchanged across GB phases. This exchange means that reversed domains will cascade between adjacent $Nd_2Fe_{14}B$ grains shortly after the nucleation occurs [29]. Misaligned $Nd_2Fe_{14}B$ grains are a source of reversed domains nucleation (see §3.3.1). Our EBSD analysis revealed that a high number of grains could have alignment angles up to 90° (see fig. 6.6, fig. 6.9 and fig. 6.12), which can be very detrimental to the performance of Nd-Fe-B magnets.

This study investigated the ability of GB phases to reduce the effect of misaligned grains and to achieve the magnetic isolation $Nd_2Fe_{14}B$ grains from each other. A two-grain (A & B) model where each grain has a diameter of 100 nm was used for this study (fig 7.14). The angle between the easy axes of grain A and H_{ext} (θ_A) was set to be 0° always, whereas the angle between the easy axis of grain B and H_{ext} (θ_B) was defined to be between 0-90°. Grain A was surrounded by a 2 nm shell that represents GB phase, which had either a soft ($\mu_0 M_s$=2.15T & A_{ex}=25 pJ.m^{-1}), or weak ($\mu_0 M_s$=0.5T & A_{ex}=6.25 pJ.m^{-1}) or non-ferromagnetic magnetic characteristics ($\mu_0 M_s$=0 T & A_{ex}=1 fJ.m^{-1}). The magnetic parameters of $Nd_2Fe_{14}B$ phase used in this study were the same as the values used earlier in §7.2.

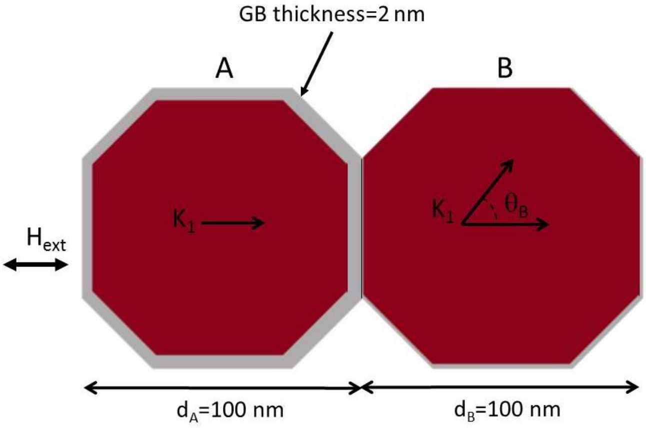

Figure 7.14 A sketch of the multigranular model shows grains A and B. The easy axes of the latter grain have an angle θ_B with H_{ext}.

The demagnetisation curves of two-grain models with magnetically soft GB phases at different θ_B (fig. 7.15a) show that both H_c and remanence (M_r) of these models decrease with increasing θ_B, which was a direct result of the lower field reversal of the misoriented grain (grain B) compared to the aligned grains (grain A). H_c of these models dropped to 9% and 42% of their initial values with θ_B of 45° and 90°, respectively (fig. 7.15b). This is compared to a 14% and 48% drop in M_r at θ_B= 45° and 90°, respectively (fig. 7.15b).

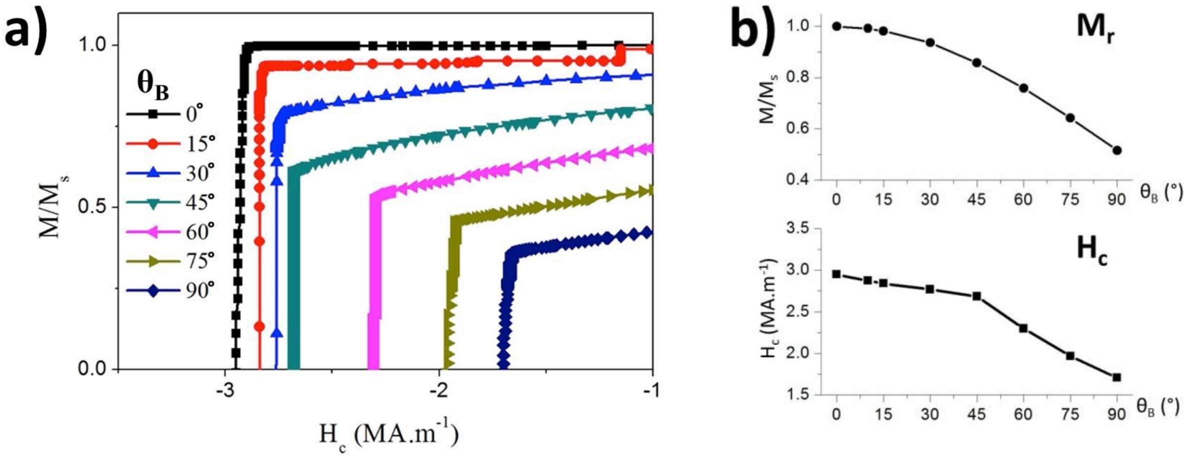

Figure 7.15 a) The modelled demagnetisation curves of the two grains models with soft GB phases at different θ_B. b) H_c and M_r change with θ_B increase.

The modelled second quadrants of the hysteresis loops (fig. 7.16a) and the magnetisation configurations of the two-grain model with soft GB phases show that in the case of θ_B=0°; a field of -2.9 MA.m^{-1} was required to switch grain A (fig. 7.16b). The full demagnetisation of this model was achieved at a field of -3.02 MA.m^{-1}. Increasing θ_B to 30° led to a decrease in the switching field of both grains with grain B switching at -2.86 MA.m^{-1} and a full demagnetisation at -2.94 MA.m^{-1} (fig. 7.16c). Introducing magnetically weak GB phases increased the field required for reversal to -4.18 MA.m^{-1} (fig. 7.16d). The full switching of this model was achieved at a field of -4.31 MA.m^{-1}. However, increasing θ_B of this model to 30° led to a drop in H_c of magnetically weak GB phases (fig. 7.16e). The switching of this model started at -2.84 MA.m^{-1} and the system was fully demagnetised at -2.9 MA.m^{-1}, which is comparable to the drop of the two-grain models and soft GB phases and θ_B=30°.

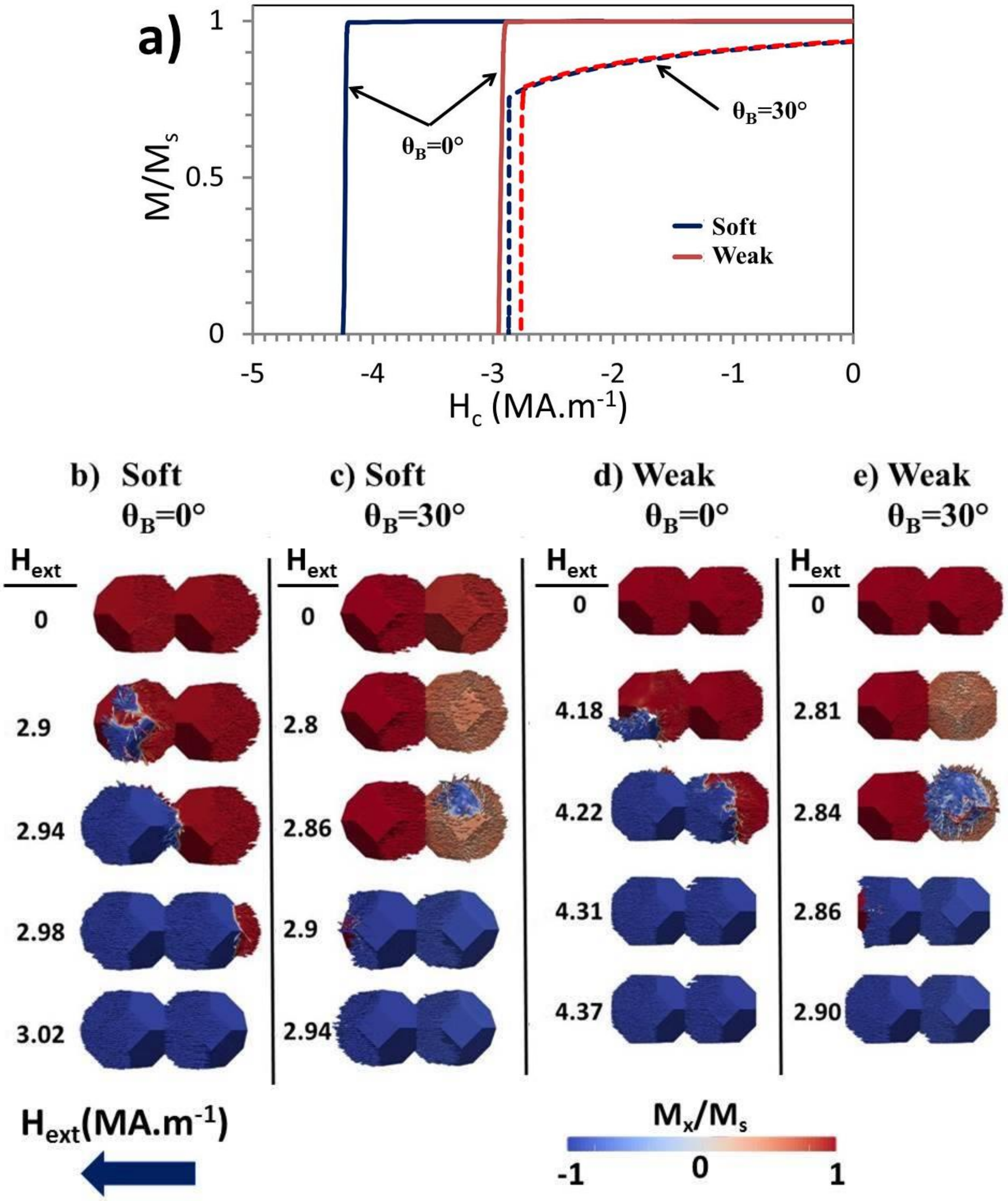

Figure 7.16 (a) The modelled 2nd quadrant of the hysteresis loops of models where θ_B is 0° (full lines) and 30° (dashed lines). Screenshots of magnetisation configuration of two 100 nm grains models with soft GB phases where θ_B is (b) 0° and (c) 30° and weak magnetic GB phases where θ_B is (d) 0° and (e) 30°.

Figure 7.17 compares H_c values of magnetically soft, weak and non-ferromagnetic GB phases with θ_B ranging from 0-90°. At θ_B=0°, weak and non-ferromagnetic GB phases increased H_c of the two-grain models up to 44% and 60% compared to H_c values with soft GB phases. This higher H_c is mainly attributed to the reduced magnetic exchange between A and B grains with weak and non-ferromagnetic GB phases. However, increasing the values of

θ_B higher than 0° led to a significant drop in H_c, which indicates that grains A and B are likely to remain magnetically exchanged even with weaker magnetic properties of GB phases. The effect of θ_B was less noticeable with soft GB phases, which produce relatively the lowest H_c values.

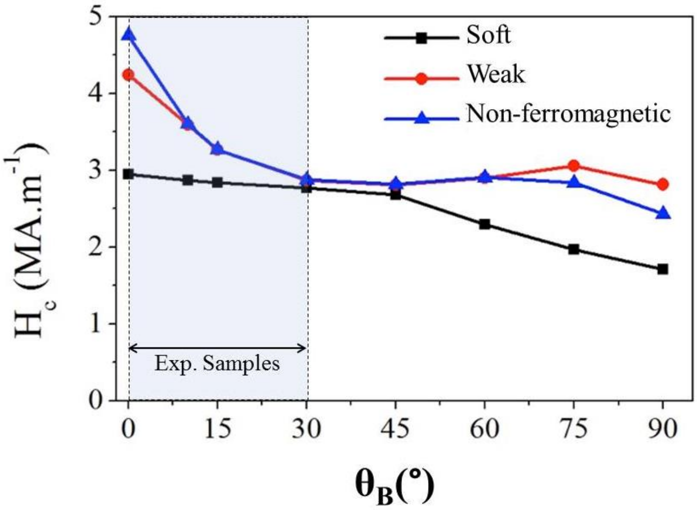

Figure 7.17 H_c of two 100 nm grains models with 2 nm GB phases at different values of θ_B.

The interactions between $Nd_2Fe_{14}B$ grains in sintered magnets are mainly represented by direct-contact and magnetostatic interactions [106]. The elimination of direct contact gives opportunity to introduce weak and non-ferromagnetic GB phases, which led to higher H_c. However, magnetostatic interactions are expected to persist even with non-magnetic GB phases [105], which explains the drop in H_c with increasing θ_B. These magnetostatic interactions between grain A and the misoriented grain B will lead to the propagation of reversed domain walls to adjacent $Nd_2Fe_{14}B$ grains even with non-ferromagnetic GB phases (fig. 7.16).

Further analysis to the simulations above was performed by analysing H_c of grains A and B separately with changing θ_B. Generally, the field-aligned grain A in models with non-ferromagnetic and weak GB phases have higher H_c compared to models with soft GB phases (fig. 7.18). However, H_c of grain A with weak GB phases was still significantly affected by θ_B. This is represented by 32% drop in H_c at θ_B=30° compared to its initial value at θ_B=0°. The effect of θ_B on grain A also persists with non-ferromagnetic GB phases, but it has almost identical H_c with increasing θ_B to >15°. The behaviour of grain A indicates that weak and non-ferromagnetic GB phases can reduce the detrimental effect of neighbouring misaligned grains to high extent; however, this effect of misalignment will not be eliminated fully.

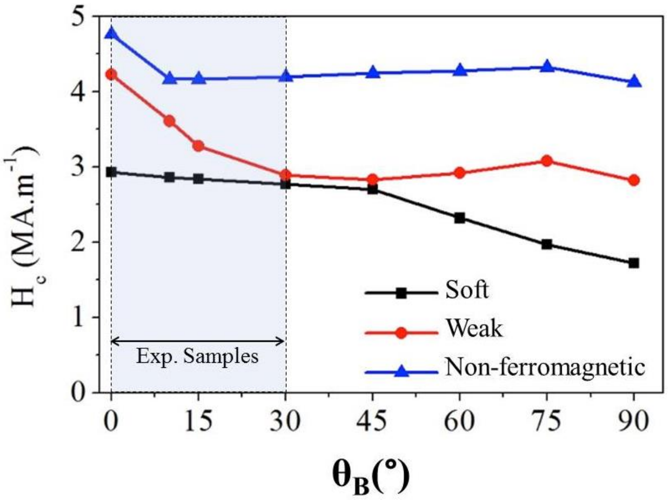

Figure 7.18 H_c of grain A (aligned to field) in the two-grain models at different θ_B angles (misalignment of grain B) with different GB phases.

The comparison of H_c values of grain B at different θ_B and GB phases indicates that GB phases also affect misoriented grains (fig. 7.19a). For example, H_c of grain B in models with non-ferromagnetic and weak GB phases were slightly higher than H_c of models with soft GB phases. Fig. 7.19b shows H_c values of single misoriented grain with no surrounding GB phases. The comparison between H_c values of grain B and the single misoriented grains indicates that soft GB phases lead to lower H_{ext} reversal of misoriented grains. On the other hand, the reversal of grain B with weak and non-ferromagnetic GB phases was closer to the H_{ext} values of misoriented grains with no surrounding GB phase. This indicates that grain A had no significant effect on H_c of grain B with these two types of GB phases.

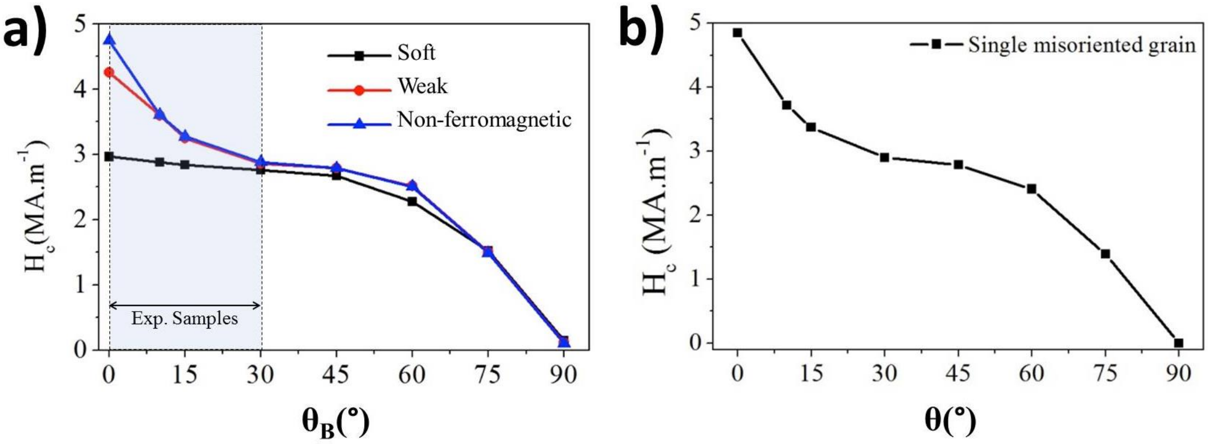

Figure 7.19 H_c of (a) grain B in the two grains models at different θ_B angles with different GB phases. (b) H_c of single grain at different alignment angles with H_{ext}.

The pole figures of Dy-free and Red-Dy magnets revealed dispersion angles (ϕ) 15° and 30°, respectively (see Chapter 6). This is likely to reduce H_c of these grains to lower values compared to H_c of perfect alignment. Previous reports suggested that reducing the grain size will lead to reductions in the magnetostatic interactions between grains [48, 87]. The reduction of grains' size means direct-exchange will be more dominant [48]. The formation of non-magnetic GB phases is likely to decrease this direct-exchange more effectively as was concluded by this study. Combining these two approaches could provide further improvements to H_c of Nd-Fe-B magnets.

7.6 The grain boundary phases effect in grains of different sizes

So far, we have only considered grains of the same size and shape. Electron microscopy analysis in Chapter 5 revealed that these features are different and related to the processing conditions of magnets. In this section, the ability of GB phases to eliminate the effect of grain size and its distribution in sintered Nd-Fe-B magnets is assessed using micromagnetic modelling.

Microscopy analysis of the microstructure of Nd-Fe-B magnets (see §6.7) revealed that adjacent grains might have significant differences in their sizes. The interaction between grains with different sizes could be very different compared to the previous uniform size grains (in §7.5). Ramesh *et al* suggested that larger size grains act as nucleation sites for reversed domain walls in magnetically exchanged grains [55]. However, the EDX analysis (see §6.4) revealed high Fe at.% at intergranular regions, which will favour a ferromagnetic exchange between grains across GB phases. Here, models that consisted of two adjacent $Nd_2Fe_{14}B$ grains (A and B) separated by a 2 nm grain boundary phase were used (fig. 7.20). The diameter of grain A (d_A) was set to be 100 nm always, while the diameter of grain B (d_B) was defined to be 50, 100 or 200 nm. This means grain B was either smaller, or equal or larger than grain A at different simulations. The angle between the anisotropy direction of grain A and H_{ext} (θ_A) was set to be 0° always, while the angle between H_{ext} and anisotropy direction of grain B (θ_B) was varied between 0-90°. The magnetic properties of the GB phases were the same as the values used earlier with strong, weak or non-ferromagnetic magnetic characteristics (see §7.5). The magnetic parameters of $Nd_2Fe_{14}B$ phase were the same as the values used earlier in §7.3. The hysteresis loops of these models were obtained by varying H_{ext} between 10T and -10T with a rate of (± 50 mT.ns^{-1}).

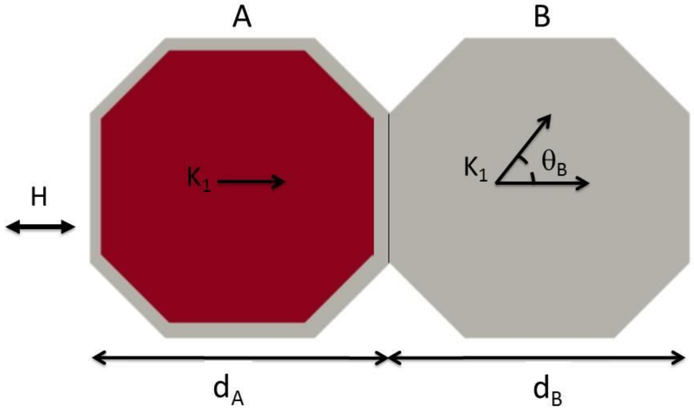

Figure 7.20 A schematic sketch of the two-grain model.

The modelled demagnetisation curves (fig. 7.21a) and magnetisation configurations of the two-grain models revealed that when d_B is 50 nm; the magnetisation of grain B (the smallest) switched earlier than the magnetisation of grain A (the largest) when GB is soft and θ_B=30° (ϕ of Red-Dy sample). This is a direct result of its grain B's misalignment from H_{ext} and its lower volume. The reversed domain walls propagated to the neighbouring grain A leading to full demagnetisation at H_{ext}=-3.14 MA.m^{-1}. When d_B=200 nm, reversed domains nucleated at grain A earlier than misaligned grain B, as shown in fig. 7.21c. This indicates that the larger size of grain B (hence stronger magnetic moment) led to an early reversal of grain A even though it has zero misalignment to H_{ext}. This was followed by the propagation of reversed domains to grain B leading to its full demagnetisation at H_{ext}=-2.47 MA.m^{-1}. These configurations indicated that the nucleation of reversed domain at adjacent $Nd_2Fe_{14}B$ grains separated by magnetically soft GB phases show a stronger dependence on their size. The misalignment of relatively larger size grains leads to an early magnetisation reversal of field-aligned neighbouring grains.

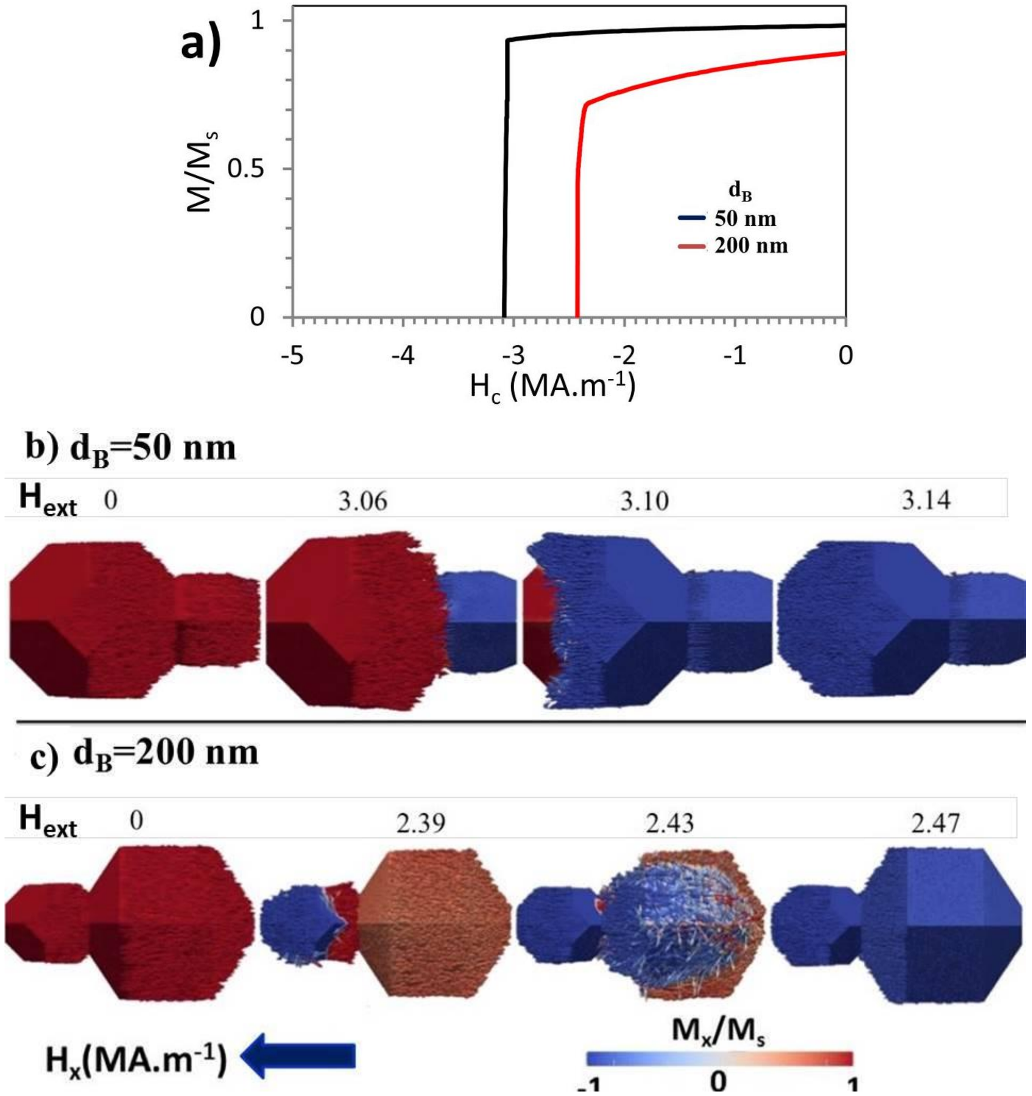

Figure 7.21 (a) The modelled demagnetisation curves and screenshots of the magnetisation configurations of the two-grain models separated by soft GB phases with θ_B=30° and (b) d_B=50 nm and (c) d_B=200 nm. The number above each screenshot represents the value of H_{ext} in $MA.m^{-1}$.

Figure 7.22a shows H_c of the two-grain models separated by soft GB phases. When both grains are aligned to H_{ext} direction (θ_B=0°), H_c increases when d_B decreased from 200 to 50 nm but decreased for θ_B>0°. Introducing magnetically weak GB phases improved H_c in all the three size of grain B at θ=0° (fig. 7.22b). However, H_c of these models dropped with increasing θ_B to higher values than 0°. For example, H_c of models with soft GB phases and θ_B=45° was observed to drop to 40% of its initial values (at θ_B=0°). H_c change in these models indicates that the demagnetisation behaviour of adjacent grains with soft GB phases shows a strong dependence on their grain sizes. Introducing magnetically weak GB phases improved H_c slightly at low θ_B (<30°). However, the effect of the size of adjacent grains was still noticeable even with weaker exchange at GB phases.

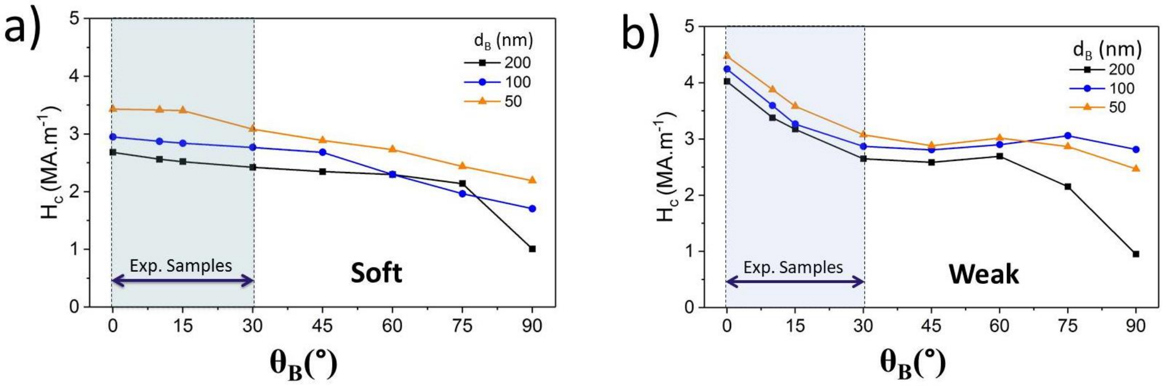

Figure 7.22 A comparison between H_c of two-grains model with magnetically (a) soft and (b) weak GB phases at different d_B and θ_B values

Non-ferromagnetic GB phases were introduced between grain A and B to provide further assessment to the ability of GB phases to eliminate the effect of grain size variation. The magnetisation configurations of two-grain models with non-ferromagnetic GB phases at θ_B=30° are shown in fig 7.23. When d_B= 50 nm, the misoriented grain (grain B) have an earlier magnetisation reversal at low H_{ext} of 3.09 $MA.m^{-1}$. The aligned grain A preserved some of its magnetisation until higher H_{ext} of 4.58 $MA.m^{-1}$, which is the field where a full magnetisation reversal of the two grains was achieved. These configurations suggest that reversed domain walls are hindered at the non-ferromagnetic GB when nucleated at a smaller size grain. When d_B=200 nm, grain B also switched at a H_{ext} of 2.67 $MA.m^{-1}$, earlier than grain A, due to its misorientation from H_{ext} (fig. 7.23b). Grain A, on the other hand, does not reverse until H_{ext} of 3.93 $MA.m^{-1}$ was achieved. This is also a strong indication that reversed domain walls were hindered at the non-ferromagnetic GB phase of grain A.

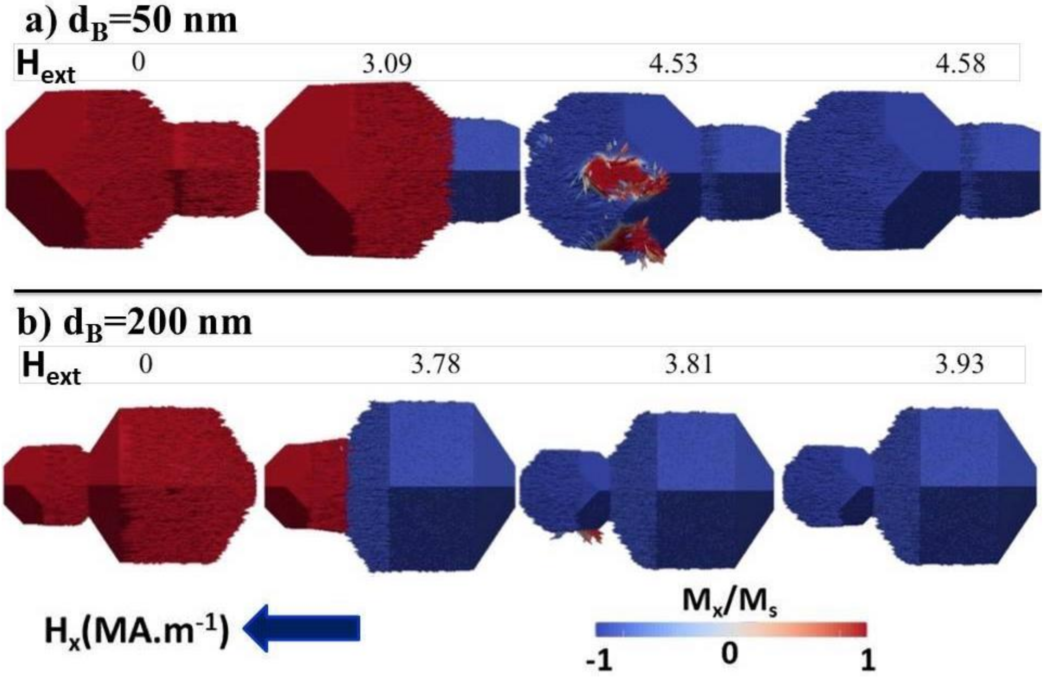

Figure 7.23 The magnetisation configurations of the two grains model separated by non-ferromagnetic GB phases with θ_B=30° where (a) d_B=50 nm and (b) d_B=200 nm. The number above each screenshot represents the value of H_{ext} in MA.m^{-1}.

H_c of the two-grain model with non-ferromagnetic GB phases at different θ_B had higher values than previous models when d_B=50 nm (fig. 7.24). The misorientation of grain B with d_B=50 nm size had a less significant effect on H_c compared to models with soft and weak GB phases. The value of H_c showed a small reduction θ_B>0°. When d_B=100 nm, the effect of grain B was more prominent at low misorientation angles (θ_B<45°). For example, H_c of the whole model at θ_B of 30° dropped to about 35% of its initial value. At θ_B>45°, H_c appeared to be independent of θ_B. The effect of grain B size was more noticeable with d_B=200 nm where H_c of these models decreased with increasing θ_B. For example, H_c dropped to 40% and 78% of its initial value at θ_B of 45° and 90°, respectively.

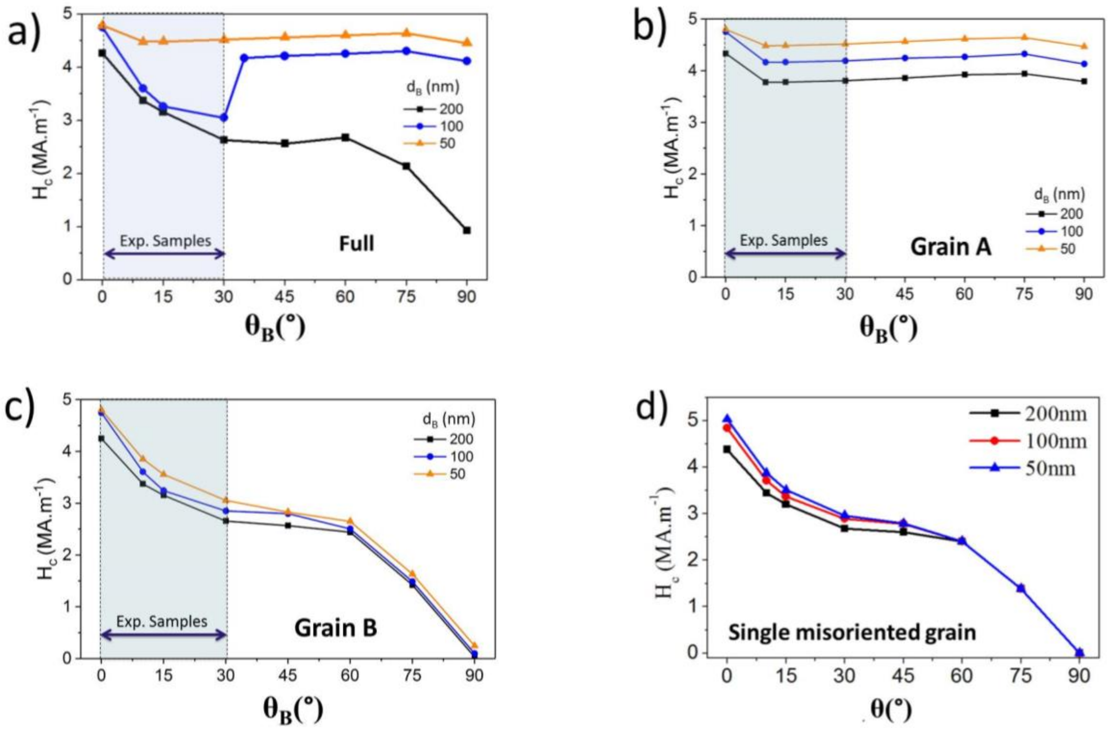

Figure 7.24 (a) A comparison between H_c of (a) two-grain model, (b) grain A and (c) grain B in models with non-ferromagnetic GB phases at different d_B and θ_B values. (d) H_c of single grain model at different d and θ values.

H_c values of grain A in two-grain models with non-ferromagnetic GB phases showed a lower response to θ_B, which suggests that non-ferromagnetic GB phases reduced the effect of the misorientation of the adjacent grain (fig. 7.24b). However, the effect of the adjacent grain B was still existent and represented by a slight drop in H_c with increasing θ_B to >0°. In addition, the difference in H_c of grain A (which has a d_A=100 nm always) with different values of d_B indicates that the size effect is not eliminated entirely. This effect of non-magnetic GB phases may be used to reduce the effect of grain size variation, which is characteristic of commercial sintered Nd-Fe-B magnets.

On the other hand, H_c values of grain B (fig 7.24c) suggested that its reversal was an individual event at all values of d_B, which is represented by the difference in the H_c of this grain compared to grain A. This individual demagnetisation behaviour of grain B was confirmed by comparing it to the behaviour of single grains with similar misorientation angles to H_{ext} (fig. 7.24d). A minor improvement is observed at when d_B=50 and 100 nm, which indicates that grain A delayed the switching of grain B with smaller or equal grain size with non-ferromagnetic GB phases. This behaviour suggests that the perfect alignment of larger size grains is essential for improved H_c in Nd-Fe-B magnets since they can delay the reversal of smaller-size adjacent grains. However, this delay is only short and the switching of reversed domains at lower H_{ext} is inevitable.

7.7 Modelling the grain size distribution of sintered Nd-Fe-B magnets

So far, our micromagnetic modelling suggested that combining improved grain alignment and the formation of non-ferromagnetic GB phases could reduce the effect of variation in the grain size of Nd-Fe-B magnets. Further assessment of this approach is performed by simulating multigranular models with a lognormal GSD that is similar to the size distribution of the experimental samples (see §6.7). A 3D model with a wide GSD separated by either magnetically soft or non-ferromagnetic exchange energy (fig. 7.25a) that consists of 402 grains with diameters varied between 20-50 nm was used. The behaviour of this (close to experimental samples) model was compared to a theoretical model with narrower GSD (fig. 7.25b), which consists of 116 grains with diameters around 50 nm. The comparison between grain volumes of both narrow and wide GSD models is shown in fig. 6.25c. Both models were defined to have an edge length of 300 nm and meshed using the regular method (see §7.2) with surface and interior mesh sizes smaller than 5 and 25 nm, respectively. The ranges of the angular distribution of grains anisotropy (ϕ) to H_{ext} were defined to be similar to angular dispersion of the Dy-free magnet (ϕ =15°) and the Red-Dy magnet (ϕ =30°). These two models were compared to a near-fully aligned magnet with ϕ =1°.

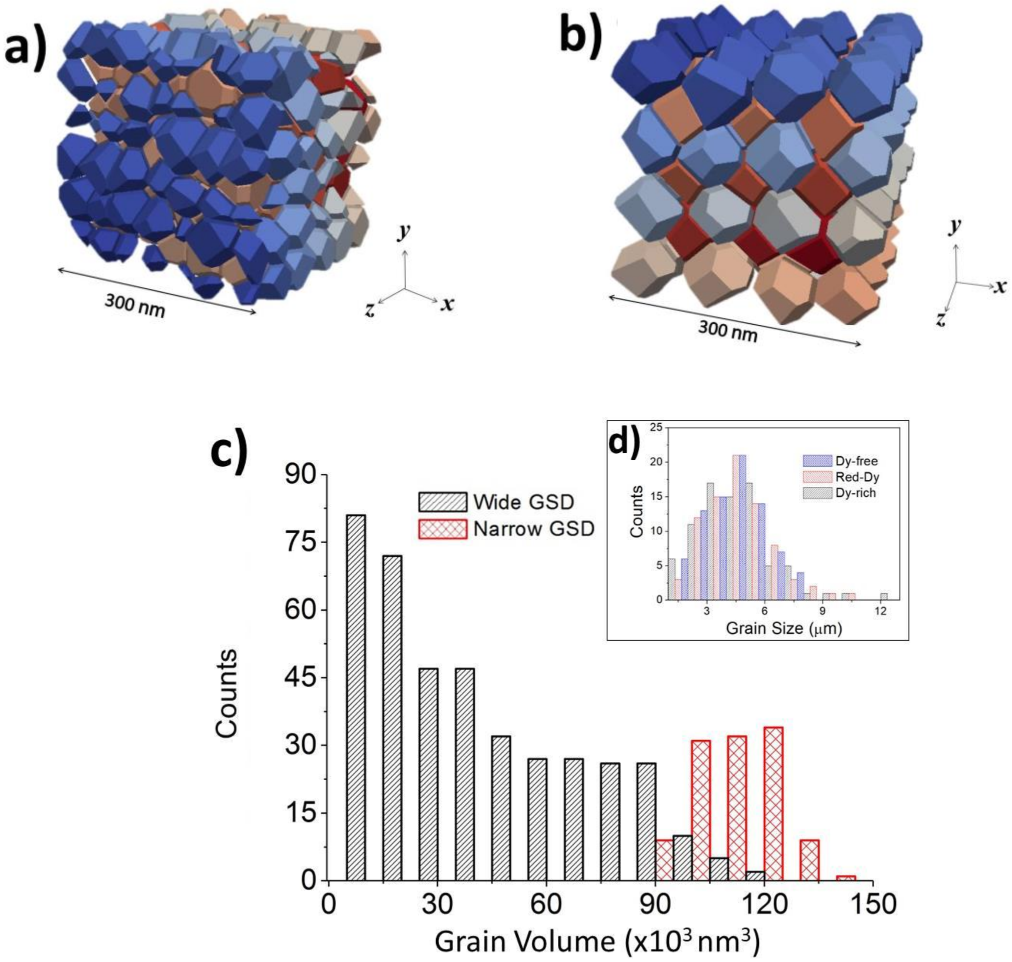

Figure 7.25 A screenshot of 3D models with (a) wide and (b) narrow grain size distribution. (c) Histograms of the grain volumes for both models. (d) Histograms of grain size distribution in experimental samples.

The models were simulated to have either strong (A=12.1 pJ.m^{-1}) or weak (A=1.0 fJ.m^{-1}) intergrain exchange stiffness constant. The magnetic properties of $Nd_2Fe_{14}B$ phase were the same as the values used earlier in §7.3. The magnetostatic energy was turned off in order to speed up the simulations. In addition, H_{ext} was applied parallel to *x*-axis and varied between 10T and -10T with a rate of 280 mT.ns^{-1}.

H_c of models with wide GSD shows a strong dependence on ϕ when grains are magnetically exchanged (fig. 7.26). This dependence is represented by H_c of 4.91 MA.m^{-1} with ϕ=1° compared to 4.6 MA.m^{-1} and 3.95 MA.m^{-1} for models with ϕ=15° and ϕ=30°, respectively. The model with ϕ=30° also showed a drop in M_r to lower values than the other two models. These reduced values of H_c and M_r are a direct consequence of misalignment of grain anisotropy from H_{ext}. The demagnetisation curves of strongly coupled magnets had a square shape, which indicates that reversed domains propagate rapidly to neighbouring grains once nucleated. The square shape of these curves is similar to the demagnetisation curves of experimental samples presented in earlier in chapter 5 (see §5.2).

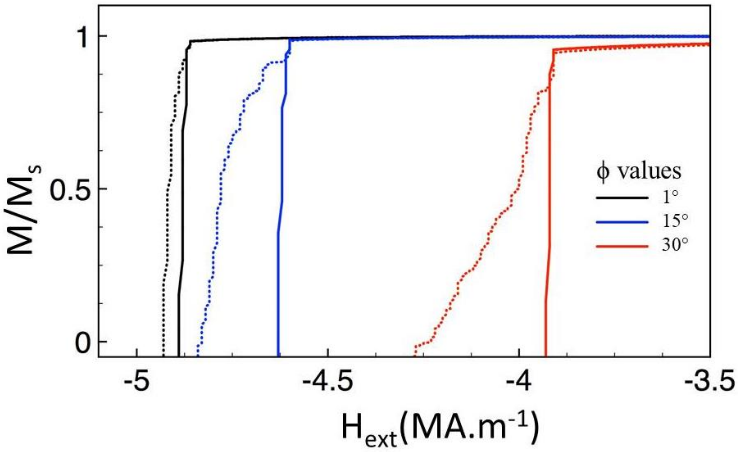

Figure 7.26 The modelled demagnetisation curves of the grain size distribution (GSD) models with strong (full lines) & weak (dotted lines) exchange at GB regions.

The values of H_c improve significantly with reduced exchange between grains, (dotted lines in fig. 7.26). For example, H_c improves by 15% and 20% of their initial values with $\phi=15°$ and 30°, respectively. This is compared to 7% improvement in H_c for the model with $\phi=1°$. These improvements in H_c are attributed to the hindering of the reversed domain walls that were nucleated at misoriented grains. The demagnetisation curves in the case of weak exchange at GB phases have many steps, which indicate a gradual grain-by-grain magnetisation reversal as opposed to the sharp reversal in strongly exchange-coupled models. For example, the magnetisation reversal in strongly exchanged model with $\phi=15°$ starts at $H_{ext}=4.61$ MA.m^{-1} (fig 7.27a). The reversed domain walls cascade rapidly to neighbouring grains leading to the full demagnetisation of the sample at 4.74 MA.m^{-1}. Even though in the weak exchange model the magnetisation reversal started at H_{ext} values similar to the strongly exchanged case (4.61 MA.m^{-1}), the reversal proceeds more gradually (fig. 7.27b) and full demagnetisation of the sample was achieved at 5.13 MA.m^{-1}.

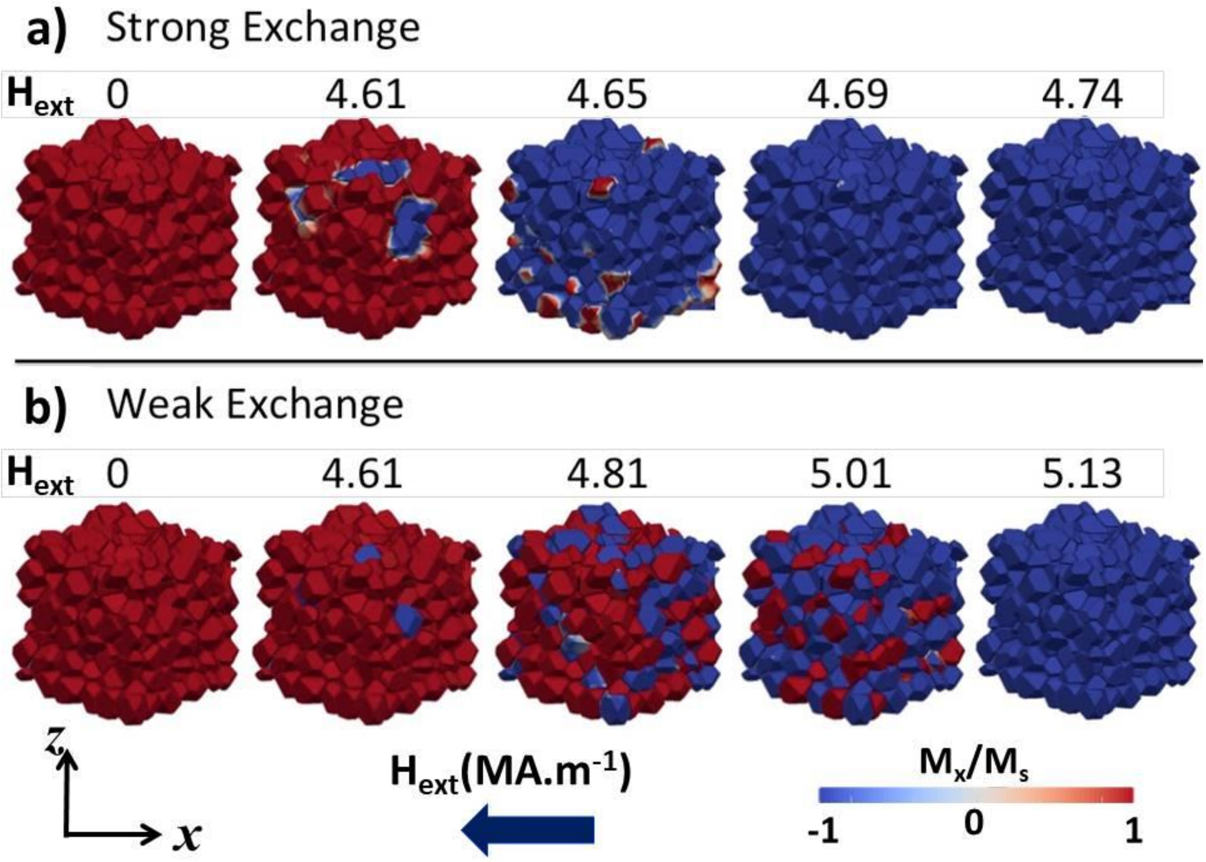

Figure 7.27 Screenshots of the magnetisation configurations of the wide GSD model with at ϕ=15° and (a) strong exchange and (b) weak exchange. The number above each screenshot represents the value of H_{ext} in MA.m^{-1}.

H_c of the wide GSD models indicated that the demagnetisation of main phase grains depends strongly on ϕ of grains. To assess the effect of narrower grain size variation, models with narrower GSD were simulated and their H_c showed the same dependence on ϕ (fig. 7.28) that was observed in strongly coupled wide GSD models (fig. 7.26). In addition, the introduction of weak coupling between grains also improved H_c of these models at all values of ϕ and a grain-by-grain magnetisation reversal was also observed.

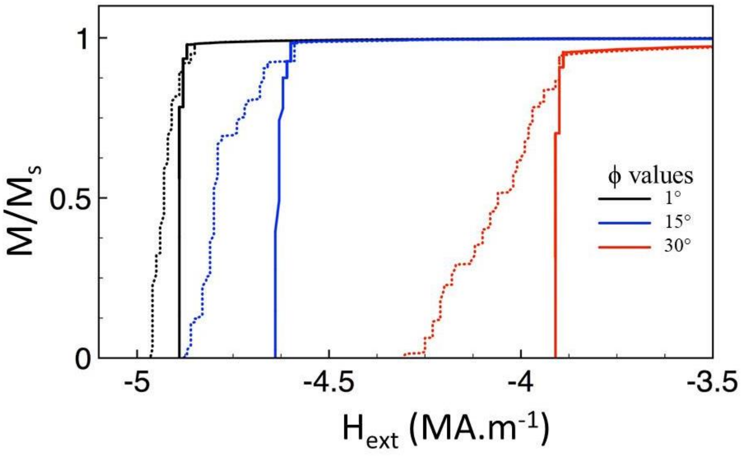

Figure 7.28 The modelled demagnetisation curves of the narrow GSD model at different with strong (full lines) & weak (dotted lines) exchange at GB regions.

The micromagnetic modelling of wide and narrow GSD models revealed that the highest improvement of BH_{max} could be achieved by decreasing ϕ (fig. 7.29). However, the rate of this improvement is different at each type of GSD. For example, BH_{max} of strongly-exchanged wide GSD increased from 510.6 kJ.m^{-3} to 515.7 kJ.m^{-3} with decreasing ϕ from 30° to 15°. BH_{max} of narrow GSD is lower than wide GSD at ϕ=30°, which suggests that relatively larger grains in highly misoriented samples can be beneficial to delay smaller grains reversal. This effect can be utilised by ensuring that relatively larger grains have a stronger alignment to H_{ext} (smaller ϕ).

Introducing weak exchange energy at GB regions produced no significant difference in BH_{max} of both wide and narrow GSD models, which is a direct consequence of gradual grain-by-grain demagnetisation of main phase grains. Although weak exchange increased H_c but with no significant change in M_r. In all models, the highest BH_{max} is observed in narrow GSD models with ϕ=1° but BH_{max} of both models decreased to ~1% of the initial values with increasing ϕ from 1° to 30°.

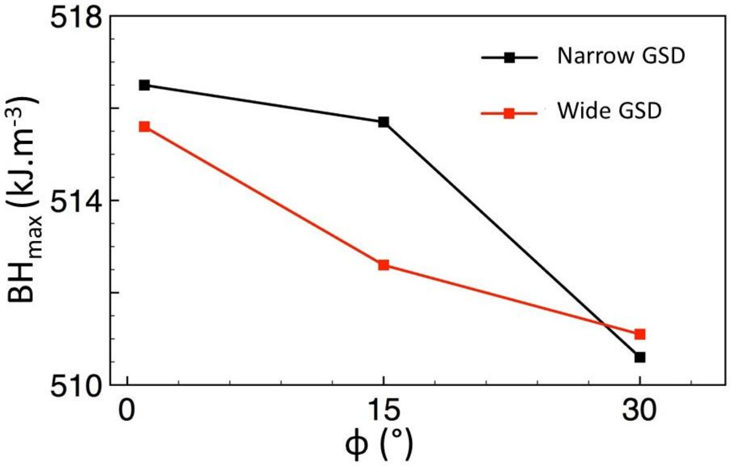

Figure 7.29 A comparison between BH$_{max}$ values of wide and narrow GSD models. Both strong and weak exchange produced identical BH$_{max}$ values.

On the other hand, the comparison between H_c of wide and narrow GSD models revealed that H_c improvements could be achieved through the production of magnets with narrow size distribution, weak exchange coupling between grains and better alignment of grains (fig. 7.30). The strongest improvement of H_c comes from lower values of ϕ. For example, H_c increases to about 25% of its initial value with decreasing ϕ from 30° to 1°. The introduction of weak exchange between grains offers ~1% increase in H_c at ϕ=1°, 5% at ϕ=15° and 8% at ϕ=30°. Finally, an extra ~1% could be possible by refining GSD distribution to narrower size distributions.

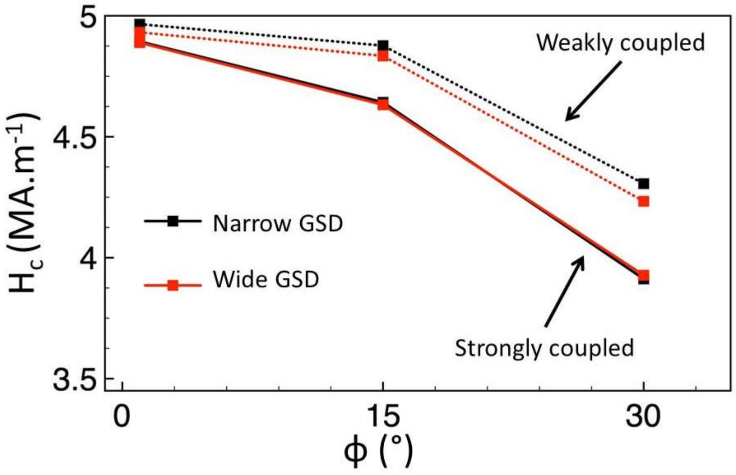

Figure 7.30 H_c comparison between wide and narrow GSD with either a strong exchange (full lines) & weak (dotted lines).

7.8 Conclusions

A micromagnetic modelling approach was developed to study the role of intergranular phases in sintered Nd-Fe-B magnets. The models were used to study the effect of the composition of intergranular phases on the nucleation of reversed domain walls and the possibility of improving coercivity of $Nd_2Fe_{14}B$ grains through domain wall pinning at intergranular phases. The use of core-shell mesh arrangements with fine surface mesh and coarse interior mesh provided significant savings to the computing capacity and time. For example, the number of elements in fine surface mesh (1.7 nm) models decreased from ~730,000 to ~36,000 elements with increasing the interior mesh size from 1.7 to 10 nm. The coercivity of the models meshed using the extended method showed a strong agreement even at larger mesh sizes.

Micromagnetic simulations revealed that soft-magnetic characteristics of intergranular phases would lead to the generation of reversed domains walls at low values of applied field and hence lower coercivity. This was also observed to allow a rapid propagation of reversed domains from adjacent reversed grains. The formation of weakly magnetic intergranular phases may prevent the early nucleation of reversed domain walls and reduce the magnetic exchange between main phase grains leading to higher coercivity. However, the effect of adjacent grains was still noticeable. The thickness of intergranular phases has an insignificant effect with weak-magnetic nature but it can be detrimental with soft (Fe-like) magnetic properties.

The fabrication of Nd-Fe-B magnets with improved grain alignment offers the most significant increase to BH_{max} compared to other hardening mechanisms, such as grain exchange-decoupling and narrow grain size distributions. While the formation of weakly magnetic intergranular phases provided significant increase to the coercivity, its effect on remanence was found to be insignificant. On the other hand, the narrow size distribution of grains can be beneficial for coercivity and BH_{max} only with improved alignment of grains. A large alignment dispersion of grains leads to lower coercivity regardless of the grain size distribution and the nature of intergranular phases. These insights can be used to design and fabricate sintered Nd-Fe-B magnets with improved performance at room temperature.

8. Modelling the Internal Structure of $Nd_2Fe_{14}B$ Grains

8.1 Introduction

This chapter describes micromagnetic modelling of Dy-rich shells that were produced by grain boundary diffusion processes in Nd-Fe-B magnets and the effect of twinning in $Nd_2Fe_{14}B$ grains.

8.2 Modelling grain boundary diffusion processes

The distribution of Dy concentration in Red-Dy and Dy-rich magnets was revealed in Chapter 5 to exist only in some $Nd_2Fe_{14}B$ grains across the microstructure but not at the grain boundary regions. This Dy distribution is different from reported samples [9] and it was accompanied in the Red-Dy and Dy-rich samples by an unexpected low H_c compared to Dy-free sample (see fig. 5.1). These observations suggest that controlling Dy additions and the microstructure is necessary to achieve the H_c increase expected from the partial replacement of Nd in $Nd_2Fe_{14}B$ phase with Dy. In addition, the higher H_c of Dy-free and Red-Dy samples compared to Dy-rich sample suggests that maintaining an acceptable H_c with lower additions of Dy is possible, which will have a significant impact on the production cost.

The principles and the use of grain boundary diffusion (GBD) processes in sintered Nd-Fe-B magnets to reduce Dy additions were introduced in §3.6.3. The processed bulk magnet benefits from the diffusion of Dy-coating into the intergranular regions during heat treatment at temperatures higher than 685°C, which lead to the formation of Dy-rich shells at the boundaries of main phase grain (fig. 8.1) [38]. The replaced Nd is discharged to the intergranular regions leading to increased rare earth (RE) concentration at these areas [38, 65]. Significant improvements in H_c of GBD samples were reported with negligible drop in M_r [38, 108]. This H_c increase was accounted to two mechanisms: the formation of the Dy-rich shell and the increased magnetic decoupling between main phase grains caused by discharged Nd [38, 63, 65, 108]. In addition, these samples indicated that the lower M_s of the Dy-rich shell has insignificant effect on the M_r of the processed magnet.

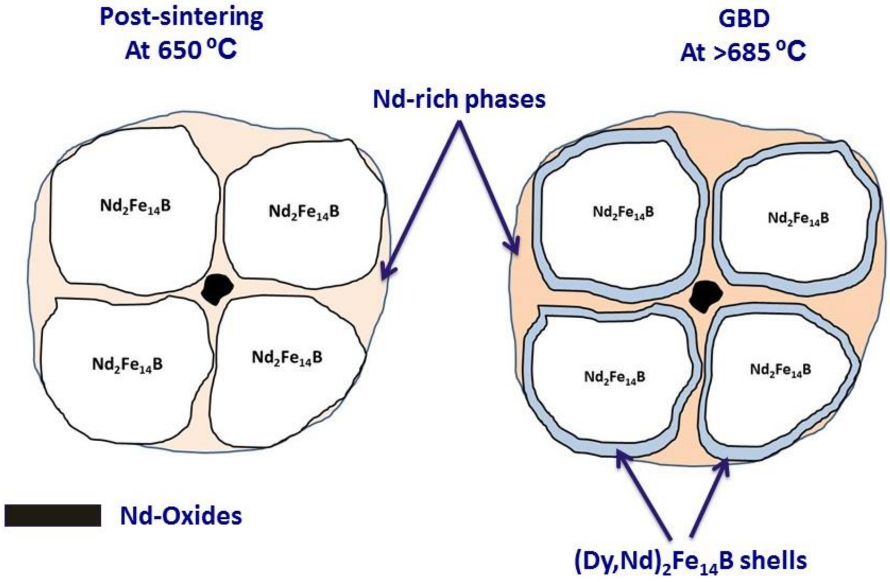

Figure 8.1 An illustration of the main features of $Nd_2Fe_{14}B$ grains after post-sintering (PSA) and grain boundary diffusion (GBD) processes.

Previous electron microscopy analysis revealed a graded diffusion of Dy in the interior of the bulk GBD samples and also a graded diffusion of Dy in $Nd_2Fe_{14}B$ grains of these samples [38, 63]. Dy concentration in the Dy-rich shells was found to be dependent on the sample dimensions, coating direction and the process temperature [63, 65]. Micromagnetic simulations performed by Bance *et al* suggested that Dy-rich shells can eliminate the adverse effect of thin defect layers at main phase grain boundaries [57]. Oikawa *et al* suggested a linear increase of H_c with increasing Dy at.% in shells [72]. However, it is important to understand the main source of H_c increase in GBD samples, which is essential to specify the optimum temperature, duration and sample thickness for GBD processes. In this study, the effect of Dy-rich shells thickness, Dy concentrations and diffusion coefficients were modelled as an attempt to assess the role of Dy-rich shells in GBD samples. This was followed by using micromagnetic modelling to compare the performance of as-sintered and GBD sample.

8.2.1 The role of Dy-rich shells thickness and composition

Dy diffusion in $Nd_2Fe_{14}B$ grains follows Fick's law of diffusion [65], which predicts a concentration change over time that can be represented by:

$$\frac{\delta c(x,t)}{\delta t} = D_c . \frac{\delta^2 c(x,t)}{\delta x^2} \tag{8.1}$$

where c is the concentration, *t* is time, D_c is the diffusion coefficient and *x* is the position. The Grube solution for Fick's law in the case of infinite solids is represented by [65]:

$$c(x,t) = C_{surface} - (C_{surface} - C_{core}) \cdot \mathrm{erf}\left(\frac{x}{\sqrt{4D_c t}}\right) \tag{8.2}$$

where $C_{surface}$ and C_{core} are the concentrations at surface and core of system, respectively (fig. 8.2). In the case of GBD sample, $C_{surface}$ and C_{core} are Dy concentrations at the Dy-rich surface and the centre of $Nd_2Fe_{14}B$ grains, respectively.

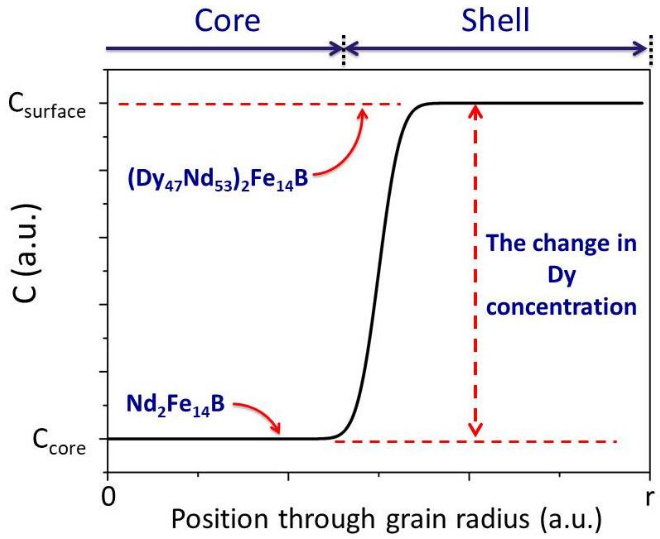

Figure 8.2 The graded concentration of Dy inside diffused $Nd_2Fe_{14}B$ grain where r=outer radius.

D_c values were reported in previous work to have significant difference with different processing conditions, duration, coating and initial elemental composition of the processed magnet (table 8.1) [65, 108].

Table 8.1 Diffusion coefficients of GBD samples processed in different conditions.

D_c (cm^2/s)	T (°C)	Duration (hours)	Coating	Comments	Ref
2.9×10^{-12}	1050	5	-	Interface of Dy -free & -rich samples	[65]
2.5×10^{-9}	900	6	Dy powder	-	[65]
8.45×10^{-7}	900	1.5	Dy foils	Dy-free magnet	[59]
1.11×10^{-6}	900	10	Dy foils	Dy-rich magnet	[59]

Here, we have attempted to simulate the role of Dy-rich shells in grain boundary diffused samples by considering in our models the graded diffusion of concentration. Single grain models with a truncated octahedron shape and 400 nm diameter were meshed with a regular mesh (<3.7 nm mesh size) across its surface and interior. The magnetic properties of each element were defined according to the position (*x*) of its centroid inside the grain interior (see equation 8.2). This was achieved by assuming that the magnetic properties of an intermediate phase between $C_{surface}$ and C_{core} were a linear function of C. $C_{surface}$ was represented by an optimum $Dy_{47}Nd_{53}Fe_{14}B$ phase with magnetic parameters K_1=5.17 MJ.m^{-3}, $\mu_0 M_s$= 1.15T [57] and A_{ex}= 12.1 pJ.m^{-1} [101] at room temperature. C_{core} was assigned the magnetic properties of $Nd_2Fe_{14}B$ phase for which K_1=4.5 MJ.m^{-3}, $\mu_0 M_s$= 1.61T, A_{ex}= 12.1 pJ.m^{-1} at room temperature [101]. The concentration distribution across the models of this study was calculated using D_c=8.45x10^{-7} cm.s^{-1} and *t*=1.5 hours [59]. This value of D_c describes an observed diffusion of Dy in GBD samples. The applied field (H_{ext}) was always parallel to K_1 direction of grains and the hysteresis loops were modelled by changing H_{ext} at a rate of ±50 mT.ns^{-1} from +10T to -10T.

First, the effect of Dy-rich shells thickness on H_c and M_r of GBD samples was studied. This was achieved by simulating single grain models with different shell thicknesses (fig. 8.3a). The shell thickness was represented by the area with any Dy content. Five models with shell thickness (t) of 20, 40, 60, 80 and 100 nm were used and compared to a grain with no Dy-rich shell (t=0 nm). Fig. 8.3b shows the transition from $C_{surface}$ to C_{core} along the grain radius for each case.

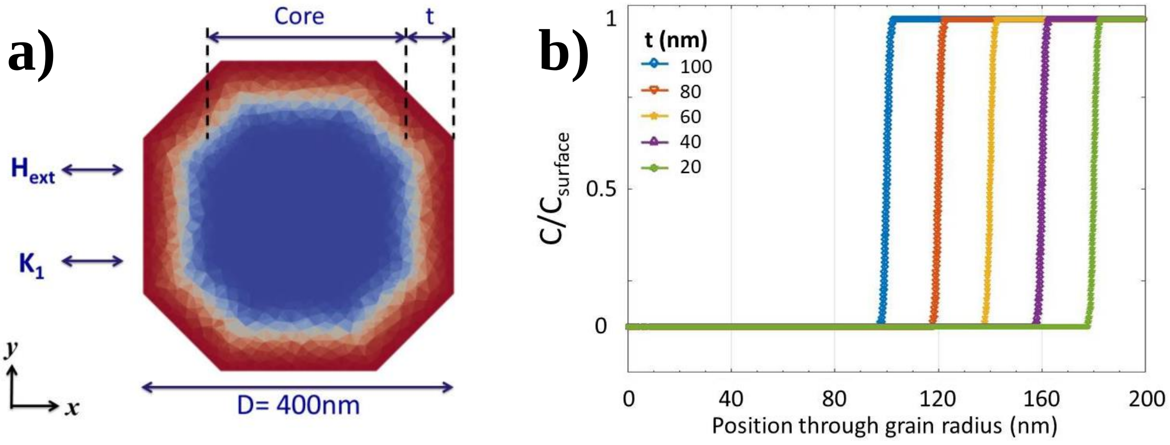

Figure 8.3 (a) A cross-section of the 400 nm models used to simulate GBD processes. (b) The Dy concentration change along the grain radius

The modelled demagnetisation curves (fig. 8.4a) show a gradual increase in H_c with increasing shell thickness in GBD samples compared to the modelled Dy-free sample (t=0 nm), while M_r shows a gradual decrease with increasing Dy-rich shell thickness (fig. 8.4a). This H_c increase was approximately 2% at t=20 nm and rises to 7% for t=100 nm (fig. 8.4b). The increase in H_c is a direct result of the larger proportion of the high anisotropy Dy-rich shells, which results from replacing Nd with Dy in the $Nd_2Fe_{14}B$ phase [38].

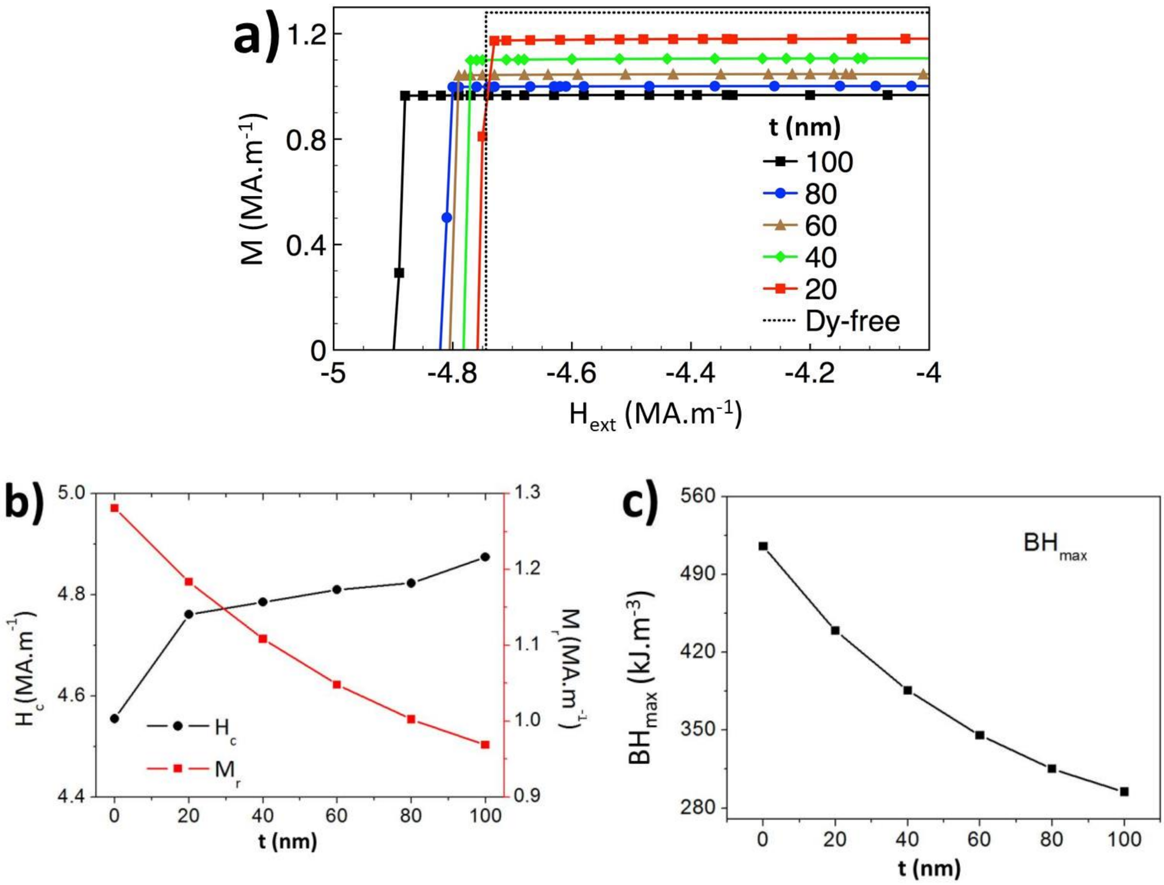

Figure 8.4 The modelled (a) demagnetisation curves, (b) H_c and M_r and (c) BH_{max} of 400 nm grains with different Dy-rich shell thickness

On the other hand, M_r with t=20 nm decreases to about 10% of the value of the Dy-free model and drops to 24% altogether for t=100 nm (fig. 8.4b), which is consistent with the lower M_s of $(Dy, Nd)_2Fe_{14}B$ phase compared to Dy-free $Nd_2Fe_{14}B$ [9]. As a result, BH_{max} of GBD models decrease gradually with increasing shell thickness (fig 8.4c). For example, BH_{max} of models with 100 nm shells drop to about 43% of the initial values (t=0 nm), which is a very significant compared to the improvement in H_c provided by the formation of Dy-rich shells. The magnetisation configurations of single grain models with t=100 nm reveal that the generation of reversed domain walls occurred at H_{ext} of 4.87 $MA.m^{-1}$ (fig 8.5a) and propagated through the rest of the sample to achieve full demagnetisation. The demagnetisation of the Dy-free sample started at H_{ext}=4.53 $MA.m^{-1}$ and achieved full reversal at H_{ext} =4.61 $MA.m^{-1}$ (fig. 8.5b).

Previous magnetic measurements of GBD samples reported a 56% increase in H_c accompanied by a 1% drop in M_r in comparison to as-sintered samples [38]. The increase in H_c in these measurements is much higher than what was predicted by our models keeping in mind that Dy concentration was measured at the shells of these diffused samples to be 3.3 at.% at sample's surface [38]. This is compared to 5.5 at.% at surface of our models, which is represented by $(Dy_{47}Nd_{53})_2Fe_{14}B$ phase. The lower improvements in H_c estimated by our models compared to actual samples could be attributed to 1) smaller grain size in our models and 2) the presence of other hardening mechanisms in experimentally diffused samples. Our models also showed far more significant drop (24%) in M_r compared to actual GBD samples. This discrepancy between the estimated change in H_c and M_r in our models could be attributed to the larger effective size of the Dy-rich shells compared to actual GBD samples. Although this will over-exaggerate the effect of Dy diffusion on M_r, the comparison between M_r and H_c of modelled grains is still useful to understand the performance of GBD samples.

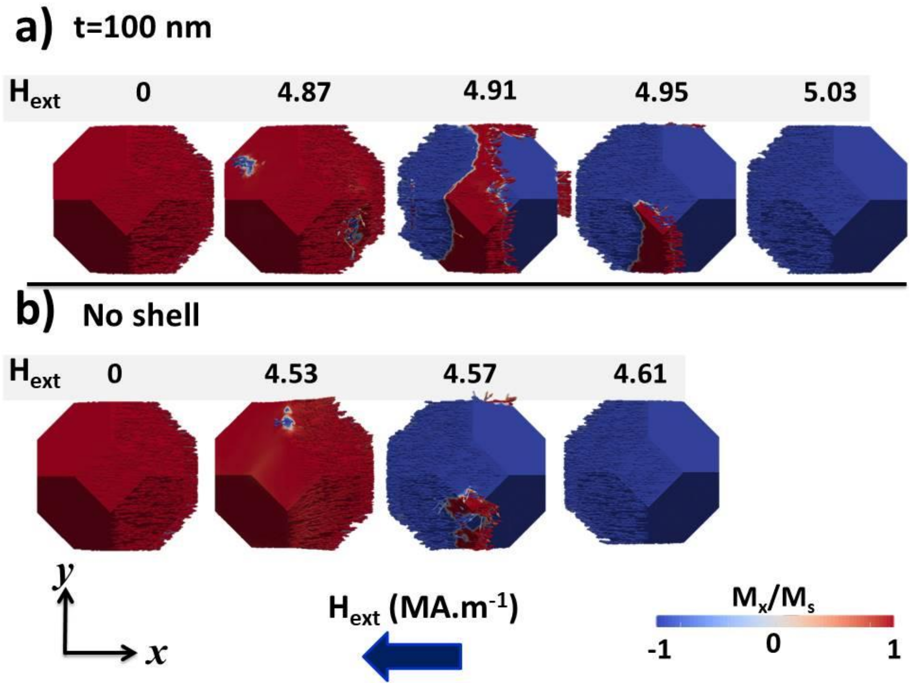

Figure 8.5 The magnetisation configurations of (a) a model with 100 nm shell thickness and (b) a model with no Dy diffusion. The number above each screenshot represents the value of H_{ext} in MA.m^{-1}.

The study described above investigated the shell thickness with assuming that the maximum Dy concentration of at the shell surface is about 5.5 at.%. However, the Dy concentration in shells surface was reported to show a strong dependence on the GBD process conditions, which resulted in a variation in Dy concentration at different depths of the sample [38, 63, 65]. For example, Dy was found to be 3.3 at.% and 1.4 at.% at the surface and centre, respectively, of GBD samples [65]. Here, GBD models with different Dy at.% at shells surface were simulated using 400 nm grains with 30 nm shell thickness. The Dy amount in the $(Dy_xNd_{1-x})_2Fe_{14}B$ phase at the shell is defined to be fractions of x, where x=0, 0.1, 0.2, 0.3, 0.4 and 0.47. The change in $C/C_{surface}$ and hence the magnetic properties across the shell (fig. 8.6) was defined using the same procedure used in the above study. H_{ext} direction was parallel to K_1 of modelled grains and the hysteresis loops were obtained by changing H_{ext} at a rate of ±50 mT.ns^{-1} from +10T to -10T.

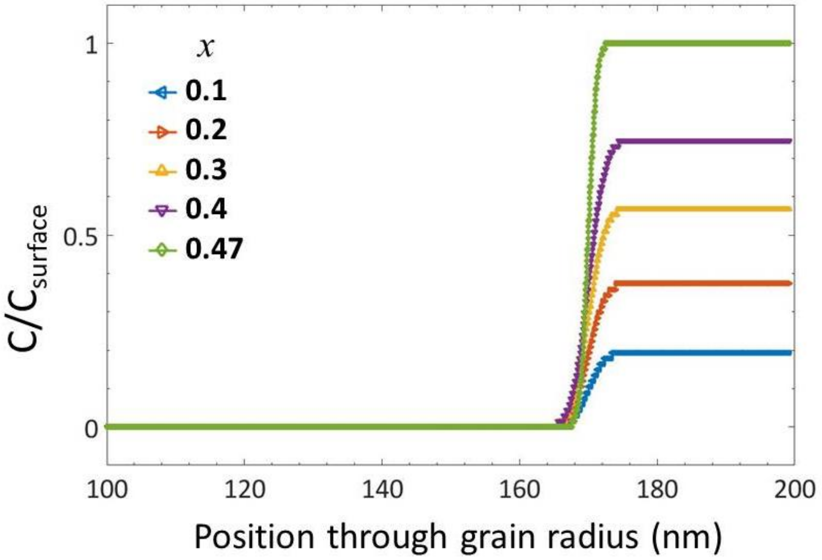

Figure 8.6 Dy concentration profile in 400 nm grains with various shell composition $(Dy_xNd_{1-x})_2Fe_{14}B$.

Modelling Dy at.% at the surface of shells revealed that increasing *x* from 0 to 0.1 increased H_c by 4% of its initial value (fig. 8.7a). This maximum increase in H_c was about 5% at *x*=0.47. On the other hand, M_r drops to 2% at *x*=0.1 and 11% at *x*=0.47 of its initial value. These changes were accompanied by a decrease in BH_{max} with increasing *x* (fig. 8.7b). For example, BH_{max} drops from 515 kJ.m^{-3} to 410 kJ.m^{-3} with *x* increasing from 0 to 0.47. These models revealed that lower Dy at.% in Dy-rich shells will lead to less H_c increase.

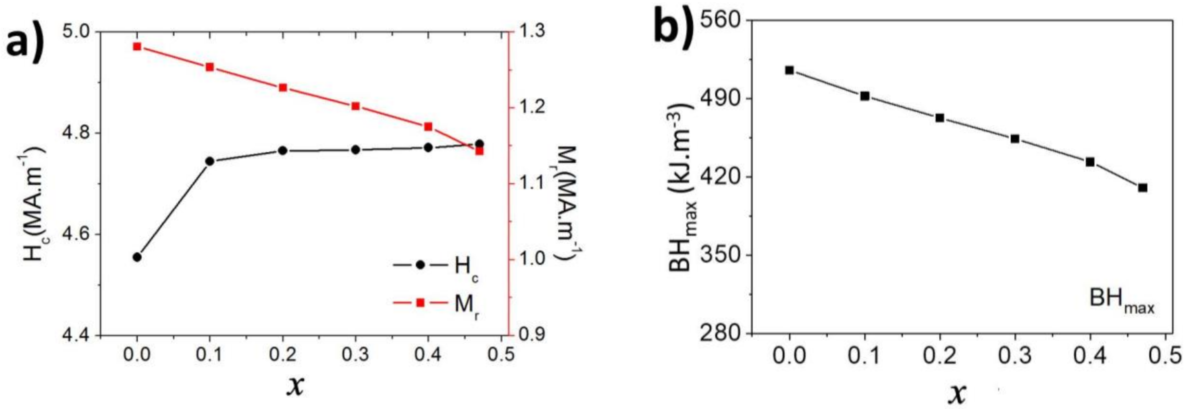

Figure 8.7 (a) H_c and M_r and (b) BH_{max} of GBD models with various shell composition $(Dy_xNd_{1-x})_2Fe_{14}B$.

8.2.2 The effect of diffusion coefficients

Previous reports revealed D_c values of GBD process that are significantly different depending on process conditions (table 8.1). Understanding the role of the distribution of Dy at.% in the shell may reveal whether a graded Dy concentration in shells is more advantageous to H_c and BH_{max} than thin Dy-rich shells with sharp transformation to a Dy-free core. For this purpose, single 400 nm grains were used to simulate models with different D_c values. The values of D_c were defined to be $8.45x10^{-7}$ $cm^2.s^{-1}$ (denoted hereafter as 'graded'), which is obtained from reference [59], and a faster D_c=$1x10^{-4}$ $cm^2.s^{-1}$ (denoted hereafter as 'sharp'). Both models have the same amount of Dy diffusion, which is 20 at.% of the rare-earth (RE) content in the whole sample. These two models were compared to a (Dy, Nd)-Fe-B models (denoted hereafter as Dy-magnet) that has an initial alloy composition with a similar amount of Dy at.% as the graded models (20 at.% of RE) (fig. 8.8). The magnetic properties of the elements at C(x,t) points were defined using the same procedure used earlier (see §8.2.1). The hysteresis loops were modelled by changing the H_{ext} from +10T to -10T at a rate of ±50 $mT.ns^{-1}$.

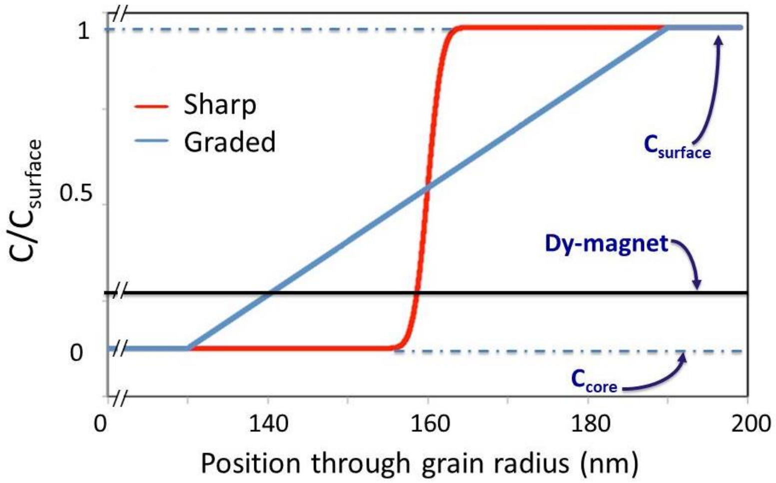

Figure 8.8 Dy concentration change in different sharp, graded and Dy-magnet samples.

The comparison between the demagnetisation curves of graded and sharp models revealed identical values of H_c with ~5% increase and ~14% drop in M_r compared to Dy-free model (fig. 8.9). On the other hand, Dy-magnet that has a uniformly distributed 20% Dy produced higher H_c and M_r compared to diffused (graded and sharp) models. This was estimated by a 10% increase in H_c and 6% drop in M_r compared to Dy-free sample. This behaviour of H_c and M_r resulted to about ~25% reduction in BH_{max} of diffused models compared to 10% decrease in BH_{max} of Dy-magnet model (table 8.2). These models confirmed that graded diffusion of Dy improves H_c compared to Dy-free models but reduces M_r significantly. In addition, a uniform Dy distribution across the sample produced better H_c, M_r and BH_{max} than graded samples using the same amounts of Dy additions. This can be attributed to the lower drop in M_s in the case of Dy-magnet compared to the diffused samples.

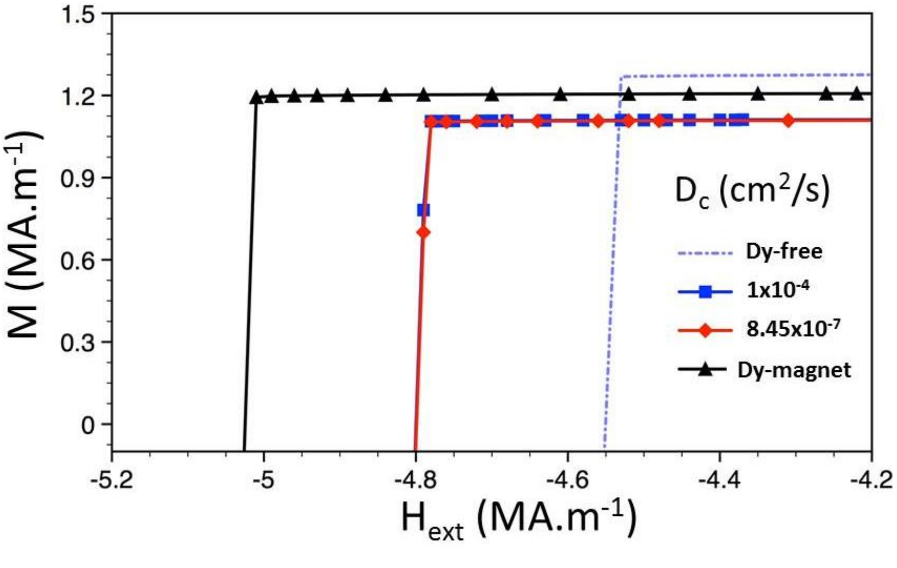

Figure 8.9 Demagnetisation curves of 400 nm models with different D_c values.

The change of H_c and M_r in these models indicates that the distribution of Dy in GBD samples is not achieving the possible increase in H_c expected from Dy additions. Here, our modelling of the diffusion coefficients in Dy-rich shells indicates that further improvements in GBD process is needed in order to supersede the benefits of (Dy, Nd)-Fe-B magnets.

These benefits include, for instance, less-requirement for heat treatment & higher H_c than GBD samples. Our models attempted to represent $Nd_2Fe_{14}B$ grain with Dy-rich shells; however, Dy-rich shells in our models have larger proportions compared to real GBD samples. Future modelling of GBD samples could be improved by using close-to-real grain/shell proportions.

8.2.3 Modelling coercivity improvement in diffused samples

Modelling the role of Dy-rich shell in GBD samples revealed that their contribution to H_c improvements is lower than reported figures [38], which means that other mechanisms are likely to accompany Dy-rich shell in GBD samples. Sepehri-Amin *et al* highlighted the role of the discharged Nd to intergranular regions, which leads to improved exchange decoupling of $Nd_2Fe_{14}B$ grains [38]. The comparison between the impact of Dy-rich shells and non-ferromagnetic GB phases on H_c and BH_{max} can be useful for future GBD processes. It could improve the understanding of most effective mechanism in GBD processes to increase H_c.

In this study, two-grain models that are in contact to each other were used to compare H_c, M_r and BH_{max} of as-sintered and GBD samples. Both grains in the two-grain models have a truncated octahedron shape with a diameter of 200 nm (fig. 8.10). In the as-sintered model, both grains are formed of Dy-free $Nd_2Fe_{14}B$ core surrounded by a shell that represents magnetically soft GB phases, which have μ_0M_s=2.15T & A_{ex}=25 pJ.m^{-1}. The thickness of this grain boundary phase is 2 nm, which is similar to the reported thickness in as-sintered samples (see Chapter 5). The GBD sample consists of grains with Dy-free core and a 20 nm graded diffusion of Dy from the outer surface towards the grain centre with D_c=8.45x10^{-7} cm^2.s^{-1} and *t*=1.5 hours [59]. Each grain in the GBD sample is surrounded by a 4 nm shell that represent non-ferromagnetic GB phases with μ_0M_s=0T & A_{ex}=1 fJ.m^{-1}. A third model was used to represent grains of a sample with a Dy-free core and a 4 nm grain boundary phase but no Dy diffusion. It could represent post-sintering annealed samples with improved GB phases distribution (see §3.6.1) or a GBD sample using Nd or Pr coating where it lead to higher RE content at GB regions only (no shell formation) [64]. This model will be referred to as the 'annealed' model to distinguish it from the other two samples. The shells in the annealed model represent a non-ferromagnetic GB phase with μ_0M_s=0T & A_{ex}=1 fJ.m^{-1}. The magnetic properties of $Nd_2Fe_{14}B$ and $(Dy_{47}Nd_{53})_2Fe_{14}B$ phases have the same values used earlier in §8.2.1. H_{ext} was applied parallel to K_1 of both grains and the hysteresis loops were modelled by changing H_{ext} at a rate of ±50 mT.ns^{-1} from +10T to -10T.

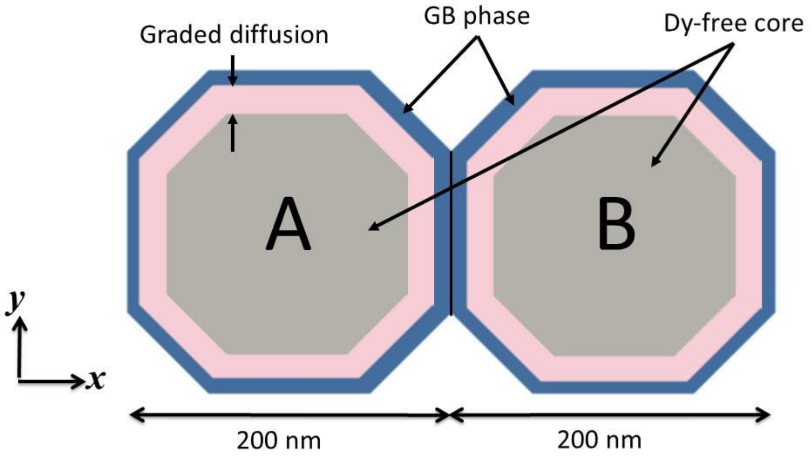

Figure 8.10 A schematic sketch of the two-grain model used to simulate as-sintered, annealed and GBD samples.

The demagnetisation curves of the three models revealed that as-sintered sample had the lowest H_c and the highest M_r compared to the other two samples (fig. 8.11). GBD sample had a 57% increase in H_c compared to the as-sintered model, which was accompanied by a 23% decrease in M_r. This improvement in H_c is close to the previously reported increase in H_c of GBD samples, which can be attributed to the higher K_1 of $(Dy, Nd)_2Fe_{14}B$ phase and the effect of discharged Nd to GB regions that led to non-ferromagnetic exchange between main phase grains. This non-ferromagnetic exchange results in a higher H_c, as was explained in chapter 7. On the other hand, the annealed sample showed a ~50% increase in H_c compared to the as-sintered sample due to the decreased magnetic exchange between main phase grains and was accompanied by a lower drop in M_r than the GBD sample ~12%.

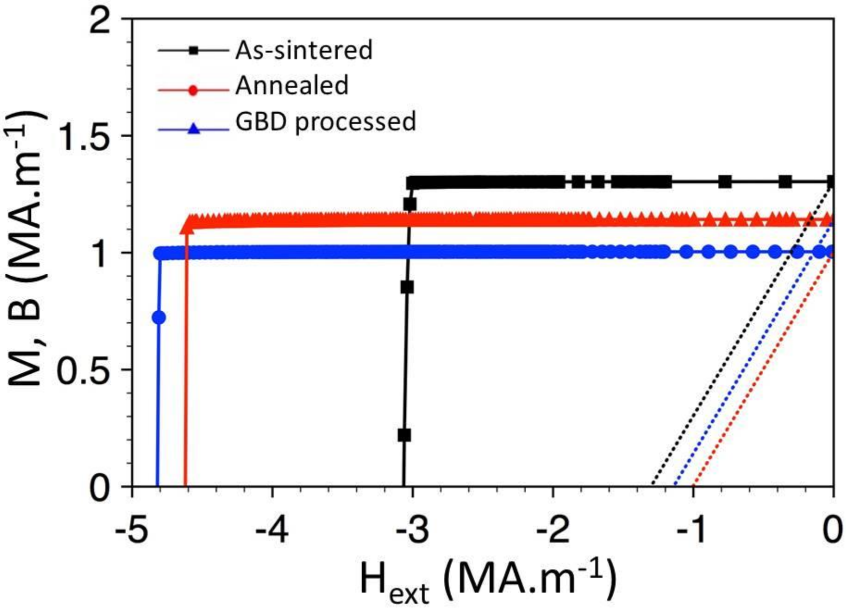

Figure 8.11 The modelled 2nd quadrant of the M-H (full lines) and B-H (dashed lines) loops of the two-grain models.

The observation of the models' magnetisation configurations again revealed magnetisation reversal by reversed domain walls generation and rapid propagation in all cases (fig. 8.12). The magnetic fields at which nucleation occurred reflect the different H_c values. These configurations indicated that non-ferromagnetic GB phases led to higher H_c. Moreover, combining the effect of non-magnetic GB phases with the diffusion of heavy RE elements in $Nd_2Fe_{14}B$ grains has led to further H_c increase.

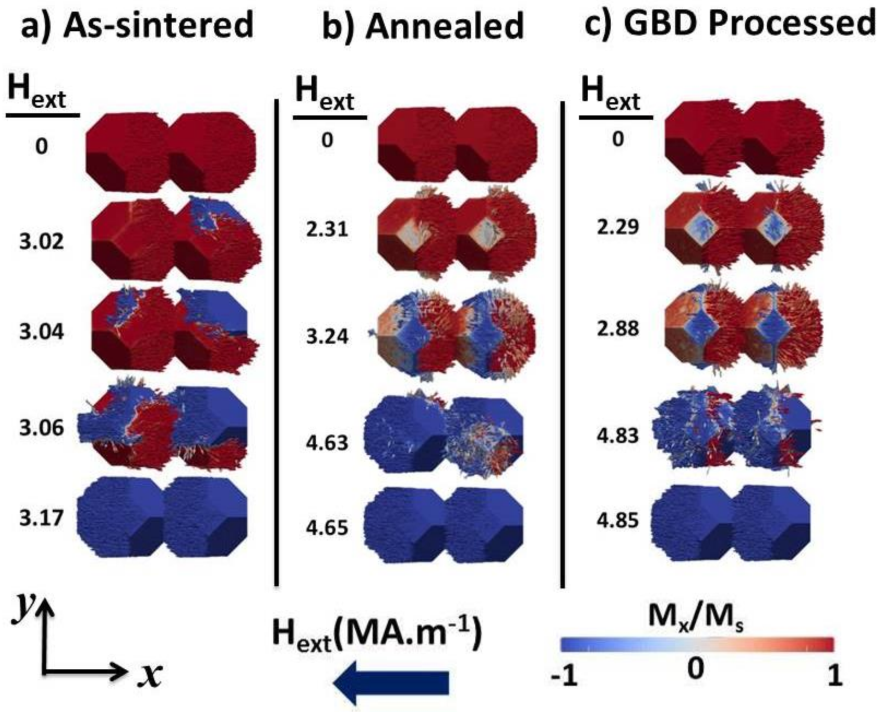

Figure 8.12 The magnetisation configurations of (a) the as-sintered, (b) annealed and (c) GBD processed samples. The number above each screenshot represents the value of H_{ext} in $MA.m^{-1}$.

The comparison between the three samples in this study revealed that using Dy diffusion increased H_c while maintaining the least possible drop in M_r may be best supported through the formation of non-ferromagnetic phases. Previous studies reported that GBD of Nd-Fe-B magnets using Dy-coating increased H_c from 1.04 to 1.62 $MA.m^{-1}$ [38], while the diffusion of $Nd_{70}Cu_{30}$ alloy increased H_c from 1.36 to 1.66 $MA.m^{-1}$ [64], which agrees with our modelled comparison between annealed and GBD samples. Our micromagnetic simulations suggested that a comparable H_c increase to GBD samples could be obtained by the diffusion of non-heavy RE elements, which is likely to reduce the exchange between adjacent $Nd_2Fe_{14}B$ grains and hence increase H_c.

8.3 Modelling twinned $Nd_2Fe_{14}B$ grains

In previous studies of this work, $Nd_2Fe_{14}B$ grains were assumed to have no structural defects in their volume. This perfect structure means reversed domain walls are more likely to be generated at the boundaries of $Nd_2Fe_{14}B$ grains or at the interface with intergranular phases [109, 110]. Then, the reversed domains walls are likely to propagate inside $Nd_2Fe_{14}B$ grains with no internal pinning sites in their way. Twinned grains are defined as grains that are divided in two or more regions with non-parallel anisotropy directions (see §3.7) [73, 74]. Hubert et al reported the presence of twinned $Nd_2Fe_{14}B$ phases with a 13° and 52° misorientation between the twin and parent regions [22]. EBSD maps of Dy-free, Red-Dy and Dy-rich magnets presented earlier (figures 6.5, 6.8 & 6.10, respectively) revealed the presence of misorientation between the anisotropy of adjacent grains. These grains may be in direct contact with each other as suggested by BSE images (see §5.4), and any misorientation in their anisotropy directions means that they behave similar to twinned regions. While twinned rhombohedral 2:17 cells were suggested improve H_c of Sm-Co magnets [78], the effect of twinned grains on the demagnetisation of Nd-Fe-B magnets has not been studied previously. Here, micromagnetic modelling was used to study the role of twinned grains in Nd-Fe-B magnets.

8.3.1 Modelling single twinned $Nd_2Fe_{14}B$ grains

The angle (θ_1 or θ_2) between the forming field (H) and the magnetocrystalline anisotropy (K_1) of the twinned regions at the alignment step prior to the sintering process (fig. 8.13) can be calculated from Zeeman energy equation (see §2.3.1), which is represented by:

$$E_z = -\mu_0 M H \cos\theta$$

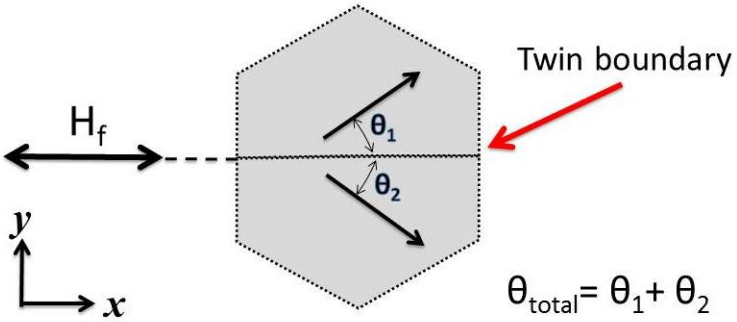

Figure 8.13 A schematic sketch of the relationship between the twin boundary and the anisotropy directions of twinned regions with the forming field (H_f).

The two twinned regions were aligned with the applied field (H) by angle θ_1 and θ_2, respectively:

$$E_z = -\mu_0 M_1 H \cos\theta_1 - \mu_0 M_2 H \cos\theta_2$$

$$E_z = [M_1 \cos\theta_1 + M_2 \cos\theta_2] \times (-\mu_0 H) \qquad (8.3)$$

the total angle between K_1 of the two twinned regions is:

$$\theta_{total} = \theta_1 + \theta_2 \qquad (8.4)$$

equation 8.3 becomes:

$$E_z = [M_1 \cos\theta_1 + M_2 \cos(\theta_{total} - \theta_1)] \times (-\mu_0 H)$$

then, by differentiating to θ_1:

$$\frac{\partial E_z}{\partial \theta_1} = -M_1 \sin\theta_1 + M_2 \sin(\theta_{total} - \theta_1) = 0$$

with assuming that both twinned regions have the same volume (fig. 8.13), hence M_1=M_2:

$$\sin\theta_1 = \sin(\theta_{total} - \theta_1)$$

$$\theta_1 = {}^{\theta_{total}}/_{2} \qquad (8.5)$$

and hence:

$$\theta_1 = \theta_2 \qquad (8.6)$$

This means the boundary between two twinned regions is likely to be parallel to H direction. In this study, the twinning plane was defined to be always parallel to applied field direction.

Here, models of truncated octahedron grains with a diameter of 100 nm that were divided in two or three regions with different anisotropy directions were used to represent twinned main phase grains. The first model consisted of two regions with the same volume and shape and was used to represent a two-fold twinned grain (fig 8.14a). The second model represented a three-fold twinned grain and it consisted of two twinned regions that have different anisotropy directions and another region that was always aligned with the H_{ext} direction (fig 8.14b). The volume of the aligned region was equal to the sum of the volumes of both twinned regions. The third model consisted of two regions with the same shape and volume separated by a layer with 10 nm thickness that represented the propagation of a twinning plane inside $Nd_2Fe_{14}B$ grains (fig 8.14c). This type of twinning was reported in Ti alloys [111].

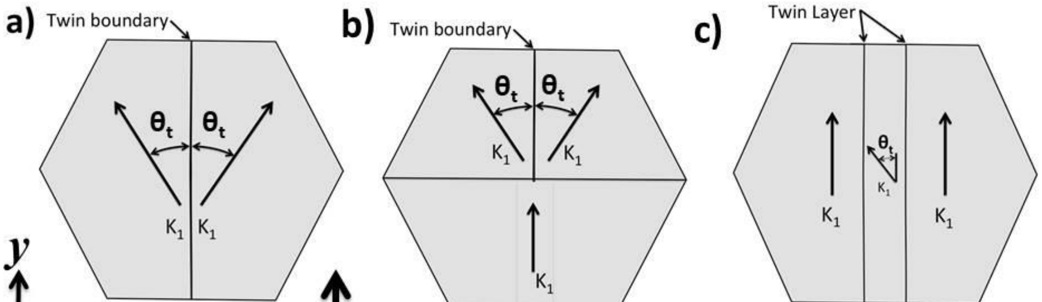

Figure 8.14 Schematic sketches of the twinned grains showing (a) two-fold, (b) three-fold and (c) layered models.

Modelling the effect of twinning on H_c and M_r of $Nd_2Fe_{14}B$ grains was achieved by simulating the three models denoted as two-fold (8.14a), three-fold (8.14b) and layered (8.14c) grains at different anisotropy directions of the twinned region (θ_t) to the applied field (H_{ext}). The value of θ_t in each model was defined to be between 0-90°. The magnetic properties of twinned phases were the same of $Nd_2Fe_{14}B$ phase, which are K_1=4.5 MJ.m^{-3}, μ_0M_s= 1.61T, A_{ex}= 12.1 pJ.m^{-1} at room temperature [101]. The hysteresis loops were modelled by changing the applied field at a rate of ±50 mT.ns^{-1} from +10T to -10T.

The modelled demagnetisation curves of two-fold twinned grain models showed that M_r and H_c decrease with increasing θ_t compared to the model with θ_t=0°, which represents a grain with no twinned regions (fig. 8.15). These reductions in H_c and M_r indicate that the generation of reversed domains walls in two-fold samples occurs at significantly low values of H_{ext}. On the other hand, H_c of two-fold (fig. 8.16a), three-fold (fig. 8.16b) and layered (fig. 8.16c) samples decreased significantly with increasing θ_t. In addition, M_r dropped in all models with increasing θ_t. However, H_c and M_r of the layered sample were less affected compared to the other two types of twinned models, which is a direct result of the smaller volume of the twinned region in the layered grain models.

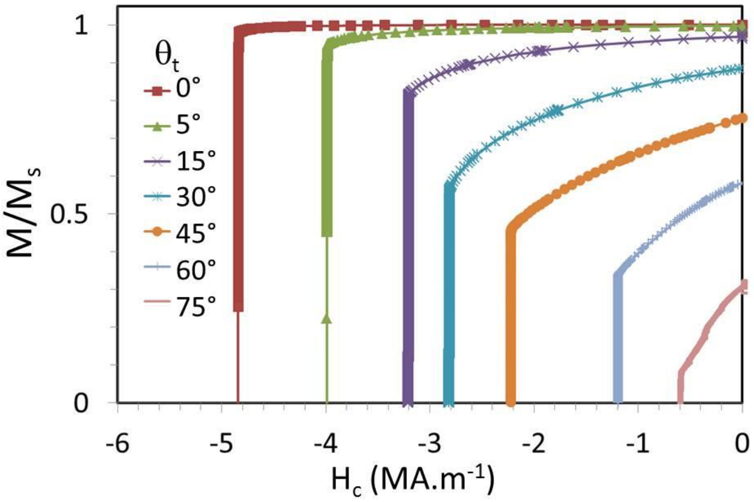

Figure 8.15 The modelled demagnetisation curves of two-fold twinned grains at θ_t=0-75°.

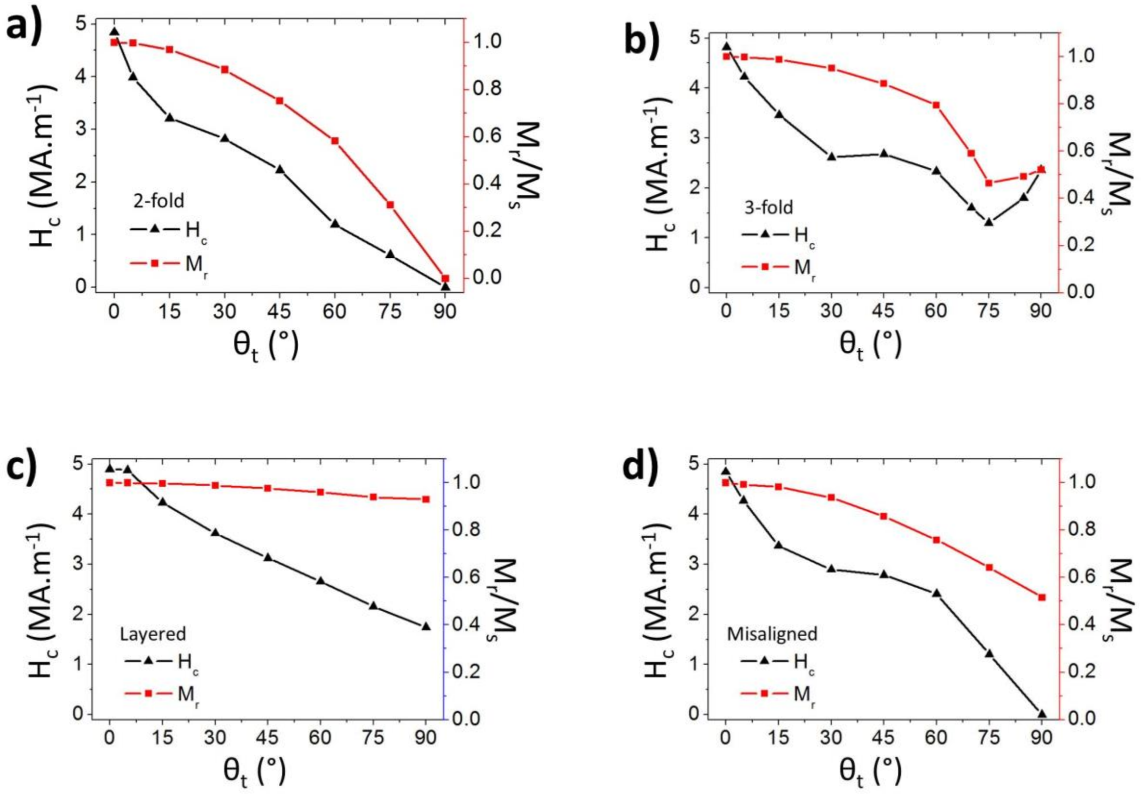

Figure 8.16 H_c and M_r at different θ_t for (a) two-fold, (b) three-fold and (c) layered models compared to (d) H_c and M_r of a misaligned grain model with no twinning in its structure.

The comparison between the models of twinned grains shows that 1) the effect of twinned regions depended strongly on their volume compared to the rest of the model and 2) the presence of twinned regions in $Nd_2Fe_{14}B$ grains is likely to reduce in H_c and M_r. Compared to a misaligned grain model with no twinned regions (fig. 8.16d), a two-fold grain can be more detrimental to H_c and M_r of Nd-Fe-B magnets. The misaligned grain showed a 42% drop in H_c and a 14% reduction in M_r at θ=45°, which is less than the reductions observed with two-fold twinned grains.

The modelled demagnetisation curves (fig. 8.16a) and configurations (fig. 8.16b) of the two-fold twinned grain model at θ_t=30° showed that the magnetisation of both twinned regions started switching in H_{ext} direction and away from the twinning plane at H_{ext}=2.03 MA.m^{-1}. The magnetisation at the interface between the twinned regions, in this case, appeared to be at an intermediate direction between the two twinned regions, which is similar to the magnetisation direction change inside a domain wall [22]. On the other hand, the reversal in the three-fold sample started at the twinned regions where an intermediate magnetisation direction at the interface area between these twinned regions was also observed (fig. 8.16c). The reversal of the layered grain model with θ_t=30° started at higher H_{ext}=3.09 MA.m^{-1} compared to the other two models (fig. 8.16c). This indicates that the magnetisation direction of smaller twinned regions was likely to be magnetically coupled to the magnetisation direction of adjacent larger regions. Yet, the generation of reversed domain walls occurred at the twinned layer and propagated to the rest of the sample. This study revealed that twinned main phase grains are likely to lead to the generation of reversed domain walls in sintered Nd-Fe-B magnets at lower H_{ext}. Although, the effect of twinned regions on H_c and M_r is dependent on their volume, the generation of reversed domain wall at lower H_{ext} is expected at these regions even when they have smaller volumes.

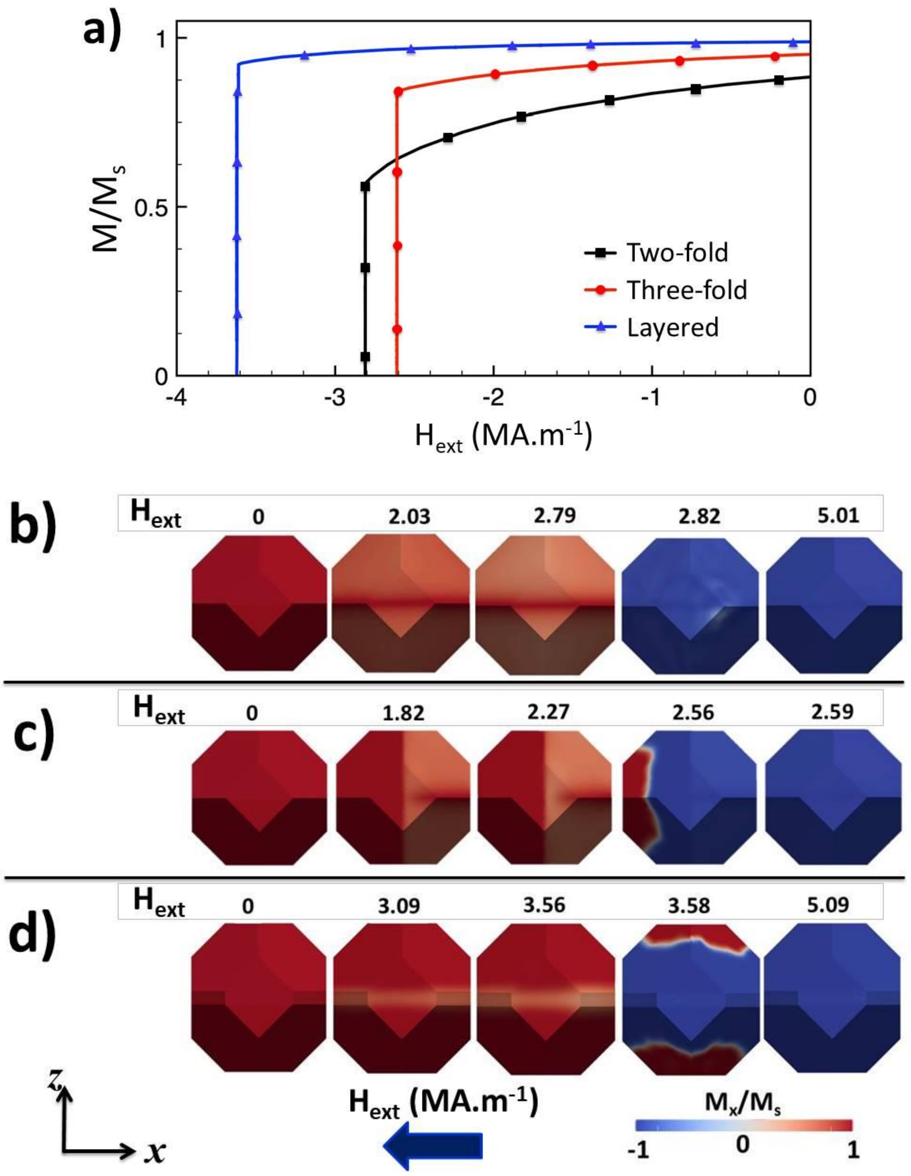

Figure 8.16 (a) The modelled demagnetisation curves and magnetisation configurations of (b) two-fold, (c) three-fold and (d) layered models at θ_t=30°. The number above each screenshot represents the value of H_{ext} in MA.m^{-1}.

The above study simulated the effect of twinned regions having θ_t with H_{ext} direction. However, the twinning boundary itself might not be aligned to forming field due to various effects such as particle relocation during sintering [26]. Here, the two-fold twinned grain model (fig. 8.14a) was used to simulate the effect of the misorientation of twinned grains from H_{ext}. The angle between the twin boundary and the applied field (ϕ) was allowed to vary between 0-90° (fig. 8.17) while θ_t was either 6.5° or 26° to represent the conditions observed experimentally (θ_{total}=13° and 52°, respectively) [22]. The magnetic properties of twinned regions were defined to be similar to $Nd_2Fe_{14}B$ phase and the hysteresis loops were modelled by changing H_{ext} from +10T to -10T at a rate of ±50 $mT.ns^{-1}$.

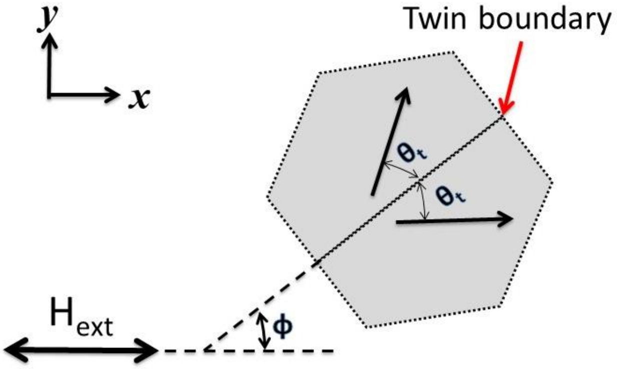

Figure 8.17 A schematic sketch of a twinned grain with a (ϕ) angle misalignment from H_{ext}.

Figure 8.18a compares H_c of twinned grains with θ_t =6.5° and 26° at different ϕ to H_{ext}. H_c of two-fold models had the highest values at ϕ =0° and decreased with increasing the angle ϕ from 0° to 30°. M_r also decreased with increasing ϕ for both models. This M_r decrease was estimated to be 29% at ϕ=45° compared to the initial values of both models (fig. 8.18b). Interestingly, M_r of θ_t =26° samples increased slightly at ϕ>60° due to the close alignment of one twinned region to the H_{ext} direction. This behaviour of H_c and M_r indicates that misaligned twinned grains are likely to have an adverse effect on H_c of Nd-Fe-B magnets than misaligned single grains (dashed line in fig. 8.18a and b).

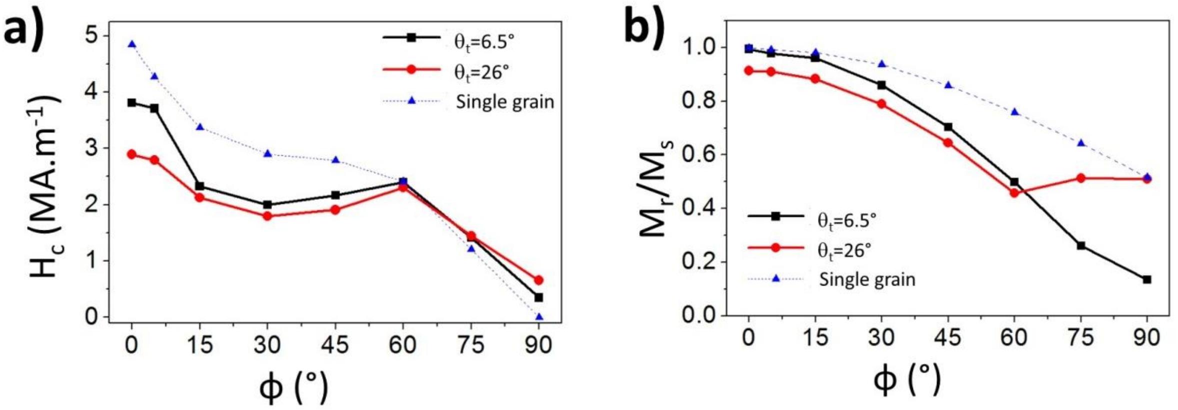

Figure 8.18 (a) H_c and (b) M_r of single two-fold grains with θ_t=6.5° & 26° at different angles ϕ with H_{ext}. The dashed line on both figures represents H_c and M_r of a single misaligned grain.

8.3.2 Eliminating the effect of twinned grains

The modelling of GB phases in Chapter 7 suggested that non-ferromagnetic GB phases could lead to the isolation of main phase grains from direct contact with each other, which in turn can reduce the effect of misaligned grains leading to improvements in H_c of Nd-Fe-B magnets. This approach can be used to eliminate the effect of twinned grains on the performance of sintered Nd-Fe-B magnets. In this study, micromagnetic modelling is used to assess the possibility of eliminating the effect of twinned grains by non-ferromagnetic GB phases.

Multigranular models of nine grains were used in this study where each grain had a diameter of 100 nm (fig. 8.19). These truncated octahedron grains are surrounded by 2 nm shells that are used to represent GB phases. The grain at the centre of the model is defined to be the twinned grain with θ_t=26° and made an angle $0° \leq \phi \leq 90°$ with the applied H_{ext}. This twinned grain was surrounded by eight non-twinned grains that each has an anisotropy direction parallel to H_{ext}. The GB phases were defined to be either soft magnetic with $\mu_0 M_s$=2.15T and A_{ex} = 25 pJ.m^{-1} or non-ferromagnetic with $\mu_0 M_s$=0T and A_{ex} = 1 fJ.m^{-1}. The magnetic properties of $Nd_2Fe_{14}B$ phase were similar to the values used earlier in §8.3.1. The hysteresis loops were modelled by changing H_{ext} from +10T to -10T at a rate of ±50 mT.ns^{-1}.

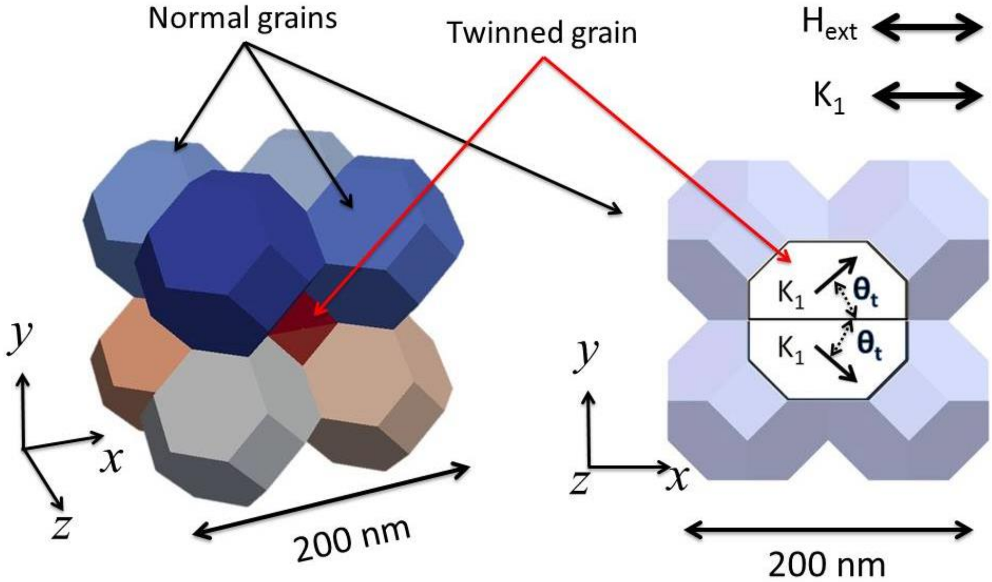

Figure 8.19 The multigranular model of a twinned grain surrounded by eight non-twinned grains showing the layout of the grains and the angular relationship between the anisotropy of the twinned regions and the applied field.

The modelled hysteresis loops of the multigranular models with ϕ=0° revealed two different demagnetisation processes depending on the type of GB phases (fig. 8.20). With soft GB phases, the magnetisation reversal was rapid with H_c=2.63 $MA.m^{-1}$. The magnetisation configurations of twinned grains with soft GB phases showed that the magnetisation reversal of twinned grains with ϕ=0° starts earlier than other grains at 2.55 $MA.m^{-1}$ (8.21a). Both twinned regions demagnetise fully at H_{ext}=2.63 $MA.m^{-1}$ and the reversed domain walls generated at these twinned regions propagate to neighbouring grains easily through the soft GB phases.

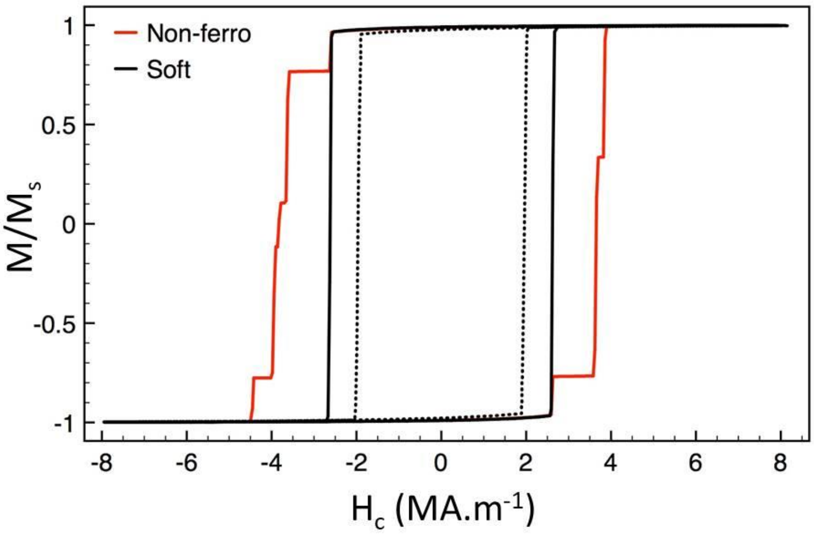

Figure 8.20 The modelled hysteresis loops of multigranular models with soft and non-ferromagnetic GB phases with ϕ=0°. The dashed line represents the hysteresis loop of a model with soft GB phase and ϕ=30°.

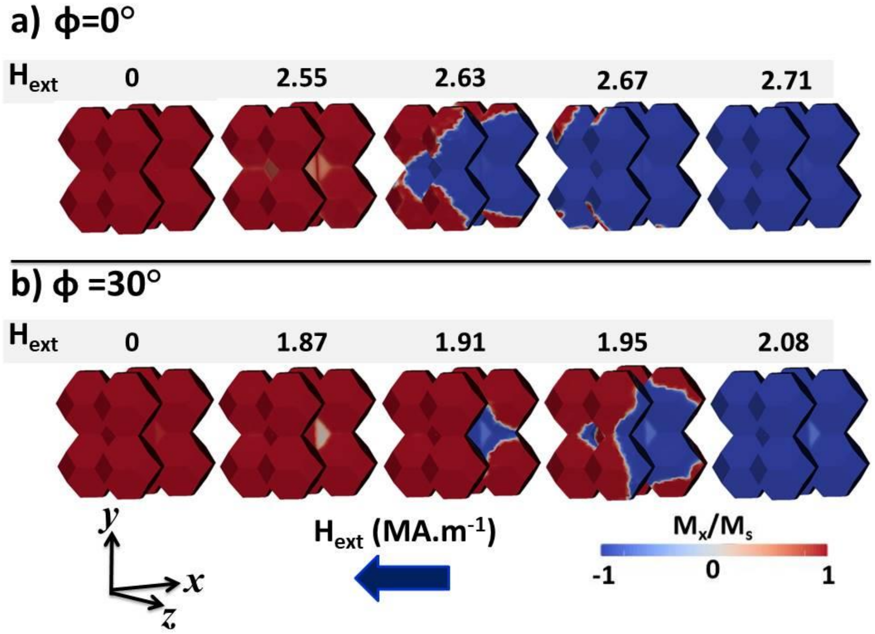

Figure 8.21 The magnetisation configuration of the multigranular model with soft GB phases and (a) ϕ=0° and (b) ϕ=30°. The number above each screenshot represents the value of H_{ext} in MA.m^{-1}.

Higher ϕ of twinned regions led to the generation of reversed domain walls at lower H_{ext} and hence lower H_C. For example, the reversal of magnetisation direction of the twinned grain with ϕ=30° (the dashed line in fig. 8.20) started at H_{ext}=1.87 MA.m^{-1} (fig. 8.21b). In this case, the reversed domain walls were generated at the particular twinned region with highest misorientation from H_{ext} direction.

The magnetisation reversal of models with non-ferromagnetic GB phases appears to start at the same H_{ext} but proceeded in a step-wise demagnetisation. The introduction of non-ferromagnetic GB phases played a similar role on twinned grains to misaligned grains (see §7.7). The magnetisation configurations of models with the $\phi=0°$ twinned grain indicated a halting to the cascade of reversed domains from the twinned grain to its neighbouring grains (fig. 8.22). In this model, reversed domain walls were also generated at the twinned grain (c) and followed by a gradual reversal of neighbouring grains with increasing H_{ext} (d, e, f and g). The full demagnetisation of the model was significantly higher than H_c of the models with soft GB phases.

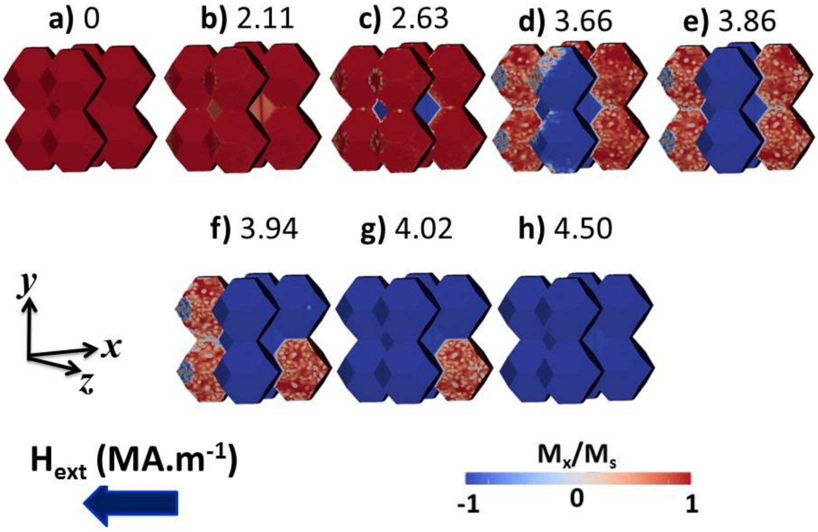

Figure 8.22 The magnetisation configuration of the multigranular model with non-ferromagnetic GB phases and $\phi=0°$. The number above each screenshot represents the value of H_{ext} in $MA.m^{-1}$.

The comparison of H_c of multigranular models with soft GB phases at $\phi=0-90°$ revealed a decrease in H_c with increasing ϕ until a value of 45°, where the values of H_c start to be almost identical even with further increase in ϕ (fig. 8.23a). This reduction in H_c was approximately

34% at ϕ=45° compared to its initial values. The introduction of non-ferromagnetic GB phases produced significantly higher H_c than soft GB models, which could be attributed to weaker exchange between the twinned grain and adjacent grains. Stronger effects are seen at ϕ>15° where GB phases eliminate the adverse effect of twinned regions.

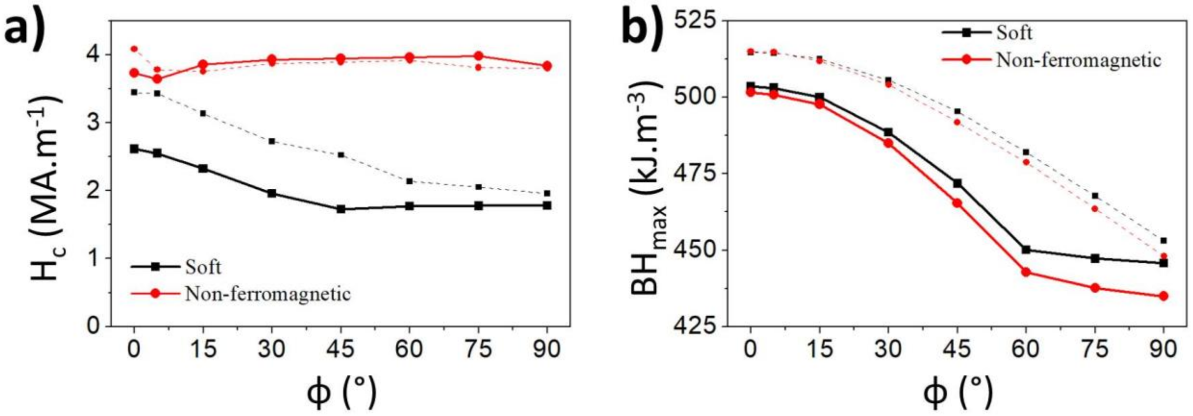

Figure 8.23 (a) H_c and (b) BH_{max} values of multigranular models with soft and non-ferromagnetic GB phases at different angles of misalignment (ϕ). The dashed lines represent eight-grain models with misaligned grains at the centre instead of the twinned grain.

Twinned grains led to reductions in BH_{max} of the samples even with non-ferromagnetic GB phases (fig. 8.23b). For example, BH_{max} of the models with soft GB phases dropped from 504 kJ.m^{-3} to 472 kJ.m^{-3} with increasing ϕ from 0° to 45°. These values of BH_{max} in samples with twinned grains compared to BH_{max}=515 kJ.m^{-3} from models with no twinned grains. Interestingly, the BH_{max} of models with non-ferromagnetic GB phases appeared to be slightly lower than models with soft GB phases. This was represented by BH_{max} of 502 kJ.m^{-3} and 465 kJ.m^{-3} at ϕ=0° and 45°, respectively. Finally, twinned grains were more detrimental to H_c and BH_{max} of Nd-Fe-B magnets compared to misaligned grains (dashed lines on both fig. 8.23a and 8.23b) with a misorientation angle equal to ϕ. The elimination of the existence or the influence of these two types of reversed domain generation sources is vital for higher H_c in Nd-Fe-B magnets.

8.4 Conclusions

Micromagnetic modelling was used to study the effect of changes in the internal structure of $Nd_2Fe_{14}B$ grains on the performance of sintered Nd-Fe-B magnets. These changes could result from post-sintering grain boundary diffusion processes and deformation twinning. For diffused samples, the micromagnetic models represented graded diffusion of Dy inside the volume of grains revealed an H_c increase with increasing thickness and Dy concentration of Dy-rich shells. In addition, the graded models revealed that these Dy-rich shells may lead to a decrease in M_r and hence BH_{max}. Our two-grain models revealed that higher rare-earth content at grain boundary regions is more promising than Dy-rich shells to achieve improvements in H_c with the least drop in M_r and BH_{max}.

Modelling twinned regions was achieved by simulating grains that consist of multiple regions with different anisotropy directions. These models revealed that twinned grains could be more detrimental to H_c and M_r than equivalent misaligned single grains. These regions led to the generation of reversed domain walls at lower H_{ext}. The amount of H_c and M_r reductions in this model was found to depend strongly on the twinning angle of twinned regions and their volume. The introduction of non-ferromagnetic exchange at grain boundary regions can lead to improved H_c as a result of pinning the reversed domain walls movement from the twinned regions to adjacent grains. However, the drop in M_r persists in models with non-ferromagnetic grain boundary phases even with increased H_c, which leads to reductions in BH_{max}. These models indicated that the presence of twinned grains could be detrimental to the performance of sintered Nd-Fe-B magnets, especially for applications that require high BH_{max} such as in clean energy production. One way to eliminate the presence of twinned grains is by reducing the average grain size of the sample. This will make the occurrence of twinning less likely compared to dislocations, for instance [75].

9.Summary and Future Recommendations

Commercial sintered Nd-Fe-B samples, that are typical of magnets used in wind turbines, were characterised using vibrating sample magnetometer, X-ray diffraction and scanning electron microscopy. These magnets have different Dy content and their microstructure was found to consist of main phase $Nd_2Fe_{14}B$ grains that are surrounded by a range of intergranular phases between adjacent grains an at triple junctions. These intergranular phases were found to have a different size, distribution and Fe/rare-earth ratios in each sample. The Dy-rich sample had the highest Dy content but was found to have lowest coercivity compared to samples with reduced amount of Dy (Red-Dy) and no Dy content (Dy-free). The latter sample was observed to have the highest coercivity. The elemental analysis through energy dispersive X-ray spectroscopy revealed that the highest Fe/rare-earth ratio in intergranular phases was found to be 2.9 in the Dy-free sample, 3.5 in the Red-Dy sample and 4.8 in Dy-rich sample. The backscattered electron diffraction analysis revealed that the angular dispersion of grain anisotropy was 15°, 30° and 75° in the Dy-free, Red-Dy and Dy-rich samples, respectively. The three samples were observed to have similar grain size distribution with the Dy-free sample showing a tighter distribution of grain sizes and the Dy-rich sample the broadest. The data obtained from microstructural characterisation was used to inform the micromagnetic modelling of rare-earth permanent magnets.

Our micromagnetic modelling used truncated octahedron shapes to represent main phase grains. The design of these models to have core-shell mesh arrangements allowed the modelling of main phase grains and their surrounding intergranular phases. In addition, the use of variable mesh sizes in these structures with a fine surface mesh (<4 nm) and a coarse interior mesh (>10 nm) produced sufficient resolution for the simulation of magnetisation processes and provided significant savings to processing time and capabilities. Modelling the microstructure of Nd-Fe-B magnets revealed that intergranular phases with high Fe/rare-earth ratios, which are likely to have soft magnetic characteristics (Fe-like), led to significant drops in the coercivity of main phase grains. In addition, these soft phases provided no pinning force to the propagation of domain walls. The formation of weakly magnetic intergranular phases (low Fe/rare-earth ratio) increased the coercive field of main phase grains and reduced the effect of misoriented grains. However, the effect of the magnetostatic interactions between adjacent grains was still noticeable.

Our micromagnetic modelling revealed that the difference in the angular dispersion of grain anisotropy in the studied Nd-Fe-B samples has the most significant effect on their coercivity. Our models revealed that decreasing the angular dispersion of main phase grains anisotropy from 30° to 1° can provide up to 25% increase in the coercivity. In addition, the elimination of the high Fe content from the intergranular phases of these samples can increase the coercivity to about 8% of its initial values; however, it is likely to lead to a step-wise hysteresis loops. The microstructure of Dy-free, Red-Dy and Dy-rich samples showed the presence of main phase grains that are significantly smaller in size compared to their adjacent grains. Our micromagnetic modelling revealed that the effect of grain size variation can be detrimental to the coercivity of these samples. The fabrication of Nd-Fe-B magnets with narrow grain size distribution eliminates this size variation and was found by our models to lead slightly increase (~1%) in the coercivity of these samples compared to their current lognormal size distribution when the grain are magnetically decoupled. However, narrowing the size distribution was revealed by our models to have no significant role on coercivity of Nd-Fe-B magnets when main phase grains are magnetically exchanged across the intergranular phases.

Micromagnetic modelling of the graded concentration of Dy in main phase grains due to post-sintering diffusion showed an increase in the sample's coercivity with increasing the Dy-rich shells thickness and Dy concentration. Our models revealed higher rare-earth content at intergranular phases has major contribution to the coercivity diffused samples. Although a significant increase in coercivity was observed in diffused sample simulations compared to as-sintered sample simulation, modelling of post-sintering annealed samples (no Dy diffusion) produced a comparable coercivity increase. Finally, micromagnetic modelling revealed that the effect of twinned grains on coercivity and remanence is more detrimental compared to misoriented grains. For example, a grain with a 45° twinning angle reduces the coercivity to about 54% of its initial values compared to a 42% drop in the coercivity of a grain with 45° anisotropy misorientation. The formation of weakly magnetic intergranular phases can eliminate the effect of twinned grains on adjacent grains but the drop in remanence and hence the maximum energy density still evident.

This work has focused on improving the understanding of the microstructural features of current sintered Nd-Fe-B magnets used in wind energy units. The combination of characterisation techniques and micromagnetic modelling attempted to assess the microstructure effect on the performance of these magnets. The results obtained can be used to improve the design and fabrication of sintered Nd-Fe-B magnets towards higher coercivity and maximum energy density at temperatures close to 200°C with maintaining reduced heavy rare-earth additions. This could be possible with production of sintered magnets with 1) small angular dispersion of main phase anisotropy, 2) the fabrication of samples with low Fe/rare-earth concentration at intergranular regions, 3) reducing the size variation of main phase grains and 4) eliminating twinned grains in the magnet microstructure.

The correlative use of electron microscopy and micromagnetic modelling can be extended to study the effect of other microstructural features. The following future work would build on the research in this thesis:

- Combine elemental analysis of intergranular phases and orientation mapping of main phase grains to investigate the relationship between the angular dispersion of main phase anisotropy and the chemistry and size of adjacent intergranular phases.
- Investigation of the effect of porosity on the reversed domain wall generation at adjacent main phase grains through electron microscopy and micromagnetic modelling.
- Transmission electron microscopy investigation of the twinning plane in the $Nd_2Fe_{14}B$ phase. The information obtained can be vital for future models of twinned grains.
- X-ray tomography of the size and distribution of intergranular phases and porosity to provide an estimate to the size proportions of these features compared to the main phase grains. This can improve the future micromagnetic models of sintered Nd-Fe-B magnets.
- Micromagnetic models of close-to-real proportions of main phase grains and Dy-rich shells. These improved models can provide an improved representation to the effect of Dy-rich shells on the coercivity and remanence.

In this thesis, it was demonstrated that the microstructure of Nd-Fe-B magnets could be optimized to produce higher coercivity than its current figures. These improvements offer an effective solution to the cost issue suffered currently in power generation and electric vehicle industries that are reliant on sintered Nd-Fe-B magnets. In addition, Nd-Fe-B magnets with improved performance offer new engineering possibilities to their current and prospective applications.

References

1. Constantinides, S. *The demand for rare earth materials in permanent magnets*. in *51st Annual Conference of Metallurgists*. 2012.
2. Gutfleisch, O., Willard, M.A., Brück, E., Chen, C.H., Sankar, S., and Liu, J.P., *Magnetic materials and devices for the 21st century: stronger, lighter, and more energy efficient.* Advanced materials, 2011. **23**(7): p. 821-842.
3. Sugimoto, S., *Current status and recent topics of rare-earth permanent magnets.* Journal of Physics D: Applied Physics, 2011. **44**(6): p. 064001.
4. Yang, Y., Walton, A., Sheridan, R., Güth, K., Gauß, R., Gutfleisch, O., Buchert, M., Steenari, B.-M., Van Gerven, T., and Jones, P.T., *REE Recovery from End-of-Life NdFeB Permanent Magnet Scrap: A Critical Review.* Journal of Sustainable Metallurgy, 2017. **3**(1): p. 122-149.
5. Hono, K. and Sepehri-Amin, H., *Strategy for high-coercivity Nd–Fe–B magnets.* Scripta Materialia, 2012. **67**(6): p. 530-535.
6. World-Wind-Energy-Association, *Small Wind World Report 2015*. 2015: Bonn, Germany: WWEA.
7. Coey, J., *Permanent magnets: Plugging the gap.* Scripta Materialia, 2012. **67**(6): p. 524-529.
8. Coey, J., *Hard magnetic materials: A perspective.* IEEE Transactions on magnetics, 2011. **47**(12): p. 4671-4681.
9. Li, W., Sepehri-Amin, H., Ohkubo, T., Hase, N., and Hono, K., *Distribution of Dy in high-coercivity (Nd, Dy)–Fe–B sintered magnet.* Acta Materialia, 2011. **59**(8): p. 3061-3069.
10. Argus, *Argus Rare Earths Monthly*. 2016: Singapore. p. 12. http://www.argusmedia.com.
11. Kronmüller, H., Fischer, R., Seeger, M., and Zern, A., *Micromagnetism and microstructure of hard magnetic materials.* Journal of Physics D: Applied Physics, 1996. **29**(9): p. 2274.
12. Kronmüller, H., *Micromagnetism in hard magnetic materials.* Journal of Magnetism and Magnetic Materials, 1978. **7**(1): p. 341-350.

13. Gutfleisch, O., *Controlling the properties of high energy density permanent magnetic materials by different processing routes.* Journal of Physics D: Applied Physics, 2000. **33**(17): p. R157.
14. Woodcock, T., Zhang, Y., Hrkac, G., Ciuta, G., Dempsey, N., Schrefl, T., Gutfleisch, O., and Givord, D., *Understanding the microstructure and coercivity of high performance NdFeB-based magnets.* Scripta Materialia, 2012. **67**(6): p. 536-541.
15. Jiles, D., *Introduction to magnetism and magnetic materials*. 2015: CRC press.
16. Spaldin, N.A., *Magnetic materials: fundamentals and applications*. 2010: Cambridge University Press.
17. O'handley, R.C., *Modern magnetic materials*. 2000: Wiley.
18. Chikazumi, S. and Graham, C.D., *Physics of Ferromagnetism 2e*. 2009: Oxford University Press on Demand.
19. Tannous, C. and Gieraltowski, J., *The Stoner–Wohlfarth model of ferromagnetism.* European journal of physics, 2008. **29**(3): p. 475.
20. Cullity, B.D. and Graham, C.D., *Introduction to magnetic materials*. 2011: John Wiley & Sons.
21. Callister, W.D., *Fundamentals of materials science and engineering: an interactive e-text.* 2001.
22. Hubert, A. and Schäfer, R., *Magnetic domains: the analysis of magnetic microstructures*. 2008: Springer Science & Business Media.
23. Allwood, D., Dean, J., and Hayward, T., *MAT6390 Magnetic materials and devices*. 2014, University of Sheffield: University of Sheffield, Sheffield, UK.
24. Croat, J.J., Herbst, J.F., Lee, R.W., and Pinkerton, F.E., *Pr-Fe and Nd-Fe-based materials: A new class of high-performance permanent magnets.* Journal of Applied Physics, 1984. **55**(6): p. 2078-2082.
25. Sagawa, M., Fujimura, S., Togawa, N., Yamamoto, H., and Matsuura, Y., *New material for permanent magnets on a base of Nd and Fe.* Journal of Applied Physics, 1984. **55**(6): p. 2083-2087.

26. Brown, D., Ma, B.-M., and Chen, Z., *Developments in the processing and properties of NdFeB-type permanent magnets.* Journal of Magnetism and Magnetic Materials, 2002. **248**(3): p. 432-440.
27. Sagawa, M., Hirosawa, S., Yamamoto, H., Fujimura, S., and Matsuura, Y., *Nd–Fe–B permanent magnet materials.* Japanese journal of applied physics, 1987. **26**(6R): p. 785.
28. Jadhav, A.P., Ma, H., Kim, D.S., Baek, Y.K., Choi, C.J., and Kang, Y.S., *Nd 2 Fe 14 B Synthesis: Effect of Excess Neodymium on Phase Purity and Magnetic Property*. Bulletin of the Korean Chemical Society, 2014. **35**(3): p. 886-890.
29. Sepehri-Amin, H., Ohkubo, T., Shima, T., and Hono, K., *Grain boundary and interface chemistry of an Nd–Fe–B-based sintered magnet.* Acta Materialia, 2012. **60**(3): p. 819-830.
30. Fidler, J. and Schrefl, T., *Overview of Nd–Fe–B magnets and coercivity.* Journal of Applied Physics, 1996. **79**(8): p. 5029-5034.
31. Woodcock, T. and Gutfleisch, O., *Multi-phase EBSD mapping and local texture analysis in NdFeB sintered magnets.* Acta Materialia, 2011. **59**(3): p. 1026-1036.
32. Buschow, K., *Permanent magnet materials based on tetragonal rare earth compounds of the type RFe12− xMx.* Journal of magnetism and magnetic materials, 1991. **100**(1-3): p. 79-89.
33. Reed, S.J.B. and Reed, S.J.B., *Electron microprobe analysis*. Vol. 2. 1975: Cambridge University Press Cambridge.
34. Herbst, J., Croat, J., and Yelon, W., *Structural and magnetic properties of Nd2Fe14B.* Journal of applied physics, 1985. **57**(8): p. 4086-4090.
35. Hrkac, G., Woodcock, T., Butler, K., Saharan, L., Bryan, M., Schrefl, T., and Gutfleisch, O., *Impact of different Nd-rich crystal-phases on the coercivity of Nd–Fe–B grain ensembles.* Scripta Materialia, 2014. **70**: p. 35-38.
36. Hrkac, G., Woodcock, T.G., Freeman, C., Goncharov, A., Dean, J., Schrefl, T., and Gutfleisch, O., *The role of local anisotropy profiles at grain boundaries on the coercivity of Nd2Fe14B magnets.* Applied Physics Letters, 2010. **97**(23): p. 232511.

37. Yin, X., Jones, I., and Harris, I., *The microstructural characterisation of Nd-Fe-B alloys. II: Microstructural investigation of cast Nd-Fe-B materials.* Journal of magnetism and magnetic materials, 1993. **125**(1-2): p. 91-102.

38. Sepehri-Amin, H., Ohkubo, T., and Hono, K., *The mechanism of coercivity enhancement by the grain boundary diffusion process of Nd–Fe–B sintered magnets.* Acta Materialia, 2013. **61**(6): p. 1982-1990.

39. Mishra, R.K., Chen, J., and Thomas, G., *Effect of annealing on the microstructure of sintered Nd-Fe-B magnets.* Journal of applied physics, 1986. **59**(6): p. 2244-2246.

40. Xin, F., Xiaolei, H., Zhiwei, D., Haibo, F., and Yanfeng, L., *Microstructural investigation of Nd-rich phase in sintered Nd-Fe-B magnets through electron microscopy.* Journal of Rare Earths, 2013. **31**(8): p. 765-771.

41. Mo, W., Zhang, L., Liu, Q., Shan, A., Wu, J., and Komuro, M., *Dependence of the crystal structure of the Nd-rich phase on oxygen content in an Nd–Fe–B sintered magnet.* Scripta Materialia, 2008. **59**(2): p. 179-182.

42. Kronmüller, H., *Theory of nucleation fields in inhomogeneous ferromagnets.* physica status solidi (b), 1987. **144**(1): p. 385-396.

43. Zhao, X.B., *Measurement and calculation of three-dimensional grain sizes and size distribution functions.* Microscopy and Microanalysis, 1998. **4**(4): p. 420-427.

44. Sagawa, M., *Review of sintering process development for Nd-Fe-B.* Journal of materials engineering, 1991. **13**(2): p. 95-101.

45. Herbst, J., *R 2 Fe 14 B materials: Intrinsic properties and technological aspects.* Reviews of Modern Physics, 1991. **63**(4): p. 819.

46. Manfred, F. and Kronmüller, H., *Micromagnetism and the microstructure of ferromagnetic solids*. 2003: Cambridge university press.

47. Fujisaki, J., Furuya, A., Uehara, Y., Shimizu, K., Oshima, H., Ohkubo, T., Hirosawa, S., and Hono, K., *Micromagnetic simulations of magnetization reversal in misaligned multigrain magnets with various grain boundary properties using large-scale parallel computing.* IEEE Transactions on Magnetics, 2014. **50**(11): p. 1-4.

48. Sepehri-Amin, H., Ohkubo, T., Gruber, M., Schrefl, T., and Hono, K., *Micromagnetic simulations on the grain size dependence of coercivity in anisotropic Nd–Fe–B sintered magnets.* Scripta Materialia, 2014. **89**: p. 29-32.

49. Elbaz, D., Givord, D., Hirosawa, S., Missell, F., Rossignol, M., and Villas-Boas, V., *Angular dependence of coercivity in sintered RFeB magnets.* Journal of Applied Physics, 1991. **69**(8): p. 5492-5494.

50. Givord, D., Tenaud, P., and Viadieu, T., *Angular dependence of coercivity in sintered magnets.* Journal of magnetism and magnetic materials, 1988. **72**(3): p. 247-252.

51. Yan, G., Williams, A., Farr, J., and Harris, I., *The effect of density on the corrosion of NdFeB magnets.* journal of Alloys and Compounds, 1999. **292**(1): p. 266-274.

52. Schrefl, T. and Fidler, J., *Numerical simulation of magnetization reversal in hard magnetic materials using a finite element method.* Journal of magnetism and magnetic materials, 1992. **111**(1-2): p. 105-114.

53. Cebollada, F., Rossignol, M., Givord, D., Villas-Boas, V., and González, J., *Angular dependence of coercivity in Nd-Fe-B sintered magnets: Proof that coherent rotation is not involved.* Physical Review B, 1995. **52**(18): p. 13511.

54. Hirosawa, S., *On the dependence of intrinsic coercivity on grain size in the nucleation-controlled rare earth-iron-boron sintered magnets.* IEEE Transactions on Magnetics, 1989. **25**(5): p. 3437-3439.

55. Ramesh, R. and Srikrishna, K., *Magnetization reversal in nucleation controlled magnets. I. Theory.* Journal of applied physics, 1988. **64**(11): p. 6406-6415.

56. Li, W., Ohkubo, T., Hono, K., and Sagawa, M., *The origin of coercivity decrease in fine grained Nd–Fe–B sintered magnets.* Journal of Magnetism and Magnetic Materials, 2009. **321**(8): p. 1100-1105.

57. Bance, S., Fischbacher, J., and Schrefl, T., *Thermally activated coercivity in core-shell permanent magnets.* Journal of Applied Physics, 2015. **117**(17): p. 17A733.

58. Vial, F., Joly, F., Nevalainen, E., Sagawa, M., Hiraga, K., and Park, K., *Improvement of coercivity of sintered NdFeB permanent magnets by heat treatment.* Journal of magnetism and magnetic materials, 2002. **242**: p. 1329-1334.
59. Loewe, K., Benke, D., Kübel, C., Lienig, T., Skokov, K., and Gutfleisch, O., *Grain boundary diffusion of different rare earth elements in Nd-Fe-B sintered magnets by experiment and FEM simulation.* Acta Materialia, 2017. **124**: p. 421-429.
60. Murakami, Y., Tanigaki, T., Sasaki, T., Takeno, Y., Park, H., Matsuda, T., Ohkubo, T., Hono, K., and Shindo, D., *Magnetism of ultrathin intergranular boundary regions in Nd–Fe–B permanent magnets.* Acta Materialia, 2014. **71**: p. 370-379.
61. Sepehri-Amin, H., Une, Y., Ohkubo, T., Hono, K., and Sagawa, M., *Microstructure of fine-grained Nd–Fe–B sintered magnets with high coercivity.* Scripta Materialia, 2011. **65**(5): p. 396-399.
62. Givord, D., Moreau, J., and Tenaud, P., *Nd5Fe18B18 (Nd1. 11Fe4B4), a new nowotny-like phase. structural and magnetic properties.* Solid state communications, 1985. **55**(4): p. 303-306.
63. Kim, T.-H., Lee, S.-R., Yun, S.J., Lim, S.H., Kim, H.-J., Lee, M.-W., and Jang, T.-S., *Anisotropic diffusion mechanism in grain boundary diffusion processed Nd–Fe–B sintered magnet.* Acta Materialia, 2016. **112**: p. 59-66.
64. Chen, F., Zhang, T., Wang, J., Zhang, L., and Zhou, G., *Coercivity enhancement of a Nd–Fe–B sintered magnet by diffusion of Nd 70 Cu 30 alloy under pressure.* Scripta Materialia, 2015. **107**: p. 38-41.
65. Löewe, K., Brombacher, C., Katter, M., and Gutfleisch, O., *Temperature-dependent Dy diffusion processes in Nd–Fe–B permanent magnets.* Acta Materialia, 2015. **83**: p. 248-255.
66. Fidler, J. and Schrefl, T., *Micromagnetic modelling-the current state of the art.* Journal of Physics D: Applied Physics, 2000. **33**(15): p. R135.
67. Gao, R., Zhang, D., Li, H., and Zhang, J., *Effects of the degree of grain alignment on the hard magnetic properties of sintered NdFeB magnets.* Applied Physics A: Materials Science & Processing, 1998. **67**(3): p. 353-356.

68. Schrefl, T., Schmidts, H., Fidler, J., and Kronmüller, H., *The role of exchange and dipolar coupling at grain boundaries in hard magnetic materials.* Journal of magnetism and magnetic materials, 1993. **124**(3): p. 251-261.
69. Suss, D., Schrefl, T., and Fidler, J., *Micromagnetics simulation of high energy density permanent magnets.* IEEE transactions on magnetics, 2000. **36**(5): p. 3282-3284.
70. Fischer, R., Schrefl, T., Kronmüller, H., and Fidler, J., *Grain-size dependence of remanence and coercive field of isotropic nanocrystalline composite permanent magnets.* Journal of magnetism and magnetic materials, 1996. **153**(1): p. 35-49.
71. Bance, S., Seebacher, B., Schrefl, T., Exl, L., Winklhofer, M., Hrkac, G., Zimanyi, G., Shoji, T., Yano, M., and Sakuma, N., *Grain-size dependent demagnetizing factors in permanent magnets.* Journal of Applied Physics, 2014. **116**(23): p. 233903.
72. Oikawa, T., Yokota, H., Ohkubo, T., and Hono, K., *Large-scale micromagnetic simulation of Nd-Fe-B sintered magnets with Dy-rich shell structures.* AIP Advances, 2016. **6**(5): p. 056006.
73. Christian, J.W. and Mahajan, S., *Deformation twinning.* Progress in materials science, 1995. **39**(1-2): p. 1-157.
74. Mahajan, S. and Williams, D., *Deformation twinning in metals and alloys.* International Metallurgical Reviews, 1973. **18**(2): p. 43-61.
75. Zhu, Y., Liao, X., and Wu, X., *Deformation twinning in nanocrystalline materials.* Progress in Materials Science, 2012. **57**(1): p. 1-62.
76. Dennis, C., Borges, R., Buda, L., Ebels, U., Gregg, J., Hehn, M., Jouguelet, E., Ounadjela, K., Petej, I., and Prejbeanu, I., *The defining length scales of mesomagnetism: a review.* Journal of Physics: Condensed Matter, 2002. **14**(49): p. R1175.
77. Chu, T.Y., Rabenberg, L., and Mishra, R., *Evolution of the microstructure of rapidly solidified Nd-Fe-B permanent magnets.* Journal of Applied Physics, 1991. **69**(8): p. 6046-6048.

78. Feng, H., Chen, H., Guo, Z., Yu, R., and Li, W., *Twinning structure in Sm (Co, Fe, Cu, Zr) z permanent magnet.* Intermetallics, 2010. **18**(5): p. 1067-1071.

79. Guinebretière, R., *X-ray diffraction by polycrystalline materials*. 2013: John Wiley & Sons.

80. Reeves-McLaren, N., *MAT6665 Materials Processing and Characterisation*. 2014: The university of Sheffield.

81. Kelsall, R.W., Hamley, I.W., and Geoghegan, M., *Nanoscale science and technology*. 2005: Wiley Online Library.

82. Schwartz, A.J., Kumar, M., Adams, B.L., and Field, D.P., *Electron backscatter diffraction in materials science*. Vol. 2. 2009: Springer.

83. Wright, S.I., Nowell, M.M., and Field, D.P., *A review of strain analysis using electron backscatter diffraction.* Microscopy and microanalysis, 2011. **17**(03): p. 316-329.

84. Randle, V., *Electron backscatter diffraction: Strategies for reliable data acquisition and processing.* Materials Characterization, 2009. **60**(9): p. 913-922.

85. Binnemans, K., Jones, P.T., Blanpain, B., Van Gerven, T., Yang, Y., Walton, A., and Buchert, M., *Recycling of rare earths: a critical review.* Journal of Cleaner Production, 2013. **51**: p. 1-22.

86. HKL, O.I., *HKL Channel 5 user manual*. 2007, Oxford Instruments: Denmark. p. 475.

87. Ramesh, R., Thomas, G., and Ma, B., *Magnetization reversal in nucleation controlled magnets. II. Effect of grain size and size distribution on intrinsic coercivity of Fe-Nd-B magnets.* Journal of applied physics, 1988. **64**(11): p. 6416-6423.

88. Higginson, R.L. and Sellars, C.M., *Worked examples in quantitative metallography*. Vol. 788. 2003: Maney Pub.

89. Kittel, C. and Galt, J., *Ferromagnetic domain theory.* Solid State Physics, 1956. **3**: p. 437-564.

90. Scholz, W., Fidler, J., Schrefl, T., Suess, D., Forster, H., and Tsiantos, V., *Scalable parallel micromagnetic solvers for magnetic nanostructures.* Computational Materials Science, 2003. **28**(2): p. 366-383.
91. Tako, K., Schrefl, T., Wongsam, M., and Chantrell, R., *Finite element micromagnetic simulations with adaptive mesh refinement.* Journal of applied physics, 1997. **81**(8): p. 4082-4084.
92. Rao, S.S., *The finite element method in engineering*. 2010: Elsevier.
93. Brenner, S. and Scott, R., *The mathematical theory of finite element methods*. Vol. 15. 2007: Springer Science & Business Media.
94. Geuzaine, C. and Remacle, J.F., *Gmsh: A 3-D finite element mesh generator with built-in pre-and post-processing facilities.* International journal for numerical methods in engineering, 2009. **79**(11): p. 1309-1331.
95. Abo, G.S., Hong, Y.-K., Park, J., Lee, J., Lee, W., and Choi, B.-C., *Definition of magnetic exchange length.* IEEE Transactions on Magnetics, 2013. **49**(8): p. 4937-4939.
96. Sasaki, T., Ohkubo, T., Une, Y., Kubo, H., Sagawa, M., and Hono, K., *Effect of carbon on the coercivity and microstructure in fine-grained Nd–Fe–B sintered magnet.* Acta Materialia, 2015. **84**: p. 506-514.
97. Sasaki, T., Ohkubo, T., Hono, K., Une, Y., and Sagawa, M., *Correlative multi-scale characterization of a fine grained Nd–Fe–B sintered magnet.* Ultramicroscopy, 2013. **132**: p. 222-226.
98. Nowell, M.M. and Wright, S.I., *Orientation effects on indexing of electron backscatter diffraction patterns.* Ultramicroscopy, 2005. **103**(1): p. 41-58.
99. Fidler, J. and Knoch, K., *Electron microscopy of Nd-Fe-B based magnets.* Journal of magnetism and magnetic materials, 1989. **80**(1): p. 48-56.
100. Sasaki, T., Ohkubo, T., and Hono, K., *Structure and chemical compositions of the grain boundary phase in Nd-Fe-B sintered magnets.* Acta Materialia, 2016. **115**: p. 269-277.
101. Sepehri-Amin, H., Prabhu, D., Hayashi, M., Ohkubo, T., Hioki, K., Hattori, A., and Hono, K., *Coercivity enhancement of rapidly solidified Nd–Fe–B magnet powders.* Scripta Materialia, 2013. **68**(3): p. 167-170.

102. Wright, S.I., Nowell, M.M., Lindeman, S.P., Camus, P.P., De Graef, M., and Jackson, M.A., *Introduction and comparison of new EBSD post-processing methodologies.* Ultramicroscopy, 2015. **159**: p. 81-94.

103. Liu, N. and Kim, A., *Abnormal grain growth in sintered Nd-Fe-B magnets.* Journal of Applied Physics, 1990. **67**(9): p. 4629-4631.

104. Bittner, F., Woodcock, T., Schultz, L., Schwöbel, C., Gutfleisch, O., Zickler, G., Fidler, J., Üstüner, K., and Katter, M., *Normal and abnormal grain growth in fine-grained Nd-Fe-B sintered magnets prepared from He jet milled powders.* Journal of Magnetism and Magnetic Materials, 2017. **426**: p. 698-707.

105. Shinba, Y., Konno, T., Ishikawa, K., Hiraga, K., and Sagawa, M., *Transmission electron microscopy study on Nd-rich phase and grain boundary structure of Nd–Fe–B sintered magnets.* Journal of applied physics, 2005. **97**(5): p. 053504.

106. Schrefl, T., Schmidts, H., Fidler, J., and Kronmuller, H., *Nucleation fields and grain boundaries in hard magnetic materials.* IEEE transactions on magnetics, 1993. **29**(6): p. 2878-2880.

107. Schrefl, T. and Fidler, J., *Modelling of exchange-spring permanent magnets.* Journal of magnetism and magnetic materials, 1998. **177**: p. 970-975.

108. Ohkubo, T., Abe, T., Hirosawa, S., and Hono, K., *Faceted shell structure in grain boundary diffusion-processed sintered Nd–Fe–B magnets.* Journal of Alloys and Compounds, 2014. **617**: p. 884-892.

109. Hadjipanayis, G.C. and Kim, A., *Domain wall pinning versus nucleation of reversed domains in R-Fe-B magnets.* Journal of applied physics, 1988. **63**(8): p. 3310-3315.

110. Khlopkov, K., Gutfleisch, O., Hinz, D., Müller, K.-H., and Schultz, L., *Evolution of interaction domains in textured fine-grained Nd2Fe14B magnets.* Journal of Applied Physics, 2007. **102**(2): p. 023912.

111. Lai, M., Tasan, C.C., and Raabe, D., *On the mechanism of {332} twinning in metastable β titanium alloys.* Acta Materialia, 2016. **111**: p. 173-186.